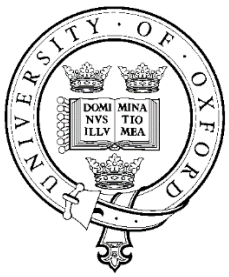
FLEXOELECTRICITY AND MULTI-DIMENSIONAL STRUCTURES FOR LIQUID CRYSTAL PHOTONICS



CHLOE C. TARTAN

Linacre College

University of Oxford

A thesis submitted for the degree of

Doctor of Philosophy

Michaelmas Term 2017

ACKNOWLEDGEMENTS

First and above all, I would like to thank my supervisors, Steve Elston and Steve Morris. As a research group, we are infinitely lucky to have the support of the two Steve's, as they both bring individual qualities that form the foundations of the best group in Oxford. Steve E, I struggle to find the words that could describe the impact that you have had on my life during my time at Oxford. Undoubtedly one of the most intelligent humans I have had the fortune of encountering, discussions with you make the most complex of problems surmountable. I thank you for all your patience and hard work in ensuring that I make it to the end. The most unexpected gift of all however has been that alongside a phenomenal supervisor, I have found a wonderful friend. Steve Morris, your kindness has no bounds and I thank you for your unwavering patience over the years, especially every time that I have knocked at your door for 'one question'. I am truly grateful that I was given the opportunity to join you on your journey to Oxford and it gives me great pleasure to see how the group has evolved from the very first day that it all began four years ago. On that note, I have a growing list of comrades to thank, especially for their support during the rocky end. David Hansford, my first friend at Oxford, I am so pleased that we have been on this journey together. Working with you is a true delight as you always manage to find a way to lighten the darkest of days. Ellis Parry, my rock and my best friend. I will never forget one of your first talks to the group about your leaky print head ('Dorothy'). From that moment on, you had my attention. To the newer members of the group, John Sanford O'Neill, I'm so pleased that our paths have crossed; your warmth and kindness knows no bounds. Serena Bolis, the genius. Thank you for your immense generosity and sharing your extensive knowledge whenever it was called upon. Konrad the warrior, it was always a delight to be greeted by your smile in the office. Julian Fells, thank you for always making the time to come and chat with me, in whatever stressful state I may have been in. Taimoor, it's been a pleasure albeit brief but I wish you all the best in your future. Also, a big thank you to Patrick Salter and Martin Booth for the fruitful discussions and long hours spent in the labs. To all my friends in Oxford that have made sure I am the best version of myself, no words can describe how grateful I am to have found you all. Last but not least, I thank my mother and my sister. Without these two incredible women I would not be where I am today or the person that I am today. So thank you, I hope to make you proud.

FLEXOELECTRICITY AND MULTI-DIMENSIONAL STRUCTURES FOR LIQUID CRYSTAL PHOTONICS

Submitted for the degree of Doctor of Philosophy

Chloe C. Tartan, Linacre College, Michaelmas Term 2017

The investigations carried out in this thesis involve the characterization and the manipulation of dielectric and flexoelectric phenomena in liquid crystalline systems. The first half of the thesis considers the flexoelectric effect in achiral and chiral nematic liquid crystals (LCs). These chapters demonstrate a new approach to measure the sum of the flexoelectric coefficients in achiral nematic LCs confined to hybrid aligned and planar-aligned geometries. The importance of ionic effects was considered, and the experimental and theoretical findings highlight the covariance between the ionic concentration and the flexoelectric coefficients.

Observations of the flexoelectro-optic (FEO) effect in chiral nematic LCs were carried out by first inducing a uniform lying helix (ULH) alignment so that an electric field could be applied perpendicular to the helical axis. A polymer templating method was implemented initially, which was found to enhance the FEO tilt angle compared with that observed following a bulk polymerization technique, but was inferior to the electro-optic response measured prior to the polymerization process.

Using an alternative approach, an in-situ direct laser writing (DLW) technique was employed to confine the polymer network to localised regions (polymer walls) within the device. Encouragingly, the ULH alignment was spontaneously formed when periodic polymer walls were written in the nematic phase (induced by applying a relatively large electric field to the device so as to unwind the helical structure) and spaced at the order of the device thickness. Fabrication of polymer walls in the chiral nematic phase was also investigated where it was found that the quality of the alignment was lower than that observed for polymer walls written in the nematic phase.

The second half of the thesis demonstrates the manipulation of electro-optic phenomena by exploiting the dynamic aberration correction element inherent in the DLW facility. It is shown that electrically tunable defects can be formed from two-dimensional polymer structures written in topologically discontinuous states. Three-dimensional polymer structures were also created in the form of arrays of pillars, polymer helices and polymer knots. In the final experimental chapter, results are presented that demonstrate the creation of reconfigurable optical elements based upon these polymerizable LC devices, whereby a simple emoticon is used to show how different features can be made to appear and disappear at specific applied voltages.

CONTENTS

GLOSSARY vii
PATENTS & PUBLICATIONS ix
PRESENTATIONS x
1. INTRODUCTION 1
1.1. Liquid Crystals 1
1.1.1. The Nematic Phase 1
1.1.2. The Chiral Nematic Phase 3
1.2. Elastic Properties 4
1.2.1. Bulk Energy 4
1.3. Electric Properties 6
1.3.1. Dielectric Energy 6
1.3.2. Flexoelectricity 8
1.4. Optical Properties 11
1.4.1. Polarization & Birefringence 11
1.4.2. Jones Matrices 12
1.4.3. Chiral Optics 14
1.5. Device Structure 17
1.5.1. A Liquid Crystal Cell 17
1.5.2. Alignment Layer 18
1.6. Reactive Mesogens 20
1.7. Numerical Model 21
1.8. Liquid Crystals for Soft Matter Photonics 23
1.9. Conclusions 24
1.10. References 25
2. THE FLEXOELECTRIC EFFECT IN HYBRID ALIGNED NEMATICS 27
2.1. Introduction 27
2.1.1. Flexoelectricity in Hybrid Alignments 27
2.1.2. The Flexoelectric Coefficients 28
2.1.3 The Flexoelectric Torque 31
2.1.4. Numerical Model 32

2.1.5. Flexoelectric Measurements 35
2.1.6. Internal Bias 38
2.2. Experimental Arrangement 41
2.2.1. Ionic Screening 42
2.2.2. Device Parameters 46
2.3. Theoretical Modelling 50
2.4. Results & Discussion 54
2.5. Conclusions 57
2.6. References 58
3. THE FLEXOELECTRIC EFFECT IN NEMATIC PI-CELLS 59
3.1. Introduction 59
3.1.1. Uniform Alignments 59
3.1.2. Non-Ionic Fréedericksz Cells 60
3.1.3 Ionic Fréedericksz Cells 61
3.1.4. Flexoelectricity in Nematic Pi-Cells 63
3.2. Numerical Model 67
3.3. Experimental Arrangement 71
3.4. Results & Discussion 73
3.5. Conclusions 76
3.6. References 76
4. THE FLEXOELECTRO-OPTIC EFFECT & POLYMER TEMPLATES 78
4.1. Introduction 78
4.1.1. The Flexoelectro-Optic Effect 78
4.1.2. The Tilt Angle 79
4.1.3. Uniform Lying Helix 82
4.1.4. Polymer Templating 83
4.2. Experimental Procedure 85
4.2.1. Materials & Sample Preparation 85
4.2.2. Reorienting the Helix 86
4.2.3. ULH Formation 89
4.2.4. Polymer Templating 90
4.2.5. Electro-Optic Response 92
4.3. Results & Discussion 94

4.3.1. Pre-Cure ULH 94
4.3.2. Post-Cure ULH 95
4.3.3. Templated ULH 97
4.4. Conclusions 102
4.5. References 103
5. DIRECT LASER WRITING & ADAPTIVE OPTICS 105
5.1. Introduction 105
5.1.1. Structuring Polymer Networks 105
5.2. Direct Laser Writing 107
5.2.1. Two-Photon Photopolymerization 107
5.2.2. Aberration Correction 109
5.2.3. In-Situ Fabrication System 112
5.3. Experimental Procedure 114
5.3.1. Materials & Sample Preparation 114
5.3.2. Optical Realignment Effects 116
5.4. Polymer Network Structures 119
5.4.1. Pillar Arrays 119
5.4.2. Disclination Networks 125
5.5. Conclusions 129
5.6. References 130
6. FAST-SWITCHING PHOTONIC STATES 132
6.1. Introduction 132
6.1.1. The Tilt Angle 132
6.1.2. Periodic Anchoring 133
6.2. Experimental Procedure 134
6.3. Results & Discussion 138
6.3.1. Homeotropic Polymer Walls 138
6.3.2. Electro-Optic Response 143
6.3.3. Chiral Nematic Polymer Walls 146
6.3.4. Electro-Optic Response 146
6.3.5. Possible Improvements in Selection of Materials 150
6.4. Conclusions 152
6.5. References 153

7. TUNABLE TOPOLOGICAL DEFECTS 155
7.1. Introduction 155
7.1.1. Colloids & Topological Defects 155
7.2. Experimental Procedure 158
7.2.1. Materials & Sample Preparation 158
7.2.2. Fabrication Procedure 159
7.3. Results & Discussion 160
7.3.1. Polymer Walls 160
7.3.1.1. Numerical Model 163
7.3.2. Polymer Cavities 171
7.3.2.1. Analytical Model 176
7.3.3. Arrays & Concentricity 185
7.3.4. Colloidal Dispersions 189
7.4. Conclusions 192
7.5. References 193
8. RECONFIGURABLE OPTICAL ELEMENTS 195
8.1. Introduction 195
8.2. Experimental Procedure 197
8.3. Numerical Model 201
8.4. Results & Discussion 203
8.4.1. Image Analysis 207
8.4.2. Colour Filters 211
8.4.3. Spatial Tuning of Arrays 215
8.4.4. Complex Structures 217
8.5. Conclusions 219
8.6. References 219
9. CONCLUSIONS 222
10. FUTURE WORK 228
10.1. References 234
A. APPENDIX 235

GLOSSARY

LIST OF ABBREVIATIONS

AGGREGATION-INDUCED EMISSION	AIE
ALTERNATING CURRENT	AC
ARBITRARY WAVEFORM GENERATOR	AWG
ASYMMETRIC SPLAY STATE	H_a-STATE
ATOMIC FORCE MICROSCOPY	AFM
BEND STATE	V-STATE
CHARGE COUPLED DEVICE	CCD
CIRCULARLY POLARIZED	CP
CYANO	CN
CYANOBIPHENYL	CB
DIRECT CURRENT	DC
DIRECT LASER WRITING	DLW
FLEXOELECTRIC-OPTIC	FEO
HELICAL TWISTING POWER	HTP
HELIUM-NEON	He-Ne
HYBRID ALIGNED NEMATIC	HAN
INDIUM TIN OXIDE	ITO
IRGACURE	IRG
LIGHT EMITTING DIODE	LED
LINEARLY POLARIZED	LP
LIQUID CRYSTAL	LC
LIQUID CRYSTAL DISPLAY	LCD
NUMERICAL APERTURE	NA
OPTICAL POLARIZING MICROSCOPE	OPM
OPTICALLY COMPENSATED BEND	OCB
PHOTOLUMINESCENCE	PL
PHOTONIC BANDGAP	PBG
POLYMER LIQUID CRYSTAL POLYMER SLICES	POLICRYPS
QUANTUM DOT	QD
REACTIVE MESOGEN	RM
SCANNING ELECTRON MICROSCOPY	SEM
SPATIAL LIGHT MODULATOR	SLM
SPLAY STATE	H-STATE
SYMMETRIC SPLAY STATE	H_S-STATE
TWIST STATE	T-STATE
TWISTED NEMATIC	TN
TWO-PHOTON ABSORPTION	TPA
TWO-PHOTON PHOTOPOLYMERIZATION	TPP
ULTRA-VIOLET	UV
UNIFORM LYING HELIX	ULH
UNIFORM STANDING HELIX	USH

LIST OF SYMBOLS

ABSORPTION CROSS-SECTION	σ
CHARACTERISTIC TIME	τ
DEVICE THICKNESS	d
DIELECTRIC PERMITTIVITY	ε
DIRECTOR	$\hat{\mathbf{n}}$
ELASTIC CONSTANT	K
ELECTRIC DISPLACEMENT	$\mathbf{D}$
ELECTRIC FIELD	$\mathbf{E}$
ELECTRIC POLARIZATION	$\mathbf{P}$
FLEXOELECTRIC COEFFICIENT	e
FLEXOELECTRIC TILT/TWIST ANGLE	Φ
FREE ENERGY (TOTAL)	F
FREE ENERGY DENSITY	f
INTENSITY (ELECTROMAGNETIC)	I
IONIC CHARGE DENSITY	ρ
IONIC CONCENTRATION	N
IONIC DIFFUSION CONSTANT	$D^{\pm}$
IONIC DRIFT CONSTANT	$J^{\pm}$
IONIC GENERATION CONSTANT	β
IONIC MOBILITY	μ
IONIC RECOMBINATION CONSTANT	α
LASER FOCUS AREA (LATERAL)	A_{f}
LASER POWER (AVERAGE)	P_{av}
LASER PULSE DURATION	τ_{pd}
LASER PULSE ENERGY	E_{p}
MOLECULAR FIELD	$\mathbf{h_f}$
OPTIC AXIS - POLARIZER ANGLE	χ
ORDER PARAMETER (SCALAR)	S
ORDER PARAMETER (TENSOR)	Q
PHASE DELAY	δ
PITCH	P
POTENTIAL VOLTAGE	V
REFRACTIVE INDEX	n
ROTATIONAL VISCOSITY	γ
SURFACE ANCHORING ENERGY	W
TEMPERATURE	T
TILT ANGLE	θ
TIME	t
TOPOLOGICAL DEFECT CHARGE	m
TORQUE	$\mathbf{\Gamma}$
TRANSITION REGION	ξ
TRANSMISSION (ELECTROMAGNETIC)	T
WAVELENGTH	λ
WAVENUMBER (LIQUID CRYSTAL HELIX)	q

PATENTS & PUBLICATIONS

1. C.C. Tartan, J. Sandford O'Neill, P.S. Salter, M.J. Booth, S.M. Morris and S.J. Elston, *UK Patent, to be filed* (2018)
2. C.C. Tartan, J. Sandford O'Neill, P.S. Salter, J. Aplinc, M.J. Booth, M. Ravnik, S.M. Morris and S.J. Elston, *submitted to Nature Mater*. (2018).
3. C.C. Tartan, P.S. Salter, M.J. Booth, S.M. Morris and S.J. Elston, *UK Patent No.* 1715566.4 (filed 26 Sept 2017).
4. S. Bolis, C. C. Tartan, J. Beeckman, P. Kockaert, S. J. Elston & S. M. Morris, *Liq. Cryst.* (2018), DOI:10.1080/02678292.2018.1425492
5. C.C. Tartan, P.S. Salter, T.D. Wilkinson, M.J. Booth, S.M. Morris and S.J. Elston, *RSC Adv*. **7**, 507-511 (2017).
6. C.C. Tartan, P.S. Salter, M.J. Booth, S.M. Morris and S.J. Elston, *J. Appl. Phys.* **119**, 183106 (2016).
7. C.C. Tartan, P.S. Salter and S.J. Elston, *Ferroelectrics* **495**: 1, 167-173 (2016).
8. C.C. Tartan and S.J. Elston, *Appl. Phys. Lett.* **107**, 081902 (2015).
9. C.C. Tartan and S.J. Elston, *Mol. Cryst. Liq. Cryst*. **610**: pp. 1-12 (2015).
10. C.C. Tartan and S.J. Elston, *J. Appl. Phys.* **117**, 064107 (2015).

PRESENTATIONS

1. “In-situ direct laser writing spatially variant birefringent liquid crystal-polymer structures”, OLC conference, Sao Paulo (Brazil) 2017.
2. “Fabrication of Micro- and Nanometre-scale Polymer Structures in Liquid Crystal Devices for Next Generation Photonics Applications”, Photon conference, Leeds (UK) 2016.
3. “Fabrication of Micro- and Nanometre-scale Polymer Structures in Liquid Crystal Devices for Next Generation Photonics Applications”, SPIE Optics & Photonics conference, California (USA) 2016.
4. “Liquid Crystals and Polymers for Next-Generation Optoelectronic Devices”, Seminar at JPL, NASA, California (USA) 2016.
5. “Fabricating Multidimensional Polymeric Structures in Liquid Crystalline Systems by Two Photon Photopolymerisation with Aberration Correction”, Oxford Photonics Day meeting, Oxford (UK) 2016.
6. “Fabrication of Micro- and Nanometre-scale Polymer Structures in Liquid Crystal Devices for Next Generation Photonics Applications”, Merck CASE conference, Southampton (UK) 2016.
7. “Fabrication of Micro- and Nano-Structures in Liquid Crystals for Next Generation Photonics Devices”, SET for BRITAIN competition, Houses of Commons, London (UK) 2016.
8. “Structured polymer networks in liquid crystals using 2-photon polymerization”, ECLC conference, Manchester (UK) 2015.
9. “Stabilising photonic switching states in chiral liquid crystals using 2-photon polymerization”, FLC conference, Prague (Czech Republic) 2015.
10. “In-Situ Structuring of Polymer Networks and Defects in Chiral Liquid Crystals for High Speed Photonics”, Oxford Photonics Day meeting, Oxford (UK) 2015.
11. “Structured Polymer Networks in Liquid Crystals for High Speed Photonic Switching Applications”, Merck CASE conference, Southampton (UK) 2015.
12. “In-situ Structuring of Polymer Networks and Defects in Chiral Liquid Crystals for High Speed Photonics and Laser Devices”, Seminar at University of Ljubljana, (Slovenia) 2015.
13. “Hybrid Aligned Nematic Based Measurement of Flexoelectric Coefficient e_1+e_3”, Oxford Photonics Day meeting, Oxford (UK) 2014.
14. “Asymmetric Director Structures and Ions in the Measurement of Flexoelectric Coefficient e_1+e_3”, ILCC, Dublin (Ireland) 2014.
15. “Hybrid Aligned Nematic (HAN) based Measurement of Flexoelectric Coefficient e_1+e_3”, Merck CASE conference, Southampton (UK) 2014.
16. “Hybrid Aligned Nematic (HAN) based Measurement of Flexoelectric Coefficient e_1+e_3”, BLCS conference, Durham (UK) 2014.

1

INTRODUCTION

1.1. LIQUID CRYSTALS

1.1.1. The Nematic Phase

A viscous fluid that possesses a degree of orientational and sometimes positional order is known as a mesophase. A liquid crystal (LC) is a thermodynamically stable mesophase with a set of unique physical attributes. LCs fall into two categories: thermotropics, which occur over a temperature range in between a crystalline solid phase and an isotropic liquid phase, and lyotropics, which exist at specific concentrations within a solvent. The latter, however, is beyond the scope of this thesis. The most common thermotropic LCs exist in the non-polar calamitic nematic phase. This least ordered phase constitutes prolate molecules that possess long range orientational order, but lack positional order.

The molecular structure of a typical nematic LC, pentyl-cyanobiphenyl (5CB), is shown in Figure 1.1. The organic mesogen is composed of two rigidly-linked phenyl rings, with terminal units of flexible hydrocarbon chains (C_5H_{11}) and a cyano (CN) group. Nematic LCs possess permanent dipoles. The inherently prolate nature of the molecules also gives rise to molecular anisotropy. The molecules rotate rapidly about their molecular long-axis thus sweeping out approximately a rod shape; nematic LCs

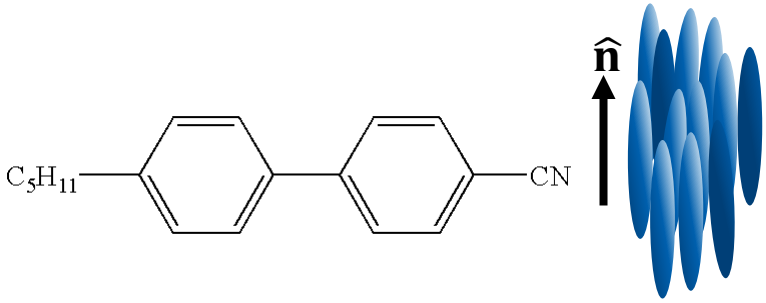


Figure 1.1. The thermotropic calamitic nematic phase. Left: The molecular structure of pentyl-cyanobiphenyl (5CB). Right: An illustration of the rod-shaped nematic molecules possessing long range orientation order that is quantified by the local director, $\hat{\mathbf{n}}$.

are therefore commonly approximated to rods as illustrated in the schematic of Figure 1.1. The resultant anisotropic physical properties that occur in the nematic phase are best described macroscopically in reference to the nematic director, $\hat{\mathbf{n}}$, which describes the average orientation of the molecules. The director is a unit vector that is aligned parallel to the time-averaged axis of a single molecule or the average axis of a system of local molecules. In addition, the intrinsic molecular symmetry in the nematic phase (a nematic LC molecule is centrosymmetric) is manifest from the invariance of the director ($\hat{\mathbf{n}} \equiv -\hat{\mathbf{n}}$).

The order parameter, *S*, is a scalar quantity that can be used to describe the degree of orientation of the molecules with respect to the local director:

$$S = \langle P_2(\cos\theta)\rangle = \langle \frac{3}{2}(\cos^2\theta - 1)\rangle. \qquad (1.1)$$

The relation is based on the second Legendre polynomial, P_2. For uniaxial nematic LCs however, a scalar order parameter can be used. The order parameter is related to the angle θ that the molecules form with respect to the local director. The <…> brackets denote the temporal and spatial averaging, over a single molecule or a system of molecules respectively, while the cosine function produces the molecular symmetry.

Nematic LCs exist over the range $0 < S < 1$, whereby $S = 0$ for the isotropic case whereas if $\theta = 0$, $S = 1$, since all the molecules are perfectly aligned without any deviation from the director.

1.1.2. The Chiral Nematic Phase

The mirror symmetry inherent in the nematic phase can be broken with the addition of a chiral dopant. A self-assembled periodicity results in which the director follows a twisted profile along a specific direction so as to form a helical structure, known as the chiral nematic phase. The symmetry of the nematic LC molecules therefore vanishes with the spontaneously-induced helicity. Figure 1.2 shows the director profile associated with the chiral nematic phase for left and right handedness. The periodicity of the helix is quantified by the pitch, P, which is the characteristic length-scale of a chiral nematic and is defined as the distance over which the local director, $\hat{\mathbf{n}}$, completes a full revolution of 2π about the helical axis. The pitch can be measured experimentally (see §1.4.3) or estimated from the helical twisting power (HTP) that controls the concentration of chiral additive required for a desired pitch:

$$P = \frac{1}{\text{HTP} \times \text{concentration}}. \tag{1.2}$$

The HTP is positive for right handed chirality and negative for left handed chirality. Other, more complex chiral phases also exist in the form of blue phases (based upon a 3-dimensional lattice of defects) as well as chiral smectics that also possess positional order; however, these are beyond the scope of the thesis.

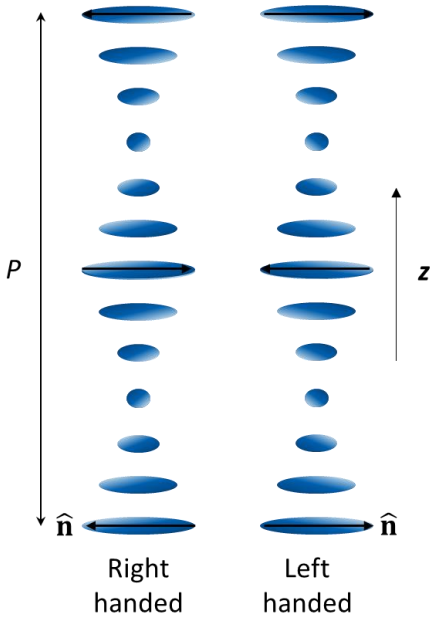


Figure 1.2. Left and right handed chiral nematic LCs. The chiral asymmetry leads to a spontaneous helical structure in which the director rotates in space. The pitch, *P*, defines the length over which the director, $\hat{\mathbf{n}}$, rotates by 2π about the helical axis.

1.2. ELASTIC PROPERTIES

1.2.1. Bulk Energy

In continuum theory, the elastic energy of a liquid crystalline material is minimized and the system is in equilibrium for uniform director fields. Distortions to the director orientation generate an elastic energy cost, the magnitude of which can be calculated from the type of distortion. Any distortion can be described in terms of three fundamental director configurations, which are illustrated in Figure 1.3. The divergence of the director ($\nabla \cdot \hat{\mathbf{n}}$) represents a splay elastic distortion; a twist in the director field is characterized by ($\hat{\mathbf{n}} \cdot \nabla \times \hat{\mathbf{n}}$), while a bend distortion can be described by ($\hat{\mathbf{n}} \times \nabla \times \hat{\mathbf{n}}$).

Based upon the three elastic distortions, the total free energy density (as described by Frank-Oseen [1]) can be expressed as,

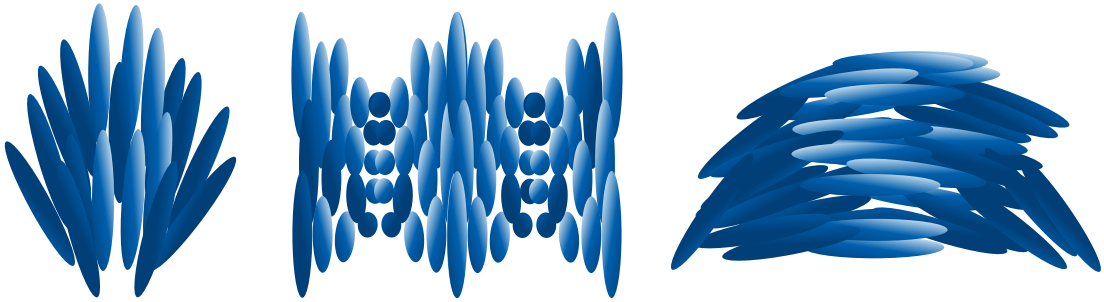


Figure 1.3. Bulk elastic distortions. Illustrations of the splay ($\nabla \cdot \hat{\mathbf{n}}$), twist ($\hat{\mathbf{n}} \cdot \nabla \times \hat{\mathbf{n}}$) and bend ($\hat{\mathbf{n}} \times \nabla \times \hat{\mathbf{n}}$) elastic distortions of the nematic director field.

$$f_{\text{elastic}}(\hat{\mathbf{n}}) = f_{\text{splay}}(\hat{\mathbf{n}}) + f_{\text{twist}}(\hat{\mathbf{n}}) + f_{\text{bend}}(\hat{\mathbf{n}}) \tag{1.3}$$

$$= \frac{1}{2}\{K_{11}[\nabla \cdot \hat{\mathbf{n}}]^2 + K_{22}[\hat{\mathbf{n}} \cdot (\nabla \times \hat{\mathbf{n}})]^2 + K_{33}[\hat{\mathbf{n}} \times (\nabla \times \hat{\mathbf{n}})]^2\},$$

where K_{11}, K_{22} and K_{33} are the splay, twist and bend elastic constants respectively, that are representative of the type of distortion. Magnitudes of the elastic coefficients are ~10pN typically with $K_{33} > K_{11}$, although they vary from one liquid crystalline material.

The twist free-energy term for the chiral nematic phase becomes slightly modified to account for the helical structure,

$$f_{\text{twist}}(\hat{\mathbf{n}}) = \frac{1}{2}K_2[\hat{\mathbf{n}} \cdot (\nabla \times \hat{\mathbf{n}}) + q]^2 \tag{1.4}$$

where $q = \frac{2\pi}{P}$ is the helix wavenumber [2]. This can be understood by considering a chiral nematic LC system such as that shown in Figure 1.2 for either handedness, where the optic axis is along the *z*-direction. The gradient operator therefore acts along the *z*-axis on the director field defined as a function of the tilt angle θ (*z*) = *qz*, generating energy components in the *z*-dimension. The term in (1.4) thus simplifies to $f_{\text{twist}}(\hat{\mathbf{n}}) = -q$, which is the lowest energy state for the chiral nematic LC.

The Frank elastic energy equation in (1.3) relates different distortions to their elastic potential energy and has proven highly successful in modelling and understanding the behaviour of LCs on a macroscopic scale (see §1.7).

1.3. ELECTRIC PROPERTIES

1.3.1. Dielectric Energy

Liquid crystals are dielectric materials. An electric polarization, **P**, is induced under the application of an electric field. The polarizability of a material is defined by the susceptibility, χ_e. For a uniaxial material, the resultant electric displacement is defined as

$$\mathbf{D} = \varepsilon_0 \mathbf{E} + \mathbf{P} = \varepsilon_0 (1 + \chi_e)\mathbf{E} = \varepsilon_0 \varepsilon_r \mathbf{E}, \tag{1.5}$$

where ε_0 is the vacuum permittivity and ε_r the relative dielectric permittivity of the material. The latter takes the form of a tensor:

$$\varepsilon_r = \begin{bmatrix} \varepsilon_\perp & 0 & 0 \\ 0 & \varepsilon_\perp & 0 \\ 0 & 0 & \varepsilon_\parallel \end{bmatrix} \tag{1.6}$$

where $\varepsilon_\perp$ and $\varepsilon_\parallel$ are the dielectric permittivities perpendicular and parallel to a director arbitrarily oriented along the *z*-axis i.e. $\hat{\mathbf{n}} = (0,0,1)$. The electric displacement therefore simplifies to

$$\mathbf{D} = \varepsilon_0 \varepsilon_\perp \mathbf{E} + \varepsilon_0 \Delta\varepsilon (\hat{\mathbf{n}} \cdot \mathbf{E})\hat{\mathbf{n}}. \tag{1.7}$$

The free energy term due to dielectric coupling can then be derived as follows

$$f_{\text{dieletric}}(\hat{\mathbf{n}}) = -\tfrac{1}{2}\mathbf{D} \cdot \mathbf{E} \tag{1.8}$$

$$= -\frac{1}{2}\varepsilon_0 \varepsilon_\perp E^2 - \frac{1}{2}\varepsilon_0 \Delta\varepsilon (\hat{\mathbf{n}} \cdot \mathbf{E})^2,$$

where $\Delta\varepsilon = \varepsilon_{\parallel} - \varepsilon_{\perp}$ is the dielectric anisotropy, which can be either positive or negative, depending on the LC material. The induced electric polarization acts to minimize the dielectric energy densities in LC systems. Thus the director will tend to align in the direction of an external electric field for a positive dielectric anisotropy ($\Delta\varepsilon > 0$), and perpendicular to it when the material has a negative dielectric anisotropy ($\Delta\varepsilon < 0$).

The dielectric energy is dependent upon the angle between the director and the applied electric field due to the LC anisotropy, such that any terms that are independent of the director orientation can be omitted. The free-energy term due to dielectric coupling, equation (1.8), can therefore be simplified to

$$f_{\text{dieletric}}(\hat{\mathbf{n}}) = -\frac{1}{2}\varepsilon_0 \Delta\varepsilon(\hat{\mathbf{n}} \cdot \mathbf{E})^2. \tag{1.9}$$

Note that the dielectric energy term is negative as it represents the change in energy related to the work done i.e. by a capacitor rather than the energy stored in the system. In the chiral nematic phase, the helical structure can be unwound under the application of sufficiently high electric field strengths at which the dielectric energy overcomes the twist component, K_{22} of the elastic distortion. This is only true for a material with $\Delta\varepsilon > 0$, whereby the molecules in the bulk align in the direction of the applied field, as the parallel component of the dielectric permittivity dominates. Figure 1.4 shows the elongation of the pitch as the applied electric field tends towards the value of E_c, and the helical structure vanishes above $E > E_c$. The chiral nematic phase is recovered below this critical unwinding field. The critical unwinding field derived by Meyer and de Gennes [3, 4] is written as

$$E_c = \frac{\pi^2}{p}\sqrt{\frac{K_{22}}{\Delta\varepsilon\varepsilon_0}}. \tag{1.10}$$

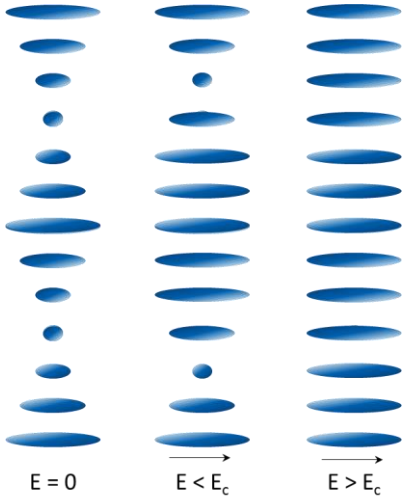


Figure 1.4. Dielectric-driven helix unwinding. The helix distortion in a chiral nematic LC with $\Delta\varepsilon > 0$ when an electric field, *E*, is applied perpendicular to the helical axis.

1.3.2. Flexoelectricity

Flexoelectricity is analogous to piezoelectricity in crystalline solids. The invariance of the nematic director field causes no net polarization to exist, despite the presence of permanent dipoles. However, the elastic distortions introduced in §1.2.1 can generate a net polarization, giving rise to an electro-mechanical interaction. Thus, a net electric polarization can be induced in a system of nematic LC molecules by a mechanical deformation of the director field ($\hat{\mathbf{n}}$). By the application of an electric field across an LC device, the inverse can also be realized. Related effects that couple polarization and mechanical distortion are also observed in solid-state materials [5, 6]. Flexoelectricity is attributed to the shape asymmetry and permanent dipole moments of the LC molecules. A net polarization is induced along the long axis of "pear"-shaped molecules when constrained to a splay geometry, while "banana" shaped molecules that are constrained to bend geometries have net polarizations along their transverse axes [7]. Figure 1.5 shows the induction of a net flexoelectric polarization as a result of the bend and splay

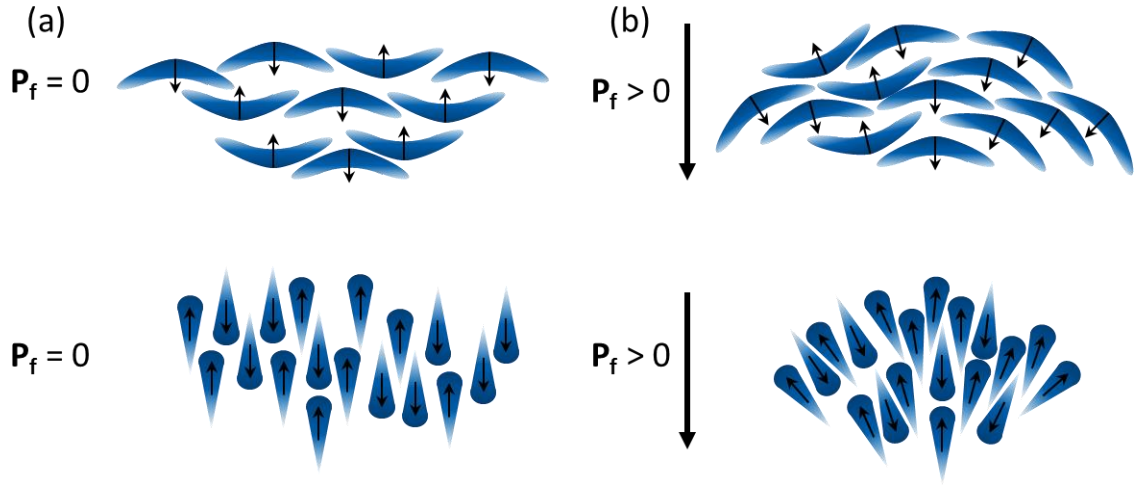


Figure 1.5. The flexoelectric polarization. A schematic showing "pear" and "banana" - shaped molecules (a) with no net polarization and (b) constrained to splay and bend geometries, respectively, which result in the generation of a net flexoelectric polarization.

distortions in the director field that breaks the symmetry of the dipole moment orientations.

The flexoelectric polarization can be described in magnitude and direction by the splay (e_1) and bend (e_3) flexoelectric coefficients as:

$$\mathbf{P_f} = e_1 \hat{\mathbf{n}} (\nabla \cdot \hat{\mathbf{n}}) + e_3 (\nabla \times \hat{\mathbf{n}}) \times \hat{\mathbf{n}}. \tag{1.11}$$

The free energy due to the flexoelectric effect is given by

$$f_{\text{flexo}}(\hat{\mathbf{n}}) = -\mathbf{P_f} \cdot \mathbf{E} = -[e_1 \hat{\mathbf{n}} (\nabla \cdot \hat{\mathbf{n}}) + e_3 (\nabla \times \hat{\mathbf{n}}) \times \hat{\mathbf{n}}] \cdot \mathbf{E}. \tag{1.12}$$

In the chiral nematic phase, the flexoelectric effect becomes manifest under the application of an electric field perpendicular to the helix axis. A tilt is induced in the optical axis that couples to the difference of the flexoelectric coefficients as

$$\tan \phi = \frac{e_1 - e_3}{K_{11} + K_{33}} \frac{E}{q}. \tag{1.13}$$

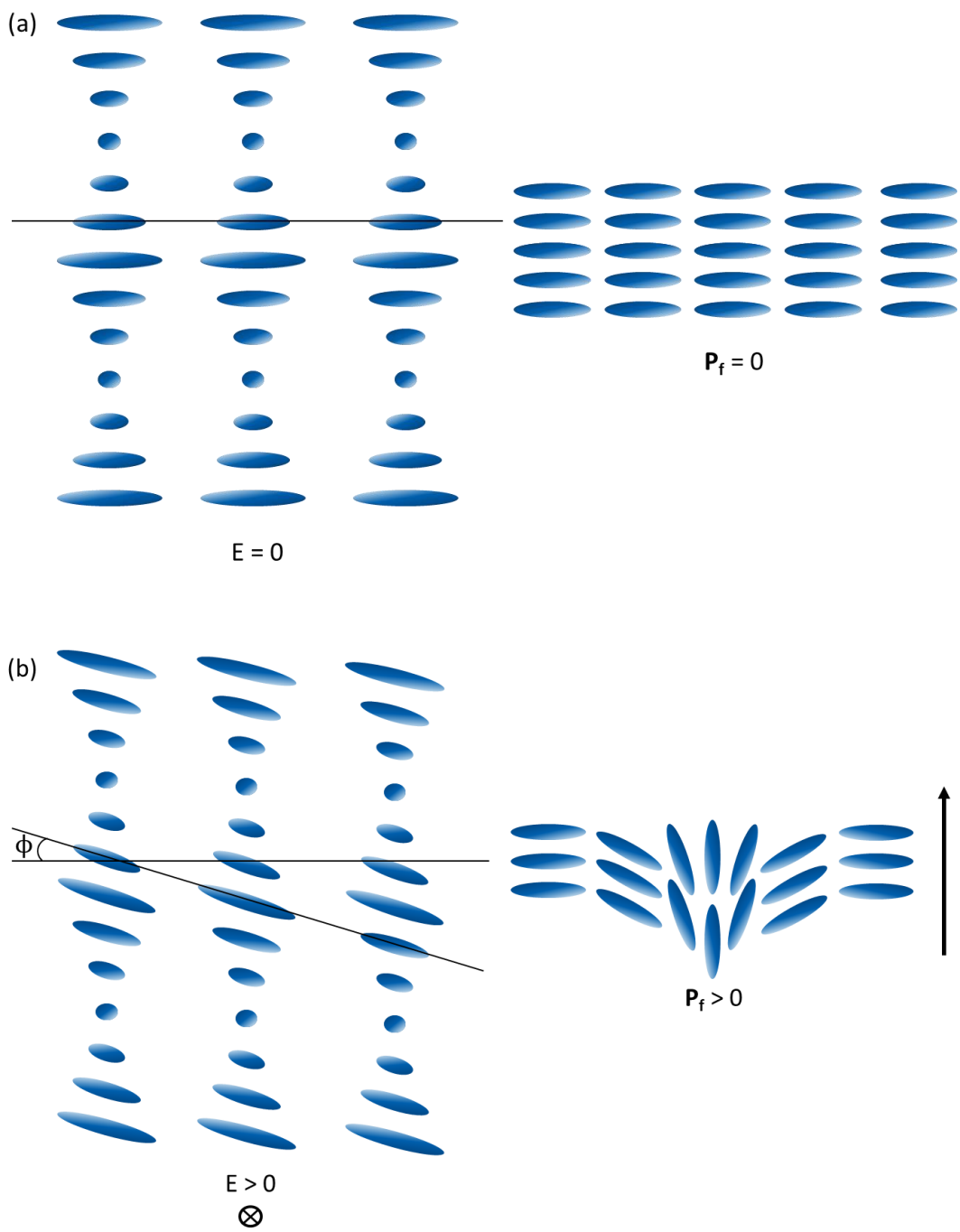


Figure 1.6. The flexoelectric effect in chiral nematic LCs. (a) Left: The chiral nematic structure in the absence of an applied electric field. Right: Bouligand plane reveals no splay or bend distortion. (b) Left: The flexoelectric tilt in the optic axis of a chiral nematic LC under the application of an electric field perpendicular to the helical axis. Right: Bouligand plane of molecules tilted with respect to the helix reveals the splay-bend distortion that induces the flexoelectric polarization.

From (1.13) it can be seen that, for small angles, the tilt angle is linear in the applied electric field. The chiral flexoelectro-optic (FEO) effect has great potential for fast-switching photonics applications, whereby short-pitch chiral nematic LCs permit fast changes of the optic axis under the application of an electric field with microsecond-range response times:

$$\tau = \frac{\gamma q^2}{K_{11}+K_{33}}, \tag{1.14}$$

where γ is the rotational viscosity of the LC material [8]. A derivation of the FEO tilt angle is provided in Chapter 4, along with an overview of the required director configuration to achieve an optimized FEO response.

1.4. OPTICAL PROPERTIES

1.4.1. Polarization & Birefringence

The refractive index, which defines the speed at which light propagates through non-magnetic materials, depends upon the relative dielectric permittivity and is written as

$$n = \sqrt{\varepsilon_r}. \tag{1.15}$$

Note that no dipole effect occurs at optical frequencies, yet the anisotropy remains on account of the molecular polarizability. LCs are, therefore, generally optically birefringent materials. Polarized components of light propagate through a liquid crystalline material at different speeds as they experience a different refractive index parallel $(n_{\parallel})$ and perpendicular $(n_{\perp})$ to the LC optic axis. The resultant phase delay between the two orthogonal polarizations can be described by the birefringence of the medium as

$$\Delta n = n_{\parallel} - n_{\perp}. \tag{1.16}$$

1.4.2. Jones Matrices

The 2 × 2 Jones matrix [9] approach is a convenient method to model different polarizations of light propagating through birefringent media. The Jones vector, *J*, describes the polarization state of light in terms of a column vector and each optical element, M, is represented by a 2 × 2 matrix, such that J_{out} = M J_{in}. Therefore, it is possible to determine the polarization state at the output of an optical system by multiplying together the Jones matrices for each optical component for a given input polarization. For example, any polarization state of light can be represented as follows,

$$\mathbf{E} = \left(\hat{\mathbf{x}}a + \hat{\mathbf{y}}be^{i\delta}\right)E_0e^{i(\omega t - kz)} \tag{1.17}$$

where $|a|^2 + |b|^2 = 1$ and δ is the phase delay between the *x*- and *y*- components. The expression in (1.15) is the sum of two perpendicularly polarized waves that differ in amplitude and phase, and corresponds to a Jones vector of

$$E_0\begin{bmatrix} a \\ be^{i\delta} \end{bmatrix} \tag{1.18}$$

whereby any common terms in *a* and *b* are absorbed by the $e^{i(\omega t - kz)}$ phase term.

The Jones vectors for linear and circular polarization states are given by

$$\text{linear} = \frac{1}{\sqrt{2}}\begin{bmatrix} 1 \\ \pm 1 \end{bmatrix} \qquad \text{circular} = \frac{1}{\sqrt{2}}\begin{bmatrix} 1 \\ \pm i \end{bmatrix} \tag{1.19}$$

where the factor $1/\sqrt{2}$ gives the vector a magnitude of unity. The + 1 and – 1 in the left-hand term refers to + 45° and – 45° linear polarization respectively, which is usually defined relative to the horizontal axis. The +*i* and –*i* in the right-hand term refers to left and right circular polarizations, respectively. The imaginary number in the circular polarization state vector incorporates a phase delay of ± π/2 between the *x*- and *y*-components, while both elements in the linear state vector are real and therefore in phase. An orthogonal vector can be defined for each polarization vector, indicated by

the change in polarity of both *y*-components in (1.19), whereby the product of the two vectors is zero. Note that the Jones vector approach can be used to describe optical systems that are fully polarised, but cannot be used to describe partial or unpolarised systems; for this, the Stokes parameters and Mueller matrices (4 × 4) are required [9].

In LC optics, a birefringent LC cell behaves as a retardation plate with variable retardation. A retardation plate of thickness d is characterized by its phase retardation, $\delta = 2\pi\Delta n_{\text{eff}} d/\lambda$, and ψ, the azimuth angle between the coordinate systems defined by the two refractive indices ($n_{\parallel}$ and $n_{\perp}$) and the *xy*-axes (i.e. the laboratory frame). Therefore, it is necessary to carry out transformations between the two different coordinate systems of the form $R(-\psi)M_0R(\psi)$, where M_0 is the Jones matrix for the retardation plate and $R(\psi)$ is the coordinate rotation matrix [9]. For an incident unpolarised beam of light propagating through the LC cell that is sandwiched between a pair of crossed (orthogonal to one another) polarizers, the transmitted beam can therefore be obtained as follows:

$$\begin{bmatrix} 1 & 0 \\ 0 & 0 \end{bmatrix} \begin{bmatrix} \cos\delta/2 & -i\sin\delta/2 \\ -i\sin\delta/2 & \cos\delta/2 \end{bmatrix} \frac{1}{\sqrt{2}} \begin{bmatrix} 0 \\ 1 \end{bmatrix} = \frac{-i}{\sqrt{2}} \begin{bmatrix} \sin\delta/2 \\ 0 \end{bmatrix}. \tag{1.20}$$

The first matrix in (1.20) is the second 2 × 2 linear polarizer (analyser), which attenuates the *y*-component of the incoming electric field. The second matrix represents the wave plate and the third term is the vector for the linearly polarized beam after passing through the first polarizer, which is orthogonal to the second polarizer (analyser). The final term is the polarization state arriving from the analyser. The transmission amplitude can then be calculated from the product of the resultant polarization vector in (1.20) and its complex conjugate;

$$T = \frac{1}{2}\sin^2\left(\frac{\pi\Delta n_{\text{eff}} d}{\lambda}\right), \tag{1.21}$$

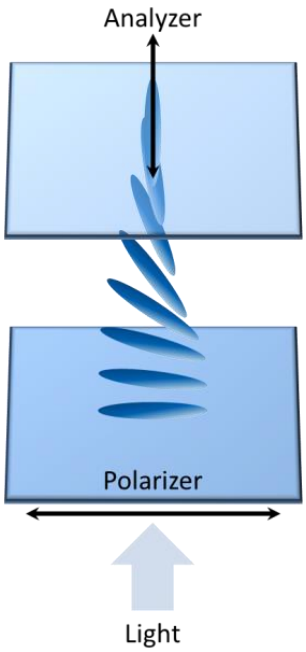


Figure 1.7. A twisted nematic (TN) cell between crossed polarizers. Light of wavelength $\lambda \ll nP$ propagating through the TN cell is guided by the $\pi/2$ twist in the director field.

which can be written in a more general form as

$$T = \frac{1}{2}\sin^2(2\chi)\sin^2\left(\frac{\pi\Delta n_{\text{eff}}d}{\lambda}\right) \tag{1.22}$$

where χ is the angle between the first polarizer and the LC optic axis. For multiple polarization manipulation elements, the Jones matrices can be simply multiplied together to give $J_{out} = M_N \ldots M_3\ M_2\ M_1\ J_{in}$. It is worth noting that the order of the optical elements must be preserved to derive the correct transmitted polarization state using this approach. Additionally, the Jones matrix approach only accounts for forward propagating waves therefore reflected components are not accounted for in the model.

1.4.3. Chiral Optics

The interaction between light of wavelength, λ, with a chiral nematic LC of a certain pitch and refractive index can be characterised by three different regimes. A chiral

nematic LC acts as a waveguide when light of wavelength $\lambda \ll nP$ propagates along the optic axis. Under this condition, which is referred to as the Mauguin regime [8], a long pitch chiral nematic behaves as a twisted nematic (TN) LC cell. Figure 1.7 shows an illustration of light transmitted through a TN cell when placed between crossed polarizers. The cell has a $\pi/2$ twist in the bulk director orientation, which is imposed by the surface conditions at the cell surfaces (see §1.5.2. for further details). The optic axis of the nematic LC is aligned close to the first substrate such that light propagating through the device is guided along the twisted structure and transmitted through the analyser. This is referred to as the 'on' state of a TN cell. If an electric field (E_z) is applied across the cell filled with a $\Delta\varepsilon > 0$ liquid crystalline material, the director orientation in the bulk would align parallel to the direction of the applied field and perpendicular to the transmission axes of the two polarizers. This configuration would lead to an 'off' state, as light passing through the first polarizer would no longer be guided in the bulk material. Thus, no light would be transmitted through the analyser.

For the case when $n_o P < \lambda < n_e P$, where n_o and n_e refer to the ordinary and extraordinary refractive indices respectively, selective Bragg reflection occurs whereby light is forbidden to propagate within a photonic bandgap (PBG). The PBG, analogous to the electronic bandgaps in semiconductors, forms due to the constructive interference of reflected components of light by the periodicity of the dielectric material. The spectral width of the PBG is related to the pitch of the chiral nematic by

$$\Delta\lambda = \Delta n P. \tag{1.23}$$

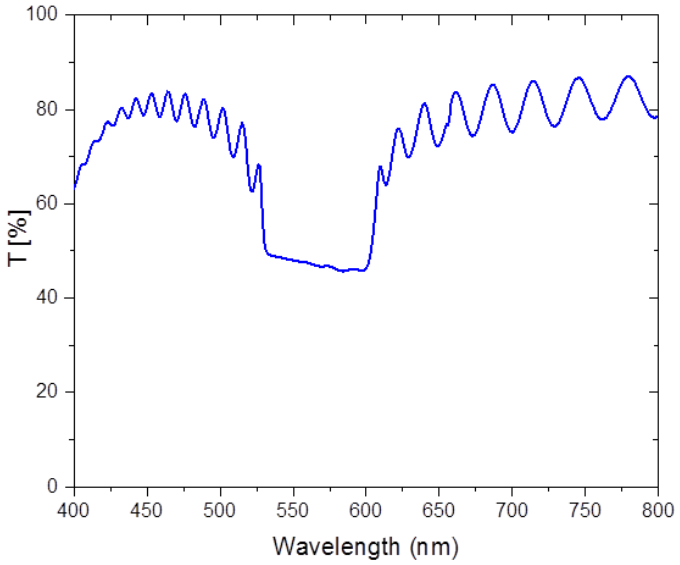


Figure 1.8. The transmission spectrum of a chiral nematic LC for light propagating parallel to helix axis. The photonic bandgap that is centred at $\lambda \sim 550$ nm reflects green-yellow visible light.

If the pitch of the chiral nematic is within the visible regime, then incident light that has a wavelength that falls within the range defined by $n_e P$ and $n_o P$ is reflected by the chiral nematic LC. Figure 1.8 shows the transmission spectrum, obtained using a Ultraviolet-Visible spectrometer, from a chiral nematic LC with a pitch of $P \sim 350$ nm. This relatively short pitch generates a bandgap that reflects green-yellow light, with short and long band edge wavelengths of 529 nm and 605 nm, respectively. Note that only ~50% of the light is transmitted through the chiral nematic LC. This is due to the chirality of the helix, whereby only circularly polarized light of the same handedness is transmitted; the chiral nematic LC therefore acts as a 1D photonic crystal for circularly polarized light of the same handedness as the helical structure.

Finally, for the case that $\lambda \gg nP$, light is no longer guided by the helix and the chiral nematic becomes optically uniaxial. For light polarized perpendicular to the helical axis, light propagates with an effective refractive index due to the electric field of the light experiencing an averaged dielectric constant over the length of a pitch:

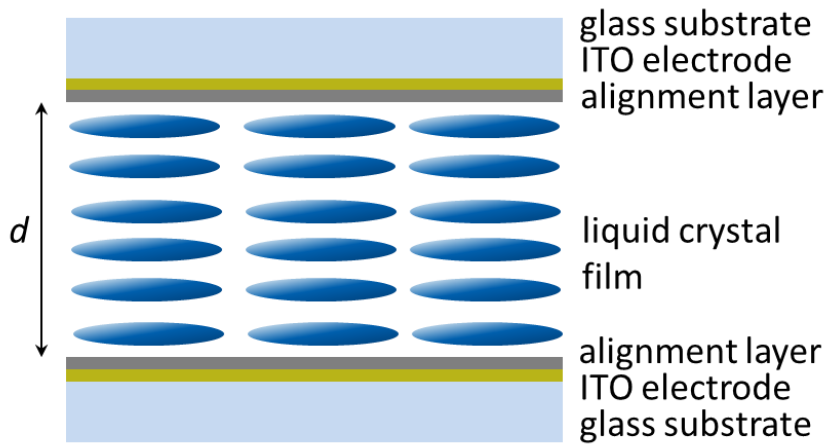


Figure 1.9. A LC cell. A LC film of varying thickness, d ~ 5 – 20 μm, is bounded by two glass substrates that are coated with an alignment layer to control the director orientation at the surfaces and a transparent conductive indium tin oxide electrode for the application of a voltage across the device.

$$n_{\text{eff}} = \sqrt{\varepsilon_{\text{eff}}} = \sqrt{\frac{1}{2}\left(n_{\parallel}^2 + n_{\perp}^2\right)}. \tag{1.24}$$

Light polarized parallel to the helical axis, however, has a refractive index $n = n_{\perp}$ and the effective birefringence becomes negative:

$$\Delta n = n_{\perp} - \sqrt{\frac{1}{2}\left(n_{\parallel}^2 + n_{\perp}^2\right)}. \tag{1.25}$$

1.5. DEVICE STRUCTURE

1.5.1. A Liquid Crystal Cell

An LC cell is a composite structure that consists of a liquid crystalline layer sandwiched between two glass substrates. The substrates are treated with a specific alignment layer to impose boundary conditions on the LC film. The substrates are also coated with transparent conductive electrodes, conventionally using Indium Tin Oxide (ITO), to permit voltage applications across the device. Figure 1.9 shows an illustration of the device geometry, of thickness d ~ 5 – 20 μm, for a homogeneous planar aligned LC cell.

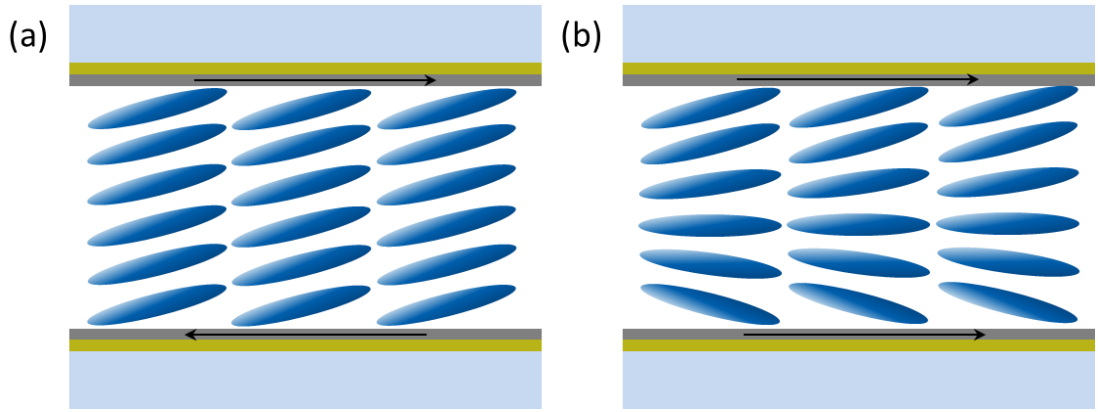


Figure 1.10. Illustrations of pre-tilted planar aligned LC cells. (a) A Fréedericksz cell, constructed from anti-parallel rubbed polyimide alignment layers. (b) A nematic pi-cell, fabricated from parallel rubbed polyimide alignment layers. In both cases, a pretilt (of a few degrees) is generally present at the cell surfaces.

1.5.2. Alignment Layer

The alignment layer of an LC cell is crucial to control the type of elastic distortion generated within a device. Imposing well-defined boundary conditions is therefore vital in understanding the phenomena that occur in LC physics. The surface anchoring can either be strong, moderate or weak, depending on the material that is used as the alignment layer. For planar homogeneous alignments, such as that shown in Figure 1.9, it is conventional to use a polyimide. The polymer layer can be deposited on the glass substrates using a textile cloth, which generates planar alignment as the LC molecules bind to the polymer along the rubbing direction. It is also convention to include a pretilt of some angle, θ, in the director orientation at the surfaces. The magnitude of the pretilt leads to the formation of different director profiles when addressing the device with external electric fields. Figure 1.10 shows two LC cells that possess distinct rubbing directions and pretilts relative to the cell surfaces. A Fréedericksz cell (a) is produced from anti-parallel rubbed, planar alignment layers, while a nematic pi-cell (b) results when the alignment layers are parallel-rubbed, as indicated by the black arrows. A

higher pretilt in the latter example generates topologically distinct LC states under different voltage applications, which leads to interesting electro-optic phenomena that will be explored in Chapter 3.

For a Fréedericksz cell with a small pre-tilt, a voltage threshold exists below which no reorientation of the director is induced [10]:

$$V_{th}(\text{Fréed}) = \pi\sqrt{\frac{K_{11}}{\varepsilon_0 \Delta\varepsilon}}. \tag{1.26}$$

In its lowest energy state, the Fréedericksz cell has a planar tilted alignment induced by the pretilt at the surfaces as illustrated in Figure 1.10 (a). The voltage threshold represents the minimum amount of dielectric energy required to compensate for the cost in elastic energy incurred when electrically switching the LC device from its planar ground state. Note that the relation in (1.26) is independent of the device thickness and instead, depends on the elastic (splay) and dielectric material parameters.

A voltage threshold also exists for a nematic pi-cell device. However, various LC states result under the application of an electric field although this will be explored in detail in Chapter 3. Another important parameter to consider is the time taken for the Fréedericksz cell to relax to its equilibrium state upon removal of an applied field. The characteristic timescale can be written as

$$\tau = \frac{\gamma d^2}{\pi^2 K_{11}} \tag{1.27}$$

where γ is the rotational viscosity of the LC.

Homeotropic cells, where the director is oriented perpendicular to the glass substrates, can also be created by surfactant treatment. Natural egg lecithin is a common surfactant used to generate homeotropic alignment layers. Pipetting a few drops of the surfactant onto the cell surfaces and subsequently spin-coating at ~3000 rpm for ~30

seconds ensures a uniform thickness across the substrates. Note that the presence of dust and dirt can act as nucleation sites for defects in the alignment layer; therefore it is vital that the glass substrates are prepared in a clean room environment.

The chiral nematic phase with planar surface anchoring favours a uniform standing helix configuration, in which the helicity is oriented perpendicular to the cell surfaces. A short-pitch chiral nematic with homeotropic surface anchoring generates a scattered state with randomly oriented helices, on account of the degeneracy in the director field at the cell surfaces. In contrast, a homeotropic cell filled with a long pitch chiral nematic can lead to a fingerprint texture. Weak homeotropic alignment can be energetically favourable for the formation of a uniform lying helix alignment, where the helical axis orients parallel to the glass substrates. The formation of this state is non-trivial and will be the topic of investigation in Chapter 4. Overall, it is clear that the alignment layer in a liquid crystalline cell dictates the LC states that are formed within the bulk of a device. Thus, the alignment is an important design parameter to consider during the fabrication of liquid crystalline devices.

1.6. REACTIVE MESOGENS

Reactive Mesogens (RMs) are LC monomers that carry functional groups, such as acrylates, which react in the presence of photo-initiators and UV light to form a rigid polymer network [11]. The photoinitiator is excited under the exposure to light with a wavelength that overlaps with the absorption spectrum, preferably the absorption maximum. Free radicals are then released that bind to the RMs, forming the polymer chains within the vicinity of the illumination region.

The photopolymerization process captures the director orientation at the moment of exposure to UV light whereby different director profiles can be 'locked-in' by controlling key parameters such as the temperature and externally applied electric field [12]. The mechanical properties of RM films can vary from solid, glasslike materials to more flexible polymer films and gels, depending on the type and concentration of monomer groups used [11, 12]. These versatile properties make RMs very attractive as a variety of different LC states can be locally 'locked-in' and stabilised. It is even possible to create templates of certain phases that can impart their properties onto other mesogenic materials [13]. This method will be discussed further in Chapter 4 where it is adopted to enhance the flexoelectro-optic properties of chiral nematic systems.

1.7. NUMERICAL MODEL

Liquid crystalline phenomena are well described by numerical models derived from continuum theory [1]. The continuum model is based upon the minimization of the total free energy in a system of nematic LC molecules, taking into account contributions from the elastic, dielectric and flexoelectric effects:

$$F = f_{\text{elastic}}(\hat{\mathbf{n}}) + f_{\text{dielectric}}(\hat{\mathbf{n}}) + f_{\text{flexo}}(\hat{\mathbf{n}}) \tag{1.28}$$

$$= \frac{1}{2}\{K_{11}[\nabla \cdot \hat{\mathbf{n}}]^2 + K_{22}[\hat{\mathbf{n}} \cdot (\nabla \times \hat{\mathbf{n}})]^2 + K_{33}[\hat{\mathbf{n}} \times (\nabla \times \hat{\mathbf{n}})]^2\} - \frac{1}{2}\varepsilon_0 \Delta\varepsilon(\hat{\mathbf{n}} \cdot \mathbf{E})^2$$

$$- [e_1 \hat{\mathbf{n}}(\nabla \cdot \hat{\mathbf{n}}) + e_3(\nabla \times \hat{\mathbf{n}}) \times \hat{\mathbf{n}}] \cdot \mathbf{E}\,.$$

The model is used in conjunction with an optics model, such as the Jones Matrix approach introduced in § 1.4.2, to simulate the propagation of light through various LC director configurations.

A one-dimensional numerical model can be developed based on the director field as a function of the tilt angle, $\hat{\mathbf{n}}(\theta)$ (c.f. Chapter 2 for further details). The LC cell, defined in a coordinate system in the *xy*-plane, has an electric field applied perpendicular to the cell surfaces along the *z*-dimension. The discretized director field is then described in terms of its equilibrium state and basic device parameters, such as the cell thickness and LC viscosity (see §2.2.2), are established using data-theory fits. An Euler Lagrange equation of the form,

$$\frac{\partial F}{\partial \hat{\mathbf{n}}(\theta)} - \frac{\partial}{\partial z}\left(\frac{\partial F}{\partial(\partial \hat{\mathbf{n}}(\theta)/\partial z)}\right) = 0 \tag{1.29}$$

is satisfied when the LC device is in the minimum energy state. Here, the left-hand side of (1.29) is equated to a viscous dissipation term, $-\gamma \frac{\partial \theta}{\partial t}$, to allow for dynamic behaviour. Finite difference approximations can be used to solve differentials in the director field:

$$\left.\frac{\partial \theta}{\partial z}\right|_i = \frac{\theta[i+1]-\theta[i-1]}{2\cdot\Delta},\ \left.\frac{\partial^2 \theta}{\partial z^2}\right|_i = \frac{\theta[i+1]-2\theta[i]+\theta[i-1]}{\Delta^2} \tag{1.30}$$

where i denotes the time step and Δ the grid spacing defined in the numerical model. Now,

$$\theta_{t+1}[i] = \theta_t[i] + NR \cdot G \tag{1.31}$$

where $NR = \frac{\Delta t}{\gamma}$ is the relaxation constant and G is the left-hand side of (1.29). The relation in (1.31) is based on a relaxation method, which uses an iterative process to output the equilibrium response from the device set by its initial boundary conditions. Each iteration results in a torque that acts on the director field; the electric properties are adjusted with each iteration until there is a negligible change in the director field.

The continuum model is well-suited to describe topologically continuous LC behaviour, such as the work outlined in Chapters 2 and 3 for studies of the electro-optic behaviour in nematic systems. Topologically discontinuous LC behaviour arises due to

the presence of defects in the director field. In this case, it is necessary to incorporate resultant variations in the order parameter and energy costs incurred from the elastic distortions around a defect site. The Landau-de Gennes (LdG) phenomenological approach based on the Q-tensor theory [14] can be used to describe more complex systems as it incorporates the order parameter alongside a minimization of the total free energy density in (1.28). Theoretical work based upon the LdG phenomenological approach is presented in Chapter 8.

1.8. LIQUID CRYSTALS FOR SOFT MATTER PHOTONICS

Over recent decades, liquid crystalline materials have played a major role in the development of soft matter photonic-based technologies. Their unique electric and optical properties make them particularly attractive for optoelectronic applications. LCs are most well-known for revolutionizing the flat-panel displays industry, and show great potential for the next generation of displays and analogue phase modulators on account of their microsecond range response times that occur in specific director configurations (c.f. Chapter 4 and 6). More recently, the electrohydrodynamic instabilities induced in chiral nematic LCs have been used in the reduction of speckle resultant from coherent laser light that is used in holographic applications [15].

Liquid crystalline materials are highly sensitive to external stimuli, such as light, temperature, electric fields and mechanical forces. As a result, they often find applications in photonic devices that can be tuned in response to these stimuli. For example, chiral LC lasers have been demonstrated through the addition of a suitable gain medium that provides amplification of the feedback generated in the periodic helical structure [16]. The lasers can be tuned in response to changes in temperature and

electric fields. Combining polymer composites in the fabrication process leads to the creation of stretchable gels, the PBG of which can be tuned by compression of the pitch under mechanical forces [17].

LCs have found potential applications in solar technology, such as solar luminescent concentrators that take advantage of the directionality introduced by the LC director field so as to enhance the amount of light reaching photovoltaic cells [18, 19]. Colloidal dispersions of other functional materials such as semiconductors have also proven that LCs are an excellent host medium that impart a degree of order onto colloidal particles [20]. These are just a few of the examples that illustrate the extent that liquid crystalline materials have had on the field of soft matter photonics, which will be addressed further in the latter half of this thesis.

1.9. CONCLUSIONS

The fundamental concepts that govern the behaviour of liquid crystalline materials have been introduced in this chapter. The key theory that describes their unique electro-optic properties has been presented, which will be implemented in the investigations carried out in this thesis. The main motivation of the thesis is to engineer novel LC-polymer composites for a range of soft matter photonics applications. The thesis has two main focuses: the first half focuses on the characterization of fundamental electro-optic properties in the nematic and chiral nematic phases. This work inspires the latter part of the thesis, which attempts to enhance these properties using a bespoke fabrication set-up to engineer novel multidimensional polymer structures.

1.10. REFERENCES

[1] F. C. Frank, *Discussions of the Faraday Society* **25**, 997 (1958).

[2] P. Rudquist, Ph.D. thesis, Chalmers University of Technology, Goteborg (1997).

[3] R. B. Meyer, *Appl. Phys. Lett.* **14**, 208 (1969).

[4] P. G. de Gennes, *Solid State Comms*. **6**, 163 (1968).

[5] T. D. Nguyen, S. Mao, Y-W. Yeh, P. K. Purohit and M. C. McAlpine, *Adv. Mater.* **25**, 946 (2013).

[6] A. D. Rey, P. Servio and E. E. Herrera Valencia, *Chem. Phys. Chem.* **15**, 7, 1405 (2014).

[7] R. B. Meyer, *Phys. Rev. Lett.* **22**, 918 (1969).

[8] R. A. M. Hikmet, J. Lub and D. J. Broer. *Adv. Mater.* **3**, 7, 392 (1991).

[9] P. Yeh and C. Gu, *Optics of Liquid Crystal Displays*, John Wiley & Sons, Inc (1999)

[10] V. Fréedericksz and A. Repiewa, *Zeitschrift für Physik*, **42**, 7, 532 (1927).

[11] D. J. Broer, J. Lub and G. N. Mol. *Macromolecules* **26**, 6, 1244 (1993).

[12] J. Lub, D. J. Broer, R. A. M. Hikmet and K. G. Nierop, *Liq. Crys.* **18**, 2, 319 (1995).

[13] F. Castles, F. V. Day, S. M. Morris and D-H. Ko, D. J. Gardiner, M. M. Qasim, S. Nosheen, P. J. W. Hands, S. S. Choi, R. H. Friend and H. J. Coles, *Nat. Mater.* **11** (2012).

[14] P. G. de Gennes and J. Prost, *The Physics of Liquid Crystals*, 2nd Edition, Clarendon Press, Oxford (1993).

[15] D. J. Hansford, J. A. J. Fells, S. J. Elston and S. M. Morris, *Appl. Phys. Lett.* **109**, 261104 (2016),

[16] H. Coles and S. Morris, *Nat. Photon.* **4**, 676 (2010).

[17] S. M. Wood, F. Castles, S. J. Elston and S. M. Morris, *RSC Advances*, **6**, 31919 (2016).

[18] F. Meinardo, A. Colombo, K. A. Velizhanin, R. Simonutti, M. Lorenzon, L. Beverina, R. Viswanatha, V. I. Klimov and S. Brovelli, *Nat. Photon* **8**, 392 (2014).

[19] A. L. Rodarte, Z. S. Nuno, B. H. Cao, R. J. Pandolfi, M. T. Quint, S. Ghosh, J. E. Hein and L. S. Hirst, *ChemPhysChem*, **15**, 7, 1413 (2014).

[20] T. Hegmann, H. Qi and V. M. Marx, *J. Inorganic and Organometallic Polymers and Mater.*, **17**, 3 (2007).

2

THE FLEXOELECTRIC EFFECT IN HYBRID ALIGNED NEMATICS

2.1. INTRODUCTION

2.1.1. Flexoelectricity in Hybrid Alignments

The flexoelectric effect in nematic liquid crystals (LCs) is of particular interest for displays applications due to potential high-speed switching effects, with possible applications in field sequential colour displays, as well as for the exploration of new avenues in fast-switching photonic devices. So far, flexoelectricity has been aimed at the creation of new display modes that exploit the polar response to realize bistable/multi-stable electrical switching phenomena [1]. One example of such a system is a zenithal bistable display, which consists of a nematic LC combined with a surface relief grating structure, and has found commercial applications as a reflective display of ambient light in the form of electronic shelf labels [1]. Given the commercial relevance of the flexoelectric effect, experimental determination of the splay and bend coefficients is of importance in the development of new materials. A brief overview of the theory behind

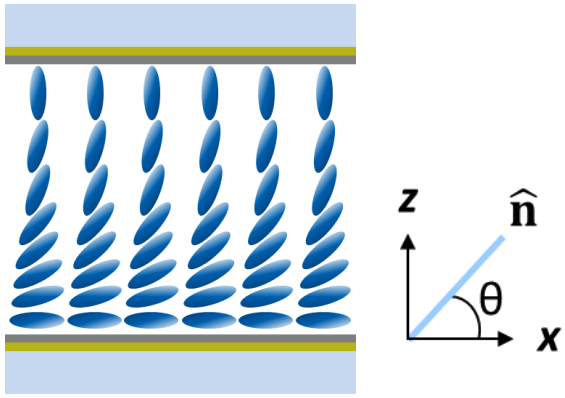


Figure 2.1. The director profile in a Hybrid Aligned Nematic (HAN) LC device. The different surface aligments at the cell boundaries results in a strong splay-bend distortion in the *xz*-plane.

the flexoelectric effect is provided in the following sections before a comparative literature review of previous measurements of the splay and bend coefficients is presented in §2.1.5.

Confining the director to a hybrid aligned nematic (HAN) geometry as shown in Figure 2.1 results in homeotropic alignment at one boundary surface and homogeneous planar alignment at the other. Unlike a Fréedericksz device, the HAN cell does not have a voltage threshold for the director to align with an applied electric field. A strong splay-bend distortion field is induced on account of the asymmetry in the molecular distribution, which is potentially useful for the measurement of flexoelectric polarization. In this chapter, a new method is developed based upon analytical, experimental and numerical means to measure the sum of the flexoelectric coefficients in hybrid aligned systems.

2.1.2. The Flexoelectric Coefficients

An external electric field applied across a HAN cell can couple to either the sum or the difference of the flexoelectric coefficients, depending on whether it is parallel or

orthogonal to the plane of the nematic director, respectively. Dozov et al. [2] showed that applying a uniform electric field perpendicular to the plane of the director (E_y) in a nematic LC results in a coupling to the difference between the flexoelectric coefficients (e_1 - e_3). The tilt angle (θ) defines the orientation of the director field in the xz plane. Applying the electric field along the *y*-axis induces a twist, $\phi(z)$, in the xy plane. The components of the director field along the *x*, *y* and *z*- axes can be written in spherical polar coordinates as

$$\hat{\mathbf{n}} = \begin{pmatrix} n_x \\ n_y \\ n_z \end{pmatrix} = \begin{pmatrix} \cos\theta\cos\phi \\ \cos\theta\sin\phi \\ \sin\theta \end{pmatrix}. \tag{2.1}$$

The gradient operator is given by

$$\nabla = \begin{pmatrix} 0 \\ 0 \\ \partial/\partial \mathrm{z} \end{pmatrix}. \tag{2.2}$$

Substituting (2.1) and (2.2) into the expression for the flexoelectric polarization,

$$\mathbf{P_f} = e_1\hat{\mathbf{n}}\,(\nabla\cdot\hat{\mathbf{n}}\,) + e_3(\nabla\times\hat{\mathbf{n}}\,)\times\hat{\mathbf{n}}. \tag{2.3}$$

and dotting the result with the electric field component in the *y*-direction gives the terms for the flexoelectric free energy density,

$$e_1[\hat{\mathbf{n}}(\nabla\cdot\hat{\mathbf{n}})]\cdot\mathbf{E} = e_1\cos^2\theta\sin\phi\frac{\partial\theta}{\partial z}E_y, \tag{2.4}$$

$$e_3[(\nabla\times\hat{\mathbf{n}})\times\hat{\mathbf{n}}]\cdot\mathbf{E} = -e_3\left(\sin^2\theta\sin\phi\frac{\partial\theta}{\partial z} - \sin\theta\cos\theta\cos\phi\frac{\partial\phi}{\partial z}\right)E_y. \tag{2.5}$$

In the minimization of the bulk LC energy, the second term in (2.5) cancels, therefore the equilibrium flexoelectric free energy relates to the difference between the flexoelectric coefficients, variations in the tilt angle profile and the applied electric field along the *y*-axis;

$$f_{\mathrm{flexo}}(\hat{\mathbf{n}}) = -\mathbf{P}_{\mathrm{f}}\cdot\mathbf{E} = -\sin(\phi)\frac{\partial\theta}{\partial z}(e_1\cos^2\theta - e_3\sin^2\theta)E_y. \tag{2.6}$$

If an applied electric field is parallel to the plane of the director along the *z*-axis (E_z), LC molecules with positive dielectric anisotropy tend to align in the direction of the field in the HAN geometry and the electric field couples to the sum of the flexoelectric coefficients ($e_1 + e_3$). In this case, the director field in the *xz* plane is written as

$$\hat{\mathbf{n}} = \begin{pmatrix} n_x \\ n_y \\ n_z \end{pmatrix} = \begin{pmatrix} \cos\theta \\ 0 \\ \sin\theta \end{pmatrix}. \tag{2.7}$$

Using the expressions in (2.2), (2.3) and (2.7), the energy terms are then given by

$$e_1[\hat{\mathbf{n}}\,(\nabla \cdot \hat{\mathbf{n}})] \cdot \mathbf{E} = e_1 \sin\theta \cos\theta \frac{\partial\theta}{\partial z} E_z, \tag{2.8}$$

$$e_3[(\nabla \times \hat{\boldsymbol{n}}) \times \hat{\boldsymbol{n}}] \cdot \boldsymbol{E} = e_3 \sin\theta \cos\theta \frac{\partial\theta}{\partial z} E_z. \tag{2.9}$$

Substituting the double angle formula, ½ sin (2θ) = sinθ cosθ, into (2.8) and (2.9) and summing the expressions gives the free energy density due to flexoelectricity in terms of the sum of the flexoelectric coefficients, variations in the tilt angle profile and the applied electric field along the *z*-axis;

$$f_{\text{flexo}}(\hat{\mathbf{n}}) = -\boldsymbol{P}_f \cdot \boldsymbol{E} = -\frac{1}{2}(e_1 + e_3)\sin(2\theta)\frac{\partial\theta}{\partial z} E_z. \tag{2.10}$$

For an electric field applied in the *z*-direction, the free dielectric energy from (1.9) can be expressed as

$$f_{\text{dieletric}}(\hat{\mathbf{n}}) = -\frac{1}{2} D_z \cdot E_z = -\frac{1}{2}\varepsilon_0 \varepsilon_{zz} {E_z}^2, \tag{2.11}$$

where $\varepsilon_{zz} = \varepsilon_\perp + \Delta\varepsilon \sin 2\theta$. Taking into account contributions from the elastic, dielectric and flexoelectric effects, the total free energy of the system can therefore be written as

$$\begin{aligned} F &= f_{\text{elastic}}(\hat{\mathbf{n}}) + f_{\text{dielectric}}(\hat{\mathbf{n}}) + f_{\text{flexo}}(\hat{\mathbf{n}}) \\ &= -(K_{11}\cos^2\theta + K_{33}\sin^2\theta)\left(\frac{\partial^2\theta}{\partial z^2}\right) \\ &\quad + \left\{(K_{11} - K_{33})\left(\frac{\partial\theta}{\partial z}\right)^2 - \Delta\varepsilon\varepsilon_0 {E_z}^2 + (e_1 + e_3)\left(\frac{\partial E_z}{\partial z}\right)\right\}\sin 2\theta. \end{aligned} \tag{2.12}$$

2.1.3. The Flexoelectric Torque

The flexoelectric polarization in (2.3) gives rise to a bulk torque on the director field [4], which is described in terms of the molecular field as,

$$\boldsymbol{\Gamma}_{\text{flexo}}^{\text{b}} = \hat{\mathbf{n}} \times \mathbf{h}_{\mathbf{f}}\,, \tag{2.13}$$

where

$$\mathbf{h}_{\mathbf{f}} = (e_1 - e_3)[\mathbf{E}(\nabla \cdot \hat{\mathbf{n}}) - (\nabla \otimes \hat{\mathbf{n}})\mathbf{E}] - (e_1 + e_3)(\hat{\mathbf{n}} \cdot \nabla)\mathbf{E}. \tag{2.14}$$

It is clear from (2.14) that bulk flexoelectric torques appear in two terms. The torque from the difference of the flexoelectric coefficients is related to gradients in the director ($\partial\theta/\partial z$). For a HAN structure with an applied electric field parallel to the plane of the director, the e_1 - e_3 dependence is removed as the two terms in the parentheses cancel out;

$$\mathbf{E}(\nabla \cdot \hat{\mathbf{n}}) = \cos\theta \frac{\partial \theta}{\partial z} E_z, \tag{2.15}$$

$$-(\nabla \otimes \hat{\mathbf{n}})\mathbf{E} = \left(\begin{bmatrix} 0 \\ 0 \\ \partial/\partial \mathrm{z} \end{bmatrix} [\cos\theta \quad 0 \quad \sin\theta] \right) \boldsymbol{E} = -\begin{bmatrix} 0 & 0 & 0 \\ 0 & 0 & 0 \\ -\sin\theta \frac{\partial \theta}{\partial z} & 0 & \cos\theta \frac{\partial \theta}{\partial z} \end{bmatrix} \boldsymbol{E}$$

$$= -\cos\theta \frac{\partial \theta}{\partial z} E_z. \tag{2.16}$$

The remaining final term in (2.14) is related to field gradients through the sum of the flexoelectric coefficients,

$$\mathbf{h}_{\mathbf{f}} = -(e_1 + e_3)(\hat{\boldsymbol{n}} \cdot \nabla)\boldsymbol{E} = -(e_1 + e_3)\sin\theta \left(\frac{\partial E_z}{\partial z}\right). \tag{2.17}$$

The resultant bulk flexoelectric torque is

$$\boldsymbol{\Gamma}_{\text{flexo}}^{\text{b}} = -\frac{1}{2}(e_1 + e_3)\sin(2\theta)\frac{\partial E_z}{\partial z}. \tag{2.18}$$

Flexoelectricity can be attributed to sign-dependent responses on account of the linear dependence on an externally applied electric field, highlighted by the coupling between the flexoelectric sum and field gradients in (2.18). The dielectric effect on the other

hand, is quadratic in the applied electric field and therefore is largely sign-independent. Thus, the flexoelectric coupling is expected to either enhance or suppress the dielectric response of the cell under the application of an electric field, depending on the polarity of the applied electric field. The following section employs numerical means to illustrate this interplay between the dielectric and flexoelectric effects.

2.1.4. Numerical Model

Differences between the dielectric and flexoelectric responses in a HAN structure can be revealed through simulations of the director profiles under the application of forward and reverse bias DC voltages. A numerical model is written in terms of the director field expressed as a function of the tilt angle, $\hat{\mathbf{n}} = \mathbf{n}(\theta)$, defined in (2.7). The model uses a finite difference of the Euler-Lagrange equation, $\frac{\partial}{\partial \theta} - \frac{\partial}{\partial z}\left(\frac{\partial}{\partial(\partial\theta/\partial z)}\right)$, to determine the minimization of the free energy due to elastic, dielectric and flexoelectric contributions, which is equated to a viscous dissipation term;

$$-(K_{11}\cos^2\theta + K_{33}\sin^2\theta)\left(\frac{\partial^2\theta}{\partial z^2}\right) + \frac{1}{2}\left\{(K_{11} - K_{33})\left(\frac{\partial\theta}{\partial z}\right)^2 - \Delta\varepsilon\varepsilon_0 {E_z}^2 + (e_1 + e_3)\left(\frac{\partial E_z}{\partial z}\right)\right\}\sin 2\theta = -\gamma\frac{\partial\theta}{\partial t}, \quad (2.19)$$

where γ is a rotational viscosity.

The model is based upon the relaxation method, which uses an iterative process to output the equilibrium response from the device set by the initial boundary conditions (see §1.7 for further details). The local electric field, E_{local}, is derived by neglecting changes occurring in the x and y directions and initially assuming there are no free charges. The non-uniform electric field that appears in the dielectric energy density in (2.11) can be written in terms of a constant displacement field (D_z),

$$E_z = \frac{D_z - P_f}{\varepsilon_0 \varepsilon_{zz}}. \tag{2.20}$$

The potential applied across the cell is then derived as follows;

$$-V = \int_0^d E_z \, dz = \int_0^d \frac{D_z - P_f}{\varepsilon_0 \varepsilon_{zz}} \, dz = \frac{1}{\varepsilon_0}\left(D_z \int_0^d \frac{1}{\varepsilon_{zz}} \, dz - \int_0^d \frac{P_f}{\varepsilon_{zz}} \, dz\right). \tag{2.21}$$

Rearranging (2.21) gives an expression for the displacement field,

$$D_z = \frac{-\varepsilon_0 V + \int_0^d \frac{P_f}{\varepsilon_{zz}} dz}{\int_0^d \frac{1}{\varepsilon_{zz}} dz}, \tag{2.22}$$

which is substituted back into (2.20) for the local electric field along the *z*-axis,

$$E_{local} = \frac{-\varepsilon_0 V + \int_0^d \frac{P_f}{\varepsilon_{zz}} dz}{\int_0^d \frac{1}{\varepsilon_{zz}} dz} - \frac{P_f}{\varepsilon_0 \varepsilon_{zz}}, \tag{2.23}$$

The parameters used in the model are those of the standard commercial eutectic E70 nematic LC mixture, whose dielectric, elastic and optical parameters are listed in Table A.1 of the Appendix. For the purposes of this study, a positive dielectric anisotropy material is used. Figure 2.2 shows the director fields output from the model under different flexoelectric/dielectric conditions with DC voltages of + 3 V and - 3 V applied across a 5 µm-thick HAN device. The voltage was chosen by observing the distortion in the simulated director profiles that is maximized at values > ± 1V, in order to enhance the differences between the flexoelectric and dielectric responses.

Removing flexoelectric contributions altogether ($e_1 + e_3 = 0$) reveals an identical dielectric response when changing the polarity of the applied voltage (dashed lines). In the absence of dielectric anisotropy ($\Delta\varepsilon = 0$), identical director profiles result for both signs of the applied electric field under the flexoelectric effect (dotted lines), for an artificially large value of $e_1 + e_3 = 100$ pC m^{-1}. This is in accordance with the relation for gradients such that the flexoelectric effect couples to the external electric field. However, the curvature of the director profile in this instance reveals a self-coupling to the internal

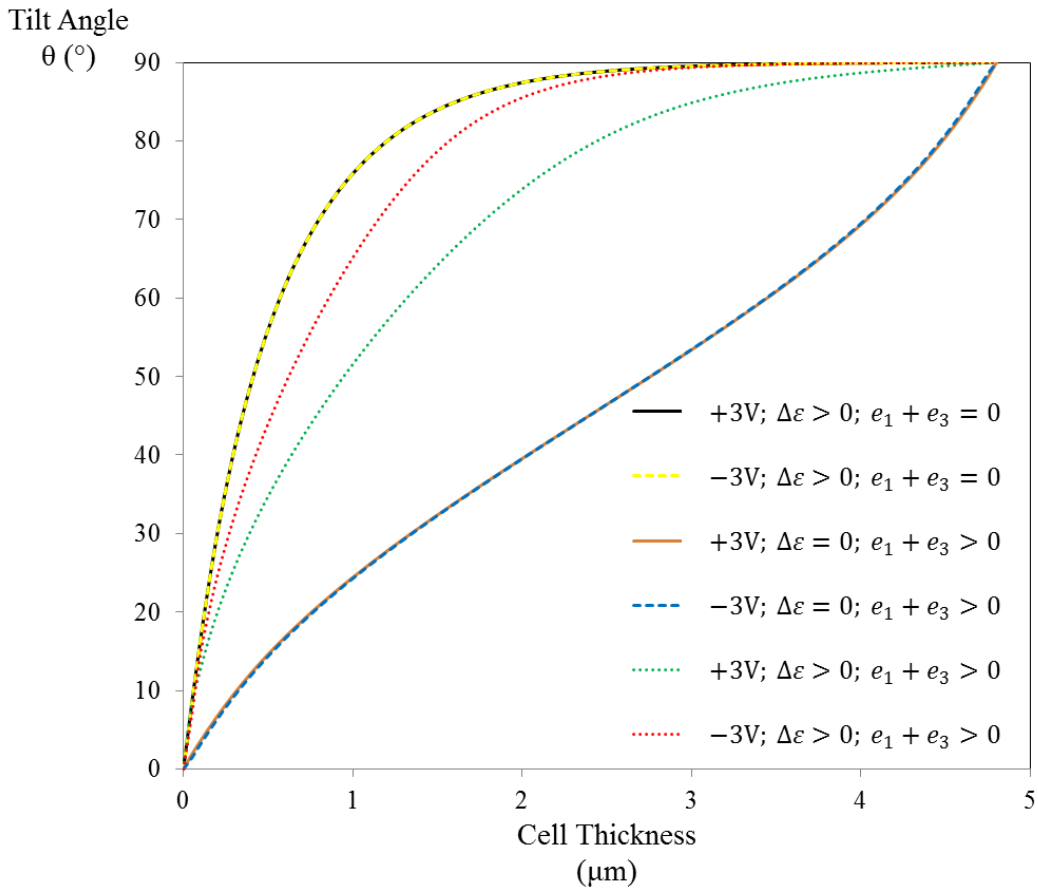


Figure 2.2. Distinguising between flexoelectric and dielectric coupling. Simulated director profiles for a HAN device under the application of a ± 3 V DC electric field when dielectric coupling (Δε), flexoelectric coupling (e_1 + e_3), or both effects are included in the model. Sign-dependent responses can be attributed to flexoelectricity while sign-independent responses are dielectric.

flexoelectric field. When both dielectric and flexoelectric effects are included in the model (solid lines), the flexoelectric polarization couples to the external electric field and enhances the dielectric response under a positive field (-V), while suppressing the response under a negative applied field (+V). Therefore, the director profiles produced from a numerical model that is based upon a minimization of the free energy densities in (2.12), suggest that the flexoelectric effect can be readily distinguished from the dielectric response of the LC device under different polarities of an externally applied electric field. Yet, there is a complex interplay between the different electric energies

present in the system, which will be addressed further by consideration of previous flexoelectric measurements carried out in hybrid aligned geometries.

2.1.5. Flexoelectric Measurements

The implication from the results of the numerical model is that a liquid crystalline material confined in a hybrid aligned system is a suitable geometry to quantify the flexoelectric effect, through sign-dependent responses that are attributed to flexoelectricity and sign-independent responses that are largely dielectric. Previous HAN based measurements, however, have proven to be nontrivial [3, 5 - 8]. Furthermore, difficulties arise in the separation of different polar terms due to the presence of charged impurities in liquid crystalline materials. The possibility of an electrochemical reaction taking place at the electrodes, ionic screening and charge accumulation due to an applied DC voltage [6] therefore need to be taken into account when carrying out measurements of the flexoelectric coefficients.

Madhusudana and Durand [3] reported a method to measure the flexoelectric sum using a mechanism that is localized to surface regions by considering the anchoring energy (W) at the cell boundaries. In the strong anchoring limit, the surface orientation does not depend on the electric field. Moreover, the expression for the flexoelectric torque in (2.18) reveals that the flexoelectric effect is not observed if there are no bulk field gradients ($\Delta\varepsilon = 0$). Assuming infinite W at the planar orienting surface and weak anchoring at the homeotropic boundary of a HAN cell, Madhusudana and Durand developed a model that solves the free elastic energy and flexoelectric terms when equated to the surface torque, giving an expression that relates the optical path difference (Δl) to the linear electro-optic effect ($e_1 + e_3$) associated with weak anchoring conditions.

Their simplified model is based on the assumption that the energy due to the dielectric anisotropy is negligible as the flexoelectric effect dominates at small electric field strengths. Through measurements of Δl between extraordinary and ordinary light rays in two HAN cells, Madhusudana and Durand calculated values for the flexoelectric sum by comparing Δl at the corresponding positive and negative applied voltages.

In Ponti et al.'s [5] comment on [3], the authors highlighted that flexoelectricity couples to the bulk of a HAN cell and, therefore, cannot be localized to surface regions alone. The distinct polar effect observed in Madhusudana and Durand's results can instead be attributed to the presence of charged impurities (ions are likely to exist in any sample), producing strong variations in the electric potential due to the ionic screening effect that acts to lower the elastic free energy at the surface regions [5].

In a strong anchoring limit, Ponti et al. [5] estimate an effective flexoelectric internal bias induced by the flexoelectric polarization due to the deformation of the director field as

$$V_b = \frac{e}{2\varepsilon_a \varepsilon_0} \ln \frac{\varepsilon_\perp}{\varepsilon_\parallel}, \tag{2.24}$$

where ε_a is the dielectric anisotropy, $\varepsilon_\perp$ and $\varepsilon_\parallel$ are the perpendicular and parallel dielectric permittivities respectively, and $e = (e_1 + e_3) / 2$ is an average of the flexoelectric coefficients. While the impurities play an important role in the measurement of Δl at lower voltages due to ionic screening of the electric field, the voltage shift in (2.24) is responsible for the discrepancy between actual and nominal voltages between electrodes at higher voltages, and therefore can be attributed to the polar optical response seen in the data of [3].

The period of an applied waveform is another important factor to consider when carrying out electro-optic measurements to probe flexoelectricity. There are two

characteristic timescales which need to be considered when a DC field is applied to an ionic liquid; one concerned with ionic mobility and the other with absorption from the electrode. The first characteristic time depends on the sample thickness, liquid conductivity, and applied voltage, and is independent of the nature of the electrode. Subsequently, the ions are collected close to the electrodes and a screening effect occurs, whereby the ionic absorption from the electrode depends on the absorption energy of the surfaces with respect to the ions [7]. To this end, the ionic contribution to the electric field distribution must be taken into account in order to accurately model a liquid crystalline system.

Barbero and Evangelista [7] comment on the inaccuracy of the assumptions made in a paper by Mazulla et al. [6], where they ignore the bulk charge distribution in a HAN cell under the application of low voltages and assume that the LC is a perfectly insulating material. Under an applied voltage range of V_a = 0 –1.5 V, an 8 µm- thick HAN cell filled with a nematic LC mixture (5CB) has an ionic mobility (μ) in the range of 10^{-6} – 10^{-5} $cm^2\ V^{-1}\ s^{-1}$ and an ion transport time given by

$$\tau = d^2/\mu V_a. \tag{2.25}$$

Implementing these parameters into (2.25) results in an ion transport time of ~100 ms. The period of the applied signal (1 s) used in the experimental work of [6] is much longer than both the LC response and ion transport times; therefore, ions do in fact contribute to the molecular orientation of the LC director induced by the electric field. Moreover, the effective ionic mobility depends on the nematic director; therefore, the ion transport time depends on the applied voltage polarity.

The literature presented on previous HAN-based flexoelectric measurements outlines the difficulties that arise in the separation of polar terms attributed to flexoelectricity,

nominally due to the presence of charged impurities in LC materials. An additional complication arises from the different surface alignment polarities inherent in HAN geometries, which will be discussed further in the next section.

2.1.6. Internal Bias

The effective internal bias due to flexoelectricity, V_b in (2.24), induces asymmetry between positive and negative applied voltages similar to an internal bias, V_s, from different surface alignment polarities [5]. The simulated data shown in Figure 2.2 confirmed that this was indeed the case, as it was possible to differentiate between the dielectric and flexoelectric energies under the application of forward and reverse bias DC voltages. However, ions present in the LC lead to screening of DC fields [7]. Moreover, the asymmetric surfaces in a HAN cell that induce the strong splay-bend distortion field also give rise to different surface alignment polarities. As a result, different dielectric and flexoelectric effects may eventually become indistinguishable. The following issues therefore need to be addressed for the measurement of the flexoelectric coefficients based on sign-dependent responses:

1. Ionic screening due to the presence of charged impurities
2. Internal bias due to different surface alignment polarities, V_s
3. Effective internal bias due to flexoelectricity, V_b

The model can be used to investigate further the separation of different polar terms and sign-dependent responses. Figure 2.3 shows the modelled equilibrium director profile for 1 V applied across a 5μm-thick HAN cell, using the same E70 nematic LC material parameters listed in Table A.1 of the Appendix. For a fixed e_1+e_3, the effective flexoelectric internal bias was calculated from Ponti's relation [5] in (2.24), and in the

absence of flexoelectricity an external DC offset was deliberately applied to the voltage using this value, in order to demonstrate the equivalence between flexoelectricity and bias. Setting e_1+e_3 to an arbitrary value of + 20 pCm^{-1} and - 20 pCm^{-1} (solid lines) gave an equivalent internal bias of - 100 mV and + 100 mV (dashed lines), respectively. The director profiles show that flexoelectric effects would break the degeneracy between positive and negative applied voltages, illustrated by the asymmetry in the director profile when equivalently changing the polarity of the sum of the flexoelectric coefficients. However, under zero flexoelectric contributions, applying a positive and negative external DC offset equivalent to the calculated effective flexoelectric internal bias reveals almost identical director profiles to those due to flexoelectricity. This highlights the issue that the internal bias due to the different surface alignment polarities in the HAN cell behaves much the same way as the flexoelectric effect by inducing asymmetry in the LC response. Thus, applying electric fields of opposite polarities to identify the different electric energies, as shown in Figure 2.2, is not sufficient to probe the flexoelectric effect. The assumption that sign-dependent responses can be attributed solely to flexoelectricity is therefore no longer valid, making it difficult to distinguish between different polar terms through the director field of a HAN cell.

The simulated director fields in Figure 2.3 reveal the similarity between the flexoelectric effect and a voltage offset in the form of an internal bias. To clarify, the internal bias due to the different surface alignment polarities (V_s) cannot be distinguished from the effective flexoelectric internal bias (V_b) defined in (2.24). A measurement of the flexoelectric coefficients in HAN geometries is therefore potentially skewed by the presence of V_s. Additionally, the system is further complicated by the presence of ions in the LC material as discussed in § 2.1.5 due to the screening effect that occurs under the

application of a forward or reverse bias voltage, making it also difficult to distinguish between non-polar and polar terms i.e. the dielectric and flexoelectric responses. Yet, the effect of ionic screening on an internal bias has not previously been considered in HAN systems. Considering the ions act to screen out an applied DC voltage, a small voltage offset due to the internal bias in the device may also be screened out. The next section describes the experimental arrangement used to test this hypothesis.

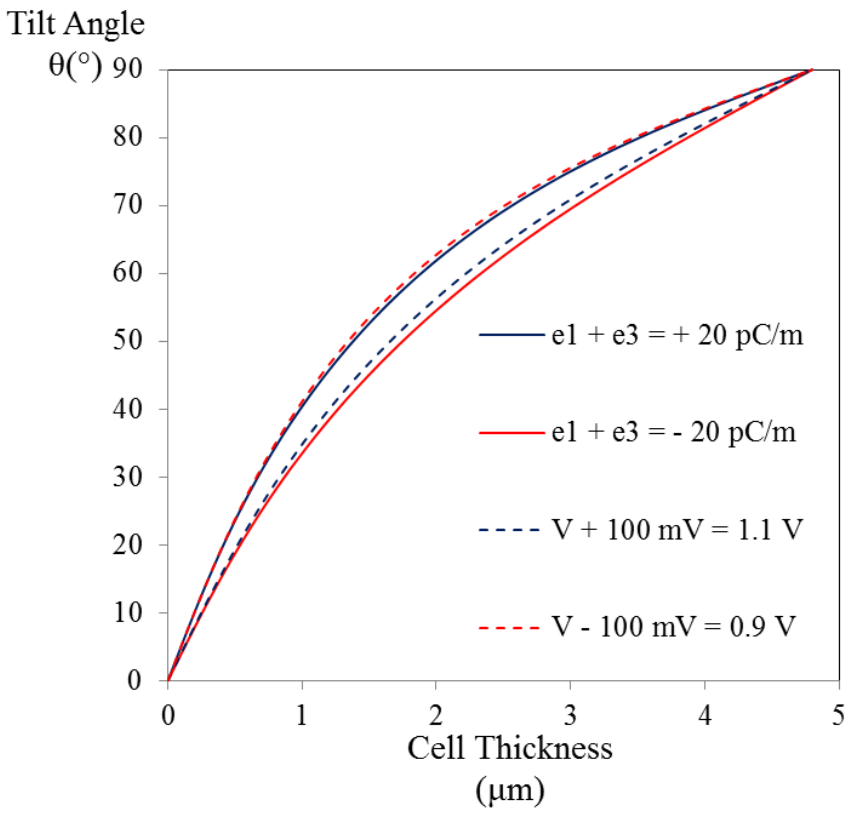


Figure 2.3. Distinguishing between flexoelectrcitiy and a voltage offset. Simulated director profiles of a HAN cell reveal the similarity between changing polarities of externally applied offsets and the flexoelectric sum.

2.2. EXPERIMENTAL ARRANGEMENT

The optical set-up as shown in Figure 2.4 illustrates the beam trajectory (red) of monochromatic light (wavelength 632.8 nm) emitted from a class 3R He-Ne laser. Light is transmitted through the test cell, which is between crossed polarizers. The device is perpendicular to the laser beam, but oriented so that the director is at 45° to the plane of polarization (polarizer and analyzer) for maximum transmission. The detected signal is observed on an oscilloscope. Two arbitrary waveform generators (AWGs) are connected across the device, one to apply the oscillating field and another to control the external DC offset. An example of the type of waveform applied across the device is shown in Figure 2.5, for a 100 Hz, ± 0.2 V square wave offset by a 1 Hz, ± 100 mV square wave.

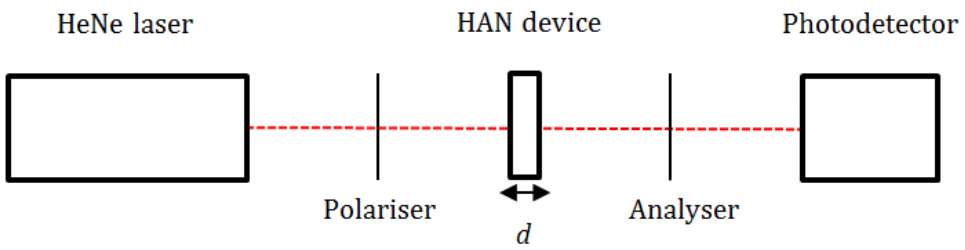


Figure 2.4. Optical set-up for the measurement of the flexoelectric sum. Light from a HeNe laser propagates through a HAN device filled with a nematic LC mixture that is positioned between crossed polarizers; transmission was observed by a photodetector.

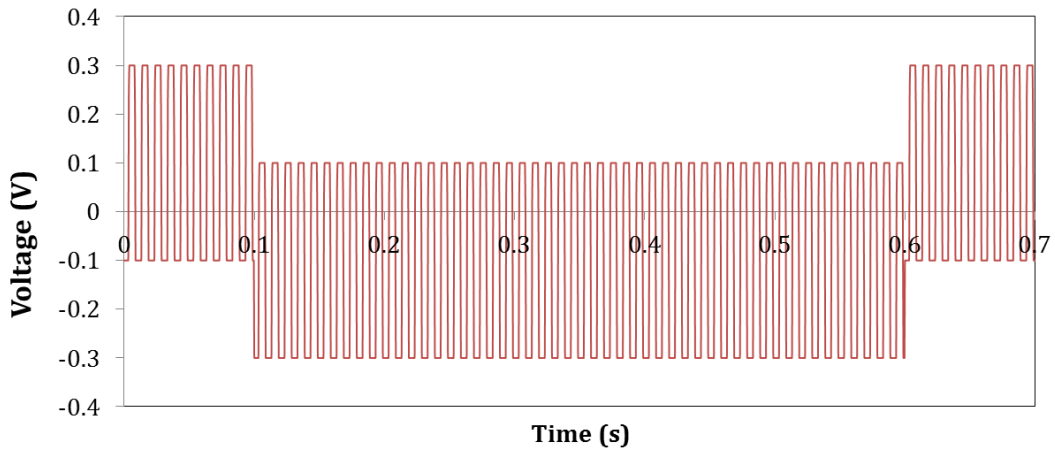


Figure 2.5. An example of the waveform produced by the two arbitrary waveform generators. A 100 Hz oscillating field ± 0.2 V in amplitude is offset by a 1 Hz, ± 100 mV square wave.

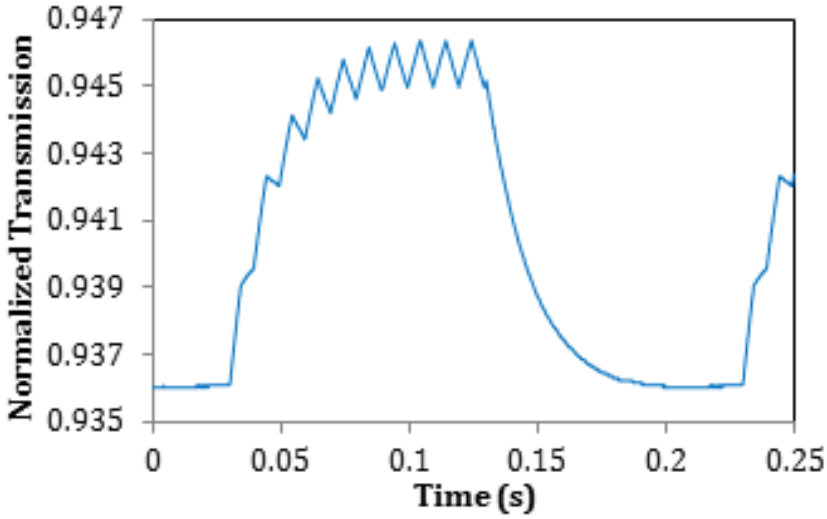


Figure 2.6. Transmission from a HAN cell filled with a pure (non-ionic) material. A 100 Hz ± 0.1 V square wave offset by a 5 Hz, ±193 mV square wave was applied across the HAN cell. The modulation due to the polar responses is exactly cancelled at an offset value of +193 mV.

2.2.1. Ionic Screening

Preliminary experiments were carried out to test whether the ions in a liquid crystalline material could be used to screen out the internal bias inherent to hybrid aligned geometries. A 5.0 μm-thick HAN cell was capillary-filled with a non-ionic material, MAT-13-1803 (Merck Chemicals Ltd.) that has a dielectric anisotropy of $\Delta\varepsilon = 7.1$ at T = 20°C, in the isotropic phase (see Table A.2 of the Appendix for other parameters). Figure 2.6 shows the transmission from the HAN device filled with the non-ionic material, measured when applying a 100 Hz, ± 0.1 V square wave. An external offset (V_{off}) was applied to the AC signal using a 5 Hz square wave, and its amplitude varied until the modulated response due to the combination of the flexoelectric internal bias and different surface alignment polarities (V_{b+s}) was exactly cancelled for one sign of the additional signal, which was found to occur at a value of +193 mV.

Figure 2.7 (a) shows the simulated LC response of the 5.0 μm-thick HAN cell filled with the non-ionic material under the application of a 100 Hz, ± 0.1 V square wave

offset by a 5 Hz, ±193 mV square wave. The simulation was produced under dielectric effects alone ($e_1+e_3 = 0$, $V_{b+s} = 0$), which does not reproduce the experimental data shown in Figure 2.6. Using Ponti's expression for the effective flexoelectric internal bias in (2.24), a voltage offset of +193 mV corresponds to an e_1+e_3 of 22.0 pCm^{-1}. Adding a flexoelectric value of 22.0 pCm^{-1} to the model reproduces the data well, as illustrated by the simulated electro-optic response shown in Figure 2.7 (b). In addition, applying an equal and opposite voltage bias (V_{b+s}) of -193 mV under zero flexoelectric contribution also replicates the data, as shown in Figure 2.7 (c).

The simulated director profiles in Figure 2.2 demonstrate the difficulties in distinguishing the flexoelectric effect from an internal bias or voltage offset. The results shown in Figures 2.6 and 2.7 highlight the difficulties in the separation of polar effects, whereby flexoelectric contributions included in the model generate the same electro-optic response as that observed under the application of an equal and opposite voltage bias. The results presented in Figures 2.6 and 2.7 address the case of a HAN cell filled with a non-ionic material.

An ionic LC material generates distinct electro-optic behaviour, whereby responses to pulses are independent to the external offset of a signal applied to a HAN device filled with an ionic material. Identical responses to square waves have been observed whether there is zero, positive or negative offset in the signal, signifying the independence of the response from a shift in the applied voltage. Driving the device with step changes in the offset leads to a transient change in the response, such that the equilibrium response remains the same. For a non-ionic material, the transmission does not return to its equilibrium value under the application of a voltage offset, as shown in Figure 2.6. In addition, the time constant of the transient effect is consistent with the relaxation time of

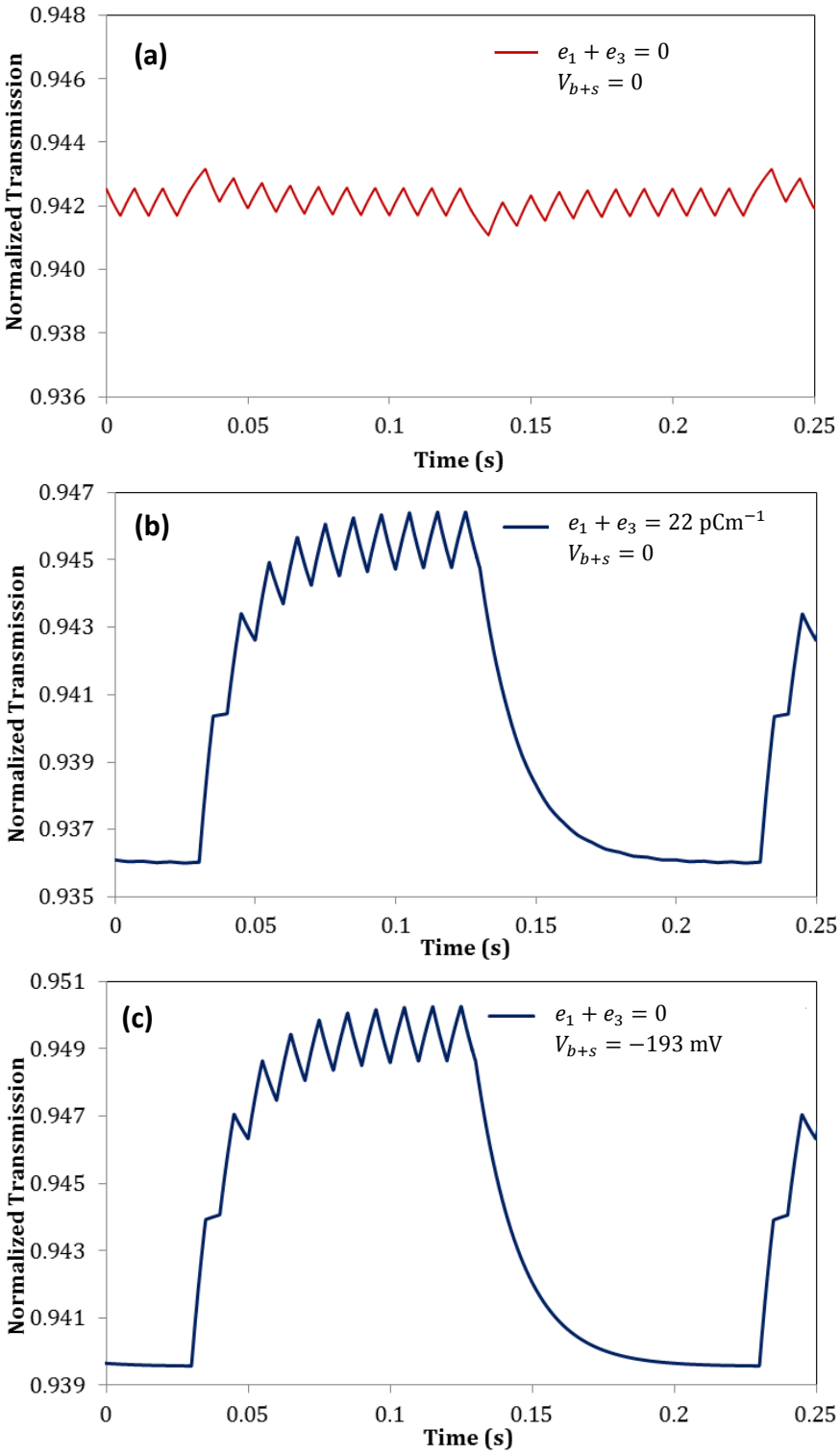


Figure 2.7. The simulated transmission as a function of time from a HAN cell filled with a non-ionic material. The LC response is shown for (a) e_1+e_3 = 0, V_{b+s}= 0, (b) e_1+e_3 > 0, V_{b+s}= 0 (c) e_1+e_3 = 0, V_{b+s} > 0. The simulation was produced for a 5 µm-thick device filled with MAT-13-1803, in the absence of ionic contributions.

the ions present in the material. Figure 2.8 shows the transmission when driving a HAN device filled with the E70 nematic LC mixture provided by Merck Chemical Ltd., with a square wave of 100 Hz, ± 0.2 V, offset by a 1 Hz, ± 100 mV square wave. A transient response is observed to the offset signal (1 Hz, ±100 mV square wave), leading to an increase/decrease in the transmission amplitude under externally applied positive/negative offsets. The offsets have no long-term effect on the cell's response, which returns to equilibrium over a timescale of ~100 ms. This timescale is of the order of the ion transport time in (2.25), suggesting a screening effect is at work. It is therefore reasonable to assume that the ions also screen out any internal bias caused by a combination of the flexoelectric polarization and the difference in the surface alignments of a HAN cell. Although the ions screen the internal bias, the modulation in Figure 2.8 is

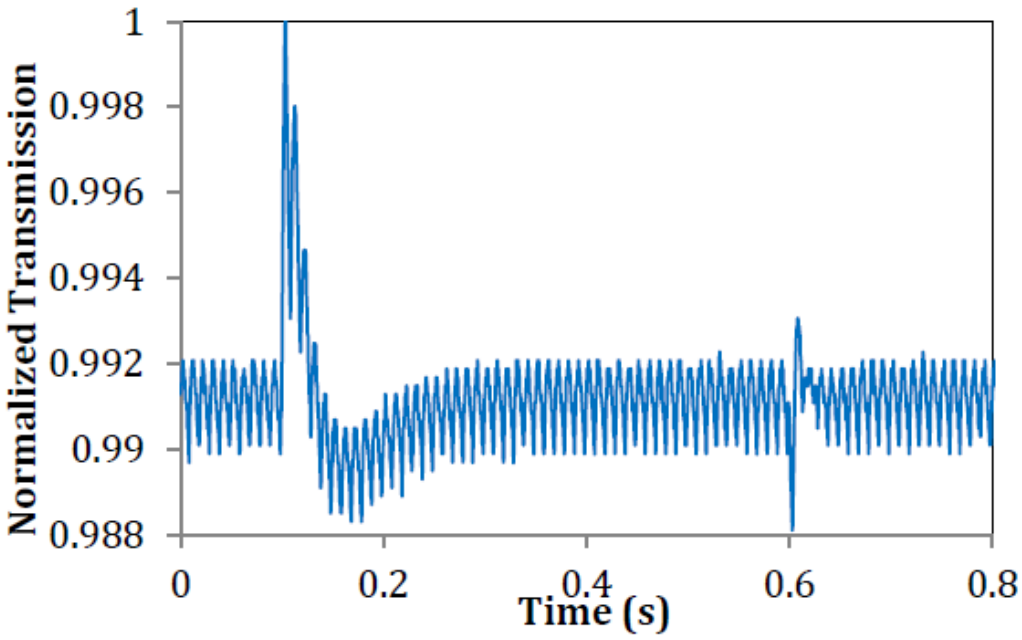


Figure 2.8. Ionic screening of a voltage offset. Transient E70 LC response to 100 Hz ± 0.2 V field with an external offset of ±100 mV at 1 Hz. A -100 mV to +100 mV transition in the offset occurs at 0.1 s, followed by a +100 mV to -100 mV transition at 0.6 s.

an indication that the dynamics due to the flexoelectric effect remain at a frequency of 100 Hz, thereby generating asymmetry in the LC response. Assuming the ions screen out the internal bias inherent to a hybrid aligned system, which is manifested by the transient response of Figure 2.8, the remaining response from the cell could then potentially be used as a measure of the flexoelectric effect. Under this assumption, basic device parameters were initially calculated from data-theory fits before implementing ions in the numerical model for measurements of the flexoelectric coefficients.

2.2.2. Device Parameters

Basic device parameters such as cell thickness (d) and rotational viscosity (γ) are obtained by fitting experimental data to the simulations. Device transmission is calculated using Jones matrices for θ (z) as described in §1.4.2, which then produces light transmission as a function of voltage, T (V) from the device under the application of an electric field. The thickness of the device is obtained from a fit of theoretically and experimentally obtained data that can be conceptually understood by modification of the transmission equation, (1.21) in §1.4.2 to

$$\frac{I_{out}}{I_{in}} = \sin^2(2\chi)\sin^2\left(\frac{\pi\Delta n_{effective}d}{\lambda}\right), \tag{2.26}$$

where χ is the angle between the director and the z-axis as defined in Figure 2.1. The ratio of output to input light intensities (I_{out} : I_{in}) is maximum i.e. there is peak transmission when the terms in the brackets are equal to $\pi/2$. At the homogeneous boundary, $\Delta n_{eff} = \Delta n = n_e - n_o$. As the voltage is increased, the director is almost entirely perpendicular to the substrates in a homeotropic alignment due to the positive dielectric anisotropy of the LC material, so that $\Delta n_{eff} \approx 0$ throughout. Light transmission is therefore modulated by fixing the cell at $\chi = \frac{\pi}{4}$ between crossed

polarisers and varying the applied voltage, which varies the effective birefringence in accordance with the second factor in (2.26).

Figure 2.9 shows the transmission curves obtained from the experimental set-up and that produced by the model. The experimental transmission curve was obtained using amplitude modulation, whereby a square wave at 1 kHz applied to the cell was modulated by a frequency of 10 mHz. The simulated response was obtained by the application of a DC field to the device, which is stepped-up with each iteration i.e. over time. Ionic and flexoelectric contributions are ignored in the derivation of the sample thickness (hence AC and DC responses are equivalent in the model).

Good agreement is achieved between the experimental and theoretical plot until the point of peak transmission. Subsequently, the simulated response undershoots the experimental data, which indicates that the program does not exactly replicate the behaviour of the cell. However, the derivation of sample thickness is related to the region of the transmission curve leading up to and including the peak, as described by (2.26), therefore the discrepancy in the data-theory fit can be ignored. A thickness of 4.8μm was established for the E70 test cell.

The flow properties of liquid crystalline materials are anisotropic. There are five independent viscosities associated with LCs; one rotational (γ) and four shear viscosities $(\eta_1, \eta_2, \eta_3, \eta_4)$. However, the measurement of the shear viscosities proves problematic and is often ignored in measurements of other LC behaviour, including flexoelectricity. Additionally, rotational viscosity is predominant in the switching of LC devices, as the optical switching effect occurs from the rotation of the director. A typical range of values for γ in the material used in displays are 70 - 200 mPa s, though more viscous materials can be synthesized [9].

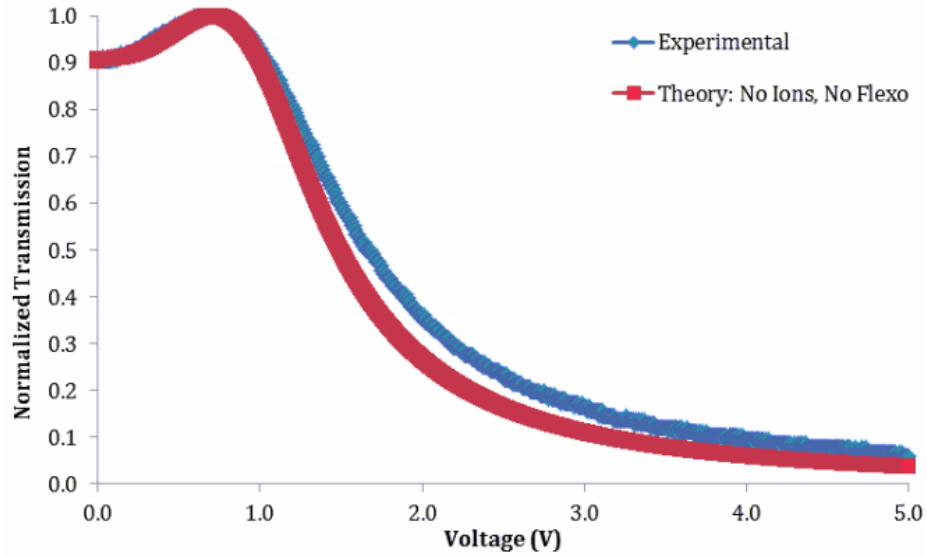


Figure 2.9. Data-theory fits for the derivation of device thickness. The experimental and theoretical transmission as a function of voltage illustrate a good fit until the point of peak transmission, giving a device thickness of 4.8 µm.

Introducing a step-input across the device from zero applied voltage produces a dynamic transmission curve as a function of time. The LC viscosity can then be derived from comparisons between data and theory for scaling of the time axis. Figure 2.10 (a) shows both experimental and theoretical transmission plots when a step-input of 2 V at 1 kHz is introduced from zero applied voltage. The viscosity was found to be 225 mPa s. The data acquired when switching off the signal is also shown in Figure 2.10 (b) and demonstrates a better fit with the simulated response for a lower value of 150 mPa s. Therefore, the switching-off data was utilized for the viscosity in the E70 test cell. Ionic and flexoelectric contributions have been ignored in the derivation.

Transmission as a function of time is recorded for the measurement of the flexoelectric sum in the low frequency ($\leq$ 100 Hz), low voltage regime (< 1V). As highlighted previously, the flexoelectric effect is linear with respect to the applied electric field; therefore, applying low voltages allows it to become dominant over the LC's dielectric anisotropy, which is quadratic with the applied electric field. The

following section describes the theory behind the addition of ions to the model that play a major role in the determination of the flexoelectric response in a hybrid aligned system.

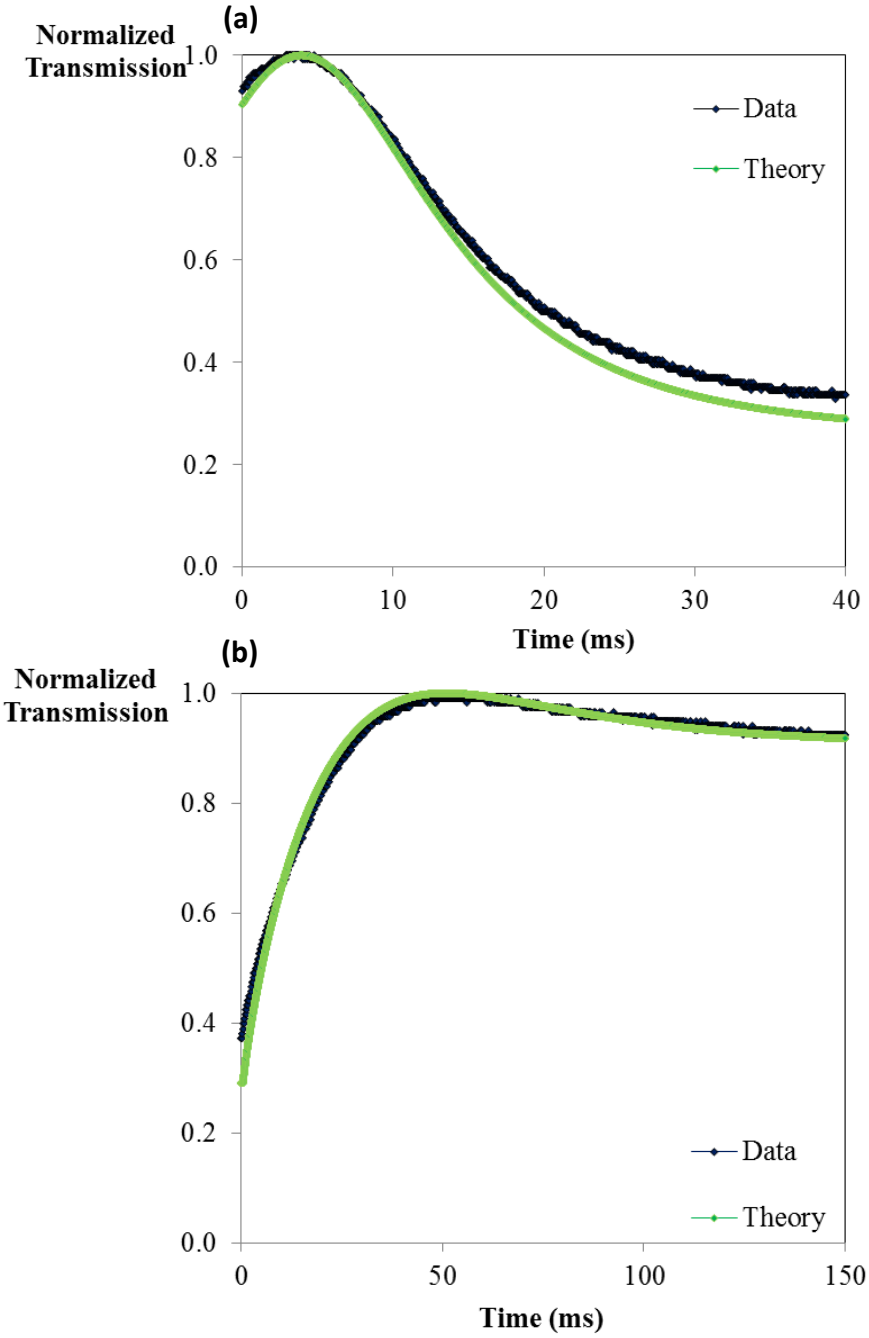


Figure 2.10. Data-theory fits for the derivation of the rotational viscosity. The transmission as a function of time obtained when a DC voltage of 2 V and a frequency of 1 kHz applied across the HAN device was switched (a) on and (b) off. The simulated transmission curve upon removal of the applied field produced a better fit to the experimental data for a viscosity value of $\gamma = 150$ mPa s.

2.3. THEORETICAL MODELLING

Ionic behaviour is implemented in the numerical model of the HAN cell by consideration of the space charge transport properties, and is drawn from a simplification of Buczkowska and Derfel's method [10-12]. The generation and recombination processes determine the ion concentration. The generation constant is dependent upon the applied electric field and is given by,

$$\beta = \beta_0 \left(1 + \frac{q^3}{8\pi\varepsilon_0 \bar{\varepsilon} {k_B}^2 T^2} \cdot E\right), \tag{2.27}$$

where the electronic charge q = 1.6×10^{-19} C, k_B = 1.38×10^{-23} m^2 kg s^{-2} K^{-1} is Boltzmann's constant, T ≃ 300K is the approximate room temperature and the average dielectric constant $\bar{\varepsilon} = (2\varepsilon_\perp + \varepsilon_\parallel)/3$. In the model, the generation constant is controlled by the parameter in the absence of an external field, β_0, which is varied arbitrarily from 10^{17} to 10^{27} m^{-3}s^{-1}. The upper limit of the range for β_0 is four orders of magnitude larger than that used in Buczkowska and Derfel's papers to allow for high ionic contamination in the E70 mixture. The recombination constant depends on the average mobility and is written as,

$$\alpha = \frac{2q\bar{\mu}}{\varepsilon_0 \bar{\varepsilon}}, \tag{2.28}$$

where $\bar{\mu}$ = ½ [(2$\mu_\perp^+$ + 2$\mu_{//}^+$)/3 + (2$\mu_\perp^-$ + 2$\mu_{//}^-$) / 3] is the average mobility. The superscripts '+' and '–' represent cation and anion mobilities, respectively. The model is based on the assumption that μ^- >> μ^+ [13]. Buczkowska and Derfel maintain a ratio of $\mu_{//}^{\pm}$ / $\mu_\perp^{\pm}$ ≈ 1.0 using the following mobility values; $\mu_{//}^+ = \mu_\perp^+$ = 1.5 × 10^{-10} m^2 V^{-1} s^{-1} and $\mu_{//}^- = \mu_\perp^-$ = 1.5×10^{-9} m^2 V^{-1} s^{-1}. This ratio is also preserved in the current investigation when varying the mobilities during data-theory fits. The average ion concentration in the

equilibrium state of zero applied voltage can be found from the generation and recombination constants,

$$N_0 = \sqrt{\beta_0/\alpha}. \tag{2.29}$$

The diffusion coefficients are given by

$$D_{\parallel,\perp}{}^{\pm} = (k_B T/q)\mu_{\parallel,\perp}{}^{\pm}. \tag{2.30}$$

The mobilities and diffusion coefficients in the direction of the applied field are written as,

$$\mu_{zz}{}^{\pm} = \mu_{\perp}{}^{\pm} + \Delta\mu^{\pm}\sin^2\theta, \qquad D_{zz}{}^{\pm} = D_{\perp}{}^{\pm} + \Delta D^{\pm}\sin^2\theta, \tag{2.31}$$

where $\Delta\mu^{\pm} = \mu_{//}{}^{\pm} - \mu_{\perp}{}^{\pm}$ and $\Delta D^{\pm} = D_{//}{}^{\pm} - D_{\perp}{}^{\pm}$ are the respective anisotropies. The model is based on a balance of currents due to drift (first term) and diffusion (second term),

$$J_z{}^{\pm} = \mp\left(\mu_{zz}{}^{\pm}N^{\pm}\frac{\partial V}{\partial z} \pm D_{zz}{}^{\pm}\frac{\partial N^{\pm}}{\partial z}\right). \tag{2.32}$$

As flexoelectricity is a bulk effect, the model can be simplified to solve the flux of ions in the bulk, using a discretization and relaxation method. The transport of ions in the bulk is governed by the continuity of ion fluxes which is written as,

$$\frac{\partial N^{\pm}}{\partial t} = [\beta - \alpha N^{+}N^{-}] - \frac{\partial J_z{}^{\pm}}{\partial z}. \tag{2.33}$$

Zero transport and surface trapping is assumed at the device boundaries, so that surface interactions can be neglected. Poisson's electrostatic equation is implemented for the potential distribution across the cell;

$$\varepsilon_0\varepsilon_{\perp}\frac{\partial^2 V}{\partial Z^2} + \varepsilon_0\Delta\varepsilon\cos^2\theta\frac{\partial^2 V}{\partial Z^2} - \varepsilon_0\Delta\varepsilon\sin 2\theta\frac{\partial V}{\partial z}\cdot\frac{\partial\theta}{\partial z} \qquad + (e_1+e_3)\cos 2\theta\left(\frac{\partial\theta}{\partial z}\right)^2 +$$

$$\frac{1}{2}(e_1+e_3)\sin 2\theta\frac{\partial^2\theta}{\partial z^2} + \rho \qquad = 0. \tag{2.34}$$

where the charge density is $\rho = q\,[N^{+} - N^{-}]$.

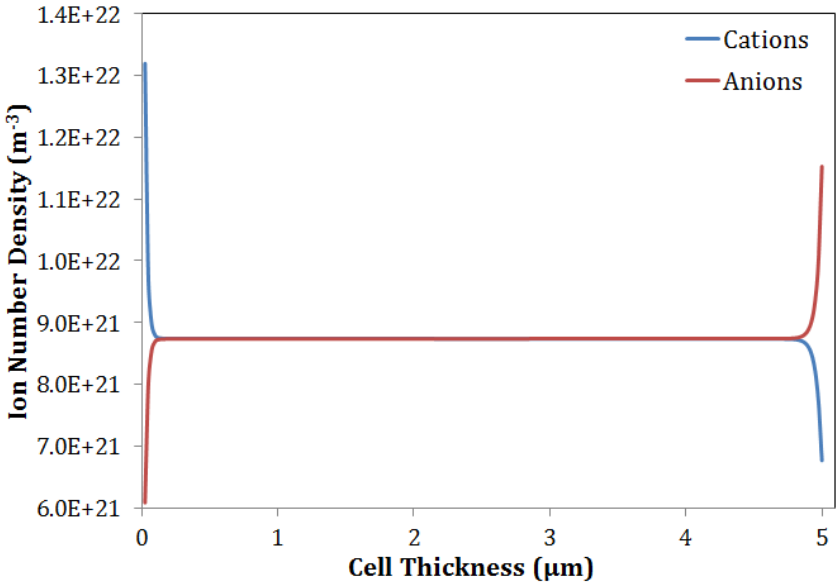


Figure 2.11. Ion number density as a function of cell thickness, for a high ionic content of 8.74×10^{21} m^{-3}, under the application of a 0.1 V DC field.

In summary, the model employs a finite difference technique to solve the following three main equations:

i. Euler-Lagrange solution to elastic, dielectric and flexoelectric torques in the bulk (c.f. §2.1.4).

ii. Poisson's equation for potential distribution, assuming zero transport at the boundaries.

iii. Continuity of ion fluxes governing transport of ions in the bulk.

As stated above, the parameters varied in the data-theory fits are the generation constant in the absence of an applied field, the ion mobilities while preserving the cation to anion mobility ratio of ~1.0, and finally the sum of the flexoelectric coefficients. Each parameter leads to a subtle difference in the shape of each data-theory fit. Figure 2.11 shows the simulated ion number density distribution for both cations and anions. It can be seen that the ions drift to the device boundaries, with a larger

distribution of positive ions at one boundary and negative ions at the other due to the different surface alignment polarities [6]. This ionic motion suggests that the ions do indeed drift to screen out an applied DC voltage of 0.1 V and therefore any internal bias resultant from the asymmetric surfaces of a HAN cell, as predicted from the experimental results in Figure 2.8.

Figure 2.12 shows simulations of the transmission as a function of time produced from the HAN cell with the inclusion of ionic effects (for an ion number density of 8.74 $\times$ 10^{21} m^{-3}), when the flexoelectric sum is varied from 10 pCm^{-1} to 50 pCm^{-1} under an oscillating field of 100 Hz, ± 0.2 V. The transmission modulation increases in amplitude and tends towards a saw-tooth form for larger e_1+e_3 values. This distinct behaviour caused by the flexoelectric response can be used to produce data-theory fits through variations in the parameters set in the model i.e. the sum of the flexoelectric coefficients and the ionic concentration.

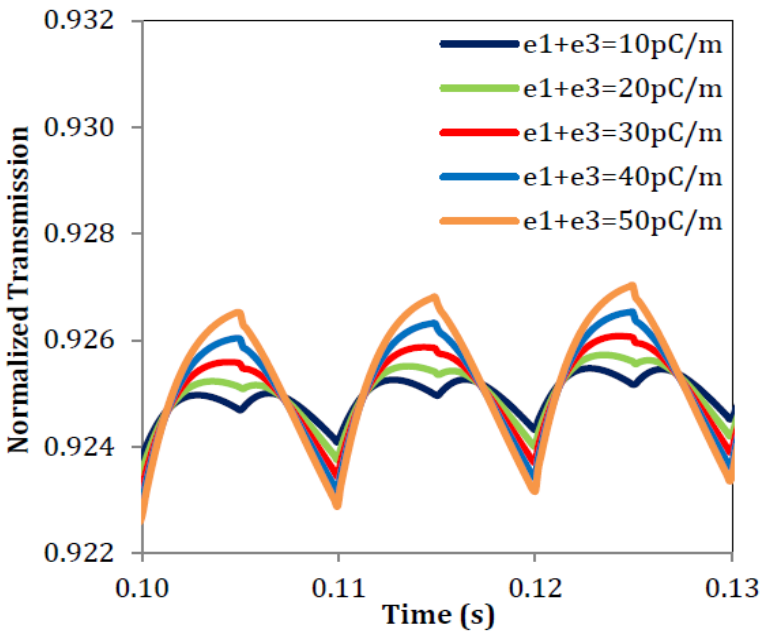


Figure 2.12. Simulated transmission as a function of time. Output from numerical model of a 5.0 μm-thick HAN cell using E70 material parameters and with an ion number density of 8.74 $\times$ 10^{21} m^{-3}. The flexoelectric sum is varied from 10 to 50 pC/m under an applied field of 100 Hz, ± 0.1 V.

2.4. RESULTS & DISCUSSION

The theoretical model outlined in §2.1.4 and §2.3 can now be used to simulate the electro-optic response from a HAN cell filled with an ionic LC material for comparison with experimental observations. Figure 2.13 shows the obtained data-theory fit for transmission as a function of time for the HAN E70 nematic LC device under an applied field of 100 Hz, ± 0.2 V. The data sets were obtained on three separate occasions, leading to variations in the surrounding temperature as well as in transmission measurements from different positions across the cell, which gave slight variations in the device thickness of ± 0.1 μm. A range of values were obtained for $|e_1+e_3|$, indicative of the margin of error in the results, with an average value established at (10 ± 2) pCm^{-1}.

Slight variations were also measured in the ion concentration, which highlights that the method relies upon the presence of ions as a general screening effect, rather than a necessity to quantify the precise ionic content. Nonetheless, a high concentration of ions (10^{21} m^{-3} ≤ N_A < 10^{22} m^{-3}) is required to achieve accurate numerical fits to the experimental data, confirming that E70 is highly contaminated with impurities. Interestingly, some covariance is observed between the flexoelectric and ionic parameters included in the model, whereby subtle changes result in the shape of the modulation similar to those described in Figure 2.12. Increasing the ionic content led to a more saw-tooth shaped modulation, as observed for increasing flexoelectric contributions. The covariance between the parameters is explored further in Chapter 3. The average E70 parameters resultant from the theoretical and experimental comparisons are summarized in Table 2.1.

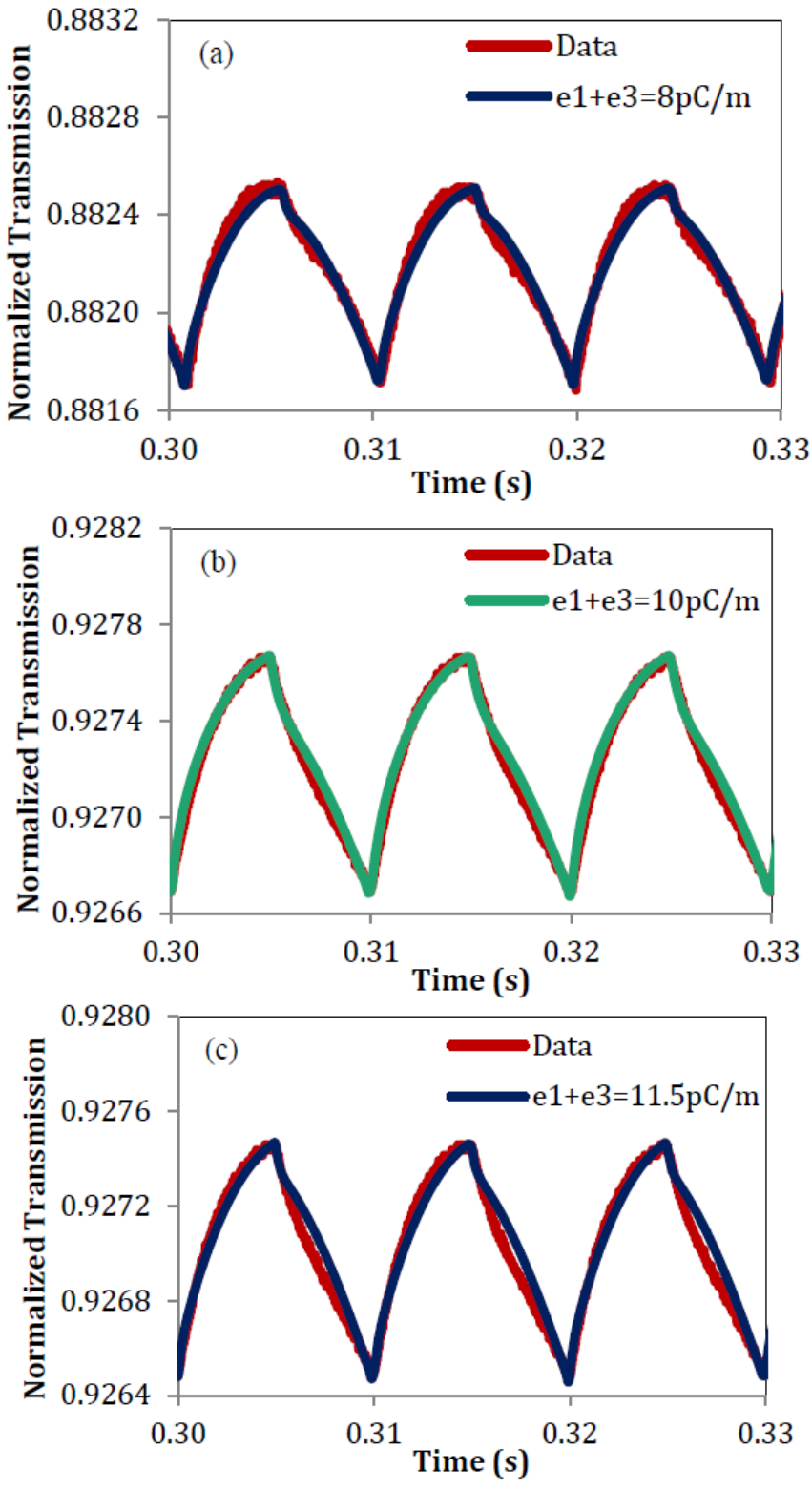


Figure 2.13. Measurement of the flexoelectric sum. Data-theory fits of transmission as a function of time for an E70-filled HAN cell taken on three separate occasions, under an applied voltage of 100 Hz, ± 0.2 V.

E70 DEVICE PARAMETERS

d	Cell Thickness	(4.9 ± 0.1) µm
γ	Viscosity	150 mPa s
N_A	Ionic Content	10^{21} m^{-3} - 10^{22} m^{-3}
$\lvert e_1+e_3 \rvert$	Flexoelectric Sum	(10 ± 2) pCm^{-1}

Table 2.1. E70 parameters established from data-theory fits.

In order to assess whether any internal bias due to the surface polarization resultant from the cell surfaces does not contribute to the device response, the parameters shown in Table 2.1 are fixed in the numerical model and an external offset of ± 0.1 V is applied. Figure 2.14 shows that the simulated transmission as a function of time after the model reaches equilibrium (i.e. t > 0). The model replicates the transient response observed experimentally, over a similar timescale to that shown in Figure 2.8. Changes in the external offset of ± 0.1 V DC are screened out; therefore, it is reasonable to assume that the internal bias due to the surface polarization is also screened out. There is, however, a significant difference in the amplitude of the modulation for changing polarities in the offset to that shown in Figure 2.8. This can be attributed to the assumptions that the model is based on; namely that surface interactions are neglected. The processes occurring at the surfaces are more complex, however for the current investigation, the inclusion of ions is to recreate the screening effect observed experimentally, which is sufficient for flexoelectric measurements in a HAN cell.

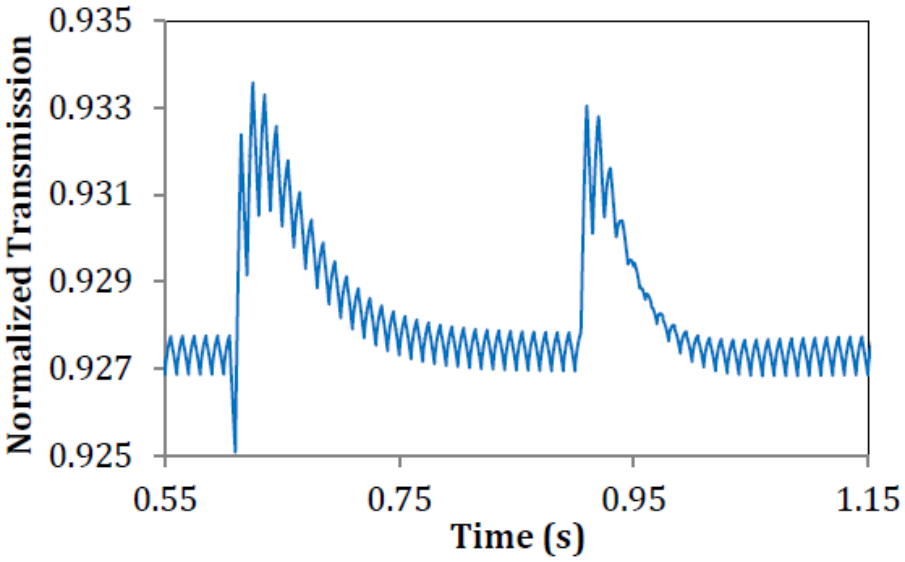


Figure 2.14.Simulated transient response due to ions. Simulated cell response under an applied voltage of 100 Hz, ± 0.2 V when an external offset transition from - 0.1 V to + 0.1 V occurs at 0.6 s, followed by a transition from + 0.1 V to - 0.1 V offset at 0.9 s. The transmission returns to the same level after screening out the applied offset.

2.5. CONCLUSIONS

A new method to measure the sum of the flexoelectric coefficients has been proposed that exploits highly ionic materials to ensure screening of the internal bias due to the different surface alignment polarities in hybrid aligned nematic liquid crystalline systems. Through data-theory comparisons, the modulus of the flexoelectric sum in the standard commercial eutectic E70 nematic LC mixture was found to be (10 ± 2) pCm^{-1}, which is in good agreement with previous measurements of similar mixtures [14].

The dependency on highly ionic LC materials to screen out the effective internal bias might be removed by considering other devices with asymmetric director structures to maximize flexoelectric contributions and that, crucially, have symmetric surfaces to avoid an internal bias due to surface polarization. This would allow direct measurement of the flexoelectric coefficients, for a broader range of materials. It would then be possible to experimentally validate the assumptions inherent to the method by

comparison of the $|e_1+e_3|$ HAN results to a device filled with the same material but with uniformly treated surfaces, thereby completely removing the dependence on the presence of ions to screen out any internal bias. It may, for example, be possible to use the so-called asymmetric H state of a pi-cell device [15], which will be explored in the following chapter.

2.6. REFERENCES

[1]P. Rudquist and S. Lagerwall, *Flexoelectricity in Liquid Crystals*, Imperial College Press, London, UK (2013).

[2] I. Dozov, P. Martinot-Lagarde and G. Durand, *J. Physique Lettres*, **43**, 365 (1982).

[3] N. V. Madhusudana and G. Durand, *J. Physique Lett*. **46**, 195 (1985).

[4] A. Derzhanski, A. G. Petrov and M. D. Mitov, *Journal de Physique*, **39**, 27 (1977).

[5] S. Ponti, P. Ziherl, C. Ferrero and S. Zumer, *Liq. Cryst.* **28**, 8, 1171 (1999).

[6] A. Mazzulla, F. Ciuchi and J. R. Sambles, *Phys. Rev. E*, **64**, 021708, 1 (2001).

[7] G. Barbero and L. R. Evangelista, *Physical Review E* **68**, 023701, 1 (2003).

[8] C. Kischka, S. J. Elston and E. P. Raynes, *Mol. Cryst. Liq. Cryst*. **494**, 93 (2008).

[9] D. Pauluth and K. Tarumi, *J. SID*, **13**, 693 (2005).

[10] G. Derfel, *J. Mol. Liq.* **144**, 59 (2008).

[11] M. Buczkowska, *Mol. Cryst. Liq. Cryst.* **543**, 1, 48/[814] (2011).

[12] G. Derfel and M. Buczkowska, *Liq. Cryst.* **40**, 2, 272 (2013).

[13] H. Naito and M. Okuda, *Phys. Rev. A*, **44**, 6, R3434 (1991).

[14] S. A. Jewell and J. R. Sambles, *J. Appl. Phys*. **92**, 1, 19 (2002).

[15] P. D. Brimicombe and E. P. Raynes, *Liq. Cryst.* **32**, 10, 1273 (2005).

3

THE FLEXOELECTRIC EFFECT IN NEMATIC PI-CELLS

3.1. INTRODUCTION

3.1.1. Uniform Alignments

Planar aligned cells filled with a nematic LC material of positive dielectric anisotropy exhibit a variety of different director configurations under externally applied electric fields. When an electric field is applied, a strong elastic distortion results in the bulk of the device due to the competition between the orienting torque in the bulk from the applied electric field and the elastic torque imposed by the anchoring conditions at the substrates. The distortion field is manifested from the induced flexoelectric polarization that couples to field gradients, as shown in (2.10) for an electric field applied perpendicular to the glass substrates of a HAN cell.

Despite the strong splay-bend distortion field of the hybrid alignment being useful for flexoelectric measurements, the method presented in Chapter 2 was heavily reliant upon highly ionic LC materials to screen out the internal bias arising from the different surface alignment polarities. This restriction may be improved by considering device geometries that have symmetric surface alignment conditions to avoid the asymmetric surface

polarization associated with hybrid alignments. In this chapter, planar aligned cells filled with a nematic LC are used, whereby the uniformly treated surfaces eliminate the need to account for an internal bias in measurements of the device's flexoelectric response.

3.1.2. Non-Ionic Fréedericksz Cells

Data-theory comparisons carried out by Brown and Mottram [1] have previously demonstrated structural changes in the director field of a planar aligned (anti-parallel rubbed) Fréedericksz device due to flexoelectricity. The theoretical model developed in Chapter 2 can be used to illustrate this effect. Figure 3.1 shows the simulated director profile i.e. the tilt angle as a function of the cell thickness, of a 5 µm-thick Fréedericksz device with a 5° pretilt under the application of a ± 5 V DC voltage. The standard commercial eutectic E7 liquid crystalline mixture used in [1], with dielectric and optical

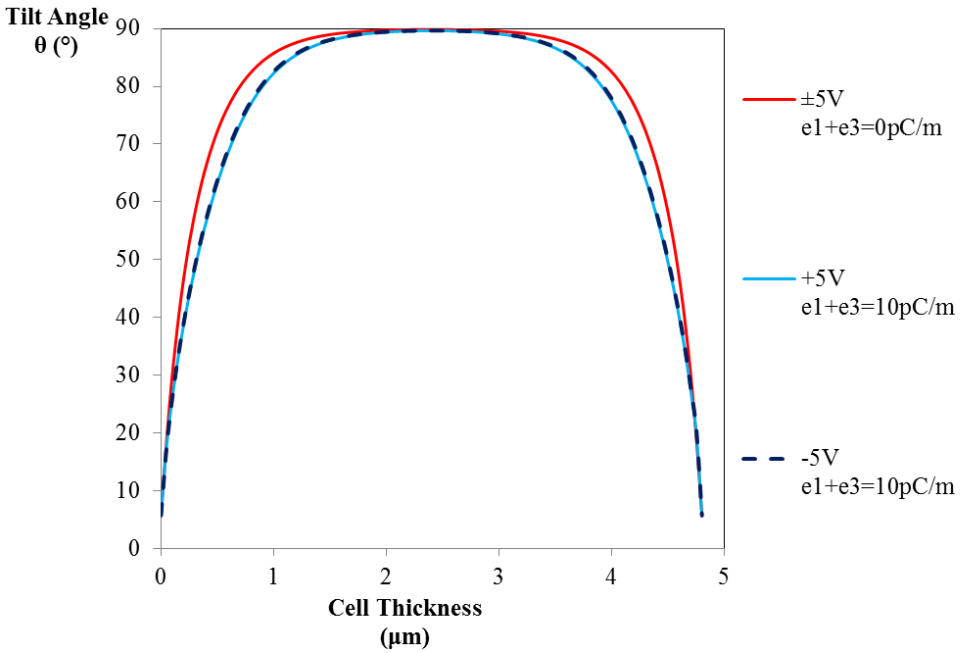


Figure 3.1. Non-Ionic Fréedericksz Cells. Simulated director profile, showing the tilt angle, θ, as a function of the cell thickness, of an E7-filled Fréedericksz device in the absence of ions under a forward and reverse DC bias voltage of ± 5V reveals structural changes due to flexoelectricity, but no polar response to changes in the polarity of the applied field.

anisotropies of $\Delta\varepsilon = 13.7$ at T = 20ºC and $\Delta n = 0.219$ at $\lambda = 632.8$ nm, respectively, is implemented in the model (see Table A.3 of the Appendix). Note that ionic contributions have been neglected here to avoid any screening effects of the applied DC field.

The theoretical model assumes infinite anchoring at the planar cell boundaries, giving rise to an elastic torque at the surfaces competing with the orienting torque in the bulk of the device under an applied electric field. The director profile is thus homeotropic in the bulk, as it aligns parallel to the direction of the applied field due to the positive dielectric anisotropy of the LC material. The director field simulated in the absence of flexoelectricity undergoes a further structural change once flexoelectric contributions are included in the model (for an average $e_1 + e_3$ of 10 pC/m [1]). However, no polar response is detected in the equilibrium state of the latter case when changing the polarity of the applied field. In other words, no modulation would be observed in the transmission from the device under the oscillating field. Thus, it would not be possible to detect the polar flexoelectric response in the current regime, in which ionic effects have been neglected.

3.1.3. Ionic Fréedericksz Cells

The simulated transmission as a function of time obtained under the application of a square wave is shown in Figure 3.2 (a). Here, both ionic and flexoelectric contributions are included in the model, for an average ion number density of 10^{21} m^{-3} (see §2.3 for derivation) [2] and a flexoelectric sum of 10 pC/m, respectively. For infinitely strong anchoring, the device's symmetric response shown under the application of a 100 Hz, ± 1 V oscillating field indicates that there is no polarity dependent flexoelectric response,

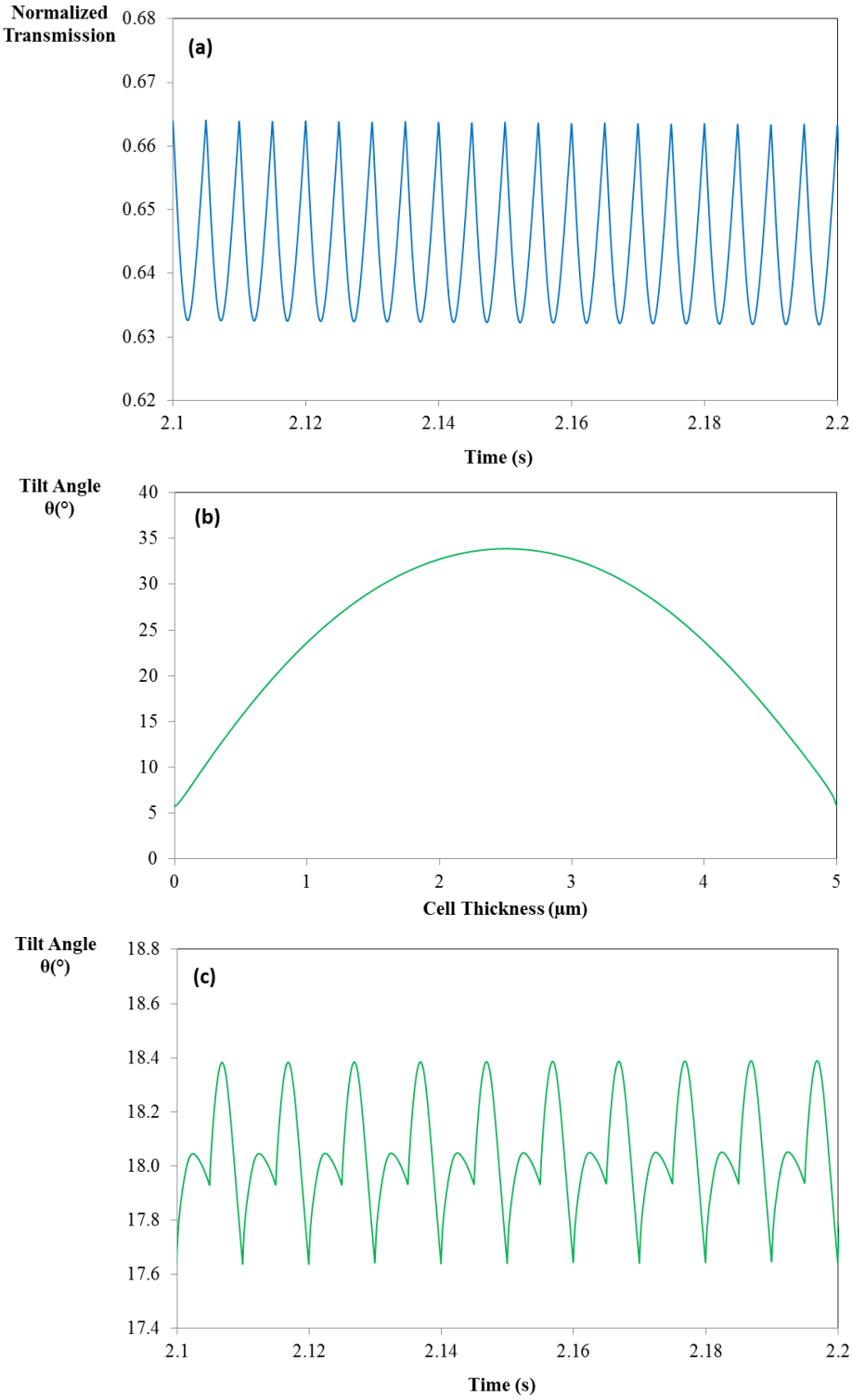


Figure 3.2. Ionic Fréedericksz Cells. Simulations of a Fréedericksz cell under the application of a 100 Hz, ± 1 V oscillating field. (a) Simulated transmission as a function of time from a Fréedericksz device under a 100 Hz, ± 1 V square wave shows a symmetric response due to the combined flexoelectric and ionic contribution. (b) Simulated director profile in the device's equilibirum state. (c) Simulated director orientation extracted one eighth across the position of the cell reveals asymmetry in the response due to flexoelectricity.

and that the observed modulation is due to a combination of flexoelectric and ionic influences.

The simulated director profile is shown in Figure 3.2 (b). A smaller orienting torque due to the applied electric field leads to a smaller reorientation angle in the bulk compared to the director profiles in Figure 3.1. The director profile alone does not provide information on the flexoelectric response. However, extracting the director orientation as a function of time, one eighth across the 5 μm cell gap (~0.625 μm from one surface) does reveal polarity in the LC's response, as shown in Figure 3.2 (c). This result demonstrates promise in probing polar effects such as flexoelectricity in Fréedericksz geometries. Nonetheless, observing the evolution of the director orientation at different points across the cell gap is non-trivial compared to measurements of the device's transmission electro-optic response.

Evidently, the inclusion of ions in the model generates a polar response (compared to the non-polar response shown in Figure 3.1 in the absence of ions) due to a combination of ionic and flexoelectric effects. The symmetry of the electro-optic response, however, makes it difficult to dissociate flexoelectric and ionic contributions. To conclude, the Fréedericksz cell may not be the optimum device geometry to measure the flexoelectric coefficients using the methodology described in Chapter 2.

3.1.4. Flexoelectricity in Nematic Pi-Cells

The planar (parallel rubbed) nematic pi-cell device is of interest due to the various phase transitions and resultant different LC states occurring under the application of an electric field. The pi-cell was first proposed by Bos and Koehler/Beran [3] in 1984 and is particularly interesting as it has shown fast response times in nematic LC display

applications due to the symmetry of the director profile leading to a higher order mode of distortion. Moreover, there is no backflow effect in the device [4], i.e. an absence of flow directed opposite to the direction of the director's final equilibrium state, and the deformations in the director field are mainly dependent on K_{33}, the largest elastic constant [5].

Figure 3.3 shows the different states that arise in a pi-cell filled with a material of positive dielectric anisotropy under the application of increasing electric field strengths. Initially, the device is in the stable, lowest energy splayed ground (H) state. Electrically addressing the device above a particular voltage threshold leads to a transition from the splayed pretilt ground state to one of the two optically equivalent asymmetric H (H_a) states; the H_a state voltage threshold is equivalent to the Fréedericksz threshold defined in (1.26). Two director configurations of equal energy (H_{a1} or H_{a2}) may form depending upon thermal fluctuations, variations from perfect symmetric alignment and gradients of the electric field. A visible boundary line separates the two states, which is highly undesirable in any real device. Pretilts at the surfaces can be chosen to prevent the formation of this multi-domain structure [6], so that one of the two H_a states becomes predominant.

At even larger electric field strengths, the device undergoes a disclination mediated transformation to the topologically distinct bend (V) state. The bend state, otherwise known as the Optically Compensated Bend (OCB) mode, is mainly attributed to fast response times (in the sub-millisecond regime). Upon removal of the electric field, regions of bend alignment collapse to a topologically continuous transient twist (T) state, before the entire device eventually relaxes back to the lowest energy ground state. Applications of the V and T states are discussed further in Chapters 5 and 7.

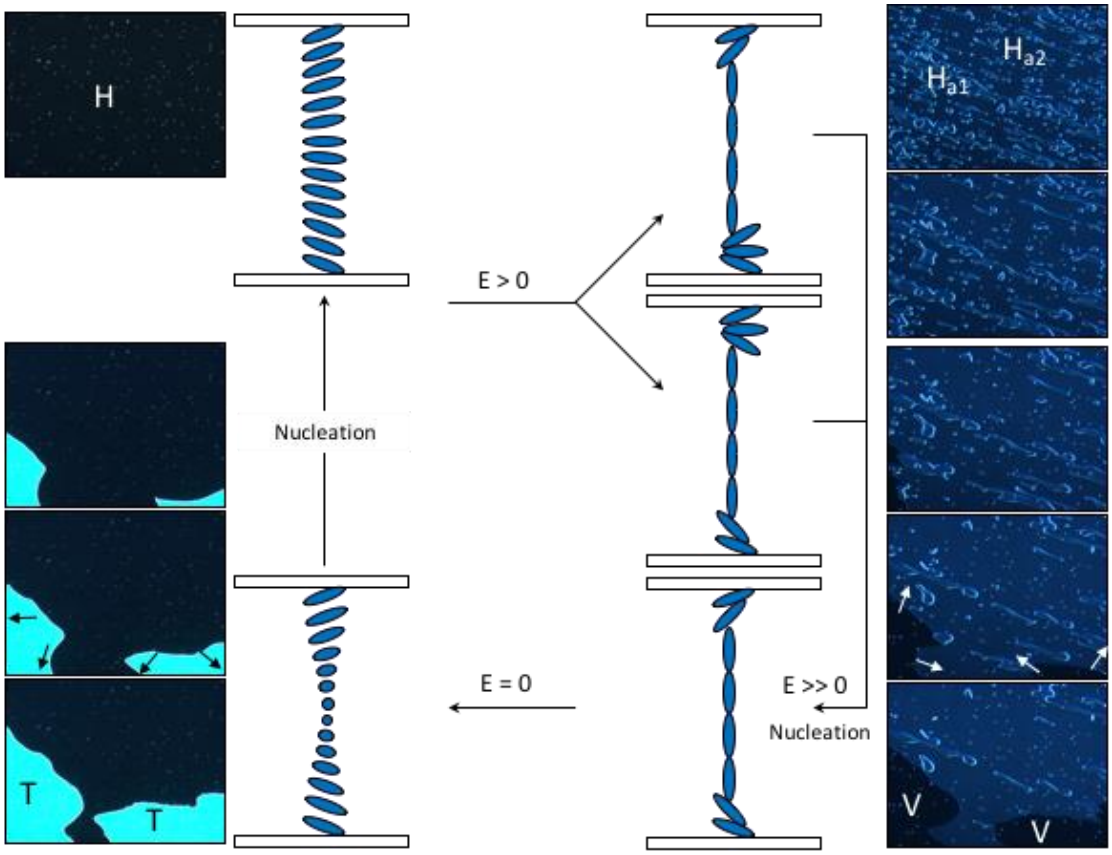


Figure 3.3. The states of a nematic pi-cell under different applied electric field strengths. Microscope images taken between crossed polarizers of a pi-cell oriented in the dark state (0º relative to the analyzer) reveal transitions from the splayed (H) ground state, to the asymmetric H states (H_{a1} or H_{a2}), followed by a nucleation process to the bend (V) state, which subsequently collapses to the transient twist (T) state upon removal of the applied field. Schematics of the different director profiles are also included.

Applying sudden step increases in the voltage across a pi-cell (above a particular threshold value) that is initially in its splayed ground state causes the formation of another transient LC state known as the symmetric H state (H_s). The H_s state can be considered as two half-thickness Fréedericksz cells [6], as illustrated by the director profiles in Figure 3.4 (a). The relaxation time of a Fréedericksz device (for negligible flow and pretilt) is written as,

$$\tau_{\mathrm{rel}}(\mathrm{Fréed}) \sim \frac{\gamma_1 d^2}{K_{11}\pi^2}. \qquad (3.1)$$

It is clear from (3.1) that the relaxation time of the H_s states is four times faster than a Fréedericksz device due to the dependence on the square of the cell thickness, making it a fast switching state (alongside the OCB mode at higher voltage applications). It has previously been demonstrated that the H_s state threshold is double the Fréedericksz threshold voltage [6]:

$$V_{th}(H_s) = 2\pi\sqrt{\frac{K_{11}}{\varepsilon_0 \Delta\varepsilon}}. \tag{3.2}$$

The fast switching H_s state, however, is unstable and subsequently decays over a few milliseconds to one or the other of the lower energy asymmetric H states (H_a), as illustrated in the schematic of Figure 3.4 (b). Applying voltages below the H_s threshold value in (3.2) but above the Fréedericksz threshold i.e. V_{th} (Fréed) < V < V_{th} (H_s), leads to the immediate formation of the asymmetric H states seen in Figure 3.3.

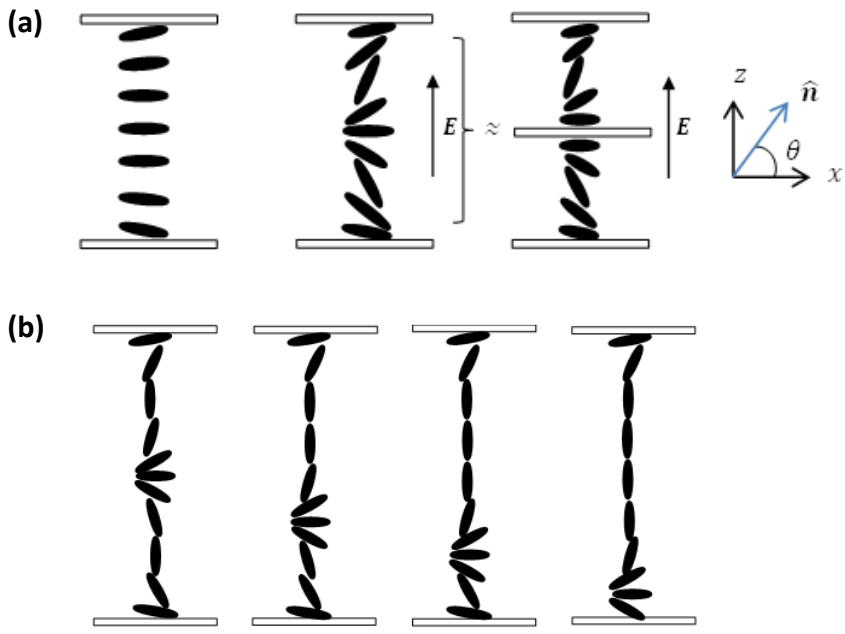


Figure 3.4. Director profiles in a nematic pi-cell device under low electric field strengths. (a) From left to right, schematics of the splayed ground state when V = 0, the symmetric H state when V > V_{th} (H_s) and two half-thickness Fréedericksz cells as a simplified view of the H_s states. (b) A schematic of the H_s to H_a transition at V > V_{th} (H_s); the central region of the director profile appears decoupled from the surfaces, but drifts towards the lower substrate over time to form one of the asymmetric H states.

The evidence shown in Figures 3.1 and 3.2 suggests that it is non-trivial probing flexoelectricity from a device that forms symmetric director fields. The pi-cell operated in the H_s and V states may therefore not be useful as the overall symmetry in the director structure is not optimum for flexoelectric measurements. Additionally, the transient nature of the H_s and T states make them difficult for use in electro-optic observations. The flexoelectric investigation carried out in a hybrid aligned nematic device that was discussed in Chapter 2 highlighted the benefits of using device geometries with asymmetric director fields but revealed inherent difficulties in distinguishing polar effects due to the different surface alignment polarities. For these reasons, using a device that has uniformly treated surfaces, but that can be driven into an asymmetric director field may prove useful for flexoelectric observations. By adjusting the applied voltage across a pi-cell to ensure that one H_a state dominates, and making subsequent observations for applied fields below the H_a to V transition may, therefore, allow the observation and study of the flexoelectric response.

3.2. NUMERICAL MODEL

The application of an electric field parallel to the plane of the director along the *z*-axis (E_z) results in a strong splay-bend distortion field on account of the asymmetry in the molecular distribution of the H_a states. In this configuration, the electric field couples to the sum of the flexoelectric coefficients as was theoretically demonstrated for a HAN device in §2.1.2. Here, the model developed in Chapter 2 based upon the director field in terms of the tilt angle, $\hat{\mathbf{n}}(\theta)$, is employed that uses a finite difference solution of the Euler-Lagrange equation to determine the minimization of the free-energy in the LC material [7]. The cell boundaries in the model are modified to incorporate the planar,

parallel-rubbed alignment associated with the nematic pi-cell. The asymmetric states can form due to variations that arise from perfect symmetric alignment at the cell surfaces. Adding a small offset (< 1°) between the pretilts at the top and bottom substrates, so that the bulge in the director profile of the H_s state is slightly off-centre, ensures that the simulated device reaches equilibrium in one of the H_a states.

Figure 3.5 shows the simulated response of a splayed pi-cell with 5° pretilt in infinite anchoring to step increases in the applied voltage (3 – 6 V), using E7 parameters (see Table A.3 of the Appendix) and neglecting flexoelectricity. Imperfect surface alignment causes decoupling of the central region of the director profile from the surfaces in the initial symmetric H state leading it to drift to one of the substrate surfaces. The drift of the director in the bulk of the cell can be seen through the plateau in the transmission curves. This is also illustrated by the schematic in Figure 3.4 (b) as equal portions of planar and homeotropic alignment remain in the bulk director profile during the decay of the H_s state, leading to a constant transmission level detected from the device. The plateau extends with larger step increases in the applied voltage indicating an increase in the lifetime of the H_s state. A key feature that should be noted from the simulated response in Figure 3.5 is that at an applied voltage of 3V, there is no decay from the H_s to H_a state whereby the device makes a fast transition into the asymmetric H state. For the interests of this study, the flexoelectric effect is therefore better observed at low applied voltages, but above the Fréedericskz threshold (i.e. $1V < V \leq 3V$), to ensure that the asymmetry in the director field is preserved.

The simulated response when flexoelectricity is added to the model for applied voltages of ± 3 V, using $|e_1 + e_3|$ values of 10 pCm^{-1} for E7 [1] along with an artificially large flexoelectric contribution of 60 pCm^{-1} for illustrative purposes, is shown in Figure

3.6 (a). The difference between the responses due to positive and negative applied voltages in the H_a state is extremely small; a 0.03% shift occurs in the transmission between forward and reverse bias DC voltages when $|e_1+e_3|$ = 10 pCm^{-1} and a 0.1% change for a flexoelectric contribution of 60 pCm^{-1}.

This non-degeneracy in the transmission profile becomes more pronounced with the addition of ions. Figure 3.6 (b) shows the simulated response when a 100 Hz, ± 3 V square wave is applied across the device, with a relatively small ion number density of 6 × 10^{18} m^{-3} and an artificially large flexoelectric sum of 60 pCm^{-1} (i.e. compared with the

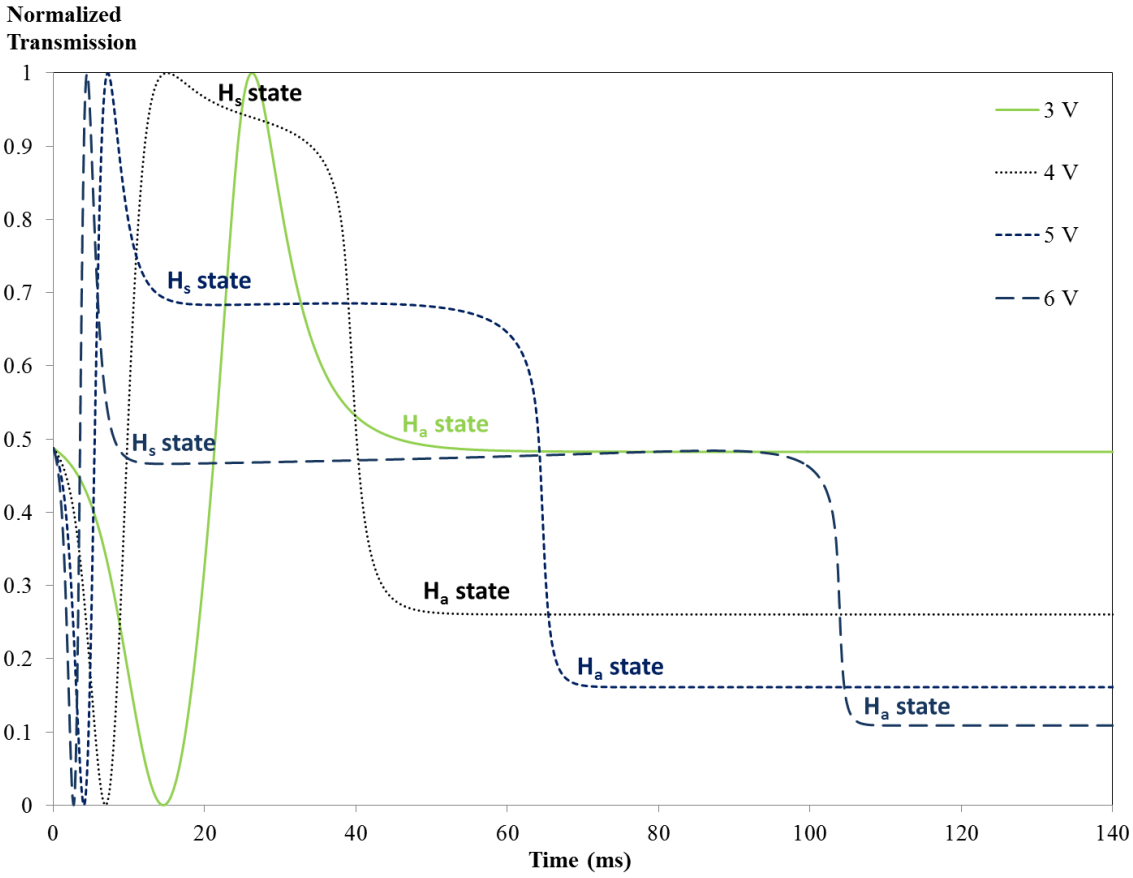


Figure 3.5. Simulated transmission as a function of time for a nematic pi-cell device, in the absence of flexoelectric and ionic effects. The increased lifetime of the H_s state with higher DC voltages is shown as it forms initially and subsequently decays to the lower energy H_a state.

values established from the data-theory fits in Chapter 2) are included in the model. The flexoelectric effect is seen through the modulated response arising as the device reaches equilibrium in the H_a state. Albeit small, the amplitude of the modulation is ~ 0.7%, which is significantly larger than the variations in transmission observed in Figure 3.6 (a). Moreover, flexoelectricity becomes predominant at low voltages due to its linear dependence on the electric field; carrying out experimental work in the low voltage regime of the H_a state, whilst probing the device under a dynamic field, may therefore be potentially useful for the measurement of flexoelectric polarization.

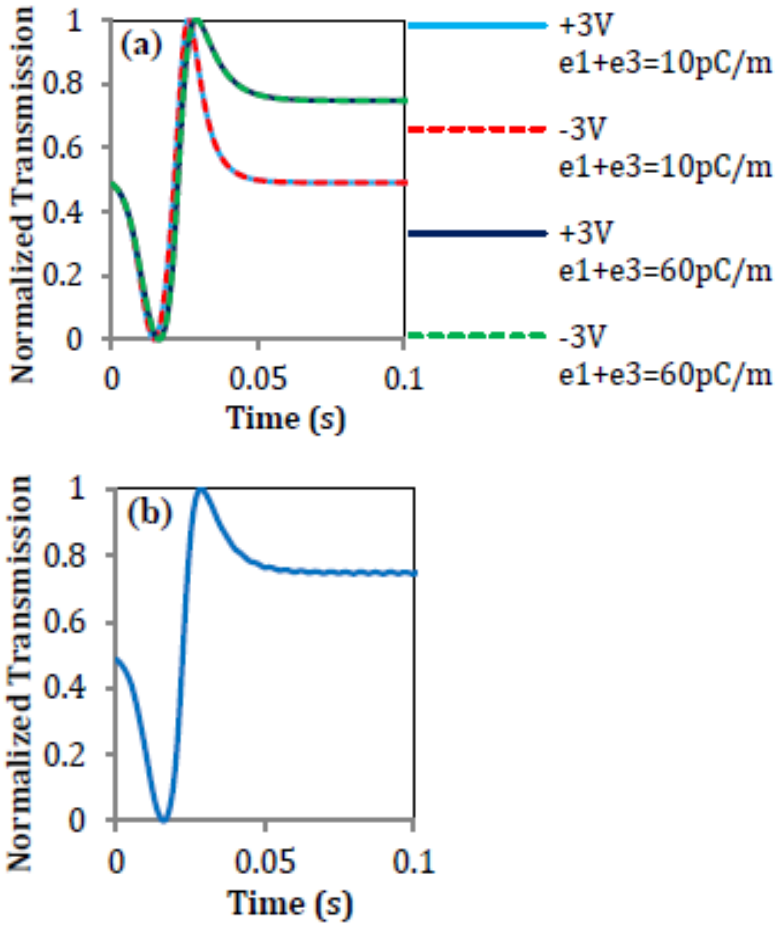


Figure 3.6. Simulated transmission as a function of time for a nematic pi-cell device with variations in the flexoelectric and ionic effects. The simulated transmission profile of a pi-cell device under the application of (a) ± 3V DC voltage due to variations in the flexoelectric sum and (b) 100 Hz, ± 3 V square wave, with a relatively small ionic content of 6×10^{18} m^{-3} and an artificially large flexoelectric sum of 60 pCm^{-1}.

3.3. EXPERIMENTAL ARRANGEMENT

A 5 μm-thick pi-cell device with 5° pretilt at the surfaces was filled with the E7 nematic LC mixture. Red light from a class 3R He-Ne laser was transmitted through the device between crossed polarizers. Device transmission was calculated using Jones matrices (see §1.4.2). Comparison between data and theory for transmission as a function of voltage (for 10 kHz AC) and time allows for the determination of the precise device thickness (d) and rotational viscosity (γ), respectively. A detailed description of the optical set-up along with the method for obtaining the basic device parameters can all be found in Chapter 2.

To ensure that flexoelectric measurements are made in the H_a state, two oscillating fields are applied in series across the device; the first applied signal is a high frequency (10 kHz) square wave at a voltage just above the Fréedericksz threshold (± 1.0 V), with the addition of a 5 Hz, ± 0.1 V square wave that acts as a small perturbation on the device in order to observe a flexoelectric response.

Transmission as a function of time was experimentally and theoretically obtained for the measurement of the flexoelectric sum. In accordance with the method described in Chapter 2, the parameters varied in the data-theory fits are the ion generation constant in the absence of an applied electric field, the ion mobilities while preserving the cation to anion mobility ratio of ~1.0, and finally the sum of the flexoelectric coefficients. The device is assumed to consist of infinite anchoring with zero ionic transport at the boundaries.

Each parameter leads to a subtle difference in the shape of the transmission. Figure 3.7 (a) shows plots from the model of the pi-cell when the ionic content is varied over the range $10^{19}\ m^{-3} \leq N_A \leq 10^{21}\ m^{-3}$ under an oscillating field of 10 kHz, ± 1.0 V, offset

by a 5 Hz, ± 0.1 V square wave, for a fixed flexoelectric sum of 10 pCm^{-1}. Increasing the ionic content changes the shape of the modulation, which tends towards a saw-tooth form at higher ion number densities. Ionic screening dominates at larger N_A values; the distinct shape in the modulation caused by the second square wave therefore becomes less prominent as it is screened out by the ions. Despite the high ionic concentration, the transient changes in the modulation arising from the 5 Hz, ± 0.1 V square wave are not screened out. It is worth noting that, in the absence of ionic effects, it would not be possible to observe this transient change in the modulation as the amplitude of the second waveform (± 0.1 V) is significantly smaller than the ± 3 V data presented in Figure 3.6, in which only a 0.03% shift in the transmission was recorded between forward and reverse bias DC voltages for $|e_1+e_3|$ = 10 pCm^{-1}. This highlights the covariance between the ionic and flexoelectric parameters in the numerical model, whereby a higher ionic content screens out the distinct shape in the modulation yet removing the ions altogether would negate any transient behaviour in the transmission caused by the 5 Hz, ± 0.1 V square wave.

Figure 3.7 (b) shows plots when $|e_1+e_3|$ is varied under a fixed ionic content of $N_A \sim 10^{22}$ m^{-3}. Increasing the flexoelectric contribution leads to an increase in the amplitude of the modulation. Thus, the amplitude is directly related to the flexoelectric sum, in contrast to the distinctive shapes of the modulation produced with variations in the ion number density on account of ionic screening effects. Overall, it is clear that the model is only valid when the ionic and flexoelectric effects are considered in conjunction with one another due to the covariance between the two parameters.

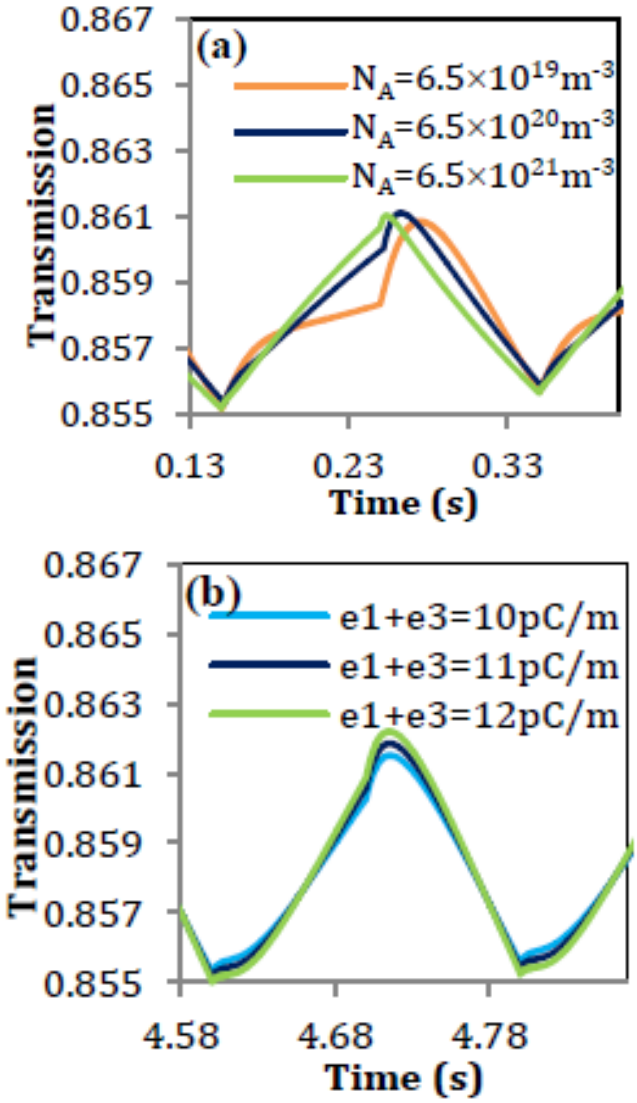


Figure 3.7. Simulated transmission as a function of time for a 5 µm-thick pi-cell device filled with E7 nematic LC. The transmission, obtained under an applied AC voltage of 10 kHz, ± 1.0 V that was offset by a 5 Hz, ± 0.1 V square wave, changes due to variations in (a) the ionic content, for a fixed e_1 + e_3 of 10 pCm^{-1}, and (b) the flexoelectric sum, for a fixed ionic content of $N_A \sim 10^{22}$ m^{-3} set by the numerical model.

3.4. RESULTS & DISCUSSION

The obtained experimental and theoretical data taken by the application of a 10 kHz, ± 1.0 V square wave and offset by a 5 Hz, ± 0.1 V square wave across a 5 µm-thick pi-cell device filled with E7 nematic LC are shown in Figure 3.8. The data were recorded once the device response reached equilibrium and was subsequently switched off in

order to simultaneously determine the LC viscosity. An ionic content of 1.5×10^{20} m^{-3} was required to reproduce the distinct shape in the modulation, and an average $|e_1+e_3|$ value was established at 10 pCm^{-1}. The flexoelectric sum established through data-theory fits is in good agreement with previous measurements of E7 [1, 8], however the ionic content measured here is an order of magnitude lower than that reported in the literature [2]. For the purpose of this investigation, ions in the model replicate the dynamic behaviour of the LC for flexoelectric measurements; thus, further work may be carried out to optimize the ionic behaviour in the model. The final E7 device measured parameters are listed in Table 3.1.

The previous HAN-based flexoelectric measurements presented in Chapter 2 were reliant upon the inclusion of ions in the numerical model to screen out the internal bias caused by the different surface polarities in the device geometry. The symmetric surfaces in pi-cells remove this ionic dependence, making the method applicable to a broader range of materials; i.e. less contaminated LC materials. Nonetheless, if ions are removed altogether, the polar response due to flexoelectricity is so small that it could be considered almost negligible. Despite the symmetric surfaces of the pi-cell removing the assumption that the ions screen out any internal bias, the polar flexoelectric response resultant in the asymmetric geometry of the H_a state is enhanced when ions are included in the model and the device is driven dynamically, under an oscillating field. This complex interplay between the parameters set in the model is likely to reduce the accuracy of the method to measure the flexoelectric coefficients. The error margin in the value of the flexoelectric sum was estimated from the range of suitable values that generated suitable fits with the experimental data.

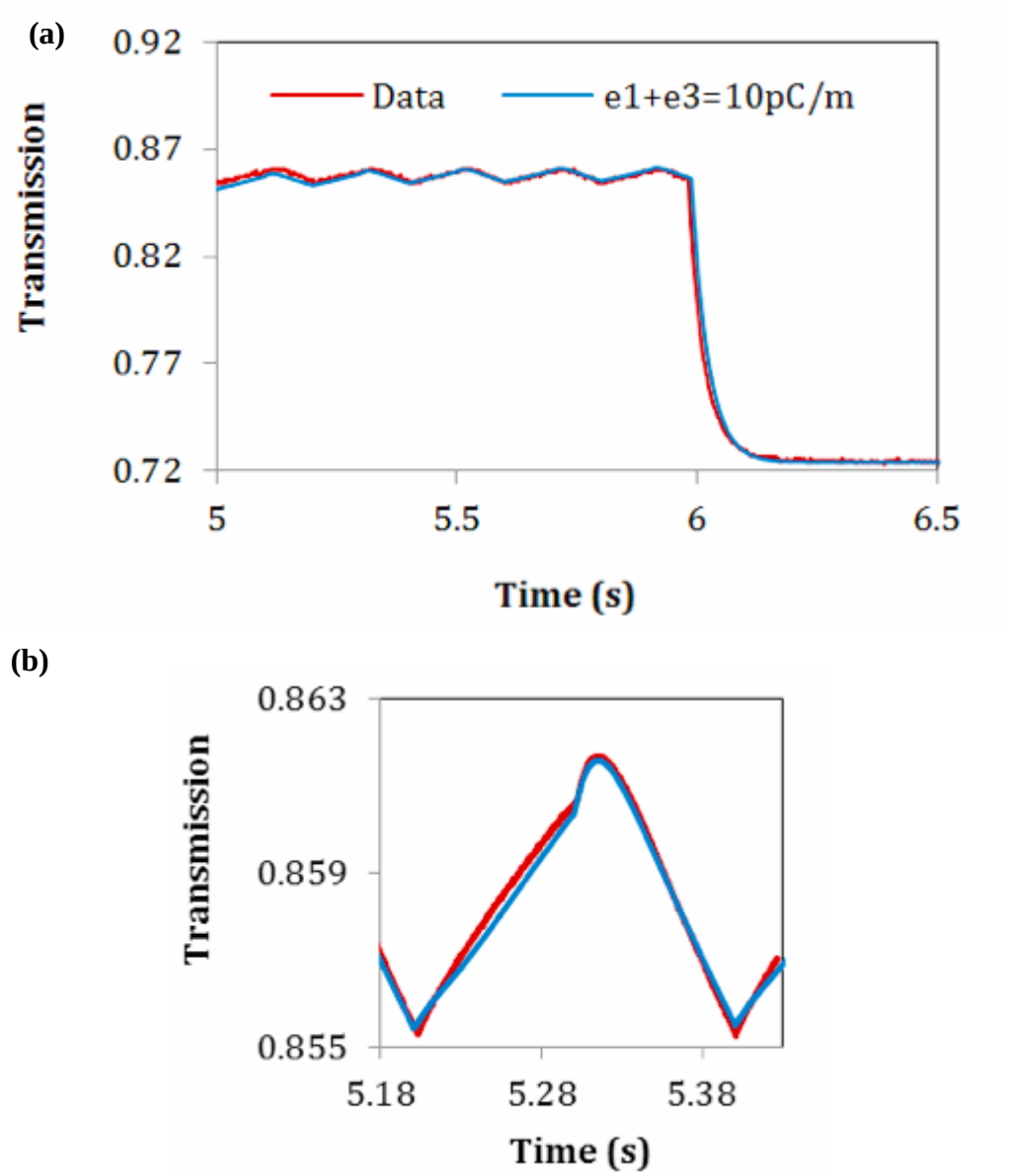


Figure 3.8. Simulated and experimentally obtained transmission as a function of time from a 5 µm-thick pi-cell device filled with E7 nematic LC. (a) The transmission, obtained under an applied AC field of 10 kHz, ± 1.0 V that was offset by a 5 Hz, ± 0.1 V square wave, led to an optimum data-theory fit for a flexoelectric sum of 10 pCm^{-1}. (b) Data-theory fit of the modulation in the device response.

SYMBOL	DEVICE PARAMETERS	
d	Cell Thickness	(4.86 ± 0.05) μm
γ	Viscosity	(75 ± 4) mPa s
N_A	Ionic Content	$(1.5 \pm 0.01) \times 10^{20}$ m^{-3}
e_1+e_3	Flexoelectric Sum	(10 ± 1) pCm^{-1}

Table 3.1. Device parameters established from data-theory fits of a nematic pi-cell device filled with E7 nematic LC.

3.5. CONCLUSIONS

In conclusion, a method to measure the sum of flexoelectric coefficients $|e_1+e_3|$ has been established in the asymmetric H state of pi-cell nematic devices. Data and theory comparisons have resulted in a measurement of 10 pCm^{-1} for the flexoelectric sum in the standard commercial eutectic E7 liquid crystal mixture, which is within the range of values previously reported in the literature (0 - 15 pCm^{-1}) [1, 8]. Interestingly, this work has also highlighted the complex nature of the processes occurring in a liquid crystalline material and the covariance of different parameters that describe its electro-optical behaviour. Using a pi-cell device for measurements of flexoelectricity removes any assumption that the ions screen out an offset due to asymmetric surfaces, yet the inclusion of ionic effects substantially enhances the flexoelectric response such that there remains a dependence on the presence of ions for the method to be valid.

3.6. REFERENCES

[1] C. V. Brown and N. J. Mottram, *Phys. Rev. E*. **68**, 3, 031702 (2003).

[2] Y. Garbovskiy and I. Glushchenko, *Crystals*, **5**, 501 (2015).

[3] P. J. Bos and K. R. Koehler/Beran, *Mol. Cryst. Liq. Cryst.* **113**, 1, 329 (1984).

[4] C. Z. van Doorn, *J. Appl. Phys.* **46**, 9, 3738 (1975).

[5] J.-W. Lee, C.-H. Lee, H.-S. Kim, J. G. Lu, E.-H. Han, S.-H. Lee, S.-J. Hong, K.-J. Shin, E.-G. Lee, M. Kang, K.-H. Kim, J.-H. Souk and S.-S. Kim, *SID '06 Digest*, **37**, 1, 1950 (2006).

[6] P. D. Brimicombe and E. P. Raynes, *Liq. Cryst.* **32**, 10, 1273 (2005).

[7] C. C. Tartan and S. J. Elston, *J. Appl. Phys.* **117**, 064107 (2015).

[8] S. A. Jewell and J. R. Sambles, *Mol. Cryst. Liq. Cryst.* **401**, 67/[181] (2003).

4

THE FLEXOELECTRO-OPTIC EFFECT & POLYMER TEMPLATES

4.1. INTRODUCTION

4.1.1. The Flexoelectro-Optic Effect

At present, the multi-billion dollar flat panel displays industry is dominated by liquid crystalline technologies. However, the main drawback with using liquid crystals (LCs) is that the shortest achievable response time is of the order of milliseconds, which is limited by the viscoelastic response in nematic LCs. So far, there has not been widespread commercialisation of any of the fast-switching electro-optic effects that can be observed in self-assembled periodic structures based upon chiral liquid crystalline materials.

The flexoelectro-optic (FEO) effect, observed in chiral nematic LCs when an electric field is applied perpendicular to the helical axis, has significant potential as it exhibits analogue switching in 10-100 μs. The electro-optic response is linear and fast, and therefore has significant potential in the realization of next generation displays applications.

The major technological barrier that prohibits the commercial realisation of this electro-optic effect is the requirement of a uniform, in-plane alignment of the helix axis between the glass substrates of the device. In this chapter, the theory behind the FEO effect in chiral nematic LCs is presented followed by a discussion of the various methods that exist to achieve the required LC alignment. A conventional annealing and bulk polymerization technique is explored to probe the FEO effect and a polymer templating method is employed to enhance the FEO response.

4.1.2. The Tilt Angle

The FEO effect is typically observed when a short pitch chiral nematic is aligned in a uniform lying helix (ULH) state. In this LC state, the helical axis of the chiral nematic is aligned uniformly between two substrates, as illustrated in Figure 4.1 [1, 2]. Under the application of an electric field perpendicular to the helix axis, an in-plane tilt (ϕ) is induced in the optical axis that couples to the difference of the flexoelectric coefficients, which for small tilt angles is linear in the applied electric field, *E*. The flexoelectric tilt angle can be derived by considering the director field in the *yz*-plane as

$$\hat{\mathbf{n}} = \begin{pmatrix} n_x \\ n_y \\ n_z \end{pmatrix} = \begin{pmatrix} \cos\theta \\ \sin\theta \\ 0 \end{pmatrix}. \tag{4.1}$$

Under the application of an electric field along the *x*-axis, E_x, the director field can be approximated to

$$\hat{\mathbf{n}} = \begin{pmatrix} \cos\theta \\ \sin\theta\cos\phi \\ \sin\theta\sin\phi \end{pmatrix} \tag{4.2}$$

where $\theta = qz$ and ϕ is the resultant tilt in the *yz*-plane under the applied electric field.

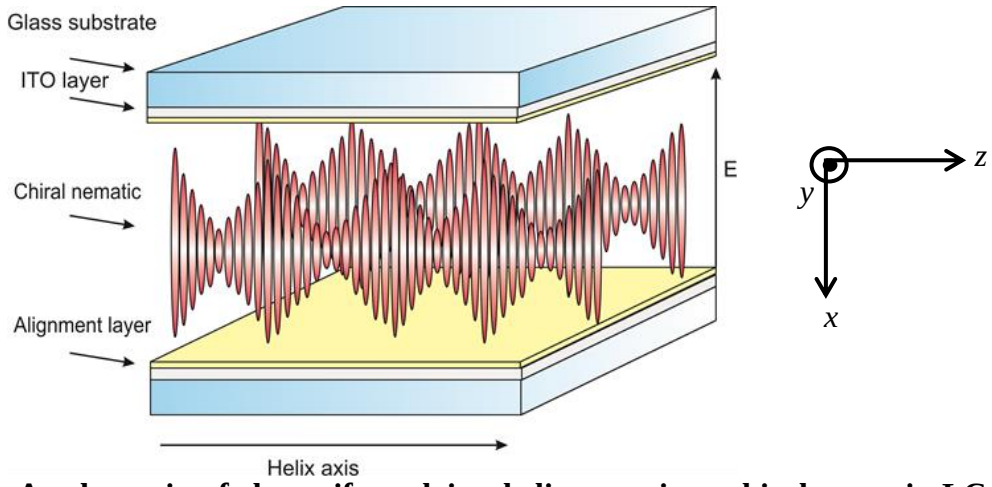


Figure 4.1. A schematic of the uniform lying helix state in a chiral nematic LC device. The optical axis is aligned along the helix, which is perpendicular to the applied electric field *E*.

The gradient operator can be written as

$$\nabla = \begin{pmatrix} 0 \\ 0 \\ \partial/\partial \mathrm{z} \end{pmatrix}. \tag{4.3}$$

Once the director field has been defined in this way, the free energies due to elastic and flexoelectric contributions can be derived (assuming that there is no dielectric anisotropy) and then minimized with respect to Φ in the Euler Lagrange routine. The free elastic energy components are given by

$$\frac{1}{2}K_{11}[\nabla \cdot \hat{\mathbf{n}}]^2 = \frac{1}{2}K_{11}\left[\sin^2\phi\cos^2\theta\left(\frac{\partial\theta}{\partial \mathrm{z}}\right)^2\right],$$

$$\frac{1}{2}K_{22}[\hat{\mathbf{n}}\cdot(\boldsymbol{\nabla}\times\hat{\mathbf{n}}) + q_0]^2 = \frac{1}{2}K_{22}\left[\cos^2\phi\left(\frac{\partial\theta}{\partial \mathrm{z}}\right)^2 - 2q\cos\phi\left(\frac{\partial\theta}{\partial \mathrm{z}}\right) + {q_0}^2\right], \tag{4.4}$$

$$\frac{1}{2}K_{33}[\hat{\mathbf{n}}\times(\nabla\times\hat{\mathbf{n}})]^2 = \frac{1}{2}K_{33}\left[\sin^2\theta\sin^2\phi\left(\frac{\partial\theta}{\partial \mathrm{z}}\right)^2\right].$$

The total free elastic energy is therefore written as

$$f_{\mathrm{elastic}}(\hat{\mathbf{n}}) = \tag{4.5}$$

$$\frac{1}{2}K_{11}\sin^2\phi\cos^2\theta\, q^2 + \frac{1}{2}K_{22}[\cos^2\phi\, q^2 - 2q^2\cos\phi + {q_0}^2] + \frac{1}{2}K_{33}\sin^2\theta\sin^2\phi\, q^2.$$

The free energy due to flexoelectricity is given by,

$$f_{\text{flexo}}(\hat{\mathbf{n}}) = -\boldsymbol{P}_f \cdot \boldsymbol{E} = -E_x[e_1 \sin\phi \cos^2\theta - e_3 \sin\phi \sin^2\theta]q \tag{4.6}$$

Averaging the energies in (4.5) and (4.6) over the length of one whole pitch by integrating with respect to *z* gives

$$\frac{1}{P}\int_0^P f_{\text{flexo}}(\hat{\mathbf{n}}) \cdot dz = -\frac{1}{2}E_x(e_1 - e_3)\sin\phi\, q, \tag{4.7}$$

$$\frac{1}{P}\int_0^P f_{\text{elastic}}(\hat{\mathbf{n}}) \cdot dz = \frac{K_{11}}{4}\sin^2\phi\, q^2 + \frac{K_{22}}{2}[q_0 - q\cos\phi]^2 + \frac{K_{33}}{4}\sin^2\phi\, q^2, \tag{4.8}$$

where $\int_0^P \cos^2\theta\, dz = \int_0^P \sin^2\theta\, dz = P/2$. The average free energy density is therefore

$$\frac{\sin^2\phi q^2}{4}(K_{11} + K_{33}) + \frac{K_{22}}{2}[q_0 - q\cos\phi]^2 - \frac{E_x}{2}(e_1 - e_3)\sin\phi\, q = 0, \tag{4.9}$$

which is set to equal zero for the minimization and minimizing with respect to Φ:

$$\sin\phi\left[\frac{(K_{11}-2K_{22}+K_{33})}{2K_{22}}\right] + \tan\phi - \frac{E_x(e_1-e_3)}{2K_{22}q_0} = 0. \tag{4.10}$$

Approximating for small tilt angles and $2K_{22} = K_{11} + K_{33}$ then

$$\tan\phi \approx \phi = \left(\frac{e_1-e_3}{K_{11}+K_{33}}\right)\frac{\mathrm{E}}{q}. \tag{4.11}$$

The term in the parentheses is also referred to as the flexoelastic ratio (*e/K*), which is an important material parameter in the synthesis of LCs designed to generate larger tilt angles [3-5].

Short-pitch chiral nematic LCs permit fast changes in the optical state leading to microsecond response times given by,

$$\tau = \frac{\gamma q^2}{K_{11}+K_{33}}, \tag{4.12}$$

where γ is the rotational viscosity [2]. Conventional nematic LCDs are limited by the viscoelastic response leading to different 'on' and 'off' response times. The ULH response time in (4.12) is the characteristic time it takes for ϕ(E) to relax to its

equilibrium value in both directions [6]. The relation in (4.12) is independent of the device thickness, which is not the case for the characteristic timescale of a Fréedericksz cell given in (1.26), but is instead governed by the length of the pitch of the chiral nematic. Therefore, the FEO effect has potential to reduce the response times from milliseconds down to sub-milliseconds for next generation displays and optoelectronic devices.

4.1.3. Uniform Lying Helix

The most challenging issue to overcome is the fact that the ULH state is incompatible with strong planar and strong homeotropic alignments, becoming unstable when the chiral nematic is confined between spatially uniform aligning surfaces, such as a conventional glass cell of the type illustrated in Figure 4.1 [7]. The degeneracy attributed to homeotropic alignments at the cell surfaces generates a scattered texture in the chiral nematic LC as there is no preferential direction for the helical axis to align in. For planar anchoring at the substrates, the chiral nematic typically adopts the standing helix (Grandjean) alignment. It is well-known that applying an external electric field parallel to the helix axis of a chiral nematic sample with a positive dielectric anisotropy causes the helix to align in random orientations, known as the focal conic texture. However, a ULH geometry can be formed upon cooling from the isotropic phase in the presence of an applied electric field [4], but this is not stable in the absence of the field and therefore relaxes back to the lower energy Grandjean state upon removal of the electric field [7].

As the ULH response times are naturally fast, maximising the intensity modulation by exploring different methods that stabilise the molecular alignment is vital. In an

attempt to ‘lock-in’ the inherently unstable ULH structure, one approach is to form polymer networks in LCs so as to stabilise the alignment [8-10]. Through the addition of a suitable reactive mesogen (liquid crystalline monomer) and photosensitive initiator (see §1.6), the polymer network can be formed by exposure to ultraviolet light. In this case, the alignment is both stable in the absence of an electric field and reappears spontaneously upon thermal cycling by either cooling from the isotropic phase or heating from the crystalline solid phase. However, formation of the polymer network results in a reduction in the electro-optic performance of the device due to the rotation of the helix (quantified by the tilt angle) becoming inhibited by the bulk polymer network. In a paper by Broughton et al. [9], it was shown that increasing the concentration of polymer resulted in a reduction in the tilt angle of the optic axis for a given electric field strength along with a decrease in the response time. The polymer network effectively ‘locks-in’ the LC director field, therefore this method leads to a trade-off between the reduction in response times that displays manufacturers are primarily interested in, and optimizing tilt angles so that next generation displays can be operated at low electric field strengths ($< 5\ V\mu m^{-1}$).

4.1.4. Polymer Templating

Polymer networks have been used in the creation of ‘templates’ that can impart one material’s properties onto another. The process involves photo-curing the network in the desired LC state using UV light and then removing the LC and unreacted mesogens to create a template of the LC state. Subsequently refilling the template with a different material imparts properties that are characteristic of the state in which the template was formed. This approach has been employed to form chiral polymer network ‘scaffolds’ in

the Grandjean state for wavelength-tunable laser emission [11]. Templates have also aided the growth of more complex LC states such as blue phases that typically exist over a limited temperature range of just a few degrees [12]. By templating a blue phase, it is possible to enhance the temperature over which the state persists across a range of 250°C. Polymer scaffolds have therefore proven to be a reliable solution to creating LC states of interest that are inherently unstable and/or difficult to grow.

Previously, analytical demonstrations have shown that imposing a pitch (P_{imposed}) on a chiral nematic material of a longer natural pitch (P) generates a significantly larger flexoelectric tilt angle [13, 14] expressed in the following relation,

$$\phi_0(E) = \frac{e_1 - e_3}{K_1 + K_3} \frac{P}{2\pi} E \cdot \left\{1 + \frac{2K_2}{K_1 + K_3}\left(\frac{P_{\text{imposed}}}{P} - 1\right)\right\}^{-1}. \tag{4.13}$$

From (4.13), it can be seen that if $P \equiv P_{\text{imposed}}$, the second term in the curly bracket disappears such that the tilt angle is equivalent to the expression in (4.11). If $P = 2P_{\text{imposed}}$, the tilt angle increases by a factor of $(K_1 + K_3)/(K_1 + K_3 - K_2)$, while if $P \to \infty$, the tilt angle increases by a factor of $(K_1 + K_3)/(K_1 + K_3 - 2K_2)$. Using the values for the nematic LC, E7 (see Table A.3 of the Appendix), refilling a template with a pitch that is double the imposed pitch should increase the FEO tilt angle by a factor of 1.3, while it is expected to be doubled in the case that $P \to \infty$.

Thus, the elastic energy of the chiral nematic material determines the amount by which the flexoelectric tilt angle increases when constraining another chiral nematic material of differing pitch, assuming that both materials share the same elastic constants. With respect to the templating of different materials, the relation in (4.13) suggests that refilling a ULH polymer scaffold of pitch P_{imposed} with a chiral nematic LC of a longer pitch, P, leads to an enhancement of the FEO tilt angle. The following

section describes the experimental procedure employed to characterize the FEO effect under these different regimes.

4.2. EXPERIMENTAL PROCEDURE

4.2.1. Materials & Sample Preparation

The commercial eutectic E7 nematic LC mixture was used as the host material, which has a birefringence and dielectric anisotropy of $\Delta n = 0.219$ at $\lambda = 632.8$ nm and $\Delta\varepsilon = 13.7$ at 1 kHz at a temperature of T = 20°C. The chiral nematic mixture (used in the initial formation of the ULH state and the polymer scaffolds) consisted of 65.3 wt % E7 and 4.7 wt % of the high twisting power chiral dopant R5011 (Merck Chemicals Ltd.). The polymer network was created from a mixture of reactive mesogens, photoinitiator and thermal inhibitor with a concentration of 30 wt % UCL-011-K1 (DIC). The photonic bandgap of the mixture existed outside the detectable range of the UV-Vis spectrometer. However, the pitch can be estimated from the helical twisting power (HTP) of R5011 ($\sim 10^8$ m^{-1}) from $(\text{HTP} \times \text{concentration})^{-1} \approx 200$ nm. A 5 µm-thick cell, with planar alignment layers on the inner surfaces of the substrates along with conductive indium tin oxide (ITO) layers, was capillary filled with the LC-monomer mixture above the clearing temperature of the host LC (T = 70°).

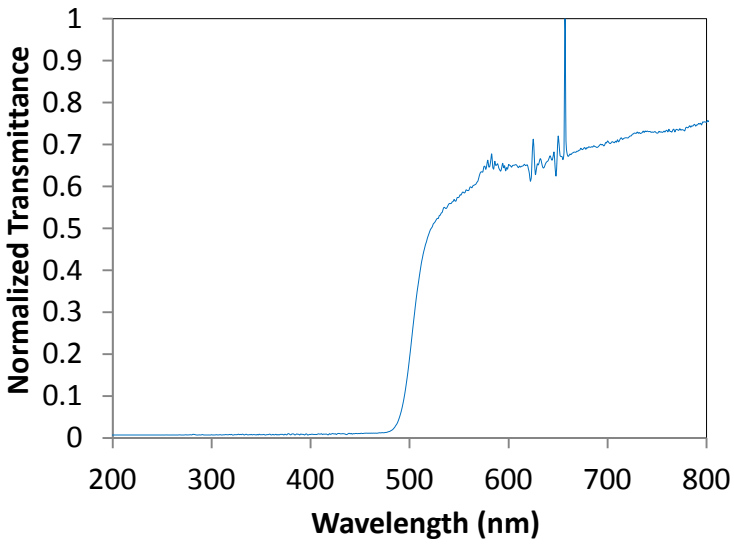


Figure 4.2. Transmittance spectrum of UV-Filter. The UV-filter was inserted above the bulb of the microscope during device characterization in order to help prevent polymerization of any residual monomer remaining in the LC mixture.

Two LC mixtures, chiral and achiral nematic, were used to refill the polymer templates (c.f. §4.2.4 for the fabrication procedure). The chiral nematic LC mixture consisted of 96.1 wt % E7 and 3.9 wt % of the high-HTP chiral dopant BDH1281 (Merck Chemicals Ltd). The mixture exhibits a reflection band in the range 530 – 605 nm, resulting in a pitch of ~350 nm. Neat E7 was used for the achiral nematic mixture, whereby the pitch, *P*, can be assumed to be infinitely long for discussions of the pitch constraint study.

4.2.2. Reorienting the Helix

Once cooled to room temperature, the device was mounted on a hot-plate on an optical polarizing microscope (OPM) and connected to an arbitrary waveform generator. A UV-filter was inserted above the microscope's bulb in order to prevent polymerization in the bulk. Figure 4.2 shows the transmittance spectrum of the UV-filter measured

using a UV-Visible spectrometer. The filter efficiently blocks light of wavelengths up to ~500 nm. Additional precautionary measures were taken to prevent residual polymerization by setting the microscope bulb to a low light intensity and carrying out all characterization in a dark room.

Figure 4.3 (a) – (f) shows a series of OPM images taken between crossed polarizers of the chiral nematic LC device under the application of an increasing electric field amplitude (0 V/µm to 2 V/µm). The Grandjean state or uniform standing helix (USH) can be seen in Figure 4.3 (a). The short pitch corresponds to a photonic bandgap outside of the visible regime, causing the bulk LC to appear dark between crossed polarizers. Defect regions in the form of oily streaks can also be seen. These occur when the helix axis is not uniformly aligned, such that some regions of the helix are oriented in the plane of the cell. As the applied electric field strength is increased from (b) to (f), the focal conic texture nucleates from these defect sites until the entire device consists of randomly oriented helices.

Figure 4.4 (a) – (d) shows a sequence of microscope images taken upon removal of the applied electric field (2 V/µm to 0 V/µm). The device, which is primarily in the focal conic state, eventually relaxes into the lowest energy Grandjean state as seen in Figure 4.4 (d). This highlights the need for a stabilization mechanism to ensure that the required LC state is 'locked-in', as will be discussed in the next section. Note that there is a significantly higher concentration of oily streaks after electrically addressing the device relative to its initial state in Figure 4.3 (a). This is likely to be a result of the defect sites being pinned in by the spacer beads that dictate the cell-thickness.

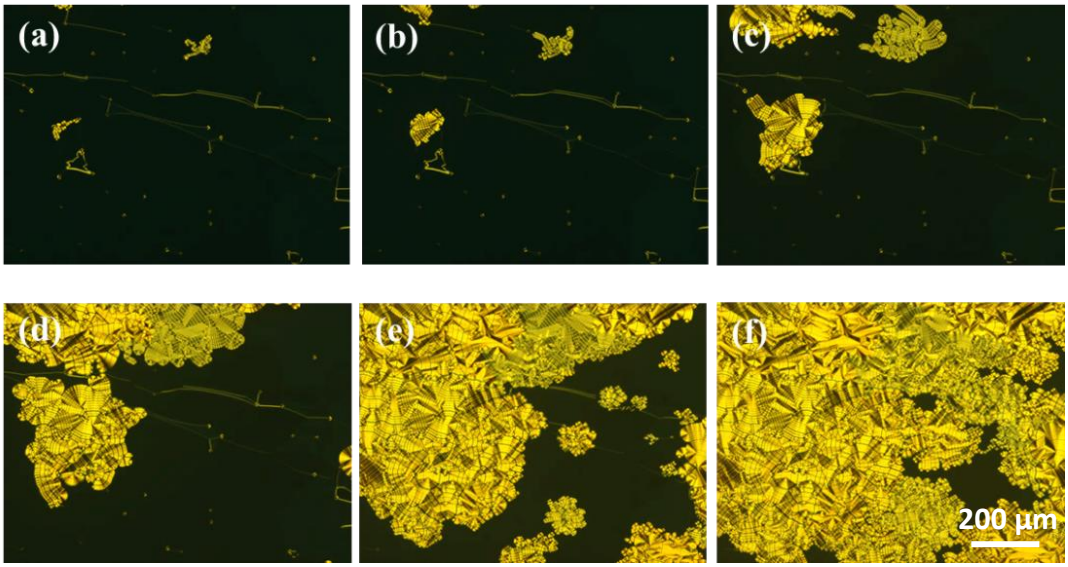


Figure 4.3. OPM images reveal the evolution of a chiral nematic LC device under the application of an increasing electric field amplitude (0 V/µm to 2 V/µm). (a) Oily streaks can be seen in the bulk LC device, which is aligned in a USH (Grandjean) state. (b) Randomly oriented helices in the form of a focal conic texture can be seen to nucleate from the defect regions (oily streaks). (c) – (f) The focal conic texture grows until the device is no longer in the Grandjean state.

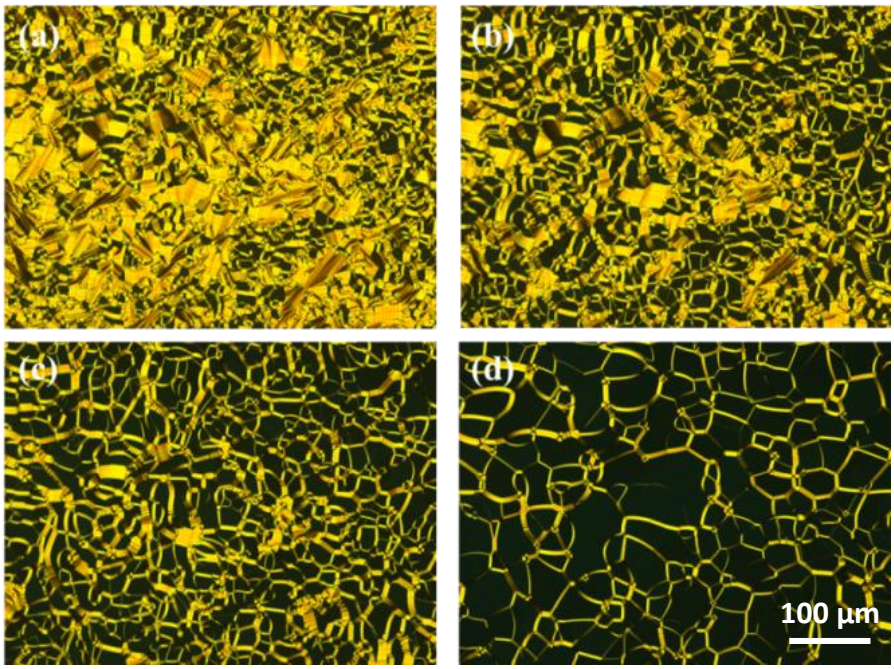


Figure 4.4. Relaxation of a chiral nematic LC device upon removal of an externally applied electric field (2 V/µm to 0 V/µm). (a) The electric field is removed when the device is in the focal conic state. (b) – (d) Over a total time period of a few seconds, the device relaxes back to the lowest energy Grandjean (USH) state. A higher concentration of oily streaks remains after electrically switching the device.

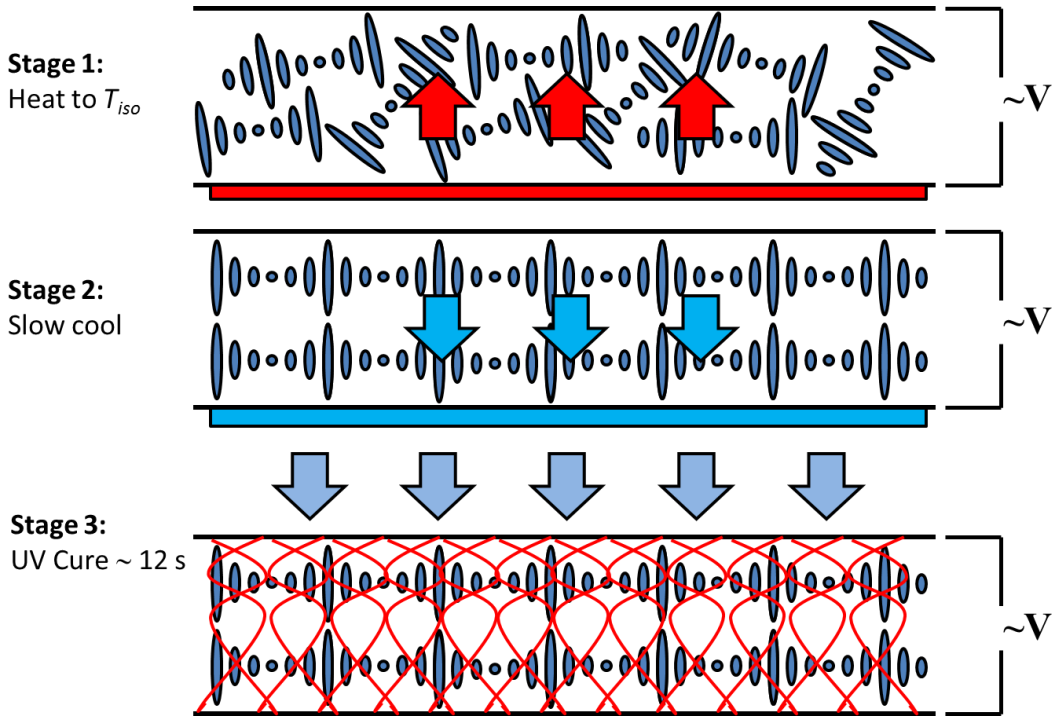


Figure 4.5. A schematic of the ULH annealing and polymerization procedure. The device, initially in the lowest energy Grandjean state, is heated to the isotropic phase under the application of an external electric field (Stage 1). The focal conic texture begins to form as the helices orient in random directions. The device is gradually cooled from the isotropic phase (T_{iso}) to room temperature, which leads to the formation of the ULH state (Stage 2). The inherently unstable ULH texture is locked-in by polymerization, under the exposure of a UV-source for 12 seconds (Stage 3).

4.2.3. ULH Formation

The ULH annealing and stabilization procedure is illustrated in the schematic of Figure 4.5. Initially, the device is heated to the isotropic phase under the application of a 100 Hz, ± 10 V square wave. The electric field generates the focal conic texture (Stage 1). However, gradually cooling the device from the isotropic phase (T_{iso}) under the externally applied electric field leads to the subsequent formation of the ULH alignment (Stage 2). Mechanically shearing the sample also improves the alignment on account of shear flow in the LC, wherein the helical axis forms orthogonally to the direction of flow. If the electric field is removed at this stage, the ULH will collapse into the lower

energy Grandjean state as demonstrated in Figure 4.4. Therefore, a stabilization mechanism is required to 'lock-in' the desired state. In Stage 3, the sample is photo-cured by exposure to light from a UV LED at a distance of 10 cm, emitting at λ = 365 nm and at a power density of 185 mW cm^{-2}, for 12 seconds. This stage ensures that the polymer network 'locks-in' the required LC alignment such that the externally applied electric field can be removed and the ULH state remains stable for subsequent FEO measurements.

4.2.4. Polymer Templating

Figure 4.6 illustrates the polymer templating process. After the desired LC alignment is achieved and 'locked-in' by the polymer chains, the device is immersed in a bath of acetone in order to remove any residual LC-monomer (Stage 1). The washing out process is normally complete after a 24 hour period, although this can vary depending upon the density of the polymer network, which is dictated by the concentration of reactive mesogen in the mixture along with the UV-curing conditions. Therefore, the washed-out device is characterized on the microscope to ensure that there is no remaining residual LC before continuing to the next stage of the templating procedure. An additional check to ensure that the template is ready to be refilled involves measuring the electro-optic response from the device, which should be zero if the LC has been completely removed. Stage 2 involves refilling the template with the new material, whereby the device is mounted on a hot-plate (as in §4.2.3) and capillary-filled in the isotropic phase (T_{iso}). The duration of time required to fill an empty cell is normally no longer than a few minutes. In contrast, the template can take up to a few hours to fill uniformly, as the LC material needs to diffuse through the porous polymer

network. Once the LC has filled into the template, the device can be left to cool to room temperature (Stage 3), during which time the scaffold imparts its alignment properties onto the new material. For example, a scaffold formed in the chiral nematic phase should impart the self-assembled periodicity inherent to the phase when the template is refilled with an achiral nematic LC. For this investigation, four templates were fabricated under identical experimental conditions in order to ensure that the observed FEO response was accurate and repeatable.

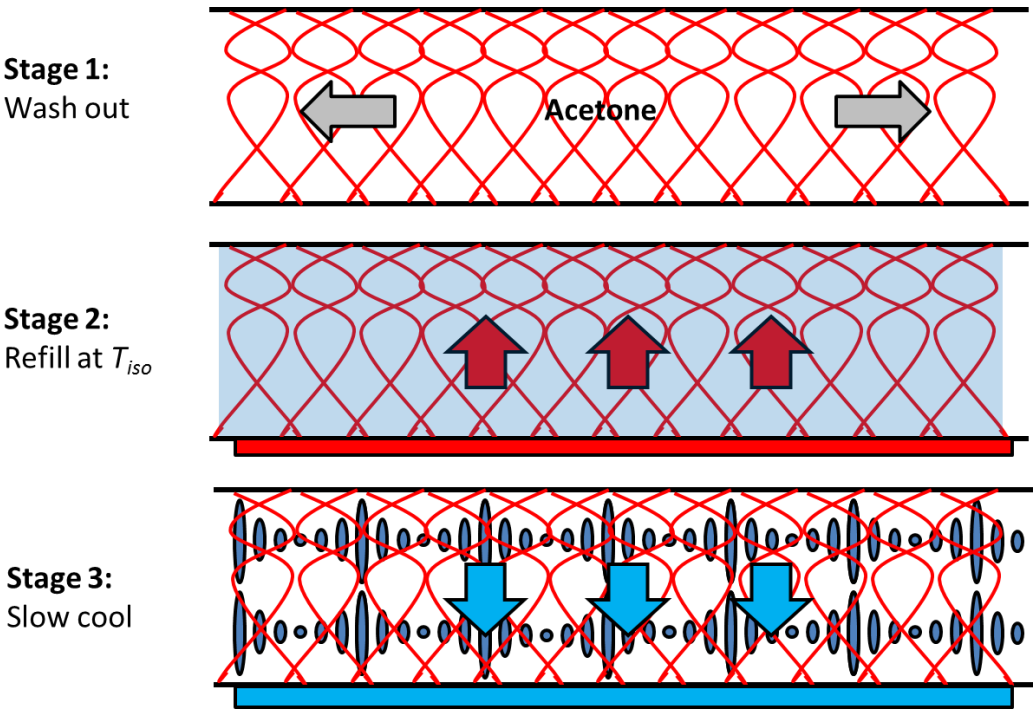


Figure 4.6. A schematic of the polymer templating process. The polymerized chiral nematic LC device is immersed in a bath of acetone for at least 24 hours, in order to remove the residual LC-monomer (Stage 1). Once the washing out stage is complete, the acetone is left to evaporate from the device at room temperature before refilling with pure LC in the isotropic phase (Stage 2). The new LC alignment imposed by the polymer scaffold is observed upon cooling the device to room temperature (Stage 3).

4.2.5. Electro-Optic Response

The difference in the flexoelectric coefficients, $e_1 - e_3$, can be extracted from the rotation of the LC's optic axis as a function of the applied electric field. Using the relation for transmission between crossed polarizers from (1.20),

$$T = \frac{1}{2}\sin^2(2\chi + 2\phi)\sin^2\left(\frac{\pi\Delta n_{\text{effective}}d}{\lambda}\right), \tag{4.14}$$

the tilt angle can be measured from the electro-optic response of the device, which relates to the flexoelectric coefficients by (4.11).

The device is mounted on the rotation stage of the polarizing microscope. A photodiode is used to detect the transmission from the device, which is connected to an oscilloscope for measurements of the electro-optic response. The device is initially rotated until the maximum and minimum transmission levels are recorded on the photodiode, where the helicoidal axis aligns in the plane of the cell at an angle of χ = 45° and 0° to the polarizer, respectively. The difference between the transmission maxima and minima is denoted T_0. The device orientation is then adjusted until the photodiode detects the midpoint between the two transmission levels, $T_0/2$, when $\chi \sim$ 22.5°. At this device orientation, the flexoelectric effect will have an approximately linear electro-optic response such that the transmission is dependent upon the electric field polarity.

The device is then connected to an arbitrary waveform generator. Under the application of a 1 kHz, 10 Vrms square wave, tilt angles were measured by initially rotating the device between the maximum and minimum transmission amplitudes, whereby the difference between the two is equivalent to 2Φ. However, rotating the device through small angles gives rise to large errors in the measurements of small tilt

angles. Therefore, a different approach was adopted that involves measuring the change in transmission with respect to the angle that the optic axis of the LC makes with the polarizer, $\partial T/\partial \chi$. For a constant birefringence, device thickness and wavelength of light, the transmission can be written as

$$T(\chi) = T_0 \sin^2(2\chi + 2\phi). \tag{4.15}$$

Differentiating (4.15) with respect to χ gives,

$$\frac{\partial T}{\partial \chi} = 4T_0 \sin(2\chi)\cos(2\chi), \tag{4.16}$$

which simplifies to $\partial T/\partial \chi = 2T_0$ at χ = 22.5°. Defining the difference between the transmission at the positive and negative voltages of the applied square wave as ΔT gives $\Delta T/\Delta \chi = 2T_0$. The change in the flexoelectric tilt angle, $\Delta\phi$, corresponds to $\chi/2$ (i.e. half of the oscillation angle from +V to –V). Therefore, the tilt angle can be calculated from the change in transmission as

$$\Delta\phi = \frac{\Delta T}{4T_0}. \tag{4.17}$$

Note that the same electric field strength was applied across all four test devices in order to carry out consistent measurements, since the tilt angle is a function of the electric field according to (4.11) and all electro-optic measurements were carried out at room temperature.

4.3. RESULTS & DISCUSSION

4.3.1. Pre-Cure ULH

The OPM images in Figure 4.7 show the bright (45°) and dark (0°) states of the ULH device annealed using the shear-flow technique. The images were taken once the device had been cooled to room temperature whilst under the application of the external electric field, before the photo-curing process was initiated. A fairly uniform ULH alignment can be seen on a local scale; defects are visible across larger regions of the device due to pitch jumps resultant from discontinuities in the helix formation. However, good contrast has been achieved between the bright and dark states.

The FEO response obtained from the transmission measurements under the application of a 1 kHz, ± 10 V square wave is shown in Figure 4.8. The modulation corresponds to a tilt angle of $\phi = 1.6° \pm 0.2°$, and flexoelectric difference of $e_1 - e_3 = 12.3 \pm 1.0$ pCm^{-1}. This value is in good agreement with previous E7 flexoelectric measurements reported in the literature ($e_1 - e_3 = 12.1 \pm 1.0$ pCm^{-1}; $e_1 - e_3 = 12.5 \pm 1.3$ pCm^{-1}) [15, 16].

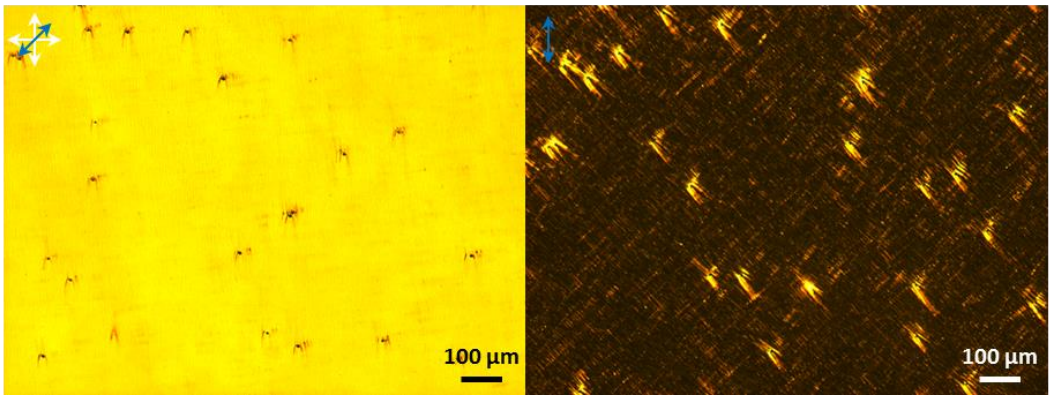


Figure 4.7. OPM images showing the bright (left) and dark (right) states of a ULH texture before UV-curing. The ULH texture grown by shear flow shows defects where the helical axis is discontinuous across large regions. A fairly uniform ULH alignment can be seen locally, with good contrast between the bright and dark states. The direction of the polarizers and LC optic axis are indicated by the white and blue arrows, respectively.

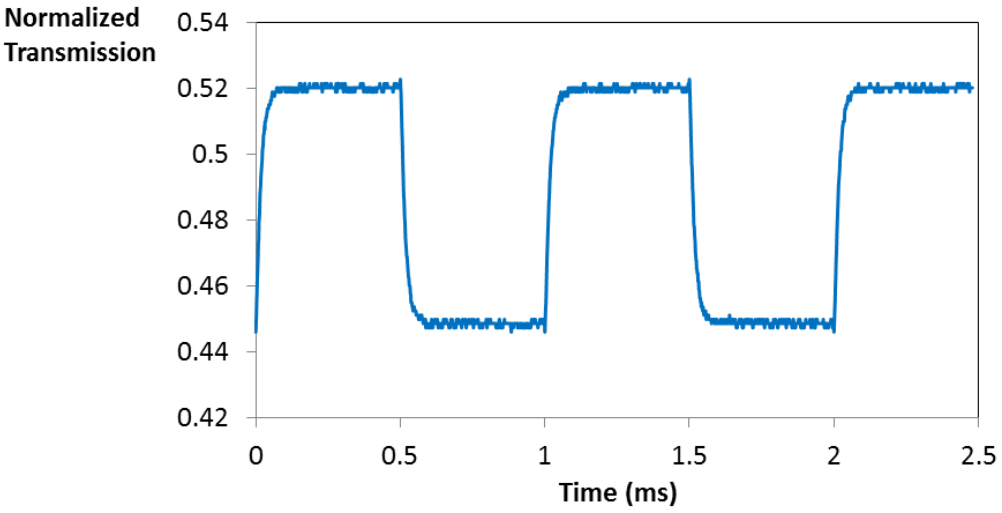


Figure 4.8. The FEO response obtained from a ULH prior to UV-curing. A 1 kHz, 10 Vrms square wave was applied to observe the FEO modulation while the device was oriented mid-way (22.5°) between the bright (45°) and dark (0°) states that correspond to maximum and minimum transmission, respectively. The modulation reveals a tilt angle of $\phi = 1.6° \pm 0.2°$, which correlates to a flexoelectric difference of $e_1 - e_3 = 12.3 \pm 1.0$ pCm^{-1}.

4.3.2. Post-Cure ULH

The OPM images in Figure 4.9 were taken after the device had been photo-cured by exposure to light from the UV LED for 12 seconds. The images were taken upon removal of the applied electric field, and therefore reveal the stability of the ULH texture as it no longer collapses to the lowest energy Grandjean state (c.f. Figure 4.4). However, a significant degradation in the ULH alignment can be seen from the poor contrast between the bright and dark states, relative to the pre-cure images in Figure 4.7. Therefore, the formation of the polymer network visibly disrupts the quality of the ULH alignment.

Figure 4.10 shows the associated FEO response detected from the polymerized device. The amplitude of the modulation has fallen by a factor of forty, resulting in a tilt

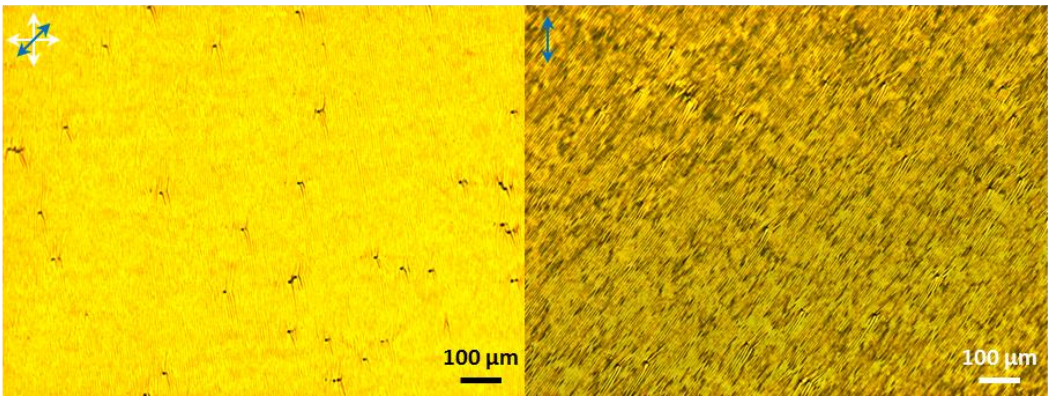


Figure 4.9. OPM images showing the bright (left) and dark (right) states of a ULH texture after UV-curing. The ULH alignment degrades significantly upon photo-curing, evidenced by the poor contrast between the bright and dark states of the device relative to the pre-cured states (c.f. Figure 4.7).

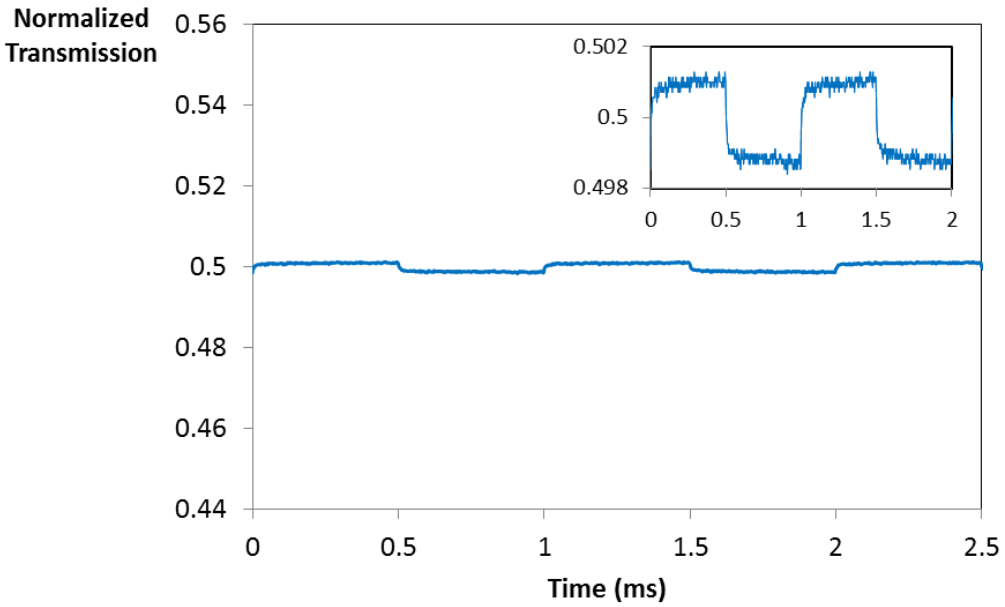


Figure 4.10. The FEO response obtained from a ULH post UV-curing. A 1 kHz, 10 Vrms square wave was applied to observe the FEO modulation while the device was oriented mid-way (22.5°) between the bright (45°) and dark (0°) states that correspond to maximum and minimum transmission, respectively. The modulation falls significantly relative to the pre-cure response, with a tilt angle of $\phi = 0.041° \pm 0.020°$ and flexoelectric difference of $e_1 - e_3 = 0.31 \pm 0.20$ pCm^{-1}. Inset: the FEO response with scaled axes.

angle of $\phi = 0.04° \pm 0.02°$ and effective flexoelectric difference of $e_1 - e_3 = 0.3 \pm 0.2$pCm^{-1}. As expected, the polymer network hinders the switching angle. The

flexoelectric properties, however, are inherent to the LC material; therefore this measurement is an effective value that is a consequence of the polymerization process. This reduction in the switching angle, however, is accompanied by a factor of four reduction in the response time of the device, from 80 µs (pre-cure) to 20 µs (post-cure). This apparent trade-off between the reduced FEO modulation and device response time is discussed in detail by Broughton et al [9].

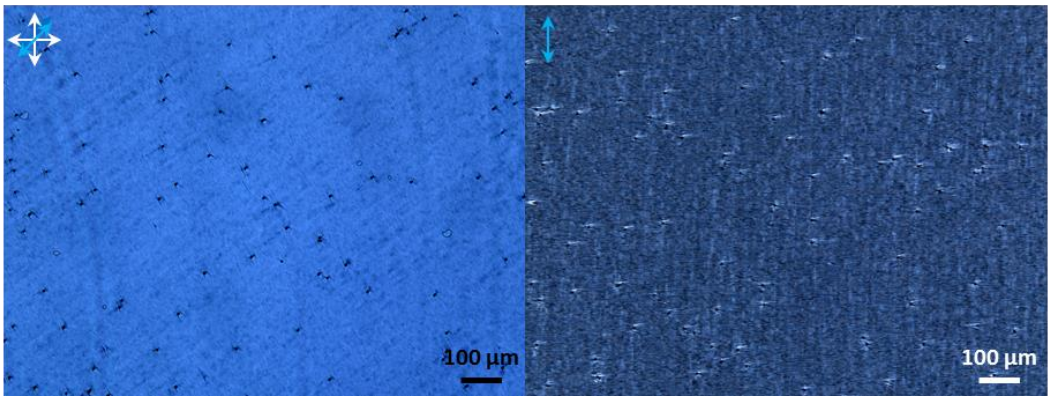


Figure 4.11. OPM images showing the bright (left) and dark (right) states of the polymer template. After washing out the LC and non-crosslinked monomer by immersing the device in a bath of acetone, the polymer scaffold reveals the LC director orientation that is retained by the polymer network when rotated between crossed polarizers due to the density of the polymer network.

4.3.3. Templated ULH

Figure 4.11 shows OPM images of the template (after Stage 1 of the templating procedure in Figure 4.6. The dense polymer network retains the director orientation of the host liquid crystalline material in which it was formed. Although, the actual residual birefringence is small, the image brightness is enhanced to reveal the differences between the two device orientations; the bright and dark states remain visible when rotating the template between crossed polarizers despite the removal of the unreacted

mesogens and LC. However, no electro-optic response was detected from the device confirming that the uncured host LC had been completely removed.

The OPM images in Figure 4.12 show the bright and dark states of the refilled template consisting of the chiral nematic LC mixture (P ~ 350 nm ≈ 1.5 P_{imposed}). The images show that the ULH state has been recovered, with improved contrast between the bright and dark states relative to that shown in Figure 4.9 taken after photo-curing. From (4.13), the flexoelectric tilt angle is expected to increase by $(3K_{11} + K_{33})/(3K_{11} + K_{33} - 2K_{22})$. Using the elastic constant parameters for E7 (K_{11} = 10.7 pN, K_{22} = 6.5 pN, K_{33} = 16.2 pN), the tilt angle is predicted to increase by a factor of ~1.4. However, the FEO response shown in Figure 4.13 reveals a decrease in the switching angle of ~22% to ϕ = 0.031° ± 0.010° and a resultant effective flexoelectric difference of $e_1 - e_3$ = 0.24 ± 0.50 pCm^{-1}.

The data obtained from the four test devices revealed an increase in the FEO response in two cases and a reduction in the other two devices. This data is summarised in Table 4.1. This is potentially due to the fact that there is a small difference between the constrained and imposed pitches, with only a factor of ~1.4 predicted by the analytical derivations. Moreover, inhomogeneities in the ULH alignment of each device may lead to variations in the detected electro-optic performance of the device, as the shear-flow technique does not provide perfectly uniform textures. Refilling the template with a chiral nematic material that has $P >> P_{\text{imposed}}$ may provide a better indication of whether the constrained pitch leads to an enhancement of the flexoelectric effect and clarify the discrepancy in the obtained data.

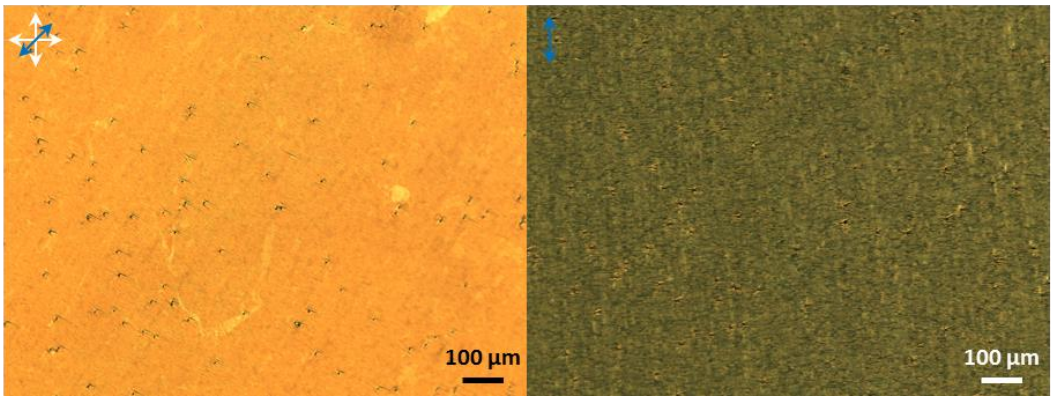


Figure 4.12. OPM images showing the bright (left) and dark (right) states of a ULH texture in the polymer template refilled with a longer pitch chiral nematic mixture. An improvement can be seen in the contrast between the bright and dark states of the refilled template relative to the post-cure ULH.

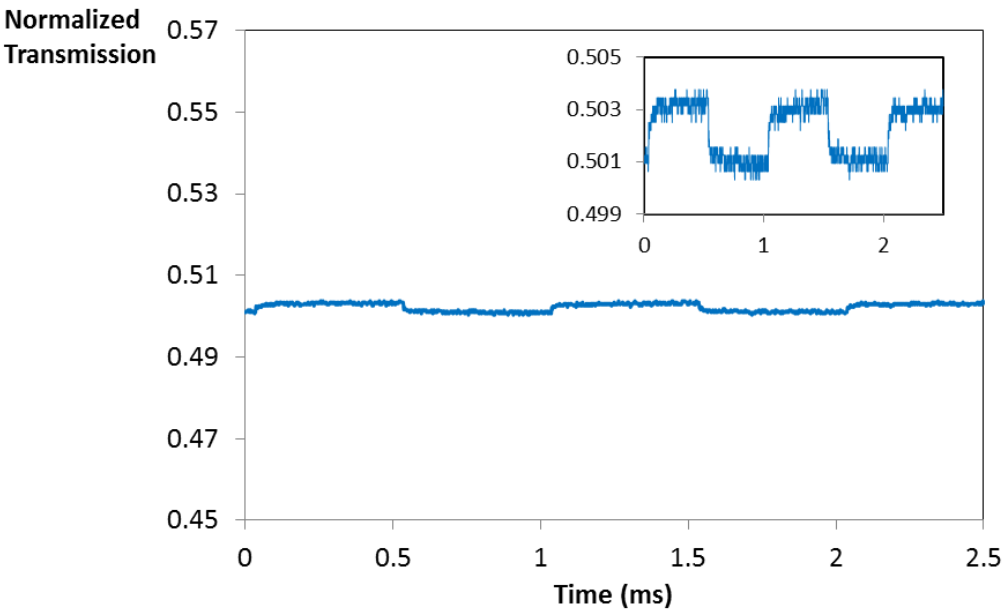


Figure 4.13. The FEO response obtained from a ULH template refilled with a longer pitch chiral nematic mixture. A 1 kHz, 10 Vrms square wave was applied to observe the FEO modulation while the device was oriented mid-way (22.5°) between the bright (45°) and dark (0°) states that correspond to maximum and minimum transmission, respectively. The amplitude of the modulation reveals a ~22% reduction relative to the post-cure FEO response, with a tilt angle of $\phi = 0.031° \pm 0.010°$ and flexoelectric difference of $e_1 - e_3 = 0.24 \pm 0.50$ pCm^{-1}. Inset: the FEO response with scaled axes.

Refilling the template with the achiral nematic E7 leads to the formation of the ULH state shown in Figure 4.14. The texture has once again been recovered upon refilling with a different material, despite the lack of inherent chirality in the achiral nematic E7 mixture. The FEO response recorded from the achiral nematic-filled template is shown in Figure 4.15. As discussed in §4.1.4 for the condition when $P \rightarrow \infty$, the resultant tilt angle is expected to increase by a factor of ~1.9. The template refilled with E7 reveals an increase in the flexoelectric tilt angle of ~35% to $\phi = 0.056° \pm 0.040°$, giving a flexoelectric difference of $e_1 - e_3 = 0.42 \pm 0.30$ pCm^{-1}.

Table 4.1 summarises the FEO measurements from the four different test devices taken during the different stages of the polymerization and templating process. Despite the inconsistencies between the analytical predictions and the measured φ from the template refilled with the chiral nematic mixture, the enhancement of the FEO response for the template refilled with pure E7 is promising. The discrepancies between the measurements are likely to be a result of inhomogeneities in the ULH alignment that arise when using the shear-flow technique, highlighting the need for a more reliable alignment technique. In addition, the high density of polymer network required to form the template significantly restricts the full extent of molecular switching under an applied electric field compared with the pre-cure electro-optic response; the flexoelectric tilt angles are an order of magnitude smaller than those measured before polymerization. The degradation of the electro-optic response might be avoided by considering different fabrication techniques that could provide localised control over the formation of the polymer network rather than photo-curing through the bulk

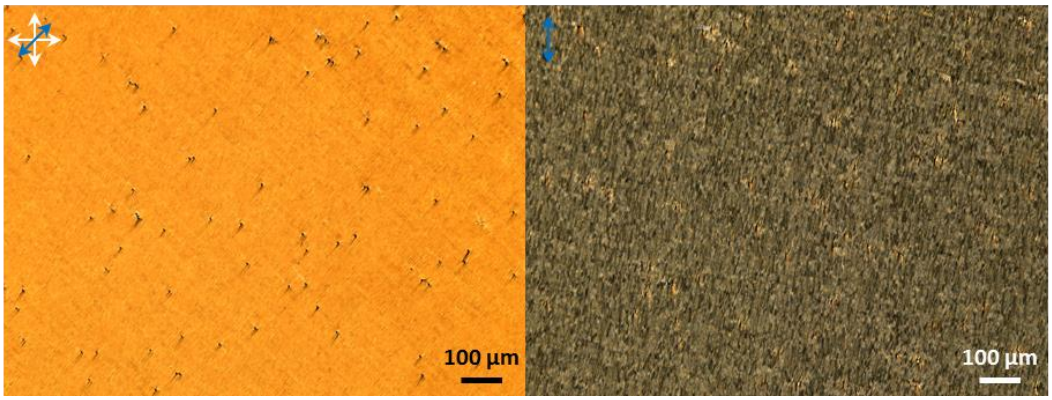


Figure 4.14. OPM images showing the bright (left) and dark (right) states of a ULH texture in the polymer template refilled with pure E7. The helicity of the ULH texture has been imparted from the polymer scaffold to the pure nematic LC.

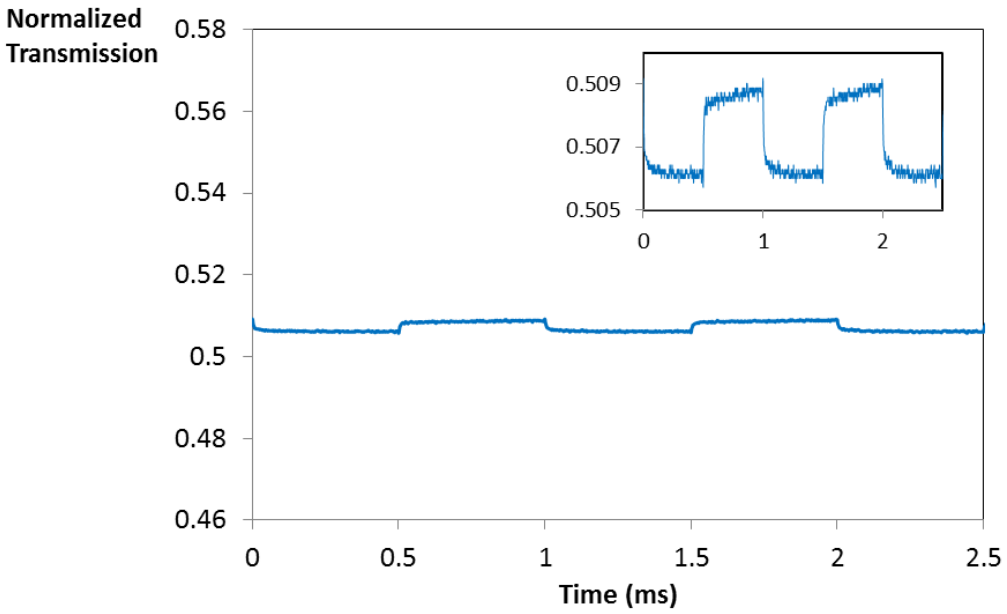


Figure 4.15. The FEO response obtained from a ULH template refilled with the achiral nematic LC, E7. A 1 kHz, 10 Vrms square wave was applied to observe the FEO modulation while the device was oriented mid-way (22.5°) between the bright (45°) and dark (0°) states that correspond to maximum and minimum transmission, respectively. The amplitude of the modulation has increased by ~35%, with a tilt angle of $\phi = 0.056° \pm 0.040°$ and flexoelectric difference of $e_1 - e_3 = 0.42 \pm 0.30$ pCm^{-1}. Inset: the FEO response with scaled axes.

CELL	PRE-CURE	POST-CURE	REFILLED CHIRAL	REFILLED ACHIRAL
1	11.0 pC/m	0.285 pC/m	0.263 pC/m	0.369 pC/m
2	12.9 pC/m	0.365 pC/m	0.587 pC/m	0.380 pC/m
3	10.8 pC/m	0.436 pC/m	0.380 pC/m	0.562 pC/m
4	12.3 pC/m	0.313 pC/m	0.238 pC/m	0.421 pC/m

Table 4.1. Measured FEO responses from four ULH devices. Electro-optic data was obtained under the application of a 1 kHz, ± 10 V square wave prior to polymerization, after UV-curing, after washing out and refilling with a chiral nematic LC with a longer pitch and an achiral nematic LC. The most consistent results were obtained for the template refilled with achiral nematic LC, showing an enhancement of the FEO response in all four cases.

4.4. CONCLUSIONS

Flexoelectricity has been discussed in chiral nematic systems as an electro-optic effect that shows great potential for the next-generation of fast-switching photonics applications. In order for the electro-optic effect to be realised, an external electric field must be applied orthogonally to the helical axis of the chiral nematic material. However, the uniform lying helix alignment in which the FEO effect is used is inherently unstable in conventional device geometries. Polymer networks have been used here to 'lock-in' the desired LC alignment. However, the polymerization process hinders the molecular switching under externally applied electric fields and a resultant degradation in the electro-optic performance of the device. The fabrication of polymer templates that can be refilled with different materials could be considered as a potential solution to enhance the FEO modulation.

The polymer templates presented in this work have successfully imparted the properties of the ULH state in which they were formed onto other LC materials that do not possess the same properties i.e. achiral nematics. In addition, it has been shown that

there is potential to enhance the FEO response by refilling templates with materials that possess an infinite pitch relative to the imposed pitch (of the polymer scaffold). However, the tilt angles and effective flexoelectric coefficients still remain significantly smaller than those measured prior to photo-curing. Therefore, it is necessary to explore different fabrication methods that permit the localization of the polymer network to specific regions in the device rather than in the bulk. Creating periodic polymer structures that pin the ULH state in may generate a larger FEO response as the molecules would then be free to switch in the bulk device. The next Chapter explores the use of a more sophisticated fabrication technique in the form of direct laser writing, to resolve this issue.

4.5. REFERENCES

[1] R. B. Meyer, *Phys. Rev. Lett*. **22**, 918 (1969).

[2] J. S. Patel and R. B. Meyer, *Phys. Rev. Lett*. **58**, 15 (1987).

[3] H. J. Coles, B. Musgrave, M. J. Coles and J. Willmott, *J. Mater. Chem.* **11** (2001).

[4] A. E. Blatch, M. J. Coles, B. Musgrave, and H. J. Coles, *Mol. Crys. Liq. Crys*. **401** (2003).

[5] H. J. Coles, M. J. Clarke, S. M. Morris, B. J. Broughton and A. E. Blatch, *J. Appl. Phys*. **99**, 034104 (2006).

[6] P. Rudquist and S. Lagerwall, *Flexoelectricity in Liquid Crystals*, Imperial College Press, London, UK (2013).

[7] P. S. Salter, G. Carbone, S. A. Jewell, S. J. Elston and P. Raynes, *Phys. Rev. E* **80**, 041707 (2009).

[8] P. Rudquist, L. Komitov and S. Lagerwall, *Liq. Cryst*. **24**, 3 (1998).

[9] B. J. Broughton, M. J. Clarke, S. M. Morris, A. E. Blatch and H. J. Coles, *J. Appl. Phys*. **99**, 023511 (2006).

[10] G. Carbone, D. Corbett, S. Elston, P. Raynes, A. Jesacher, R. Simmonds and M. Booth, *Mol. Crys. Liq. Cryst*. **544**, 37 (2011).

[11] S. M. Wood, S. J. Elston and S. M. Morris, *Mol. Crys. Liq. Cryst*. **632** (2016).

[12] F. Castles, F. V. Day, S. M. Morris, D-H. Ko, D. J. Gardiner, M. M. Qasim, S. Nosheen, P. J. W. Hands, S. S. Choi, R. H. Friend and H. J. Coles, *Nat. Mater*. **11** (2012).

[13] B. Outram, *Flexoelectric and Dielectric Phenomena in Helicoidal Liquid Crystals*, Department of Engineering Science PhD Thesis, Ph. D. Dissertation, University of Oxford, UK (2013).

[14] L. A. Parry-Jones, S. J. Elston and G. P. Alexander, *Proceedings for 21st ILCC*, Keystone, Colorado USA (2006).

[15] S. Bolis, C. C. Tartan, J. Beeckman, P. Kockaert, S. J. Elston & S. M. Morris, *Liq. Cryst.* (2018), DOI:10.1080/02678292.2018.1425492

[16] B. Outram and S. Elston, *J. Appl. Phys.* **113**, 043103 (2013).

5

DIRECT LASER WRITING & ADAPTIVE OPTICS

5.1. INTRODUCTION

5.1.1. Structuring Polymer Networks

So far, it has been demonstrated that a bulk polymerization technique can be used to stabilise liquid crystalline states that do not naturally occur. Removing the uncured polymer in a solvent bath also leads to the formation of polymer templates that can be used to impart the properties of one material onto another. However, the bulk polymer network restricts the molecular switching and incurs a penalty in the electro-optic performance of the states in which they were formed. This reinforces the need for a more sophisticated fabrication technique that could be used to structure polymer networks within localised regions of the device.

Direct laser writing (DLW) is a powerful nonlinear fabrication technique that provides high intensities in the focal plane of a sample for the creation of multidimensional structures with submicron feature sizes [1]. In this chapter, a novel approach to DLW of polymeric structures is adopted, whereby the photo-sensitive material is liquid crystalline and aligned within electrically addressable LC devices. The

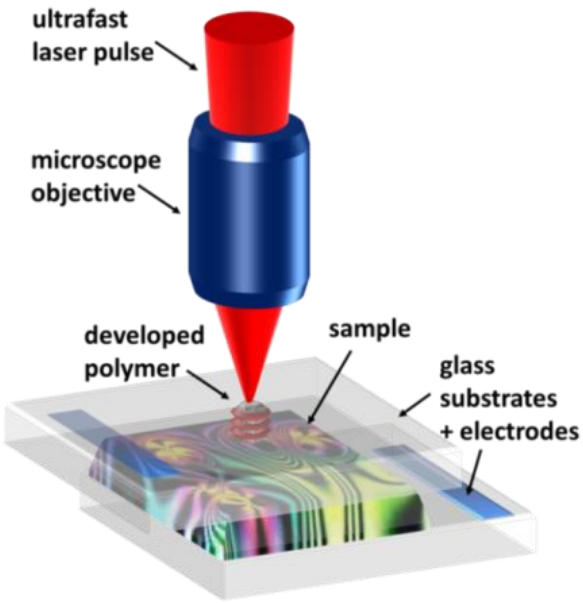


Figure 5.1. In-situ DLW fabrication process. An ultrafast laser pulse is tightly focused by the microscope objective lens into the LC-monomer sample, which is bounded by two glass plates. Spatially variant birefringent polymer structures are developed at the focal spot of the laser under the application of external electric fields.

custom-built DLW system incorporates adaptive optics for aberration correction and opens the door to a range of potential novel structures that are not readily realisable using conventional alignment techniques.

The resultant in-situ fabrication procedure is illustrated in Figure 5.1. Laser written polymer structures are shown to retain the optical properties of the LC during photo-polymerization i.e. at the moment of exposure to the laser beam. Thus, birefringent polymer structures can be written, with the orientation of the optic axis tuned during fabrication through switching of the LC with an applied electric field. This gives the potential to create complex spatial variations of the polymer refractive index on a micron scale. Furthermore, a range of structures are presented for controlling the LC alignment in devices, including two-dimensional arrays of polymer pillars, a polymer checkerboard that creates a controllable disclination network, and 3-dimensional helical

polymer ribbons and knots. This work introduces a new degree of freedom for the DLW of advanced photonic materials and structures as well as offering significant advances for the control of soft matter.

5.2. DIRECT LASER WRITING

5.2.1. Two-Photon Photopolymerization

Direct laser writing (DLW) involving two-photon photopolymerization (TPP) is a nonlinear optical process that enables polymer structures to be fabricated with sub-micron feature sizes [1]. The TPP process based upon two-photon absorption (TPA) permits the fabrication of structures with three dimensional resolution that would not otherwise be attainable using conventional single photon laser fabrication techniques [2 - 4]. Figure 5.2 shows the energy diagrams for one- and two-photon excitation. TPA results from the simultaneous absorption of degenerate (same frequency) photons, whereby the absorption of one photon at $\lambda/2$ is equivalent to the absorption of two photons at the wavelength of the incident light, λ, through a virtual intermediate energy state. TPA occurs if the absorbing material is transparent at the two-photon wavelength (λ) such that a second photon arrives within the virtual state lifetime, τ, caused by high intensities at the focal spot. The intensity, I [W/m^2], of the incident light is an important parameter since structural modification of a material by an *N-photon* process scales as I^N, thus TPA scales quadratically to the intensity (energy [J] and fluence [J/m^2]) of the incident light [4].

Intensities sufficient to initiate the nonlinear optical process are often realized using a pulsed, tightly focused laser beam. Focussing ultrafast laser light within transparent materials is achieved using sufficiently high numerical aperture (NA) objective lenses

(NA $\geq$ 0.5). At the focus, the electric field of the intense laser beam is high enough for non-linear absorption to occur. The laser field imparts energy to an electron, which becomes excited to a higher energy state. The excited electron impact-ionizes an additional electron, which is followed by an avalanche ionization process and the creation of free radicals [5]. Energy is subsequently transferred to the material upon recombination of the excited electrons and ions leading to structural modifications in the host material. The ultrashort nature of the pulsed light confines these modifications to the focal volume, such that 3-dimensional structures can be embedded within transparent materials without affecting the surface or surroundings. The resolution of the fabricated structures in both lateral $\Delta(x, y)$ and axial (Δz) directions can be estimated by the following relations [6],

$$\Delta x, \Delta y \approx \frac{\lambda}{2\mathrm{NA}}, \ \Delta z \approx \frac{3n\lambda}{2\mathrm{NA}^2}, \tag{5.1}$$

where n is the refractive index of the material. It can be seen that higher resolutions are attainable through the use of higher NA objective lenses, particularly in the axial direction that scales quadratically with the inverse NA value, and/or smaller incident wavelengths. Altering the wavelength of the laser, however, is non-trivial and would also potentially require changing the photoinitiator in the photo-sensitive material in order to match the peak absorbance in the two-photon absorption cross-section with $\lambda/2$ to ensure that polymerization occurs. Therefore, high NA (>1) oil immersion lenses are typically used to create sub-micron feature sizes.

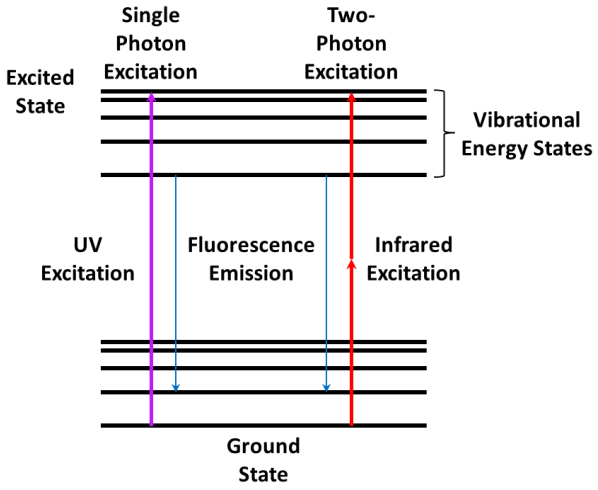


Figure 5.2. Single and two-photon excitation energy diagrams. Single photon excitation by UV irradiation results in a single transition from the ground state to an excited energy state. Two-photon excitation by infrared irradiation involves two transitions via a virtual intermediate energy state. Fluorescence emission results when an excited electron returns to the lower energy ground state.

5.2.2. Aberration Correction

An important application of TPP is the fabrication of photonic materials. For example, three dimensional polymer scaffolds manufactured by DLW have subsequently been further functionalized by infusion with liquid crystalline (LC) materials to give dynamic tuning of the optical properties [7 - 11]. More recently, it has been shown that DLW can also be used to fabricate elastomeric materials directly inside the LC host [12, 13]. Despite these notable achievements, there have not been any reports dedicated to the fabrication of polymer structures directly into a fully assembled device where, crucially, the LC can be electrically addressed during laser writing so as to create a complex spatial variation of the refractive index on a micron scale. The primary reason for this is that the relatively thick bounding glass substrates (~ 1 mm) that contain transparent conductive coatings are some orders of magnitude thicker than the LC layer (~ 5 – 20 μm), and introduce strong spherical aberrations that lead to an enlarged focal spot.

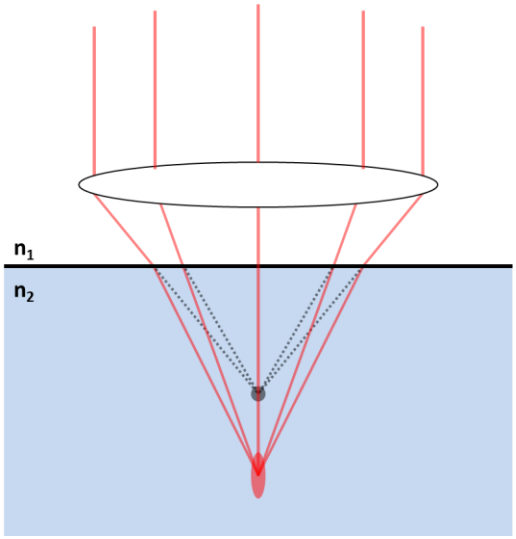


Figure 5.3. Spherical aberrations. A schematic of the spherical aberrations in a LC device induced by the refractive index mismatch ($n_1 \neq n_2$) due to the thick glass substrates.

Aberrations induced from the thick glass substrates of the LC device distort the wavefronts passing through the lens pupil. Figure 5.3 illustrates the enlarged focal region due to the spherical aberrations that are predominantly depth dependent when focussed through a mismatch in the refractive index; the resultant effects of which include blurring across adjacent planes along the optic axis and an overall loss of efficiency [14]. Thus, aberrations increasing with depth, numerical aperture and magnitude of the refractive index mismatch restrict the minimum size of the structures that can be directly fabricated into a LC device. Note that these aberrations can be minimized using a cell with a thin (~100 μm) ITO coated glass cover slip as the superstrate. However, difficulties arise in the soldering process of the wires to the electrodes due to the inherent fragility of the thin sheet of glass. It would therefore be beneficial to address the issue of aberration correction induced from readily available commercial LC cells and eliminate the need to design customised cells for micro-fabrication.

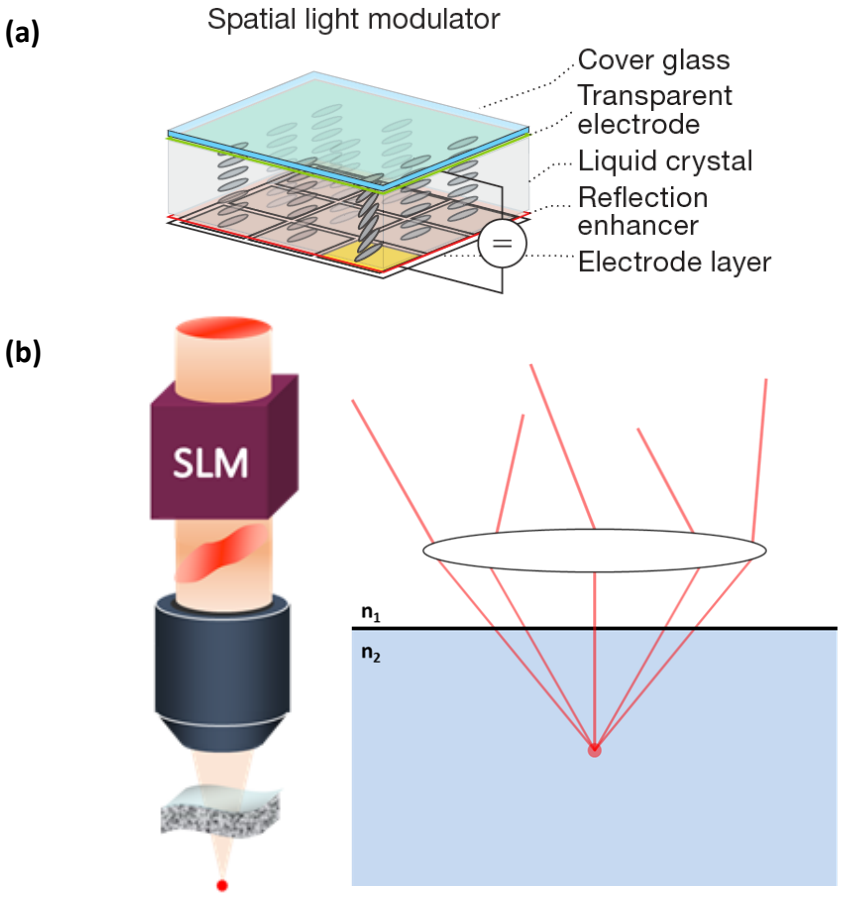


Figure 5.4. Adaptive optics elements for aberration correction. (a) A schematic of a LC spatial light modulator (SLM). (b) An illustration of the flat wavefront propagating through the adaptive optics element (SLM) which introduces equal and opposite phase aberrations to those induced by the glass substrates of the LC device. The corrected (conjugate phase) wavefront focused by the lens into the LC device cancels out the aberrations induced by the thick glass substrate, thereby restoring the diffraction-limited focus within the thin LC layer.

Spherical aberrations are modelled as phase variations in the pupil of the objective lens. Introducing equal but opposite phase aberrations with the aid of an appropriate correction element can therefore compensate for the phase variations induced by the thick glass substrates of the LC device. A LC phase-only nematic spatial light modulator (SLM) enables adaptive beam-shaping and is well suited to correct for aberrations in optical systems. SLMs are often used in research applications, specifically in micro- and nano-fabrication, optical trapping (tweezers) and optical data

storage [14]. Figure 5.4 (a) shows a schematic of a SLM; each pixel in the device is controlled with an applied voltage to create a high resolution hologram. Light reaching the SLM is reflected onto the pupil plane (Fourier plane) of the objective lens with the aid of a reflection layer incorporated within the device. The projected hologram can be adapted dynamically during fabrication to alter the ellipticity and orientation of the focused light, as well as to vary the writing power of the laser. The SLM can also incorporate flatness correction through a corrective phase pattern in order to compensate for its uneven surface. Figure 5.4 (b) shows an incoming flat wavefront entering the SLM adaptive optics element, which outputs the corrected (conjugate phase) wavefront that is cancelled out by the spherical aberrations when subsequently focused into the device by the objective lens. The use of a SLM in conjunction with direct laser writing enables aberration correction in-situ that consequently restores the diffraction-limited focus and system resolution [14].

5.2.3. In-Situ Fabrication System

Figure 5.5 shows a schematic of the custom-built DLW system. The light source was a Titanium Sapphire oscillator, emitting 100 fs laser pulses at λ = 790 nm, with a repetition rate of 80 MHz and a maximum power of 300 mW. Another laser mode is also available in the form of a regeneratively amplified beam with a lower repetition rate of 1 kHz; the high repetition rate oscillator beam was used throughout the investigation, unless otherwise stated (cf. §5.4.1). The beam is expanded and directed onto the phase-only nematic LC SLM (Hamamatsu X10789-02) which is subsequently imaged in a 4f configuration onto the back aperture of the focussing objective lens for aberration correction. The 4f system consists of a telescope with finite conjugates one

focal distance to the left of the objective lens (left of pinhole) and one focal distance to the right of the collector lens (right of pinhole), consisting of a cascade of two Fourier transforms. A built-in CCD camera permits imaging during fabrication, while the device is illuminated by a red LED ($\lambda = 635$ nm).

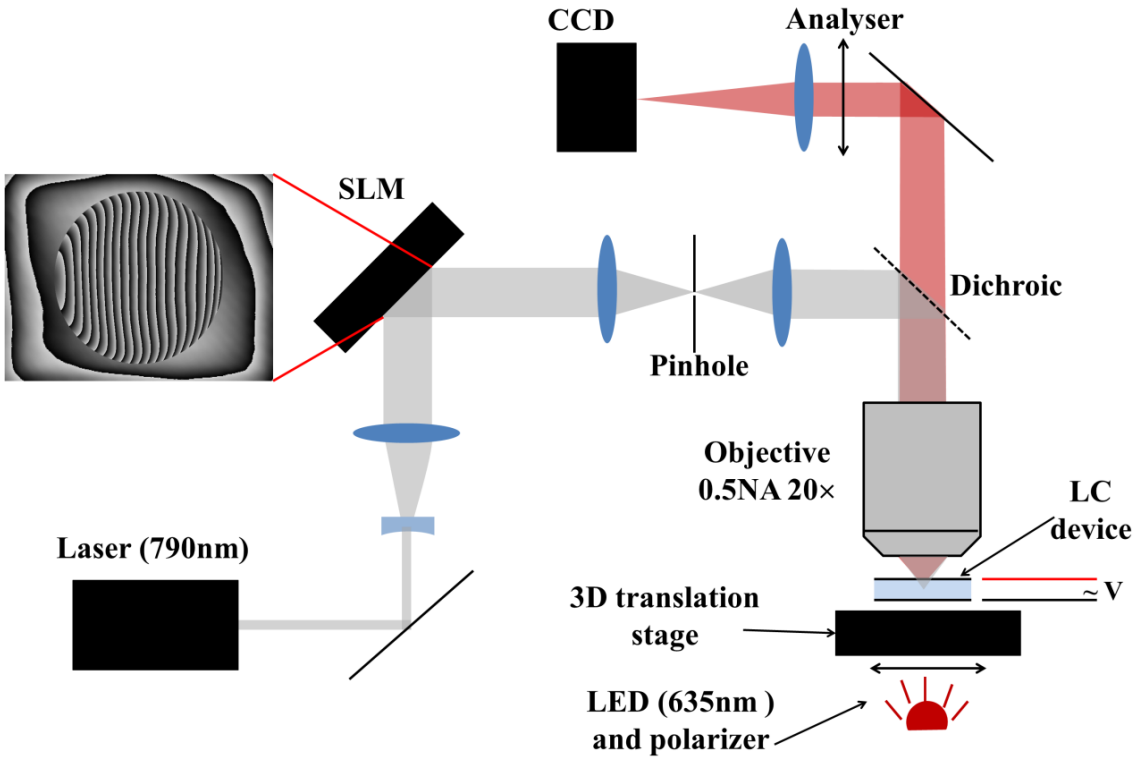


Figure 5.5. In-situ DLW optical set-up. The TPA-based fabrication system with a SLM as the adaptive optics element. Ultrafast pulses of laser light are transmitted through various optical components, reaching a blazed phase grating that is projected onto the SLM to correct for aberrations in the sample due to the refractive index mismatch between the device's thick glass substrates and the LC layer. A 0.5 NA objective lens is also used to fabricate structures at submicron resolutions and a red LED is used to illuminate the sample so that it can be monitored during the fabrication procedure.

An example of a hologram projected onto the SLM is shown in Figure 5.5, in which the background phase profile corrects for aberrations. A blazed phase grating of period 0.5 mm (25 pixels) is displayed on the SLM that redirects the incident laser beam, and ensures the maximum diffraction of light into the first order. It is worth noting that the writing focus must be a diffracted order of light to avoid interference effects with unmodulated light from the SLM [15]. Reducing the modulation depth (from 2π) enables the adjustment of the writing power, wherein a smaller proportion of light is directed to the first order and hence to the objective [16]. A pinhole, which was positioned in the Fourier plane of the SLM, only passed light that was steered by the SLM grating, blocking the zeroth order of diffracted light.

5.3. EXPERIMENTAL PROCEDURE

5.3.1. Materials & Sample Preparation

The photo-polymerizable mixture used in this investigation consisted of 69 wt. % of the nematic LC host, E7 (Merck Chemicals, Ltd.), 30 wt. % of the reactive mesogen RM257 (Merck Chemicals, Ltd.) and 1 wt. % of the photoinitiator IRG819 (Merck Chemicals, Ltd.). The LC host material was chosen as it exhibits a nematic phase at room temperature and it has a positive dielectric anisotropy such that the LC molecules align along the direction of an applied electric field. The nematic LC host has a birefringence of $\Delta n = 0.219$ at $\lambda = 632.8$ nm and a dielectric anisotropy of $\Delta\varepsilon = 13.7$ at 1 kHz at a temperature of $T = 20°C$. It is also possible to estimate whether TPA yields a sufficient number of free radicals from the photoinitiator molecule Irgacure 819

(IRG819). The probability for one photoinitiator molecule to be excited during one laser pulse can be estimated by [17]

$$p_{(\mathrm{abs})} = \frac{1}{2}\tau_{\mathrm{pd}}\sigma_{\mathrm{TPA};\lambda}\phi^2 \tag{5.2}$$

where τ_{pd} is the pulse duration, $\sigma_{\mathrm{TPA};\lambda}$ is the TPA absorption cross-section at the incident wavelength λ and the photon flux is $\phi = E_p/(\tau_{\mathrm{pd}} A_{\mathrm{f}}\, E_{\mathrm{ph}})$; the lateral area of the laser focus $A_{\mathrm{f}} = \pi$ (0.8 μm)^2 using the 0.5 NA objective lens, the pulse energy $E_{\mathrm{p}} \approx$ 1.3 nJ and the photon energy $E_{\mathrm{ph}} = hc/\lambda$. The photoinitiator molecule IRG819 has a peak TPA absorption cross-section of $\sigma_2 = 5 \times 10^{-50}$ cm^4 s [17]. The TPA absorption cross-section at λ ~ 790 nm can be estimated from the one-photon excitation spectrum [17] assuming that its shape is similar at λ/2 then, $\sigma_{\mathrm{TPA;790nm}} \approx (\sigma_{\mathrm{1PA;395nm}}/\sigma_1) \cdot \sigma_2 =$ 3.75×10^{-51} cm^4 s. Using these parameters, the probability for one photoinitiator molecule to be excited during one pulse is only ~0.13%. However, for a high repetition rate of 80 MHz and a typical exposure time of t_{ex} = 30 ms, the photoinitiator is exposed to >2 million pulses, generating >1000 excitation events per molecule assuming instantaneous decay back to the ground state. Thus, it is reasonable to assume that there will be a sufficient number of free radicals arising from the chemical bond breaking process to initiate cross-linking,.

The LC cells presented in this work were initially capillary-filled on a hot-plate at T = 80°C, when the photosensitive mixture was in the isotropic phase. After cooling to room temperature, the devices were mounted on an *xyz*-translation stage (Aerotech ABL10100) of the DLW set-up and connected to an arbitrary waveform generator for the application of an external voltage. The translation stage offers high precision motion over 100 mm in the *x* and *y* directions, and 3 mm in the *z* direction, moving relative to

the focus of the laser beam during fabrication. A 20× Zeiss objective lens with a 0.5 NA was used throughout the investigation, unless otherwise stated. The NA of the objective lens and the refractive index of the host LC material ($n \sim 1.5$) provide estimates of the resolution of the DLW fabricated structures using the relations in (5.1): $\Delta(x, y) = 0.8$ µm and $\Delta z = 7$ µm. The devices were characterized on an optical polarizing microscope (OPM) between crossed polarizers at room temperature. A UV-filter was inserted above the bulb of the microscope and device characterization was carried out in a dark room to prevent residual polymerization in the bulk (see §4.2.2 for further details).

5.3.2. Optical Realignment Effects

To begin with, optical realignment effects were investigated by writing polymer structures that lock-in the birefringence associated with different LC alignments. A series of polymer walls were written into a 5 µm-thick, planar (parallel rubbed) nematic pi-cell filled with the LC – monomer mixture under a range of applied electric field strengths (0 V/µm, 0.4 V/µm, 0.8 V/µm, 1.2 V/µm, 1.6 V/µm). The walls were formed by translating the device through the laser focus at a speed of 25 µm/s and under continuous exposure to the femtosecond pulsed laser beam with an average power of P_{av} = 30 mW arriving at the device. A set of three walls were fabricated at each electric field strength with the writing laser beam being either circularly (CP) or linearly polarized (parallel (LP_{II}) and perpendicular ($LP_{\perp}$) to the fabrication direction, to investigate whether any optical realignment of the LC director takes place during the polymerisation process.

The OPM image on the left of Figure 5.6 was taken when the device was heated to the isotropic phase at T = 80°C. Evidently, the walls remain visible when the device is

oriented in the bright state (45°) between crossed polarizers, revealing that the polymer structures display a degree of birefringence that changes according to the amplitude of the electric field that was applied to the device during laser writing. At 0 V/µm, the director field is in the splayed ground state (c.f. §3.1.4 for a detailed discussion of the different voltage-dependent states in a nematic pi-cell device). Thus, the polymer walls written at E = 0 V/µm retain the planar splayed alignment such that the components of orthogonally polarized light propagating through the device experience the maximum birefringence associated with the planar aligned director at this device orientation. The director field in the bulk tends to align perpendicular to the glass substrates under the application of an electric field and remains planar at the cell surfaces due to the surface anchoring. Thus, polymer walls written at higher electric field strengths become less distinct as the birefringence of these higher LC states decreases. The voltage-dependent LC states (0 V, ±2 V, ±4 V, ±6 V, ±8 V) are recovered upon subsequent cooling to room temperature, as seen in the OPM image on the right of Figure 5.6.

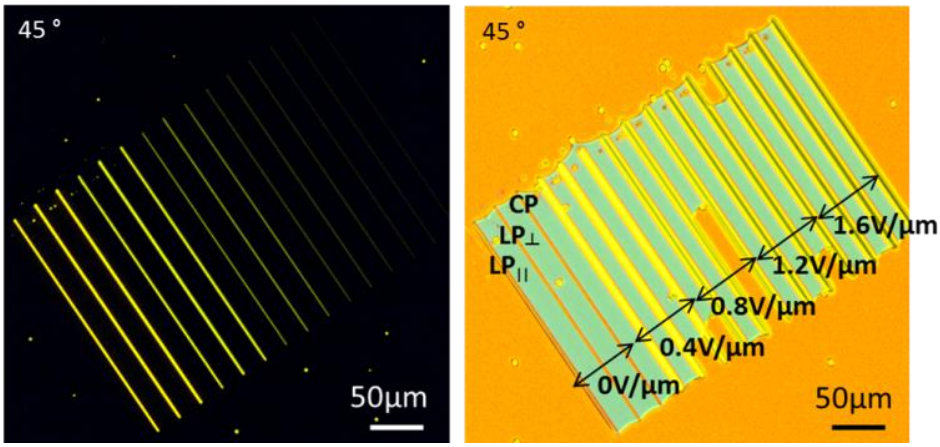


Figure 5.6. Voltage-dependent birefringence and optical realignment in a nematic pi-cell. OPM images of polymer walls fabricated under different electric field strengths (shown in the right hand Fig.), and subsequently heated to the isotropic phase (left) at T = 80°C before cooling to room temperature (right), when the device is oriented in the bright state (45°) between crossed polarizers.

The results in Figure 5.6 show that walls fabricated with different polarizations of light are relatively indistinguishable from one another, which suggests that the amplitude of the electric field component of the laser is not large enough to distort the LC alignment during fabrication. This can also be demonstrated analytically by considering the pulse as a spatial bell-shaped Gaussian profile, and using the following relation to estimate the intensity [18];

$$I_p = 2E_p/\tau_{pd}\pi {w_0}^2 \tag{5.3}$$

where the beam waist, $w_0 = 0.61\ \lambda / \mathrm{NA} = 0.96\ \mu m$, is a measure of the beam size at the focus (based upon the Rayleigh criterion for a diffraction-limited system). Substituting values for the pulse duration (τ_{pd} = 100 fs) and energy (E_p = 1.3 nJ) into (5.3) gives $I_p \sim 1$ TW/cm^2. This value provides an estimate of the intensity at the peak of the Gaussian pulse rather than that reaching the device over one duty cycle. Modifying the expression in terms of the average laser power reaching the device ($P_{av} \sim 30$ mW) at the focal spot, $I_{av} = 2P_{av}/\pi {w_0}^2$, this relates to an average intensity of $I_{av} \sim 2$ MW/cm^2.

The intensity can also be expressed in terms of the laser field from the time-averaged Poynting vector of the beam;

$$I = \tfrac{1}{2} \cdot c / n \cdot \varepsilon_0 \varepsilon_r E^2 \tag{5.4}$$

where c is the speed of light, n is the refractive index of the medium, ε_0 is the dielectric permittivity of a vacuum and ε_r is the relative permittivity (approximated to n^2). Thus, the average intensity (2 MW/cm^2) calculated from (5.3) provides an estimate of the electric field strength in the plane of the device as E ~3.2 V/μm.

The dielectric anisotropy arising from the polarizability anisotropy at optical frequencies is much lower than that observe for an applied frequency of 1 kHz (Δε

(1kHz) = $\varepsilon_{\parallel} - \varepsilon_{\perp}$ = 13.7 whereas Δε (optical) = $n_{\parallel}{}^2 - n_{\perp}{}^2$ = $1.738^2 - 1.519^2$ = 0.713). Yet, due to the large electric field component incident from the laser beam (~3.2 V/μm), the resultant dielectric torque (proportional to $\varepsilon_0 \Delta\varepsilon E^2$) is more than three times greater than that imposed by the smallest applied electric field used in Figure 5.6 (E ~ 0.2 V/μm).

Overall, the theoretical arguments provided above suggest that it is reasonable to expect some optical realignment from the laser field. However, the experimental data in Figure 5.6 shows that the optical reorientation may be approximated to a minor perturbation with respect to the alignment induced from the applied electric field. Thus, for the purposes of this study, optical realignment effects will be assumed to be negligible.

5.4. POLYMER NETWORK STRUCTURES

5.4.1. Pillar Arrays

To investigate the structuring of LC-polymer networks into different arrays, two-dimensional square and hexagonal lattices of polymer pillars were engineered in a 20 μm-thick nematic pi-cell LC device. Arrays of pillars have previously been created in photoresists that are subsequently treated to induce certain alignments of the LC director post-fabrication for the generation of bi-stable states in displays [19]. Epitaxial assembly has also been employed for the formation of more complex LC phases [20]. However, such methods are unable to exploit the different director profiles that occur within a LC device under different applied electric field strengths.

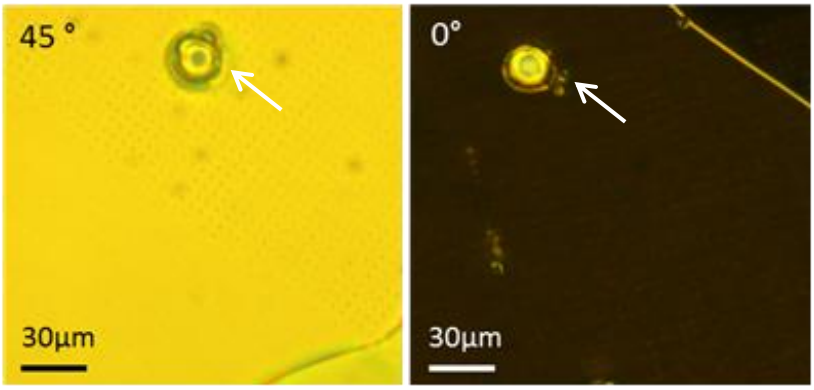


Figure 5.7. A square-shaped pillar array. OPM images of a pillar array fabricated in the absence of an electric field, taken between crossed polarizers in the bright (45°) and dark (0°) states of the LC device. The white arrows indicate the position of the spacer bead that controls the 20 µm-cell thickness.

The custom-built DLW system described in §5.2.3 has the capability to 'lock-in' voltage-induced alignments of the LC director within the polymer networks. In the example provided here, square and hexagonal arrays of polymer pillars were fabricated at 5 µm spacings, with the sizes of the individual pillars dictated by the size of the focal spot of the laser (~1 µm). The pillars were written sequentially using a 30 ms gate open time on the mechanical shutter, with one pillar corresponding to one exposure (> 2 million pulses) of the ultra-fast laser.

The OPM images in Figure 5.7 show the bright and dark states of a square-shaped pillar array fabricated in the absence of an applied electric field, whereby the device is in its splayed ground state. Evidently, the polymer structures have had little impact on the surrounding LC alignment confirming that there is only a minor perturbation to the LC alignment from the laser field, which is consistent with the assumption of negligible optical realignment effects. Note that a spacer bead can be seen in the image (indicated by the white arrows), which is used to define the cell thickness (c.f. §1.5).

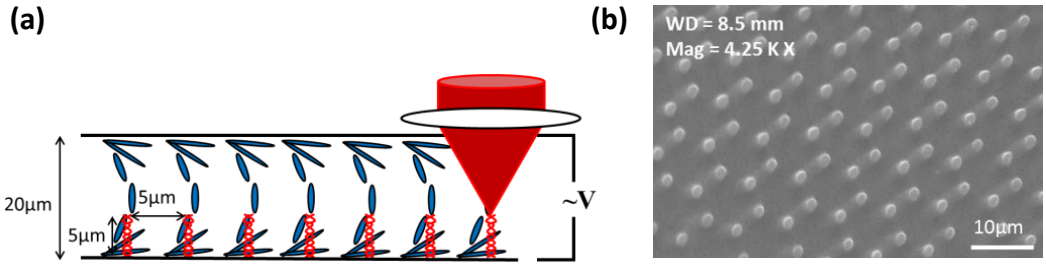


Figure 5.8. Fabricating pillar arrays. (a) An illustration of the fabrication of the polymer pillars in a 20 µm-thick, nematic pi-cell device under the application of an electric field of E = 0.4 V/µm. (b) an SEM image of a hexagonal-shaped pillar array.

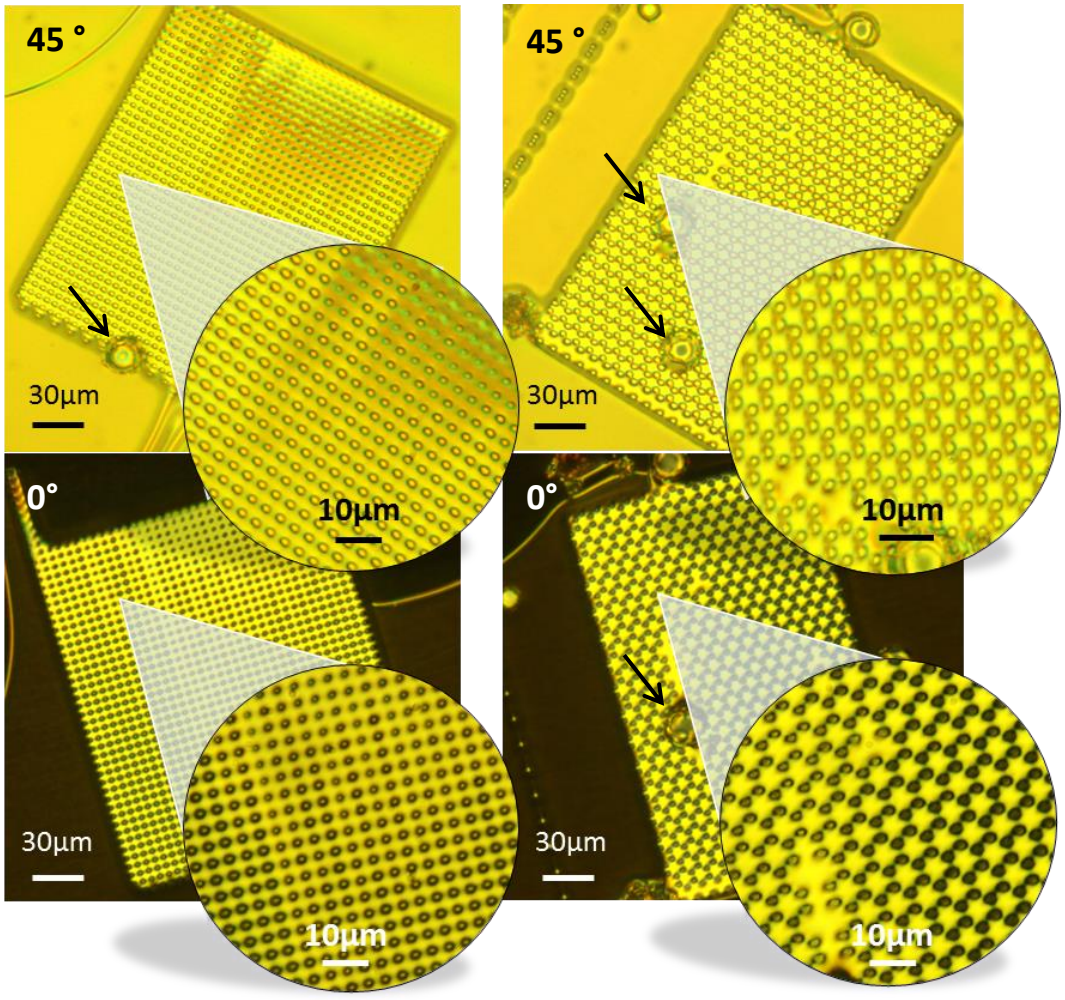


Figure 5.9. Square and hexagonal-shaped pillar arrays. OPM images of square and hexagonal shaped pillar arrays taken between crossed polarizers in the bright (45°) and dark (0°) states of a device, in the absence of an applied electric field. Spacer beads are indicated by the black arrows.

An array of polymer pillars fabricated in-situ under the application of a 0.4 V/µm electric field, where the molecules align in a bend configuration, is illustrated in the schematic of Figure 5.8 (a). In this case, the polymer network is expected to lock-in a hybrid (planar to homeotropic) director profile within the pillars, while the remaining regions are able to switch freely when subjected to different electric field strengths due to the absence of a polymer network. Scanning Electron Microscope (SEM) images such as that shown in Figure 5.8 (b) of the hexagonal shaped pillar arrays revealed the dimensions of the pillars to be ~1.5 µm in diameter and ~5 µm in height. SEM images were obtained by disassembling the substrate and superstrate, and coating the surfaces in a 27.5 nm-thick gold layer for imaging using a secondary electron detector. A 15 kV electron beam voltage was used at a working distance of 8.5 mm.

Figure 5.9 presents OPM images of square (left) and hexagonal (right) arrays in their dark and bright states at two different device orientations (0° and 45° to the crossed polarizers, respectively). The images were taken in the absence of an applied electric field. Evidently, the polymer network appears denser than the structures fabricated in the absence of an applied electric field seen in Figure 5.7. Changing the shape of the array does not appear to alter the LC alignment, but is a good demonstration of the versatility of the DLW fabrication suite. It is worth noting that the spacer beads (indicated by the black arrows) can appear larger than their actual size (20 µm here), since the pillars do not extend through the bulk of the cell so the microscope objective is not focused in the plane of the cell. In addition, the LC alignment can be distorted due to the presence of the spacer beads, which effectively act as defect sites that disrupt the continuity in the director profile. This misalignment however is localized in the vicinity of the spacer beads, as can be seen in the microscope images of Figure 5.9.

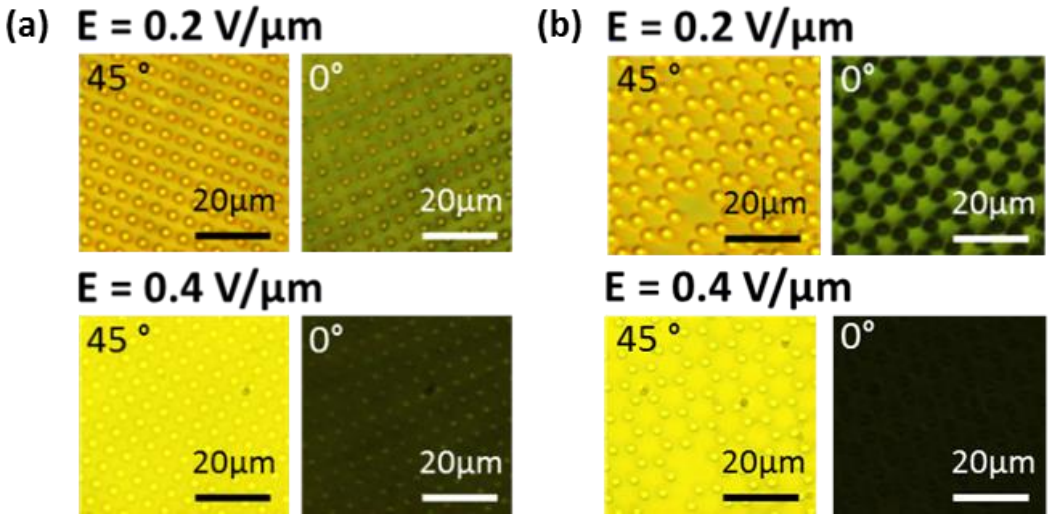


Figure 5.10. Electrically addressing square and hexagonal pillar arrays. A series of microscope images showing (a) the square and (b) the hexagonal shaped pillar arrays in a 20 µm-thick nematic pi-cell device oriented in its bright and dark states between crossed polarizers, for an applied electric field of E = 0.2 V/µm and E = 0.4 V/µm.

Figure 5.10 (a) and (b) are images of the dark and bright states for two different electric field strengths applied during the image capture. For most amplitudes of the electric field, the alignment in and around the pillars is clearly distinguishable from the surrounding regions of the device: the one exception being when the same electric field as that used during fabrication is applied to the LC device. In this case, when the LC device is subjected to an electric field of E = 0.4V/µm, the director alignment within the region defined by the pillars was the same as that observed for the surrounding regions, indicating that the polymer pillars had indeed frozen-in the director profile of the LC that was present during fabrication. In addition to voltage cycling, the polymer structures remain stable during heating through the nematic-isotropic phase transition.

The addition of a high resolution, adaptive optics element also permits parallel optical fabrication using the low repetition rate (1 kHz) regeneratively amplified beam, for the creation of larger arrays of polymer structures [21]. A holographic diffraction

grating is generated on the SLM that creates multiple focal spots simultaneously [21]. Aberration correction is also incorporated in the design, thus enabling fabrication in a fully assembled LC device under externally applied electric fields. Figure 5.11 (a) shows a schematic of the parallel optical fabrication process, whereby multiple focal spots are generated from the modulated wavefront that is subsequently focused through the objective lens. Figure 5.11 (b) shows an example of the hologram used to create 100 foci whilst simultaneously correcting for aberrations through the background phase profile, with the resultant fabricated pillar array shown in the OPM images of Figure 5.11 (c). Here, the pillars were written under the application of a 0.4 V/μm electric field strength.

The pillars formed using the regeneratively amplified beam reveal visibly distinct properties to those shown in Figure 5.9, which were written using the oscillator beam at the same electric field strength. Furthermore, the pillars in Figure 5.11 (c) do not remain stable during thermal cycling through the nematic-isotropic clearing point. This suggests that the regeneratively amplified beam does not fully initiate the polymerization process as observed with the oscillator beam, but rather modifies the LC alignment through a different mechanism. The total pulse energy here was measured to be 1100 nJ for all 100 foci, producing E_p ~ 11 nJ per pulse i.e. per pillar, which is significantly higher than the pulse energy from the oscillator beam (E_p ~ 1.3 nJ). As a result, the mechanism in which the pillars in Figure 5.11 (c) were created is likely to involve a combination of heating with some degree of polymerization, whereby some melting of the LC occurs during exposure to the regeneratively amplified beam. The lower density of polymer network in the pillars of Figure 5.11 (c) is therefore potentially due to localized melting and subsequent rapid cooling that freezes-in the

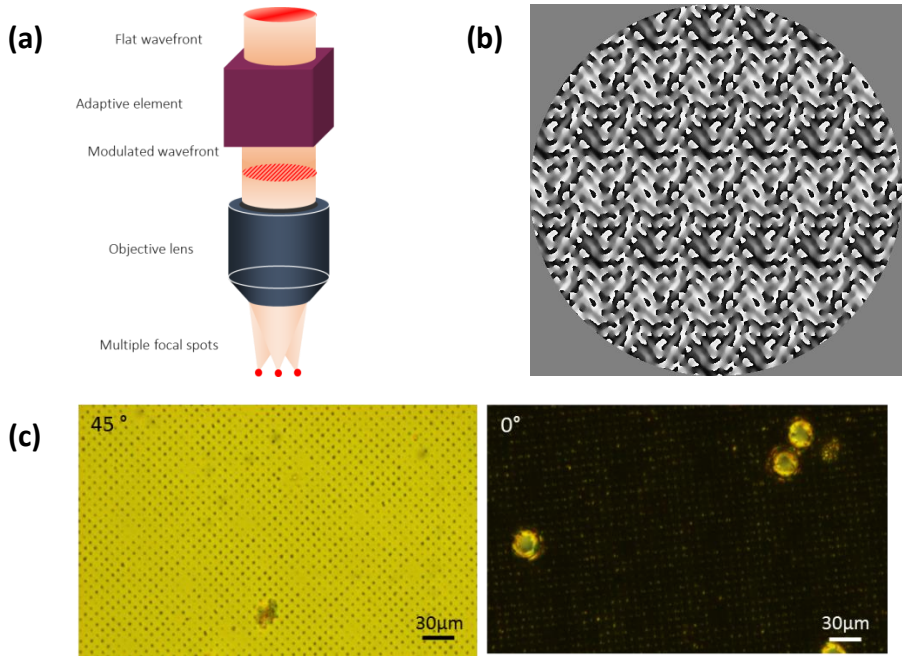


Figure 5.11. Parallel optical fabrication for the creation of large arrays of polymer pillars. (a) An illustration of the parallel optical fabrication process using a modulated wavefront produced by the SLM. (b) The hologram used for both aberration correction and parallel optical fabrication of large arrays. (c) OPM images of a 5 µm-spaced pillar array that was formed by parallel optical fabrication, showing the bright and dark states of the device when rotated between crossed polarizers.

higher-temperature state [5]. Therefore, despite the regeneratively amplified beam being useful in the creation of large polymer arrays, the mechanism by which the oscillator beam produces structures is better suited for the study of different birefringent LC-polymer structures associated with voltage-dependent LC states.

5.4.2. Disclination Networks

By applying an electric field during the laser writing process, it is also possible to create networks of disclinations directly within the LC device. Figure 5.12 shows a fabricated checkerboard-type polymer structure consisting of periodic walls that locked-in topologically distinct LC states. The device undergoes a disclination mediated transformation from the equilibrium H state to the V state under an applied electric

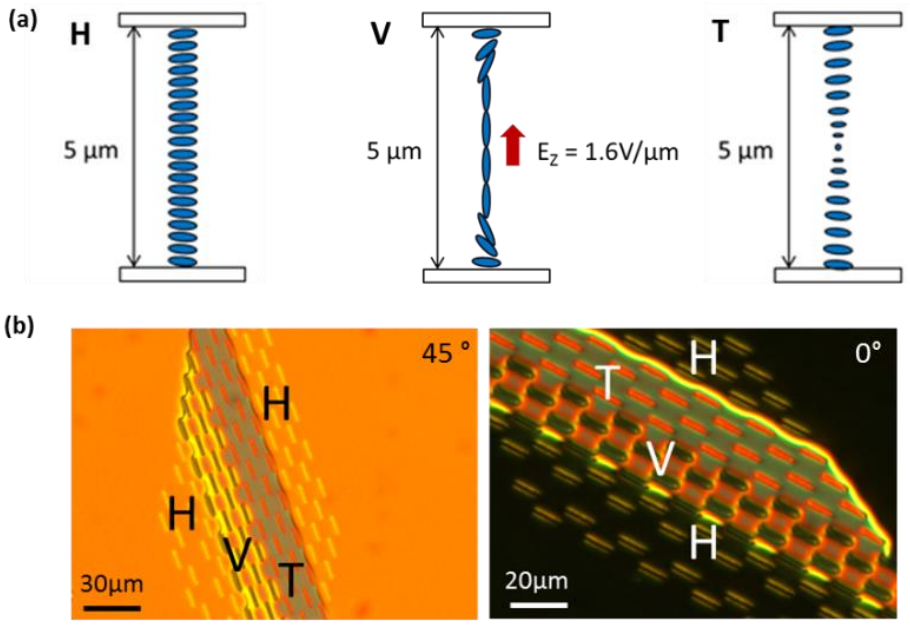


Figure 5.12. A network of disclination lines. (a) Illustrations of the splayed ground (H), bend (V), and twisted (T) nematic states of a pi-cell. (b) OPM images of the checkerboard-type polymer structure showing the bright and dark states of the 5 µm-thick, nematic pi-cell when rotated between crossed polarizers in the absence of an applied electric field.

field, as illustrated in Figure 5.12 (a) and outlined in §3.1.4, which then relaxes to the T state when the field is removed. The polymer walls, which extend through the bulk of the device from one substrate to the other, were written while the device was in each of these 3 states: specifically, the walls are 10 µm in length and spaced at 5 µm intervals. The resultant checkerboard-type structure can be seen in Figure 5.12 (b) in the absence of an applied electric field during image capture. The region of the structure labelled 'H' is continuous with the bulk alignment around the checkerboard pattern as it was written in the absence of an electric field and so there is no discernible difference between the region defined by the checkerboard and the surrounding region. The second region that was fabricated, labelled 'V' was written under an E = 1.6 V/µm electric field, which was sufficiently large to ensure that the entire device had been driven into

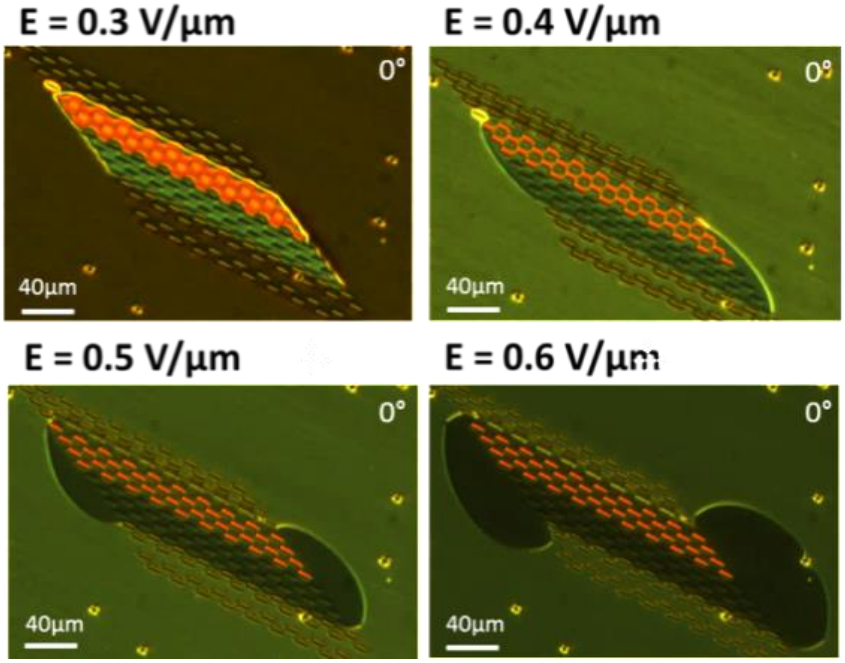


Figure 5.13. The nucleation of high energy disclination lines. The series of OPM images taken between crossed polarizers show the checkerboard-type structure in its dark state under increasing electric field strengths. The disclinations lines separate topologically discontinuous regions, with higher energy states nucleating at higher voltage amplitudes.

the V (bend) state such that the polymer network then captured that alignment during the fabrication process.

Subsequently, upon removal of the applied electric field, it is known that the bend state collapses into a transient twisted alignment (T) state [22 - 24]. Therefore, to capture and freeze-in the transient T state, the polymer network was formed before the device relaxed back to the ground (H) state. A final set of walls were then written once the device had returned to the H state (see Figure 5.12 (b)). Overall, the checkerboard pattern, therefore, consists of a series of polymer walls that were written at different electric field strengths, thereby locking-in topologically distinct director profiles, with a disclination loop separating the different regions. The close proximity of the polymer walls allows for the controllable introduction of disclination networks into a LC device.

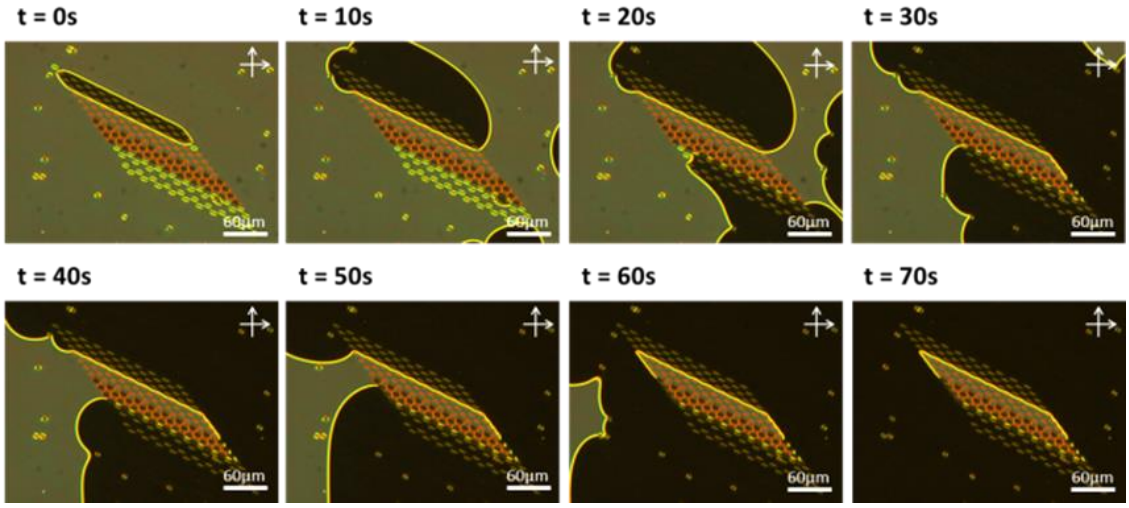


Figure 5.14. The relaxation of high energy disclination lines A series of microscope images showing the checkerboard-type structure in its dark state between crossed polarizers as the device relaxes back to its equilibrium state upon removal of a 1 V/µm applied electric field. The disclination lines separating the topologically distinct LC states diminish as the lowest energy splayed state is recovered after 70 seconds.

Figure 5.13 presents a sequence of OPM images captured post-fabrication as the device is addressed with an increasing electric field. As the electric field strength is increased, the bend state grows out of the polymer structures that were fabricated either in the bend (field on - V) or twisted (removal of field – T) states, as these are energetically equivalent due to their topological continuity.

Upon removal of a 1 V/µm electric field (t = 0 s), Figure 5.14 shows regions of the V state (bulk device) collapse into the transient T state, which can be seen from the continuity between the bulk nematic LC and the region that consists of polymer network that has locked-in the bend and twisted alignments. A domain wall forms around the topologically discontinuous line array that has locked-in the H state. Over time, the H state emanates from these structures written in the absence of an electric field (i.e. that have locked-in the H state) until the entire bulk relaxes to this lowest energy ground state (t = 70 s). In summary, the in-situ fabrication capability permits the control of disclinations separating energetically distinct states through the formation of polymer

networks in different LC states. The concept of controlling the size and shape of defects in nematic pi-cell devices is further explored in Chapter 7

5.5. CONCLUSIONS

A direct laser writing system combined with a high resolution adaptive optics element in the form of a spatial light modulator has been presented in this chapter. The in-built aberration correction facility restores the diffraction-limited focus at the liquid crystalline sample for in-situ fabrication. Polymeric structures can be engineered into a photo-polymerizable LC sample whilst simultaneously electrically addressing the device so as to access different director profiles.

Using this technique, is has been possible to demonstrate the fabrication of complex, multi-dimensional micron-scale polymer structures with a tuneable birefringence under the application of an electric field. An array of different fabricated structures has been presented, including two-dimensional arrays of polymer pillars and a polymer checkerboard that locks-in topologically distinct states to create a controllable disclination network. Collectively, these findings demonstrate the ability to create a complex spatial variation in the birefringence directly within a LC device that is on the micron-scale, opening up many new avenues in both soft matter physics and the DLW of photonic materials. The remaining chapters of the thesis will employ the in-situ fabrication technique to explore the creation of novel soft matter photonics based technologies, ranging from fast-switching photonics applications to the generation of novel electro-optic phenomena in the form of electrically tunable defects and voltage-induced invisibility.

5.6. REFERENCES

[1] S. Kawata, H.-B. Sun, T. Tanaka And K. Takada, *Nature* **412**, 697 (2001).

[2] J. Hohmann, M. Renner, E. Waller And G. Von Freymann, *Adv. Opt. Mater.* **3**, 1488 2015.

[3] M. Farsari And B. N. Chichkov, *Nat. Photonics*, **3**, 450 (2009).

[4] M. Malinauskas, M. Farsari, A. Piskarskas And S. Juodkazis, *Phys. Reports*, **533** (2013).

[5] K. Itoh, W. Watanabe, S. Nolte and C. Schaffer, *MRS Bulletin*, **31**, 620 (2006).

[6] R. Benninger and D. Piston, Curr. Protoc. *Cell Biol.* **59**, 4.11 (2013).

[7] C.-H. Ho, Y.-C. Cheng, L. Maigyte, H. Zeng, J. Trull, C. Cojocaru And D. Wiersma, *Appl. Phys. Lett.* **106**, 021113 (2015).

[8] C. Jisha, K.-C. Hsu, Y. Lin, J.-H. Lin, C.-C. Jeng And R.-K. Lee, *Cleo-Pr*, (2013).

[9] D. Mcphail, M. Straub And M. Gu, *Appl. Phys. Lett.* **87**, 091117 (2005).

[10] F. Serra, S. Eaton, R. Cerbino, M. Buscaglia, G. Cerullo, R. Osellame And T. Bellini, *Adv. Funct. Mater.* **23**, 3990 (2013).

[11] Z. Ji, X. Zhang, B. Shi, W. Li, W. Luo, I. Drevensek-Olenik, Q. Wu And J. Xu, *Opt. Lett.* **41**, 336 (2016).

[11] T.-P. Kao, K.-C. Hsu, C.-H. Hung, C.-Y. Tai And C.-C. Sun, *Oecc2010* (2010).

[12] H. Zeng, D. Martella, P. Wasylczyk, G. Cerretti, J.-C. Gomez Lavocat, C.-H. Ho, C. Parmeggiani And D. Wiersma, *Adv. Mater.* **26**, 2319 (2014).

[13] H. Zeng, P. Wasylczyk, G. Cerretti, D. Martella, C. Parmeggiani And D. Wiersma, *Appl. Phys. Lett.* **106**, 111902 (2015)

[14] M. Booth, *Phil. Trans. R. Soc. A.* **365**, 2829 (2007).

[15] P. Salter And M. Booth, *Opt. Exp.* **20**, 19978 (2012).

[16] P. Salter, A. Jesacher, J. Spring, B. Metcalf, N. Thomas-Peter, R. Simmonds, N. Langford, I. Walmsley And M. Booth, Opt. Lett. **37**, 470 (2012).

[17] T. Baldacchini, *Three-Dimensional Microfabrication Using Two-Photon Polymerization*, Elsevier, UK (2016).

[18] E. Gamaly, S. Juodkazis, V. Mizeikis, H. Misawa, A. Rode, W. Krolikowski, *Phys. Rev. B.* **81**, 054113 (2010)

[19] S. Kitson And A. Geisow, *Appl. Phys. Lett.*, **80**, 3635 (2002).

[20] Honglawan, D. Beller, M. Cavallaro, R. Kamien, K. Stebe And S. Yang, *Adv. Mater.* **23**, 5519 (2011).

[21] A. Jesacher and M. Booth, *Opt. Exp.* **18**, 21090 (2010).

[22] P. Brimicombe And E. Raynes, *Liq. Cryst.* **32**, 1273 (2005).

[23] P. Brimicombe And E. Raynes, *Appl. Phys. Lett.*, **89**, 031121 (2006).

[24] P. Bos And K. Koehler/Beran, *Mol. Cryst. Liq. Cryst*. **113**, 329 (1984).

6

FAST-SWITCHING PHOTONIC STATES

6.1. INTRODUCTION

6.1.1. The Tilt Angle

So far, there has not been widespread commercialisation of the fast-switching flexoelectro-optic (FEO) effect in the chiral nematic phase as the required LC state is notoriously difficult to align uniformly, resulting in a poor optical contrast ratio [1-4]. A solution to these alignment challenges would open up potential avenues for a fast-switching LC mode to be realised and may potentially enable field sequential colour generation thereby removing the dependency on colour filters. This could then lead to LCD screens with an improved brightness and colour gamut, or potentially lead to more advanced display technologies by resolving multiple images for the realization of multi-view autostereoscopic 3D displays [5].

In Chapter 4, a polymer templating method was implemented to stabilise the uniform lying helix (ULH) for observations of the FEO effect. The resultant degradation of the LC alignment and decrease in the FEO switching angle due to bulk polymerization highlighted the need to improve the alignment technique. In this chapter, periodic polymer structures are engineered in a chiral nematic LC device using the direct laser

writing (DLW) technique described in Chapter 5, both in the nematic and chiral nematic phases by virtue of the in-built adaptive optics permitting in-situ fabrication.

6.1.2. Periodic Anchoring

Initially proposed by Patel and Meyer [6], an alternative approach to stabilizing the ULH texture without polymerizing the bulk LC as shown in Chapter 4, involves introducing a set of defects or periodic distortions at the ULH/substrate interface. Komitov et al. [7] have reported the fabrication of periodic anchoring conditions using hard-contact photolithography to pattern a photoresist and stabilise the ULH texture in the presence of an applied electric field.

Weak homeotropic alignment has also been shown to give a lower energy ULH relative to the Grandjean texture. However, the degeneracy of the homeotropic anchoring and resultant rotational symmetry in the director, causes the lying helix alignment to collapse into focal conic domains. Carbone et al. [8] exploited this stable, low energy ULH texture occurring at the homeotropic substrate by breaking its rotational symmetry using two-photon absorption (TPA) laser scanning lithography to form periodic surface relief structures with a periodicity equal to the pitch of the bulk chiral nematic. In their study, the authors demonstrate a stable ULH even in the absence of an electric field, although fairly poor contrast is obtained between the bright and dark states of the device by commercial standards.

The ULH structure may also be aligned and stabilised through confinement in polymer channels. This has previously been implemented using holographic techniques such as Polymer Liquid Crystal Polymer Slices (POLICRYPS), but this can result in large areas of polymerised LC that inhibits the electro-optic performance of the device

[9]. The aim of the work presented in this chapter is to maintain the FEO performance while still aligning and stabilising the ULH through the creation of a periodic diffuse polymer network. DLW is used to selectively illuminate the LC layer to photo-activate the polymerisation. This can be done while a voltage, sufficient to unwind the helix, is applied across the device. Thus, regions of diffuse network may be formed thereby locking in a homeotropic alignment, allowing the ULH to form between the periodic polymer structures when the voltage is removed. Alternatively, polymer walls can be fabricated parallel and perpendicular to the helical axis once the ULH is formed using conventional annealing techniques. It is shown that devices prepared in this manner have the potential to enhance the observed FEO switching, relative to conventional bulk polymerization techniques that can inhibit the electro-optic effect. The advantages of writing in either the nematic or chiral nematic phases are also discussed in terms of the measured FEO response.

6.2. EXPERIMENTAL PROCEDURE

The commercial eutectic nematic LC mixture, E7, was used as the host material, which has a birefringence and dielectric anisotropy of $\Delta n = 0.219$ at $\lambda = 632.8$ nm and $\Delta\varepsilon = 13.7$ at 1 kHz, at a temperature of T = 20°C (see Table A.3 of the Appendix). The chiral nematic mixture consisted of 68.5 wt % E7, 4.1 wt % of the high twisting power chiral dopant, BDH1281 (Merck Chemicals Ltd.), 26.8 wt % of the reactive mesogen, RM257 (Merck Chemicals Ltd.) and 0.6 wt % of the photoinitiator, IRG819 (Merck Chemicals Ltd.) for absorption at UV wavelengths. The resultant pitch was estimated to be ~ 320 nm from measurements of the spectral width of the Bragg reflection band (c.f. §1.4.3.) and using the expression in (1.21). The polymer walls (for both chiral and achiral

nematic phases) were fabricated in two 5 μm-thick cells that have homeotropic alignment layers on the inner surfaces of the substrates along with indium tin oxide (ITO) layers so that the device can be electrically addressed. In addition, a third cell was used as a reference device for the FEO response detected before and after bulk polymerization. The three cells were capillary filled with the pre-polymerised-LC mixture in the isotropic phase, before being cooled to room temperature for fabrication.

For fabrication in the nematic phase, a cell was mounted on the *xyz*-translation stage of the DLW optical set-up and connected to an arbitrary waveform generator. Polymer structures were engineered within the LC layer while the device was addressed by a ± 42.5 V square wave (electric field strength, E = 8.5 Vμm^{-1}). This electric field strength was above the critical unwinding field, E_c ~ 7.1 Vμm^{-1} estimated from (1.10), whereby the dielectric coupling causes the helix to unwind as discussed in §1.3.1. The fabrication procedure commences once the entire device is driven into a uniform homeotropic alignment ($E > E_c$). The fabrication process of the polymeric walls with varying periodicities, using the 200 mW Ti:S laser across regions of 0.2 mm by 1 mm, can be seen in the schematic of Figure 6.1. Writing polymer walls that extend across the bulk of the device in the nematic phase are therefore expected to break the rotational symmetry of the homeotropic substrates and exploit the energetically favourable ULH state. A 20× Zeiss objective with a 0.5 NA and working distance of 2 mm was used to focus light into the LC devices. At a sample translation speed of 150 μm/s, the laser power was varied in-situ until narrow and uniform polymer walls were formed (by observation on the built-in CCD), which correlated to an optimum power of 75 mW.

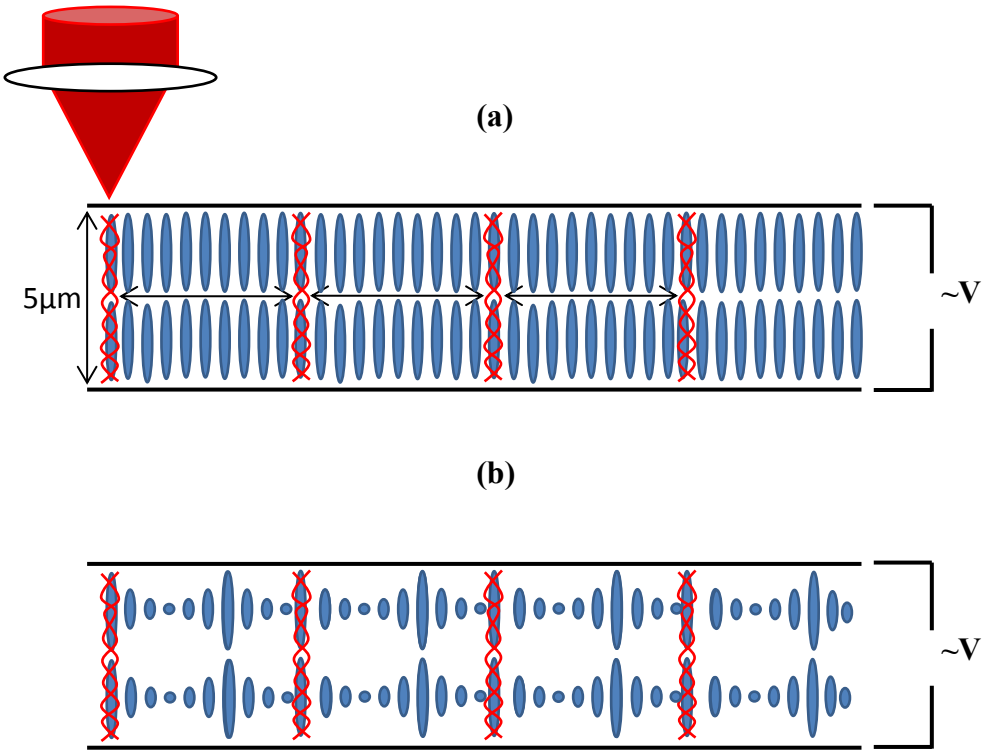


Figure 6.1. Polymer structuring in the nematic phase. A schematic of the fabrication process showing the formation of the polymer network structures while the chiral nematic LC device with homeotropic boundaries is initially in the nematic phase (a), whereby light from the laser is used to write periodic polymer walls of varying periodicities under the application of an external electric field and at an optimal writing speed of 150 µm/s. (b) The energetically favourable ULH alignment forms in the chiral nematic phase upon reduction of the applied electric field, whereby the helical axis tends to lie down in between the homeotropic polymer walls.

For fabrication in the chiral nematic phase, polymer structures were engineered in the second 5 µm-thick homeotropic device after a ULH had been initially formed through annealing under the application of a ± 27.5 V square wave. Upon cooling to room temperature, the sample was then mounted on the *xyz*-translation stage of the DLW set-up. Polymeric walls were engineered parallel and perpendicular to the helical axis whilst maintaining the applied electric field.

For comparison with the structured network, a 'reference' ULH was also formed by bulk polymerization using the annealing technique discussed in Chapter 4. The 5 µm-

thick cell was filled with the same chiral nematic LC-monomer mixture and cooled to room temperature under the application of a ± 27.5 V square wave. The sample was then UV-cured by exposure to a mercury vapour lamp at a distance of 10 cm, emitting at λ = 365 nm and at a power density of 185 mW cm^{-2}, for 12 seconds.

Optical polarizing microscope (OPM) images were taken of the devices containing the structured polymer networks and the electro-optic responses were measured from all three devices (before and after bulk polymerization in the case of the reference cell). Tilt angles related to the FEO effect from the formalism in (4.11) were then obtained using the transmission measurements described in Chapter 4, under the application of a ± 27.5 V square wave. Relatively large electric field strengths are required to detect significant transmission modulation amplitudes in the photodetector on account of the high concentration of reactive mesogen in the chiral nematic LC-monomer mixture. The electric field applied to measure the FEO response (5.5 $V\mu m^{-1}$) is well below the critical electric field required to unwind the helix (>7 $V\mu m^{-1}$), yet high enough to obtain a measurable response from the device polymerized in the bulk. A 20× objective lens was used to focus onto an equivalent area in each device and a constant intensity of light from the microscope's halogen bulb was used to illuminate the samples, in order to accurately compare the electro-optic behaviour of the different devices. A UV-filter was also included in the microscope to prevent further polymerization in the bulk by exposure to the bulb (see Figure 4.2 for the transmission spectrum).

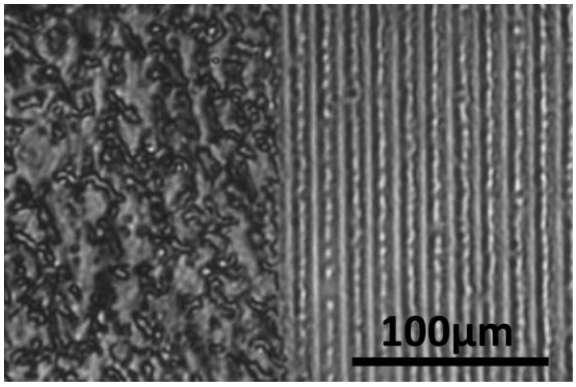


Figure 6.2. Chiral nematic fingers. Image taken between crossed polarizers on the optical microscope of the DLW set-up after the TPA fabrication process (100 fs pulses at λ = 790 nm with a power of 75 mW and a repetition rate of 80 MHz) of the polymer walls in a 5 µm-thick homeotropic device filled with the chiral nematic LC-monomer mixture. The device, with an electrode area of 1 cm^2, shows the formation of chiral nematic fingers (bright stripes) in between the homeotropic polymer walls (dark stripes), while the surrounding LC regions appear to be a focal conic texture (random alignment of the helices).

6.3. RESULTS & DISCUSSION

6.3.1. Homeotropic Polymer Walls

Polymer walls of ~1 µm thickness were engineered at varying periodicities in the nematic phase of the chiral nematic LC device. Figure 6.2 shows an example image of the polymer structures taken between crossed polarisers using the built-in optical microscope of the DLW experiment. As the electric field is gradually wound down into the chiral nematic phase, regions between the walls show the formation of chiral nematic fingers, with good optical extinction between crossed polarisers. In contrast, the remaining areas of the device that do not consist of the periodic polymer walls (left of the image) indicate that a focal conic texture has been formed in these regions.

The polymer walls appear dark between crossed polarisers, suggesting that the nematic director has indeed been 'locked-in' to a homeotropic alignment by the polymer network. This is because the polymer walls were fabricated in the homeotropic nematic

state with the application of an electric field that was greater than that required to unwind the helix of the chiral nematic phase. Additionally, it is unlikely that the dark stripes visible in Figure 6.2 could be an indication of the isotropic phase (potentially due to the LC being melted during the fabrication process) as any LC would flow into such regions. The formation of arrays of polymer walls is also supported by Scanning Electron Microscopy (SEM) images. After characterization was complete under the microscope, the substrate and superstrate were disassembled, and coated in a 27.5 nm-thick gold layer for SEM imaging using a secondary electron detector. A 15 kV electron beam voltage was used at a working distance of 17.5 mm. An example image for one particular periodicity is shown in Figure 6.3 with polymer walls that appear to be ~ 2 µm thick and spaced at 10 µm.

Figure 6.4 shows OPM images of the polymer LC structures with 10 µm, 7.5 µm, 5 µm and 2.5 µm periodicities taken between crossed polarizers. All the structures remained stable upon removal of the externally applied electric field and during thermal cycling through the isotropic-chiral nematic phase transitions.

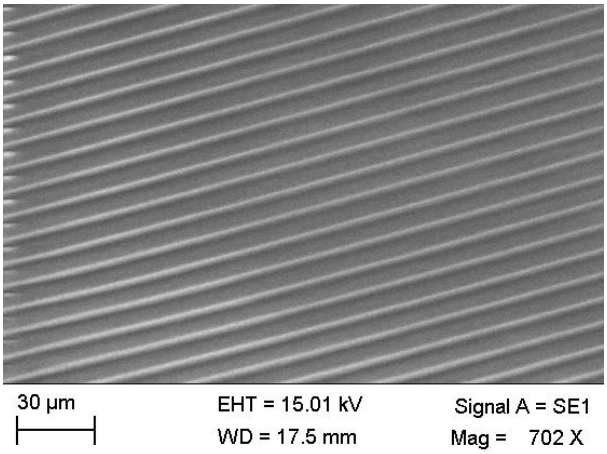


Figure 6.3. Periodic polymer walls. SEM image obtained from the disassembled polymer walls device that was coated in 27.5 nm-thick gold layer. A secondary electron detector was used at an electron beam voltage of 15 kV and a working distance of 17.5 mm. The image shows periodic polymer walls (bright stripes) fabricated by the DLW process.

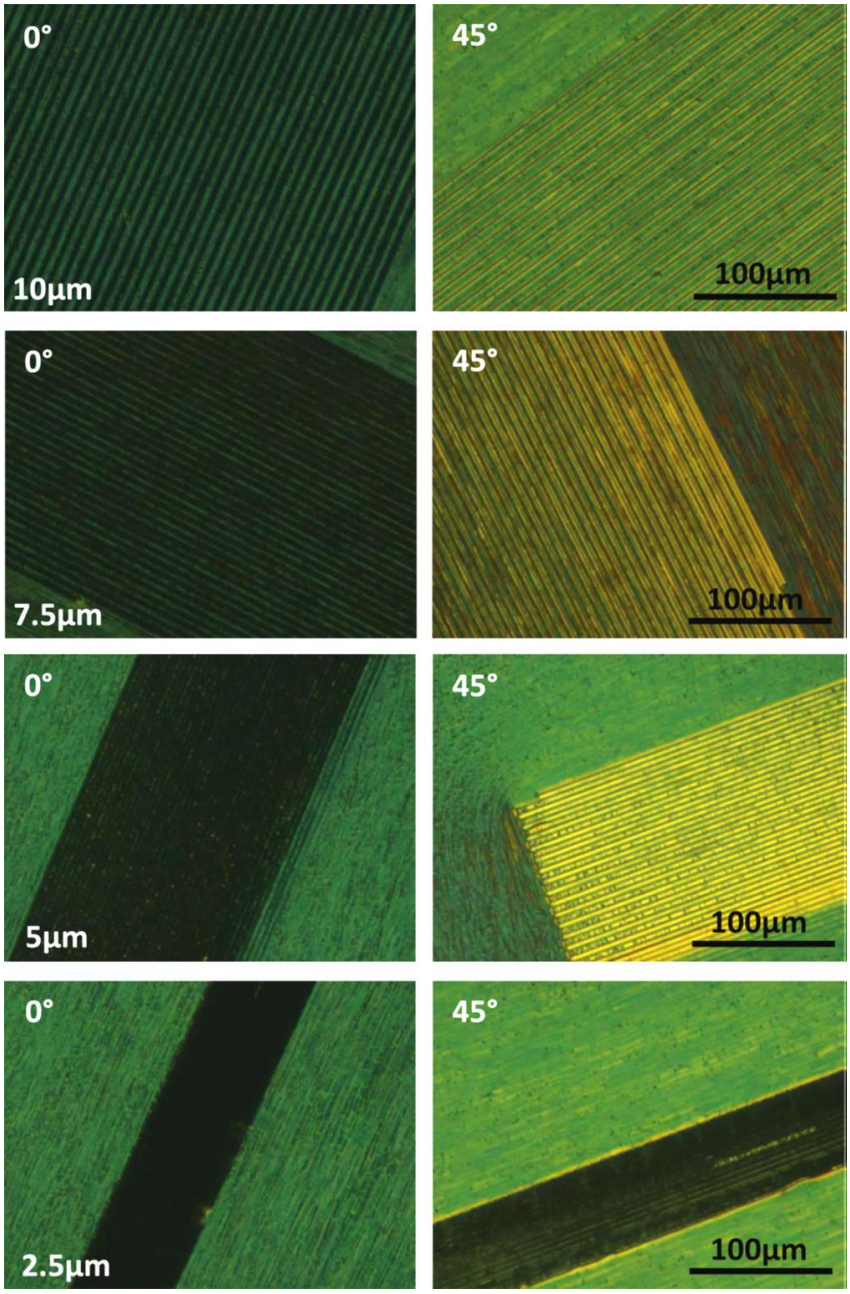


Figure 6.4. Varying the periodicity of the polymer walls. OPM images taken between crossed polarizers at optical extinction (0°) and maximum transmission (45°) of the devices with polymer walls spaced at 10 µm, 7.5 µm, 5 µm and 2.5 µm. The structures were fabricated in a 5 µm-thick homeotropic device filled with the chiral nematic-monomer mixture. The devices, with an electrode area of 1 cm^2, show homeotropic polymer walls (dark stripes) separated by channels of chiral nematic LC (bright stripes), while the surrounding LC regions appear to be a focal conic texture (random alignment). An improvement in the LC alignment can be seen as the spacing of the structures is decreased to be on the order of the device thickness.

The regions of LC or ‘microchannels’ between the 10 μm-spaced polymer walls show poor contrast between the dark and bright states, where the device is angled at 0° and 45° to the analyser, respectively. There appears to be some alignment in regions near to the homeotropic polymer walls, however, the focal conic texture dominates throughout the relatively wide microchannels (double the cell thickness). Decreasing the spacing between the polymer network structures to 7.5 μm shows a marked improvement in the ULH alignment as well as the contrast between the two states. However, there still remains some focal conic alignment in the central regions of the channels suggesting that the anchoring from the homeotropic walls is not strong enough to retain the ULH alignment over channels of this width. Optimum contrast (relative to the larger periodicities shown in Figure 6.4) is observed between the bright and dark states at a periodicity of 5 μm, whereby the ULH state dominates most of the regions between the polymer walls. When the periodicity is decreased even further down to 2.5 μm little to no transmission is observed in the bright state, suggesting that the polymer network has diffused across the microchannels and locked-in the homeotropic molecular alignment everywhere.

The Berek compensator method was used to reveal the orientation of the helical axis [10]. A quarter waveplate (λ/4) is inserted into the microscope intermediate tube with its optic axis at 45° to the polarizers, with the device oriented in the bright state between crossed polarizers. The compensator plate tilt adjustment dial is then rotated and a relative phase shift is accumulated as the polarized light propagates through the birefringent LC device and the compensator. For a known refractive index and device thickness, the Michel-Levy Interference Chart [11] is used in conjunction with the compensator to assess whether the phase shift correlates to an increase or decrease in

the birefringence. For a nematic LC, an increase in the birefringence corresponds to the LC optic axis being oriented parallel to the waveplate. In the case of a chiral nematic LC where the effective birefringence is perpendicular to the helix, a decrease in the birefringence results when the LC optic axis is parallel to the waveplate. The helix was found to be perpendicular to the 5 μm-spaced polymer walls.

Although the 5 μm-space channels produce the best alignment, all the periodicities indicate that the alignment of the chiral LC molecules in the nematic phase combined with the nematic reactive mesogens appears to encourage the helix axis to lie in the plane of the device near to the polymer walls. Additionally, Figure 6.4 reveals that the polymer network is prone to some diffusion irrespective of the wall periodicities. The walls can be interpreted as sparsely cross-linked polymer chains that are partially diffuse across the microchannels thus encouraging the helix to lie in the plane across the rest of the channel. Nevertheless, the SEM image in Figure 6.3 appears to show that, even though there is some diffusion, the walls are quite well defined (estimated to be ~1 μm in width on the OPM image, but appear to be closer to ~2 μm from the SEM image).

In the case of a short pitch chiral nematic LC with a pitch P = 320 nm, walls with a periodicity of 2.5 μm results in approximately 7 pitches of the helix between each set of walls. For this periodicity however, the network is sufficiently dense between the lines of the walls leading to homeotropic nematic alignment of the LC everywhere. This result indicates that the network diffuses roughly 1 - 2 μm either side of the polymer walls. A 5 μm periodicity leads to the formation of approximately 14 pitches of the helix between the walls and generates a well-aligned ULH since the gap between the polymer walls is large enough for the chiral nematic phase to form. However, increasing the periodicity further incorporates random orientations of the helical axis within central

regions of the channels. Thus, the boundary conditions imposed by the homeotropic polymer walls become less effective at wall separations greater than the order of the device thickness.

6.3.2. Electro-Optic Response

The electro-optic responses from the ULH state under the application of a ± 27.5 V square wave are shown in Figures 6.5 (a) and 6.5 (b) before and after bulk polymerization, respectively. Weak modulation in the transmission is detected through the bulk polymer-stabilised device; an initial pre-cure tilt angle of φ = 3.35°, measured using the device rotation method described in §4.2.5, falls to φ = 0.13° after polymerization. This substantial reduction in the switching angle is also accompanied by a fall in the LC response time, from τ = 100 μs before curing to τ = 12 μs after polymerization in the bulk. Faster switching times result from the hindrance of the LC molecules that are locked-in by the polymer network; lessening the switching angle under an applied oscillating field decreases the overall time taken to switch between each polarity reversal. In contrast, Figure 6.5 (c) shows that the fabrication of the polymer walls does not reduce the tilt angle by as large an amount (φ = 1.73°) when compared with that observed for bulk polymerization of the ULH alignment (φ = 0.13°) under the same voltage application. Furthermore, the formation of these polymer walls ensures that the ULH alignment spontaneously recovers upon thermal cycling across the isotropic to chiral nematic phase transition.

The OPM images presented in Figure 6.4 showing the bright and dark states of the device combined with the electro-optic data presented in Figure 6.5 (c), suggest that the

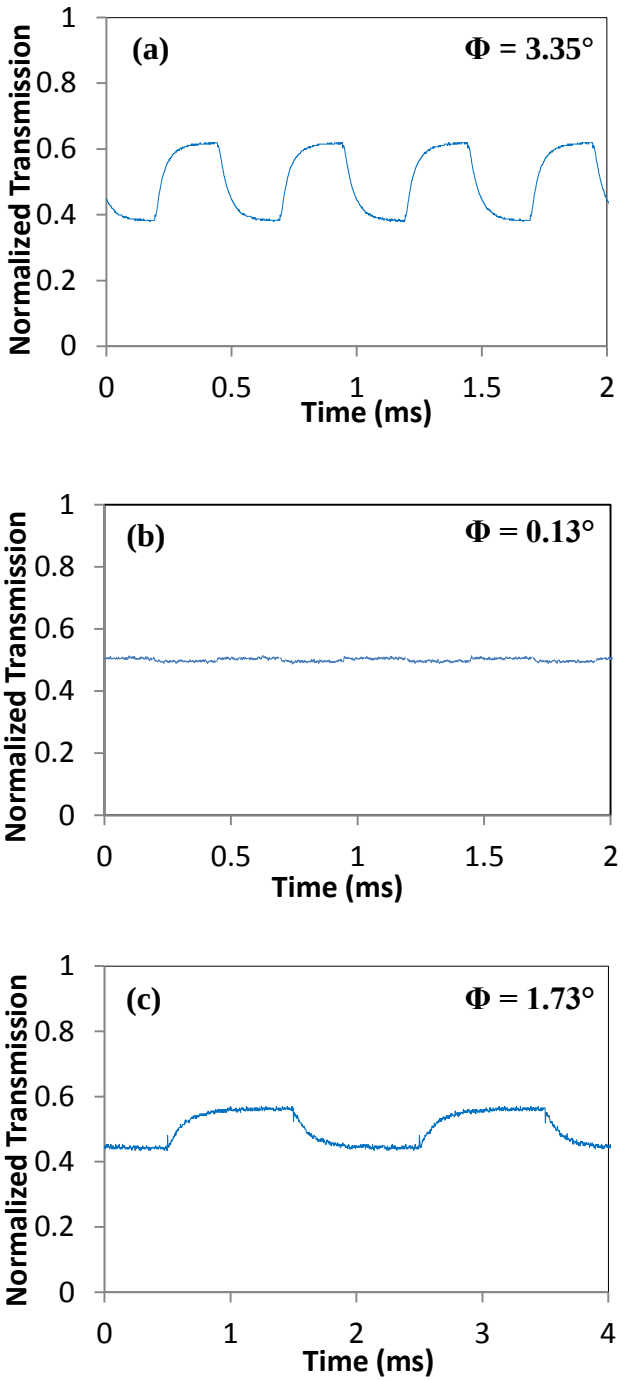


Figure 6.5. Electro-optic responses of ULH states formed with structured and bulk polymer networks. The electro-optic response of three ULH devices under the application of a ± 27.5 V square wave: (a) before polymerization (b) after polymerization in the bulk (12 seconds exposure to a UV lamp at a distance of 10 cm, emitting at λ = 365 nm and at a power density of 185 mWcm^{-2}) (c) with 5 µm-spaced homeotropic polymer walls fabricated in-situ on the TPA set-up.

helical structure is aligned in a ULH texture. The modulated light intensity detected through the device with the 5 µm-spaced polymer walls, under the application of a ±27.5 V square wave, shows a significant increase (~10%) in the transmission modulation amplitude compared with that presented in Figure 6.5 (b). Furthermore, the measured tilt angle from the device consisting of polymer walls (φ = 1.73°), which is more than ten times greater than that obtained from the device that was polymerized in the bulk (c.f. Figure 6.5 (b)). In terms of the response time, the device consisting of the polymer walls appears to be of a similar order of magnitude (i.e. ~100 µs) to that recorded before polymerization. However, the diffusion of the polymer network either side of the walls restrains the LC molecules leading to almost a 50% reduction in the tilt angle compared with the non-polymerized state, even though the structured polymer walls alone occupy less than 20% of the device area.

Although the 5 µm periodicity forms the optimum ULH alignment relative to the other periodicities shown in this study, the LC alignment overall results in a relatively low contrast between bright and dark states, as is evident from the OPM images. For example, stripes can still be seen at optical extinction, while the maximum transmission setting in the bright state is hampered by the black homeotropic polymer regions that cover almost 20% of the device area, although these regions may appear larger due to the diffusion of the polymer network between the walls, which has previously been discussed. As a proof-of-concept, this study has shown that it is possible to spontaneously induce a well-aligned ULH state using commercially available materials. Thus, the alignment could be improved further through the careful selection of the reactive mesogen mixtures to control the rate of diffusion between the polymer walls.

6.3.3. Chiral Nematic Polymer Walls

Writing structures in the chiral nematic phase removes the condition for the host LC material to have a positive dielectric anisotropy (in order to unwind the helix for fabrication in the nematic phase). Polymer walls were therefore fabricated in the chiral nematic phase at a fixed periodicity of 5 μm. Figure 6.6 (a) and (b) show OPM images of the dark and bright states of the chiral nematic device when walls of polymer network are structured parallel and perpendicular to the helical axis, respectively. During the annealing process, the ULH did not form uniformly across the device due to limitations of the shear flow alignment technique. Consequently, some regions between the polymer walls are not exactly parallel or perpendicular to the helix. Both sets of images show reasonable ULH alignment, although a marginal improvement can be seen in the contrast between the dark and bright states for the case shown in Figure 6.6 (a) i.e. walls parallel to the helix.

The periodic structures shown in Figures 6.6 (a) and (b) were written orthogonal to one another. Figure 6.6 (c) shows a non-polymerized region at the intersection between the two fabricated regions in the device, in which the helix has spontaneously aligned to form a ULH texture. Interestingly, this region located between the two polymer network structures shows very good ULH alignment with an improved contrast achieved between the bright and dark states of the device compared with the LC alignment between the fabricated polymer walls (Figure 6.6 (a) and (b)).

6.3.4. Electro-Optic Response

Figures 6.7 (a) – (c) show the electro-optic responses corresponding to the alignments shown in Figures 6.6 (a) – (c) respectively, under the application of a 1 kHz, ± 27.5 V

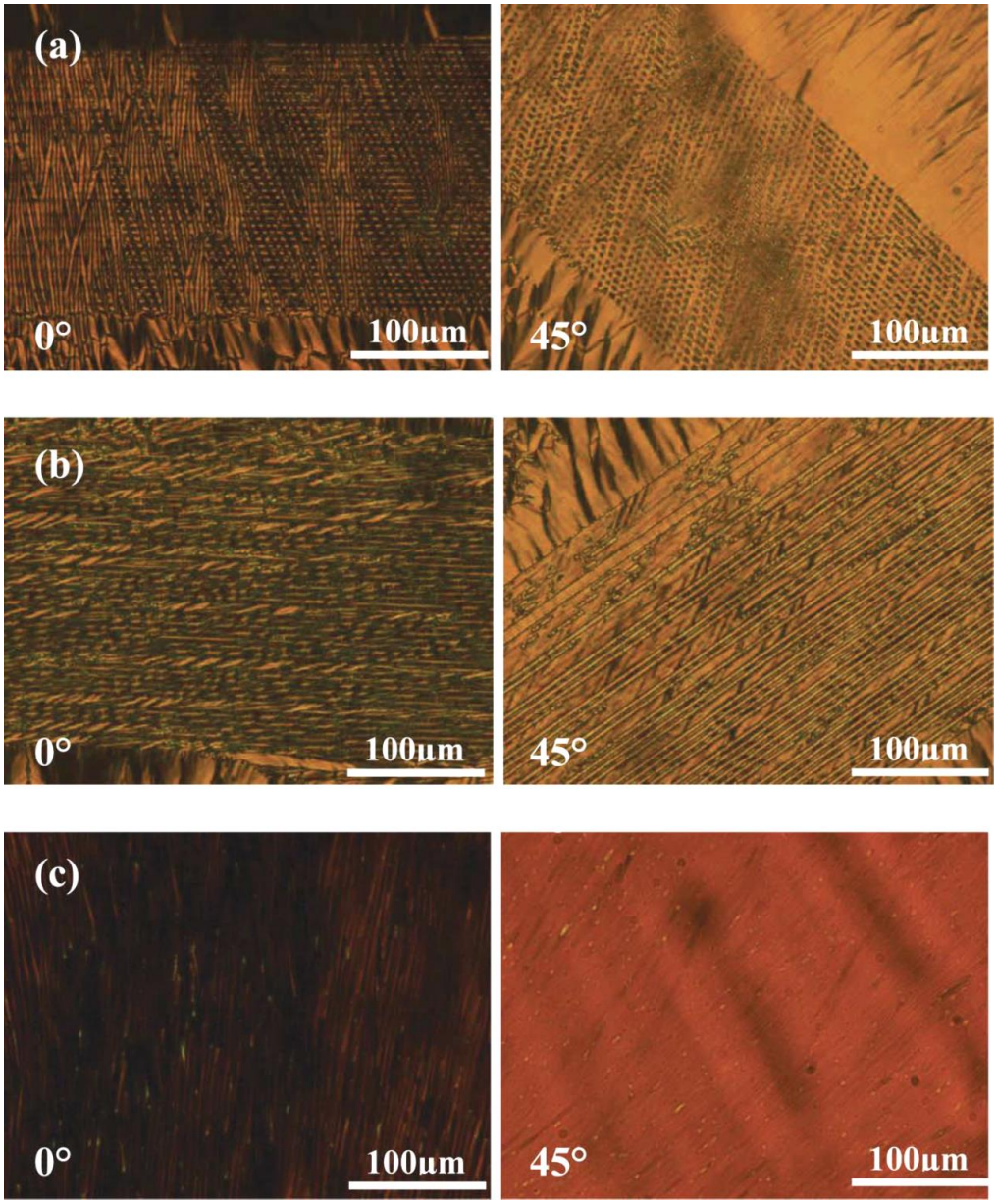


Figure 6.6. T**he ULH state formed in the chiral nematic phase.** OPM images, taken with the device angled at 0° (dark state) and 45° (bright state) to the analyser, show 5µm-spaced polymer walls engineered (a) parallel and (b) perpendicular to the helical axis that generate similar ULH alignments. A non-polymerized region (c) in between the two polymer network structures spontaneously forms a well aligned ULH texture.

square wave. Engineering polymer walls parallel and perpendicular to the helical axis generates a similar modulation in the transmission as can be seen in Figure 6.7 (a) and (b). Both measurements gave a switching angle of 1.1°. The modulation in the transmission detected from the non-polymerized region between the polymer network structures however, shown in Figure 6.7 (c), is almost double that of Figure 6.7 (a) and (b) potentially due to the fact that no polymer network has been formed here; applying mechanical shear revealed the presence of flow. A switching angle of 2.1° was measured from this non-polymerized region, which is 1.25° less than that recorded before any bulk polymerization (c.f. Figure 6.5 (a)). This difference in the switching angles suggests that, although there is presence of flow in the sample, some residual polymerization is likely to have occurred in the region shown in Figure 6.7 (c). It would be interesting, however, to fabricate polymeric walls of different shapes that could confine non-polymerized chiral nematic regions so as to ensure that the magnitude of the electro-optic effect is as large as possible whilst simultaneously achieving a uniform alignment.

Comparing the electro-optic responses presented in Figure 6.5 with those in Figure 6.7, it is clear that structuring polymer networks both in the nematic and chiral nematic phases leads to an enhancement of the measured FEO response relative to bulk polymerization techniques. Fabrication in the nematic phase is a relatively simple method that does not require multiple fabrication stages as writing in the chiral nematic phase (due to the initial ULH formation). An increased contrast can be seen between the bright and dark states of the 5 μm-spaced polymer walls fabricated in the nematic phase and a lower tilt angle was recorded from the ULH formed between the chiral nematic polymeric walls. Thus, the homeotropic anchoring in the polymer network structures

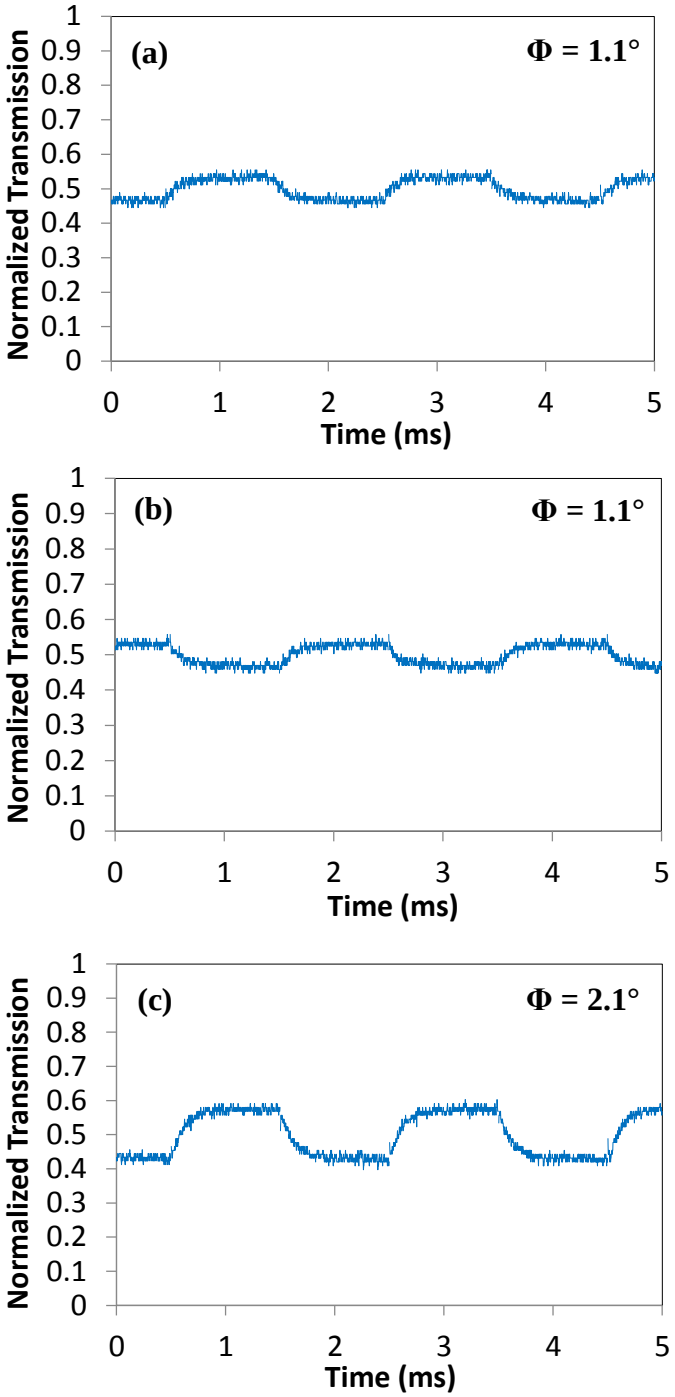


Figure 6.7. Electro-optic responses of the ULH state formed in the chiral nematic phase. The FEO responses were recorded under the application of a 1 kHz, ± 27.5 V square wave for devices with polymer walls written (a) parallel and (b) perpendicular to the helix and (c) a non-polymerized region in between the polymer network structures.

fabricated in the nematic phase generates a higher quality ULH. It is worth noting that the polymer walls fabricated in the chiral nematic phase were written at a fixed periodicity of 5 µm, as it was assumed that the wall spacing was dependent on the order of the device thickness (based on the findings presented in Figures 6.4 and 6.5). For future work, it may therefore be beneficial to write polymer walls at different periodicities during fabrication in the chiral nematic phase in order to investigate further how the relationship between the wall spacing and the number of pitches varies.

6.3.5. Possible Improvements in Selection of Materials

For practical applications, a larger tilt angle is required than those obtained from the devices presented in this investigation. As discussed before, the materials used in this investigation are not optimized to produce large tilt angles. The FEO response is limited by the dielectric coupling that tends to unwind the helix (c.f. §1.3.1); thus, more careful selection of the LC host would also be beneficial. Developments in recent years have led to new materials (bimesogenic compounds) that exhibit low dielectric anisotropy. These bimesogens extend the linear regime of the electro-optic effect and possess large flexoelastic ratios (e/K) thus ensuring that the maximum intensity modulation can be achieved with relatively low electric field strengths (e.g. 1 - 2 $V\mu m^{-1}$) [12-14]. However, the proposed fabrication technique using the polymer walls does require some dielectric coupling in order for the polymer walls to be written in the homeotropic state that occurs when the helix is unwound under an externally applied field. In this instance, a dual frequency LC compound [15, 16] may be a more suitable choice of material, whereby the polymeric structures could be fabricated in the positive dielectric anisotropy regime occurring at low frequencies when the sample is at room temperature.

Subsequently, the device could be operated around the cross-over frequency ($\Delta\varepsilon \rightarrow 0$) in order to maximise the FEO performance post-fabrication.

The use of a different reactive mesogen for the formation of the polymer networks is likely to enhance the flexoelectric tilt angle in addition to the host LC. The apparent tilt angles for the samples consisting of polymer walls (both in the nematic and chiral nematic cases) were calculated from the electro-optic response recorded over an area comprising both polymer walls and LC microchannels. As a result, this could mean that there is a locally varying electric field-induced tilt between the walls due to variations in the network density within these regions. Moreover, the high concentration of reactive mesogen in the mixture could give significant changes in the FEO response between the walls compared to that before polymerization. A potential solution to the diffusion of the polymer network into the LC channels could involve the addition of another monomer to the initial chiral nematic LC mixture that would enhance diffusion towards the focal point of the UV light source [17]. Enhancing the phase separation in this way would also limit the concentration of non-crosslinked reactive monomer remaining between the polymer walls, which may polymerize upon exposure to ambient UV light (currently, all device characterization needs to be carried out in a dark room). Evidently, this is one important issue that needs to be addressed before the technique for ULH stabilisation can be used to manufacture commercial devices. For example, in terms of preparing new optimised LC mixtures, careful consideration into the amount of monomer required to fabricate polymer walls of a precise volume, combined with additional monomers that could control the rate of diffusion towards the fabrication laser beam, should be taken into account.

6.4. CONCLUSIONS

The spontaneous formation of a uniform lying helix alignment in a short pitch chiral nematic liquid crystal has been demonstrated through the in-situ fabrication of periodic polymer network structures using a two-photon absorption laser scanning lithography technique. Combined with a spatial light modulator that corrects for aberrations in the system, this fabrication technique allows the polymer structures to be written directly into the liquid crystal under the simultaneous application of an electric field. Thus, polymer network structures were fabricated in the nematic phase by electrically addressing a homeotropic device with an electric field strength above the value of the critical unwinding field. A spontaneous ULH was generated between the homeotropic polymer walls in the chiral nematic phase, upon removal of the applied electric field. Walls spaced at the order of the device thickness appear to optimise the uniform lying helix alignment and consequently lead to an increase in the flexoelectro-optic tilt angle relative to that obtained when polymerizing the bulk of the liquid crystal device. Investigations into the optimum materials for two-photon absorption processes could further enhance the device's electro-optic performance, for example, by restricting polymer diffusion beyond the region of laser irradiation.

For fabrication in the chiral nematic phase, the alignment was controlled by polymer walls that were written in-situ either parallel or perpendicular to the helical axis, and with periodicities of the order of the device thickness. The ULH is shown to be stable upon removal of the externally applied electric field, although the alignment is not completely uniform leading to relatively low contrast between the bright and dark states. However, a non-polymerized region between the two polymer structures engineered parallel and perpendicular to the helix shows good contrast suggesting that alternative

configurations of the polymer walls may lead to a more uniform alignment and enhanced electro-optic switching. The sub-micron resolution process could be extended to fabricate more complex structures of different shapes and dimensions to control the stability of interesting electro-optic effects in liquid crystalline materials. The next chapter explores how the structuring of polymer networks effects the topology of different LC states in the nematic phase, following on from some of the examples presented in Chapter 5.

6.5. REFERENCES

[1] M. Hird, *Liq. Cryst*. **38**, 11-12 (2011).

[2] S. T. Lagerwall, *Mol. Crys. Liq. Crys*. **543**, 1 (2011).

[3] R. B. Meyer, *Phys. Rev. Lett*. **22**, 918 (1969).

[4] J. S. Patel and R. B. Meyer, *Phys. Rev. Lett*. **58**, 15 (1987).

[5] N. Koma, T. Miyashita and T. Uchida, *J. Soc. Info. Display* **9**, 8 (2005).

[6] R. B. Meyer and J. S. Patel, *Flexoelectric liquid crystal device*, US Patent 4917475 (1987).

[7] L. Komitov, G. Bryan-Brown, E. Wood and A. Smout, *J. Appl. Phys*. **86**, 7 (1999).

[8] G. Carbone, D. Corbett, S. Elston, P. Raynes, A. Jesacher, R. Simmonds and M. Booth, *Mol. Crys. Liq. Cryst*. **544**, 37 (2011).

[9] G. Carbone, P. Salter, S. Elston, P. Raynes, L. De Sio, S. Ferjani, G. Strangi, C. Umeton and R. Bartolino, *Appl. Phys. Lett*. **95**, 011102 (2009).

[10] M. Berek, *Zbl. Miner. Geol. Paleont* **388**, 427 (1913).

[11] L. Beaufort, N. Barbarin and Y. Gally, *Nature Protocols* **9**, 633–642 (2014)

[12] H. J. Coles, B. Musgrave, M. J. Coles and J. Willmott, *J. Mater. Chem.* **11**, 2709 (2001).

[13] A. E. Blatch, M. J. Coles, B. Musgrave, and H. J. Coles, *Mol. Crys. Liq. Crys*. **401,** 161 (2003).

[14] H. J. Coles, M. J. Clarke, S. M. Morris, B. J. Broughton and A. E. Blatch, *J. Appl. Phys*. **99**, 034104 (2006).

[15] H. Xianyu, S.-T. Wu and C.-L. Lin, *Liq. Cryst.* **36**, 6 (2009).

[16] M. Mrukiewicz, P. Perkowski and K. Garbat, *Liq. Cryst.* **42**, 7 (2015).

[17] R. Penterman, S. Klink, H. de Koning, G. Nisato and D. Broer, *Nature* **417** (2002).

7

TUNABLE TOPOLOGICAL DEFECTS

7.1. INTRODUCTION

7.1.1. Colloids & Topological Defects

Topological defects or disclinations in nematic systems arise from singularities within the director that describes the local orientation of the LC molecules. These disclinations separate topologically discontinuous states, and possess a strong distortion field that stems from the defect core. The defects are characterized by a topological charge, *m*, which defines the number of times that the director rotates by 2π when circumnavigating the defect [1]. Following the director orientation around the defect in a counterclockwise fashion also reveals the sign of the charge, whereby the defect is negatively charged if the direction of rotation is opposite to the direction of circumnavigation, and vice versa.

Deterministically assembling colloidal particles within a liquid crystalline matrix is expected to enhance the functionality of the host medium with potential applications in microfluidics [2], sensing and electro-optic devices [3-5]. Although the core of a topological defect in nematic LCs is only ~10 nm in size [6], the strong director

deformation causes spatial variations in the degree of orientational order that extends ~1-2 micrometres either side of the core [6]. The significantly lower degree of orientational order within the core results in attractive forces that act on colloidal particles in the vicinity of the defect [6]. As a result, particles dispersed in a LC device tend to migrate towards the distorted disclination core region [7]. This self-assembly of micro- and nano-sized particles minimizes the energy at the defect sites and also removes the need for expensive instruments such as optical tweezers (that uses the attractive/repulsive force provided by a highly focused laser beam) to position individual particles.

The formation of complex director patterns around topological defects has been employed to command the movement of colloidal particles using the strong director deformation that surrounds a defect core. Nematic LC devices infiltrated with active matter such as rodlike bacteria [2] are able to direct the flow of the self-propelling bacteria through regions of bend and splay alignments. Complex director patterns can be realized using a variety of substrate patterning techniques [8-11]. Photoalignment [10,11], which involves the photo-patterning of LC cell surfaces coated in photosensitive materials by irradiation with polarized light, has demonstrated the creation of complex director patterns such as spiraling vortices comprised of mixed bend-splay regions [2]. Bacterial locomotion that tends to be bipolar and parallel to the director in homogeneously aligned LCs changes to unipolar circular trajectories within regions of mixed bend and splay for point defects of charge $m = 1$, while defects of charge $m = \pm 1/2$ generate linear unipolar trajectories. Additionally, the self-propelling bacteria are attracted towards positively charged topological defects thereby depleting their concentration around negatively charged defects.

The inclusion of colloidal particles within liquid crystalline systems also disturbs the local orientational order on account of the interaction between the surface of the colloidal particle and the director [12-14]. This interaction can lead to the spontaneous formation of topological defects, such as Saturn ring defects on the surface of spherical particles [15]. Optical tweezers can be used to entangle these disclinations, creating a binding mechanism between neighbouring particles [16]. Non-spherical 'boomerang' shaped particles have also been infiltrated into LCs which, due to the curvature in their shape, tend to accumulate in regions of maximum bend [17]. This work was achieved again using the photoalignment technique combined with a plasmonic mask that has a predetermined design to pattern the photosensitive substrate upon irradiation with the polarized light. Although photoalignment is effective at creating interesting director patterns and topological defects, the technique does not permit direct patterning of the director in the bulk device as it is limited to the cell surfaces. Additionally, photomasks with predetermined designs do not offer the flexibility of altering the pattern in-situ. In this work, the high resolution in-situ DLW technique is employed to pattern a variety of polymer structures that extend through the bulk of the device. The added advantage of the adaptive optics inherent to the custom-built fabrication system also offers a deeper insight into the means by which a topological defect can be probed under varying electric field strengths. Patterning the director in-situ therefore provides a better understanding of the formation of the defect and crucially, the means by which its size and position can be electrically tuned translates directly to the command over colloidal particles at the defect sites. Manipulating the director by virtue of the aberration correction included in the optical set-up generates complex bend-splay patterns and

topological defects that can even be ‘frozen-in’ with perturbations to the applied voltage.

As introduced in Chapter 3, electrically addressing a planar (parallel) aligned nematic pi-cell device leads to various transitions, such that some of these voltage-dependent states are separated by ±1/2 strength topological defects in the form of disclination lines. Using the custom-built direct laser writing (DLW) system described in Chapter 5, structures of varying shapes and dimensions are fabricated including pseudo-1D walls, cylindrical polymer cavities, concentric rings and square arrays. The structures are written in-situ under the application of different electric field strengths in order to ‘lock-in’ different voltage-dependent LC states. As a result, topological defects separating the distinct LC alignment between the polymer structures can be electrically tuned such that their size and position is controlled through perturbations in the applied voltage. Numerical and analytical models are also developed for the polymer walls and cylindrical cavities respectively, in order to investigate the cost in energy that generates the movement of the topological defects when the LC is confined to different boundary conditions. An extension of this work is also considered in terms of more complex, colloidal systems.

7.2. EXPERIMENTAL PROCEDURE

7.2.1. Materials and Sample Preparation

A 5 μm-thick, nematic pi-cell with ~5° surface pretilt was capillary-filled with a photo-polymerizable LC mixture in the isotropic phase. The host liquid crystalline material was the standard commercial eutectic E7 nematic mixture (Merck Chemicals, Ltd.), which has a positive dielectric anisotropy of $\Delta\varepsilon = 13.7$ at $T = 20°C$ and a birefringence

of $\Delta n = 0.219$ at $\lambda = 632.8$ nm. The nematic host was made photo-polymerizable with the addition of 30 wt. % of the reactive mesogen RM257 and 1 wt. % of the photoinitiator IRG819, both also provided by Merck Chemicals, Ltd.

Two mixtures were prepared for the colloidal dispersions to observe how the density and size of the particles affected their movement towards the defect sites. Crucially, the surfaces of the particles were not treated to avoid any interaction with the orientational order of the nematic LC that might prevent the particles from drifting towards the defect core. A concentration of 0.07 wt % of fluorescent microspheres (Bangs Laboratories, Inc.), 50 nm in diameter and of a similar density to E7 at ~1 g/cm^3 that were dispersed in deionized water at a number density of 1.372×10^{14} microspheres/ml, was dissolved in the E7 nematic host. The solution was left on the hot plate at T = 80°C for ~1 hour in order to evaporate the deionized water. The colloidal-LC mixture was then capillary-filled into a 5 µm-thick, nematic pi-cell with ~5° surface pretilt when in the isotropic phase. The second colloidal mixture consisted of 5.2 wt % of mesoporous silica (SiO_2) beads (Sigma Aldrich), 1 µm in diameter and approximately double the density of E7, dispersed in the nematic LC host in the isotropic phase. A stirring magnet was placed in the mixture for a few hours in order to prevent the beads from aggregating at the bottom of the vial, before capillary-filling another 5 µm-thick, nematic pi-cell with ~5° surface pretilt in the isotropic phase.

7.2.2. Fabrication Procedure

A variety of polymer structures were written into the device filled with the photosensitive mixture under differing electric field strengths in order to investigate the

effect of different confined geometries on the LC alignment and resultant topological defects:

1. Two polymer walls, extending 1 mm in length, were fabricated at a separation of 100 µm. The first wall was written in the splayed H-state, in the absence of an applied electric field while the other was written in the V-state, under the application of a 1.6 V/µm electric field strength.
2. Cylindrical polymer cavities were fabricated at four different diameters (20, 30, 40 and 50 µm) with the device in the ground H-state. The polymer cavities, written at a sample translation speed of 40 µm/s, extended through the bulk of the device from the substrate to superstrate.
3. Concentric squares and rings 'locking-in' the H-V-H states were also fabricated under the same electric field conditions (E = 0 V/ µm for the H-state, E = 1.6 V/ µm for the V-state).
4. Lastly, a checkerboard of square-shaped polymer cavities was written whereby each alternating structure was written in the H- and V-states, again under the same electric field conditions.

7.3. RESULTS & DISCUSSION

7.3.1. Polymer Walls

Figure 7.1 shows an optical polarizing microscope (OPM) image taken when the device containing the fabricated polymer structures is in its bright state between crossed polarizers (oriented 45° relative to the polarizer). The splay (H) and bend (V) polymer

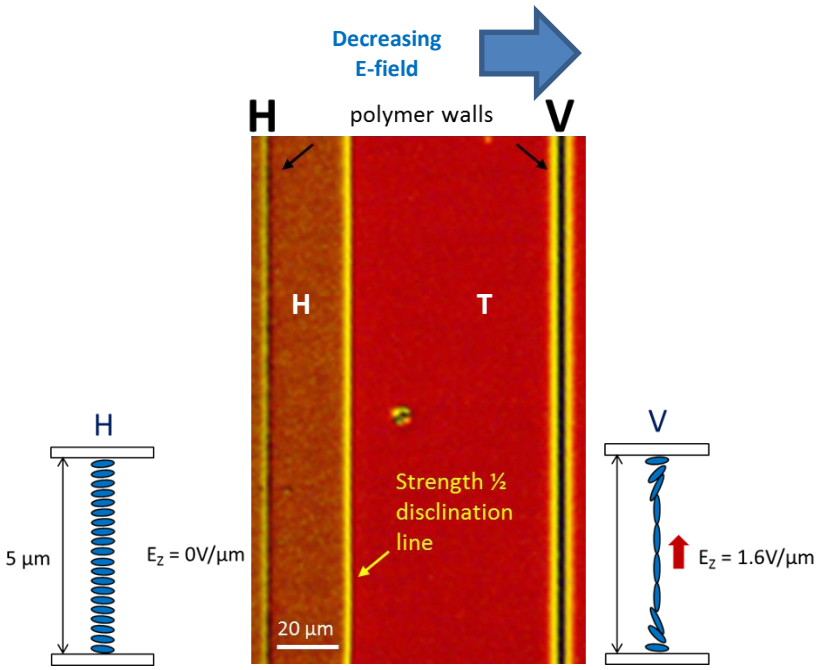


Figure 7.1. H-V polymer walls. OPM image showing two polymer walls written in the H (0 V/ µm) and V (1.6 V/ µm) states, at a separation of 100 µm. The corresponding splay (H) and bend (V) director profiles are illustrated on the left and right of the image, respectively. The position of the disclination line between the two structures can be varied according to the externally applied electric field; the defect moves right as the field strength is decreased so that the bulk LC alignment, which collapses into the transient twist (T) state, switches to the lowest energy H state.

walls, along with illustrations of their corresponding director profiles are shown in the image, which was taken upon removal of an externally applied electric field. A strength ±1/2 disclination line separating the topologically discontinuous regions can be seen in the image. The defect moves from left to right as the device relaxes to the lowest energy splayed ground state, while the bulk director collapses from the bend to the twist (T) state in the absence of the electric field.

The series of OPM images shown in Figure 7.2 are frames extracted from a video that was recorded while the device was under the application of increasing/decreasing electric field strengths. The direction of the H-V polymer walls are indicated on either side of the images. Decreasing the electric field strength until the amplitude is almost

zero results in a transition of the bulk director to the transient T-state, as shown in Figure 7.2 (a). At such low applied fields (E → 0), the lowest energy is the splay state and consequently the ±1/2 defect moves from the left to the right of the central region in between the polymer walls. Increasing the applied field results induces a transition in the bulk to the bend state, which becomes the lowest energy configuration due to the positive dielectric anisotropy of the host LC material. As a result, the defect wall moves from right to left whereby the initially splayed region becomes H_a, which diminishes under growing electric field strengths. Thus it is possible to electrically tune the position of the defect between the two topologically distinct polymer structures.

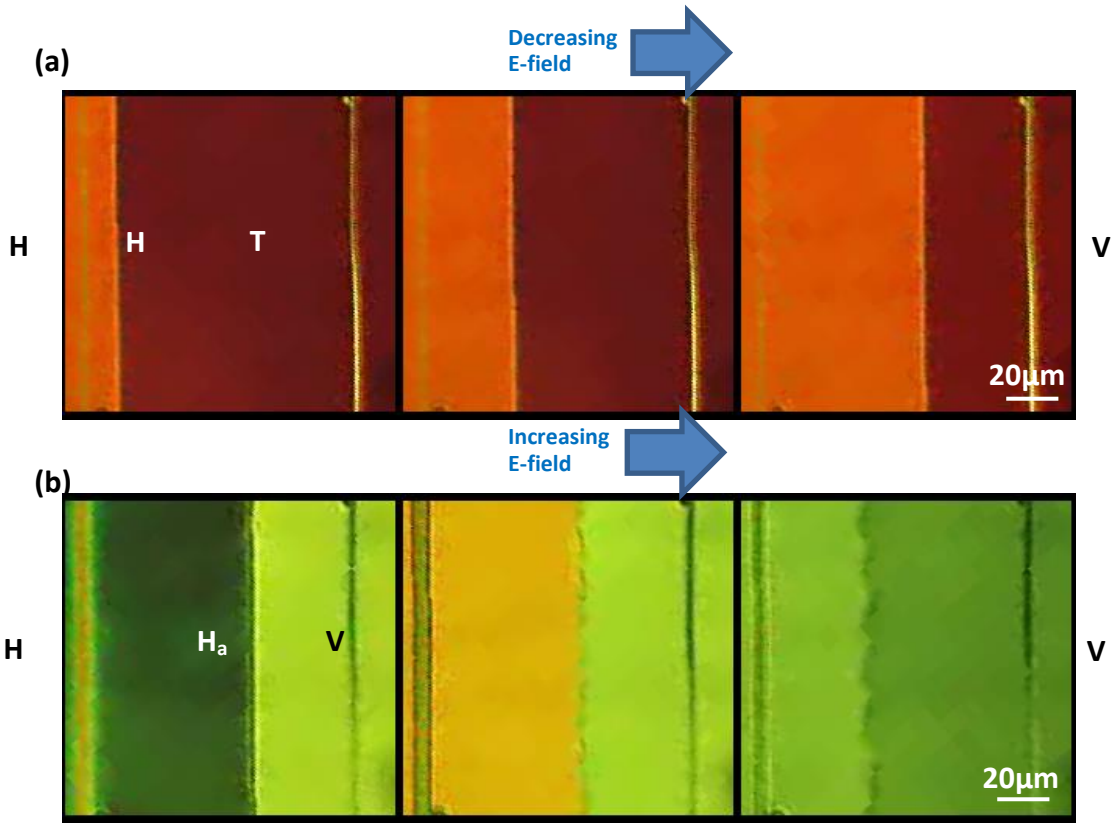


Figure 7.2. Electrically tunable defects. A series of OPM images showing the LC alignment between the H-V polymer walls separated by 100 µm. (a) As the electric field is reduced to zero (left to right), the H state nucleates from the H-polymer wall and the ±1/2 defect moves from left to right towards the V-polymer wall. (b) As the applied electric field is increased (left to right), the ±1/2 defect moves right to left towards the H-polymer wall and the bulk LC switches into the bend state.

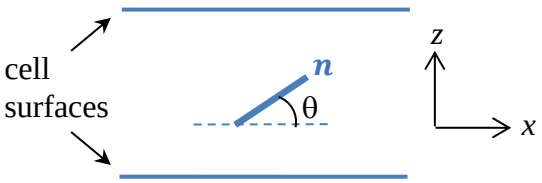


Figure 7.3. Cell configuration. A schematic of the director vector, ***n***, as a function of the angle θ between the cell surfaces in the *x*-*z* plane.

7.3.1.1. Numerical Model

A two-dimensional planar (bend-splay) version of the nematic Q-tensor theory was used to model 'simple' bend-splay walls. The use of the reduced version of the Q-tensor method allows for faster computational speeds in comparison with the full version of the Q-tensor theory [18]. The approach below does not allow for biaxiality in the vicinity of nematic defect cores, but in general the details of the defect core structure is unlikely to be important in this investigation.

In the model, the director is contained between two planes (surfaces) and remains in the plane between the surfaces (bend-splay distortion only). In this case, the director vector can be expressed as

$$\hat{\mathbf{n}} = \begin{pmatrix} n_x \\ n_z \end{pmatrix} = \begin{pmatrix} \cos\theta \\ \sin\theta \end{pmatrix}, \tag{7.1}$$

where the angle θ is a function of position within the plane perpendicular to the cell surfaces as illustrated in Figure 7.3

A two-dimensional version of the Q-tensor can then be expressed in direct analogy with the "conventional" nematic Q-tensor as

$$Q = S(\hat{\mathbf{n}} \otimes \hat{\mathbf{n}}) - \frac{1}{2} SI, \tag{7.2}$$

where *s* is the order parameter and *I* the identity matrix. This choice is analogous to the "conventional" Q-tensor, but allows variation only within bend-splay distortion, and

does not allow biaxial ordering as there is now a single order parameter. For clarity, this Q-tensor can be written in terms of the order parameter and director tilt angle as

$$Q = \begin{pmatrix} S\left(cos^2\theta - \frac{1}{2}\right) & S\cos\theta\sin\theta \\ S\cos\theta\sin\theta & S\left(sin^2\theta - \frac{1}{2}\right) \end{pmatrix}. \tag{7.3}$$

As with the "conventional" Q-tensor, the tensor in (7.3) is traceless. Here, the principal eigenvalue(s) represents half the order parameter, *S*/2. This Q-tensor can now be written in a more compact form,

$$Q = \begin{pmatrix} \rho & \phi \\ \phi & -\rho \end{pmatrix} \tag{7.4}$$

where

$$\rho = S\left(cos^2\theta - \frac{1}{2}\right) = S\left(sin^2\theta - \frac{1}{2}\right) \quad \text{and} \quad \phi = S\cos\theta\sin\theta \tag{7.5}$$

The new variables, ρ and ϕ, can be used to develop an energy functional to be minimised in order to find a solution to a director state.

Eigenvalues and nematic order:

In terms of ρ and φ the eigenvalues of the Q-tensor matrix are

$$\pm\frac{S}{2} = \pm\sqrt{\rho^2 + \phi^2}\,, \tag{7.6}$$

where the normal nematic order parameter is from the positive root, given by

$$S = 2 \times \sqrt{\rho^2 + \phi^2}\,. \tag{7.7}$$

The nematic order can also be written in terms of the trace of Q^2 since

$$Q^2 = \begin{pmatrix} \rho & \phi \\ \phi & -\rho \end{pmatrix}^2 = \begin{pmatrix} \rho & \phi \\ \phi & -\rho \end{pmatrix}\begin{pmatrix} \rho & \phi \\ \phi & -\rho \end{pmatrix} = \begin{pmatrix} \rho^2 + \phi^2 & 0 \\ 0 & \rho^2 + \phi^2 \end{pmatrix}. \tag{7.8}$$

Substituting (7.8) into (7.7) therefore gives

$$S^2 = 2 \times trace(Q^2) = 4 \times (\rho^2 + \phi^2). \tag{7.9}$$

The key advantage of taking the above Q-tensor approach, rather than a director-based approach, is two-fold:

1. It implicitly allows for the $\hat{\mathbf{n}} \equiv -\hat{\mathbf{n}}$ nematic director symmetry, allowing director continuity in the presence of, for example, strength $\pm\frac{1}{2}$ defects;
2. It allows for variation in the order parameter, as well as director orientation variation, therefore allowing for the formation of defects at points of discontinuity in the director orientation.

The particular form of the Q-tensor chosen, with its diagonal traceless form, is convenient for mathematical analysis, with eigenvalues relating directly to the order parameter, and diagonal (and off-diagonal) terms which relate conveniently to key physical tensor parameters such as dielectric permittivity.

Elastic energy:

In this analysis, the Q-tensor approach can be combined with a simple one-constant energy expression involving gradients of each tensor component in each direction. Using Q_{ij} notation, the elastic energy can be written as

$$f_d = \sum_{\substack{i=1,2 \\ j=1,2 \\ k=1,2}} \frac{L_1}{2}\left(\frac{\partial Q_{ij}}{\partial x_k}\right)^2, \tag{7.10}$$

where L_1 is a re-normalised form of the one-constant elastic-constant (K) allowing for the strength of the nematic ordering. In an x-z coordinate system as defined in Figure 7.3, the expression in (7.10) can be written in terms of ρ and φ as

$$f_d = L_1\left\{\left(\frac{\partial \rho}{\partial x}\right)^2 + \left(\frac{\partial \rho}{\partial z}\right)^2 + \left(\frac{\partial \phi}{\partial x}\right)^2 + \left(\frac{\partial \phi}{\partial z}\right)^2\right\}. \tag{7.11}$$

Order energy:

In the "conventional" Q-tensor notation, the order-energy is dealt with through a series expansion in trace(Q^2), trace(Q^3) and trace(Q^4). The simplified form of the Q-tensor

means that trace(Q^3) = 0 and therefore there are only terms in trace(Q^2) and trace(Q^4) such that trace(Q^4) = (trace(Q^2))^2. This allows the order-energy to be written in a compact quadratic form as

$$f_t = \frac{A}{16}\left(s_0^2 - 2 \times trace(Q^2)\right)^2 = \frac{A}{16}\left(S_0^2 - 4 \times (\rho^2 + \phi^2)\right)^2, \qquad (7.12)$$

where S_0 is an equilibrium order parameter and A is a parameter which represents the relative energy cost of changes in the order.

Electric energy:

Finally, it is necessary to introduce the electric field "driving" term in the energy equations. The electric energy density can be written as

$$f_e = -\frac{1}{2}\epsilon_0(\Delta\epsilon^* Q\boldsymbol{E}) \cdot \boldsymbol{E} \qquad (7.13)$$

where the dielectric anisotropy is re-normalised to allow for the strength of nematic ordering. The $\Delta\epsilon^* Q$ term is in effect the variable term of the dielectric tensor, the non-variable terms having been dropped because they do not lead to changes in energy density for variations in director states. Assuming that the electric field, E_z, is in the direction perpendicular to the cell surfaces, (7.13) can be expressed as

$$f_e = -\frac{1}{2}\epsilon_0\left(\Delta\epsilon^*\begin{pmatrix}\rho & \phi\\ \phi & -\rho\end{pmatrix}\begin{pmatrix}0\\ E\end{pmatrix}\right)\cdot\begin{pmatrix}0\\ E\end{pmatrix} = \frac{1}{2}\epsilon_0\Delta\epsilon^*\rho E^2. \qquad (7.14)$$

Total energy:

The total energy can then be obtained by summing the terms in (7.10), (7.12) and (7.13) so that $\underline{F} = F_d + F_t + F_e$, giving

$$F = \sum_{\substack{i=1,2\\ j=1,2\\ k=1,2}} \frac{L_1}{2}\left(\frac{\partial Q_{ij}}{\partial x_k}\right)^2 + \frac{A}{16}\left(s_0^2 - 2 \times trace(Q^2)\right)^2 - \frac{1}{2}\epsilon_0(\Delta\epsilon^* Q\boldsymbol{E}) \cdot \boldsymbol{E}, \qquad (7.15)$$

which in terms of the parameters ρ and φ gives

$$F = L_1\left\{\left(\frac{\partial\rho}{\partial x}\right)^2 + \left(\frac{\partial\rho}{\partial z}\right)^2 + \left(\frac{\partial\phi}{\partial x}\right)^2 + \left(\frac{\partial\phi}{\partial z}\right)^2\right\} + \frac{A}{16}\left(s_0^2 - 4\times(\rho^2+\phi^2)\right)^2 + \frac{1}{2}\epsilon_0\Delta\epsilon^*\rho E^2.$$

(7.16)

The terms in (7.16) can be put into Euler-Lagrange equations to determine equations for ρ and φ, which can then be solved to determine a director structure. The Euler-Lagrange equations for ρ and φ respectively are given by

$$0 = \frac{\partial F}{\partial\rho} - \frac{\partial}{\partial x}\left(\frac{\partial F}{\partial\left(\frac{\partial\rho}{\partial x}\right)}\right) - \frac{\partial}{\partial z}\left(\frac{\partial F}{\partial\left(\frac{\partial\rho}{\partial z}\right)}\right), \tag{7.17}$$

$$0 = \frac{\partial F}{\partial\phi} - \frac{\partial}{\partial x}\left(\frac{\partial F}{\partial\left(\frac{\partial\phi}{\partial x}\right)}\right) - \frac{\partial}{\partial z}\left(\frac{\partial F}{\partial\left(\frac{\partial\phi}{\partial z}\right)}\right). \tag{7.18}$$

Equating (7.17) and (7.18) to dissipation terms in the form of the LC rotational viscosity allows for some time-dependence in the behaviour. Substituting for *F* in each case and introducing the dissipation yields the following two equations, one for ρ and one for φ:

$$-\gamma\frac{\partial\rho}{\partial t} = -2L_1\left\{\left(\frac{\partial^2\rho}{\partial x^2}\right) + \left(\frac{\partial^2\rho}{\partial z^2}\right)\right\} - A\left(s_0^2 - 4\times(\rho^2+\phi^2)\right)\rho + \frac{1}{2}\epsilon_0\Delta\epsilon^*E^2 \tag{7.19}$$

$$-\gamma\frac{\partial\phi}{\partial t} = -2L_1\left\{\left(\frac{\partial^2\phi}{\partial x^2}\right) + \left(\frac{\partial^2\phi}{\partial z^2}\right)\right\} - A\left(s_0^2 - 4\times(\rho^2+\phi^2)\right)\phi \tag{7.20}$$

These equations can be solved numerically using a "relaxation" method on a regular grid, as described in Chapter 2, to understand bend-splay structural behaviour.

The simulated results based upon the two-dimensional planar uniaxial Q-tensor theory show good agreement with the experimental observations. Figures 7.4 and 7.5 contain plots of the order parameter and director profile respectively, produced in the absence of an applied electric field. In both cases, the defect can be seen in the central region between the H-V polymer walls. The defect can be seen from the decrease in the order plot, indicated by the small region of blue, relative to the surrounding regions of higher order (orange colour). It is worth noting that the plots are produced from a computational space that correlates to a width of 25 μm as opposed to the actual wall

separation (100 µm), therefore the position of the H-V walls are labelled solely for clarity. The strong director deformation leads to variation in the degree of orientational order in space, as illustrated by the plot in Figure 7.6. The director profile in Figure 7.7 reveals the splay state on the left hand side (LHS) of the defect with the bend state on the right hand side (RHS). In practice, regions of bend state collapse into the transient twist state in the absence of an applied field, as seen in Figures 7.4 and 7.5 (a). The model remains in the bend state upon removal of the field due to the planar constraint. However, the bend and twist states are energetically equivalent due to the one elastic constant approximation used in the model, therefore this discrepancy does not fundamentally affect the behaviour of the results in terms of modelling the defect dynamics.

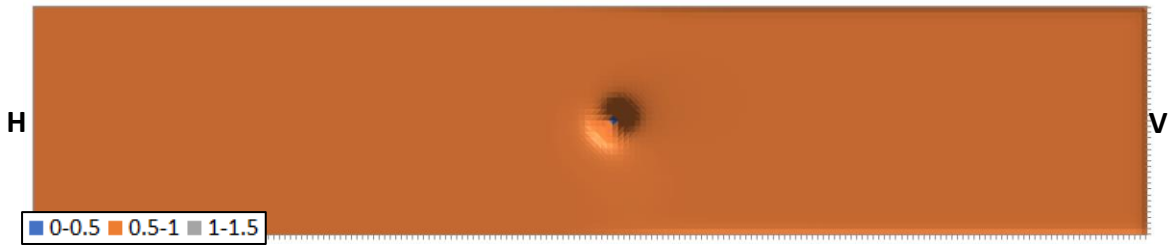


Figure 7.4. A simulated plot of the order parameter with the splay (left) and bend (right) states reveals a ±1/2 defect generated in the central region where there is a significant drop in the degree of order (blue) relative to the surrounding region (orange). Scale in arbitrary units.

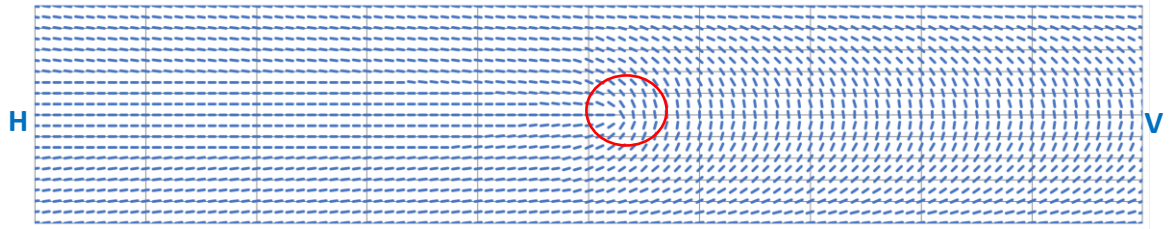


Figure 7.5. The simulated director profile between the H-V polymer walls in the absence of an applied electric field. The distortion between the splay (left) and bend (right) states leads to a discontinuity in the LC alignment that generates a ±1/2 defect within the central region of the director profile (indicated by the red circle).



Figure 7.6. A simulated plot of the order parameter after ~ 0.23 seconds. The ±1/2 defect can be seen drifting to the right at a speed of ~26.7 µm/s as the bulk director to the left of the defect relaxes into the splayed state over time. Scale in arbitrary units.

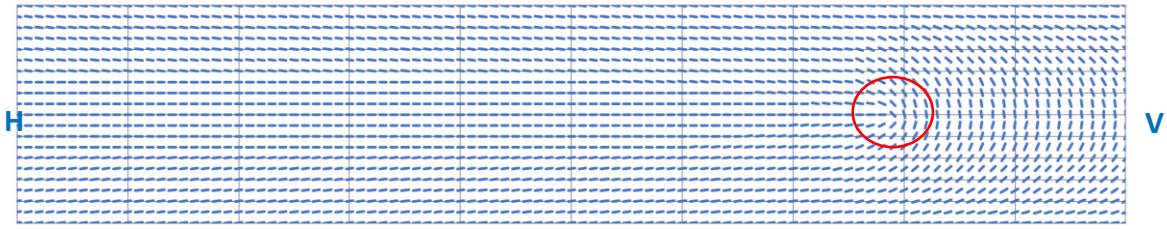


Figure 7.7. The simulated director profile after ~ 0.23 seconds. The ±1/2 defect (indicated by the red circle) can be seen drifting to the right at a speed of ~26.7 µm/s as the bulk director on the LHS of the defect relaxes into the splayed state over time.

The simulated plots of the order parameter and director profile in Figures 7.6 and 7.7 respectively, were produced again in the absence of an externally applied field but after a relaxation time of ~0.234 seconds. Estimated calculations of time are obtained using typical viscosity parameters for the nematic host E7 (γ = 150 mPa s). Both plots reveal the ±1/2 defect drifting to the right towards the V-wall, as the device relaxes into the lowest energy splayed ground state, as seen in the experimental observations. As the computational space is equivalent to 25 µm, the drift distance in this time period is ~ 6.25 µm, which corresponds to a zero-field wall-drift-speed of ~26.7 µm/s.

Figures 7.8 and 7.9 show plots of the order parameter and director profile respectively under the subsequent application of a small electric field after 0.234 seconds that is sufficient to hold the defect's position. The plots were produced after a total time of ~0.47 seconds. The director profile in Figure 7.9 illustrates that the region

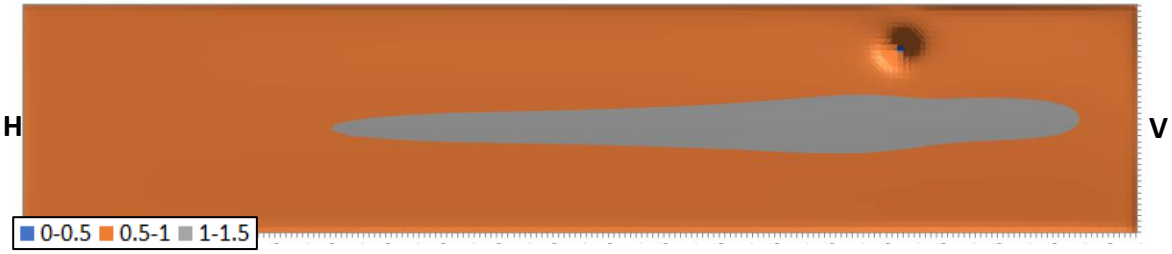


Figure 7.8. A simulated plot of the order parameter after a total time of ~0.47 seconds under the application of a small electric field strength after 0.234 seconds sufficient to 'freeze-in' the defect's position. The region that was previously in the splay state (left of the defect) has switched into the asymmetric H state under the applied voltage, thus the defect drifts towards the cell surface. The central grey region denotes an increase in the bulk macroscopic order above its equilibrium value. Scale in arbitrary units.



Figure 7.9. The simulated director profile after a total time of ~0.47 seconds under the application of a small voltage after 0.234 seconds sufficient to 'freeze-in' the defect's position. The region that was previously in the splay state (left of the defect) has switched into the asymmetric H state under the applied voltage, thus the defect (indicated by the red circle) drifts towards the cell surface.

previously in the splay state on the LHS of the defect has switched into the asymmetric H state under the applied field, changing the region of distortion to the upper cell surface in this instance. The visualization of the order parameter in Figure 7.8 shows clearly that the defect has drifted vertically towards the upper cell surface as a consequence of the bulk (LHS) transition to the H_a state.

Lastly, Figures 7.10 and 7.11 shows a plot of the order parameter and director profile respectively produced after a total time of ~0.94 seconds under the application of even higher electric field strengths after 0.47 seconds. The homeotropic alignment in the bulk due to the applied field has led to increased ordering, which can be seen in the central

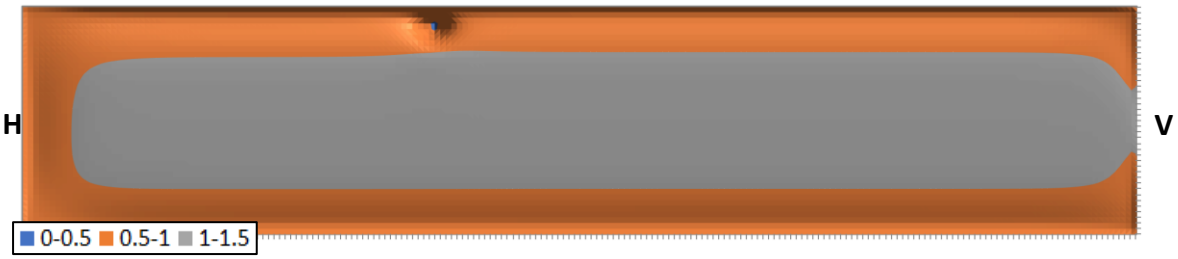


Figure 7.10. A simulated plot of the order parameter after a total time of ~0.94 seconds under the application of even higher electric field strengths after 0.47 seconds. The ±1/2 defect, which has drifted even closer to the cell surface due to the increased distortion in the H_a state, now moves 10.5 µm to the left at a speed of ~22.4 µm/s as the bulk director reorients into the bend state. The homeotropic alignment due to the applied field has led to increased ordering above the equilibrium value across the entire bulk of the device, which can be seen from the grey-coloured regions. Scale in arbitrary units.

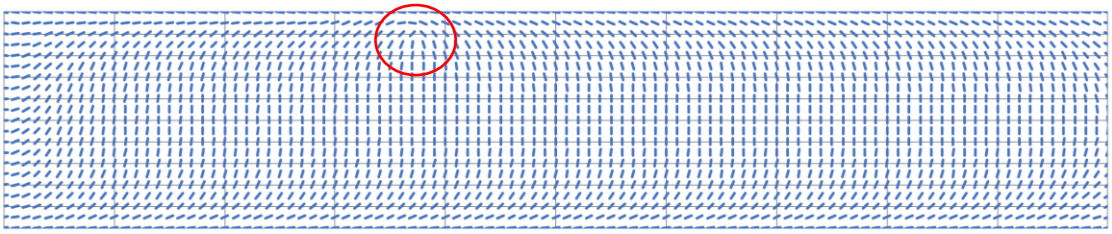


Figure 7.11. The simulated director profile after a total time of ~0.94 seconds under the application of even higher electric field strengths after 0.47 seconds. The ±1/2 defect, which has drifted even closer to the cell surface due to the increased distortion in the H_a state, now moves 10.5 µm to the left at a speed of ~22.4 µm/s as the bulk director reorients into the bend state.

grey regions of the plot. The defect has now drifted left in the direction of the H-wall, as the bend state becomes the lowest energy configuration for the director under this applied electric field. The drift distance is ~10.5 µm in the additional time of ~0.47 seconds from the previous defect position, giving a field-driven wall-speed of ~22.4 µm/s.

7.3.2. Polymer Cavities

Figure 7.12 shows a series of OPM images taken between crossed polarizers of the device containing the 50 µm diameter polymeric cylinder written in the H-state. The

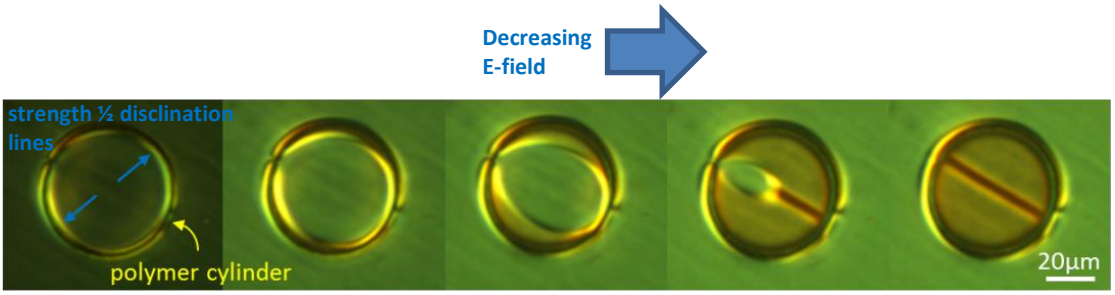


Figure 7.12. A series of optical polarizing microscope (OPM) images taken between crossed polarizers showing the evolution of a 50 µm diameter polymeric cylinder as the applied electric field is reduced from 2 V/µm to zero. Defects (thin disclination lines) can be seen as they nucleate from the polymer structure, separating the topologically discontinuous states.

sequence of images in Figure 7.12 were captured as the electric field strength was reduced from a large value (2V/µm) which had been use to form the bend state within the region of the cylinder. At the end of the sequence the region within the cylinder has collapsed into the H_a state.

Starting from the first image in the series (far left), the bulk region enclosed within the structure retains the bend alignment whereby the H-state nucleates from the polymer regions as the applied electric field is reduced. This nucleation process leads to the generation of two thin disclination lines separating the topologically discontinuous H_a and V states. The defects can be tuned with small perturbations to the applied electric field, such that the emerging regions of asymmetric H state grow or shrink accordingly. At an applied electric field strength of 0.36 V/µm corresponding to the penultimate image in the series, the two H_a states coalesce leading to the formation of a thick boundary line parallel to the device's rubbing direction. At this stage, it is no longer possible to electrically tune the defects as the bulk LC alignment within the polymer cavity relaxes into the H_a-state (final image in series). Note that the boundary wall appears significantly thicker than the disclination line separating the H- and V- states.

Figure 7.13 shows an illustrative schematic of the director profile between the two asymmetric H states and the H_a and V-states. Despite the continuity between the H_a states, the boundary between the two covers a much larger region than the defect (red circle), which appears due to a discontinuity in the alignment between the topologically distinct H_a and V-states.

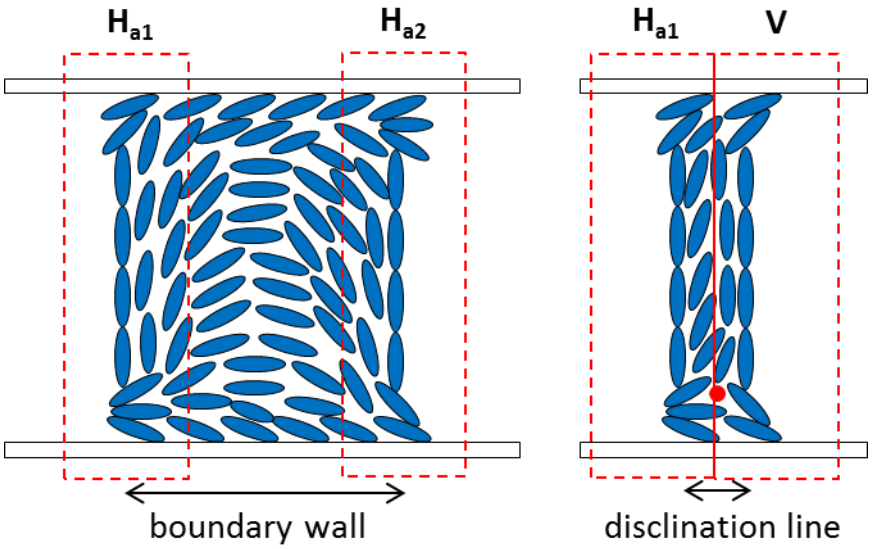


Figure 7.13. The thick boundary wall and thin disclination line. The illustrations of the director profile between the Ha1 and Ha2 states reveal the extent of the boundary wall, but also the continuity in the LC alignment. The region of discontinuous alignment between the Ha and V-states generates a defect in the form of a disclination line.

The cylindrical polymer cavity shown in Figure 7.12 is partially discontinuous on the top left of the structure as the focal spot of the laser did not return to its exact initial position. This morphology appears to pin the ±1/2 defect such that the H_{a1}-H_{a2} boundary wall seeds out of the opposing end of the H-cavity, parallel to the rubbing direction of the device. To investigate further how the morphology of the H-cylinder modifies the behaviour of the different interfaces, another polymer cavity was fabricated in the H-state that was fully continuous i.e. the laser focus returned to its initial position. Figure 7.14 shows a sequence of OPM images taken as the electric field was (a) decreased and

then (b) increased, after driving the bulk device into the bend state. The same behaviour is observed in terms of the tuning of the size of the defect within the polymer cavity with increasing/decreasing externally applied electric field strengths. However, in this instance the H_{a1}-H_{a2} boundary wall that separates the two asymmetric H states can be seen to emerge from both sides of the polymer cavity, again parallel to the rubbing direction. This observation confirms the fact that the morphology of the polymer structure does impact the defect dynamics as the defect is no longer pinned to one side of the polymer cylinder but forms a continuous disclination loop within the cavity. Upon increasing the electric field strength, the disclination loop grows in size and the asymmetric H states switch to the bend state as seen in the final image of Figure 7.14 (b).

Figure 7.15 shows a series of OPM images taken when the applied electric field is removed after the device containing the polymer cylinders was initially in the bend state (left to right). In this case, the H_{a1}-H_{a2} boundary wall does not form as the bulk LC collapses directly to the lowest energy splay state. The disclination lines shrink symmetrically within the H-written polymer cavity until they are annihilated, as the entire central region relaxes into the H-state.

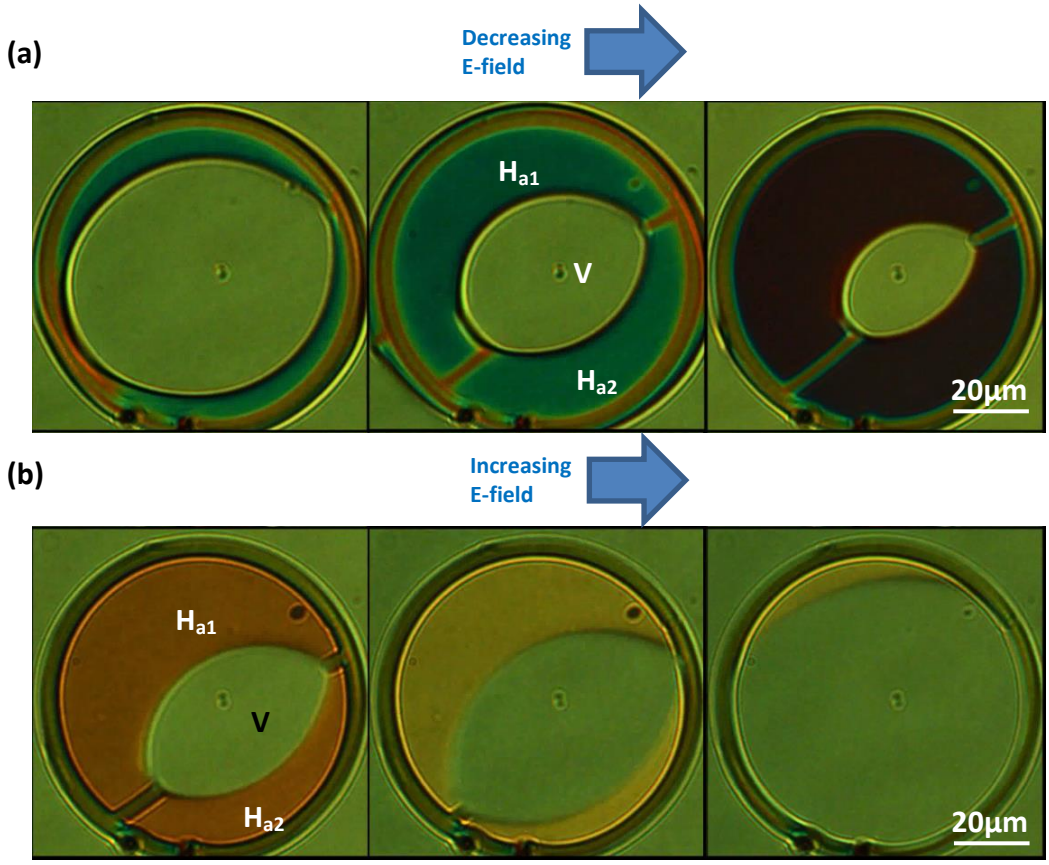


Figure 7.14. Continuous polymer cavity. A series of OPM images showing the LC alignment within a continuous 100 µm-diameter polymeric cylinder when the surrounding bulk is electrically driven into the bend state. (a) As the applied electric field is decreased (left to right), the asymmetric H states nucleate from the polymer cylinder walls, separated by the H_{a1}-H_{a2} boundary wall and the disclination lines shrink in size. (b) As the applied electric field is increased (left to right), the disclination lines grow and the bulk LC confined within the polymer cavity switches into the bend state.

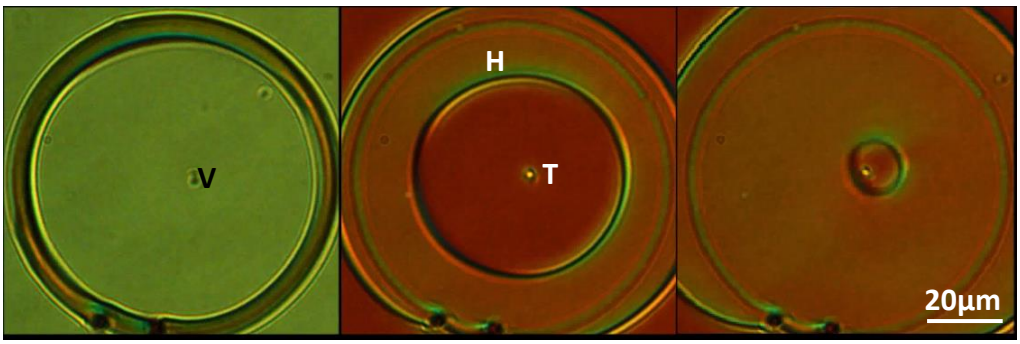


Figure 7.15. Continuous polymer cavity. OPM images showing the LC alignment within a continuous 100 µm-diameter cylinder that was written in the H-state, collapsing from the bend into the splay state upon removal of the applied electric field. Only the HV disclination loop can be seen in this instance as the H-state seeds out of the cylindrical walls.

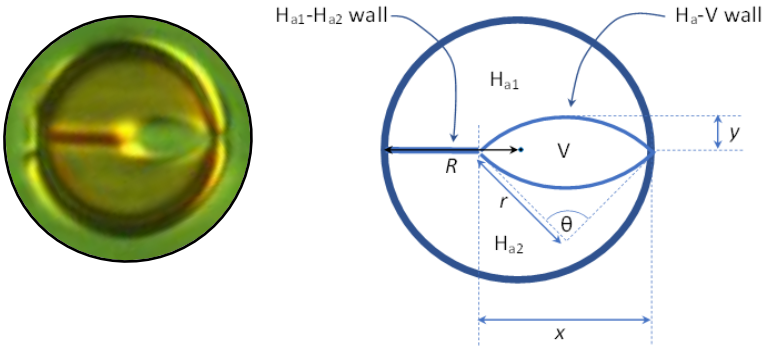


Figure 7.16. A schematic illustrating the system set-up to model the cylindrical polymer cavity 'locking-in' the H-state. The cylinder encompasses the asymmetric H states (H_{a1} and H_{a2}), separated by the region of bend alignment (V-state) that grows under increasing electric field strengths. For a cylinder of radius *R*, the variable *x* can be in the range from zero to 2*R* while y can vary from zero to *x*/2 under the application of increasing electric field strengths. Inset: OPM image of the polymer cavity corresponding to the illustration.

7.3.2.1. Analytical Model

The surface anchoring and boundary conditions enforced by the polymeric cylinder results in a complex interplay between the elastic forces, whereby the disclination lines shrink to compensate for the cost in elastic energy at the boundary of the H_a-V states when the applied electric field is reduced, and conversely grow as the electric field is increased. The polymer cavities were modelled according to the system illustrated in Figure 7.16, which corresponds to the partially discontinuous cylindrical structures presented in Figure 7.12. The cylinder on which the H-state is pinned is defined by a circle of radius *R*, and the electrical tuning of the defect is represented by the circular segment that is defined by the *x* and *y* variables, whereby *x* can vary from zero to 2*R* while *y* can vary from zero to *x*/2.

A relationship between *x* and *y* and the radius of the circular segments that separates the H_a and V states, valid provided $y \leq x/2$, can be written as

$$r = \frac{x^2+4y^2}{8y}. \tag{7.21}$$

The angle subtended by the circular segment is given by

$$\theta = 2\sin^{-1}\left(\frac{x}{2r}\right). \tag{7.22}$$

The area of the V-state can then be written as

$$A_V = 2 \times \left\{\frac{r^2}{2}(\theta - \sin\theta)\right\}, \tag{7.23}$$

while the area of the H_a state (a combination of H_{a1} and H_{a2}) can be written as

$$A_{Ha} = \pi R^2 - A_V. \tag{7.24}$$

The total length of the H_a - V walls is then

$$L_{VH} = 2 \times r\theta, \tag{7.25}$$

and the length of the H_{a1} - H_{a2} wall is given by

$$L_{HH} = 2R - x. \tag{7.26}$$

These areas and lengths can be used to define the regions and walls involved in terms of the *x* and *y* parameters. The next stage of the model involves estimating the energies associated with the H-state, V-state and interface walls. The required H and V energies are energies per unit area for these regions, and the required H_{a1}-H_{a2} and H-V wall energies are energies per unit length of these walls.

Energy Difference between H and V states:

The energies of the H_a and V state can be determined numerically or a simple estimate can be made of the magnitude of energy difference between these states. The energy difference is the critical term which drives the dominance of one or other state, rather than the absolute energies of the individual states. When a field is applied to the H_a and V states the principle difference between them is the region towards one surface, as shown in the lower part of the illustration in Figure 7.17.

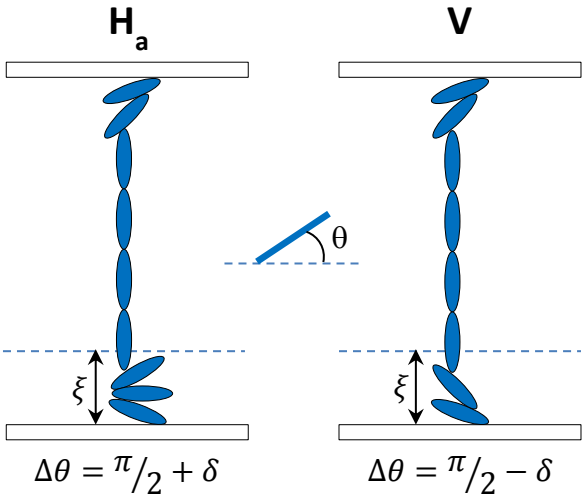


Figure 7.17. A schematic of the director profiles when the nematic pi-cell is in the asymmetric H-state (left) and V-state (right). The principle difference between the two illustrations is the region of distortion, ξ, near the lower surfaces whereby the tilt angle from the bulk to the surface orientation goes through a change of $\Delta\theta = \pi/2 \pm \delta$.

In the H_a state (left illustration), the distortion near the lower surface changes from the bulk orientation to the surface orientation through a change in angle of π/2 + δ, where δ is the surface pre-tilt. In the V-state (right illustration), the distortion near the lower surface changes from the bulk orientation to the surface orientation through a change in angle of π/2 - δ. The thickness of this transition region is likely to be the order of the field induced nematic coherence length. This can be determined in various ways (one approach is discussed in [1]). For example, one method involves starting with an energy expression as follows,

$$F = \int_0^\infty \frac{1}{2}\left[K\left(\frac{\partial\theta}{\partial z}\right)^2 - E_z{}^2\varepsilon_0\Delta\varepsilon\sin^2\theta\right]dz. \tag{7.27}$$

An Euler-Lagrange equation can then be developed as

$$K\frac{\partial^2\theta}{\partial z^2} + E_z{}^2\varepsilon_0\Delta\varepsilon\sin\theta\cos\theta = 0, \tag{7.28}$$

for which a standard solution can be sought of the form

$$\theta(z) = \frac{\pi}{2} - 2\tan^{-1}\left(e^{-\frac{z}{\xi}}\right). \tag{7.29}$$

In this way, it is possible to determine the thickness of the transition region as

$$\xi = \frac{1}{E_z}\sqrt{\frac{K}{\varepsilon_0 \Delta\varepsilon}} \equiv \frac{d}{V}\sqrt{\frac{K}{\varepsilon_0 \Delta\varepsilon}}, \tag{7.30}$$

where the overall device thickness is *d*, such that $E = V/d$ is the applied electric field. Alternatively, assuming that the transition region takes places through a linear change in angle from zero to π/2 then the thickness of the region becomes

$$\xi \approx \frac{\pi}{2E}\sqrt{\frac{K}{\Delta\epsilon\epsilon_0}} \tag{7.31}$$

The elastic energy difference per unit area between the states can then be estimated as

$$\Delta U \approx \frac{K}{2}\left\{\left(\frac{\frac{\pi}{2}+\delta}{\xi}\right)^2 - \left(\frac{\frac{\pi}{2}-\delta}{\xi}\right)^2\right\}\xi. \tag{7.32}$$

Substituting 'typical' values, such as those shown in Table 7.1, into the expression in (7.32) shows that the energy difference ΔU ~ 10^5 K per area at moderate fields. It is worth nothing however that this energy difference could be still larger at higher fields and vanishes at lower fields.

$\boldsymbol{\delta}$ **(rads)**	$\boldsymbol{\xi}$ **(μm)**	$\boldsymbol{\Delta U \times 10^5 (Jm^{-2})}$
$\pi/36$	2.5	1.1 K
$\pi/36$	2.0	1.4 K
$\pi/36$	1.5	1.8 K
$\pi/36$	1.0	2.7 K

Table 7.1. The transition region decreases as the applied electric field increases, since the bulk director tends towards homeotropic alignment at higher field strengths. Substituting 'typical' values for the transition region of thickness ξ estimated for a 5 μm - thick device with 5° surface pre-tilt (δ) into equation (7.32) shows that the energy difference per area, ΔU, is the order of 10^5 K in terms of the elastic constant *K*).

H-V wall energy:

According to deGennes [1], the line energy of the region around a defect can be expressed as

$$F = \pi K m^2 \ln\left(\rho_{max}/a\right) \tag{7.33}$$

where m is the magnitude of the defect strength (±1/2 in the case of the bend-splay distortion), a is a lower length-scale limit of the order of a molecular dimension and ρ_{max} is an upper length scale limit representing the overall size of the defect and the main elastic distortion around it. For values of a ~1 – 2 nm and ρ_{max} ~ 1 - 2 μm, the expression in (7.33) gives $F \sim 5K$. Although this does not include the defect core energy, deGennes suggests that this additional energy per unit line length is the order of the elastic constant ~K [1]. Together, this gives a total H-V wall energy of $U_{HV} \sim 6K$ per unit length; dominated by the strong distortion in the vicinity of the defect core, this energy may not be a strong function of the applied field.

H_{a1}-H_{a2} wall energy:

The H_{a1}-H_{a2} wall involves substantial bend-splay distortion through an angle change of π across the wall, extending through the thickness of the device. For a 5 μm-thick device with a wall of similar width, the contained energy per unit length is given by

$$U_{HH} \sim \frac{K}{2}\left(\frac{\pi}{d}\right)^2 \times d \times d, \tag{7.34}$$

where d is the device thickness. The relation in (7.34) results in a line energy of ~5 K per unit length. However, under large electric field strengths this wall is likely to be squeezed, increasing the energy further. Therefore, in practice the energy per length is field dependent such that $U_{HH} > \sim 5K$.

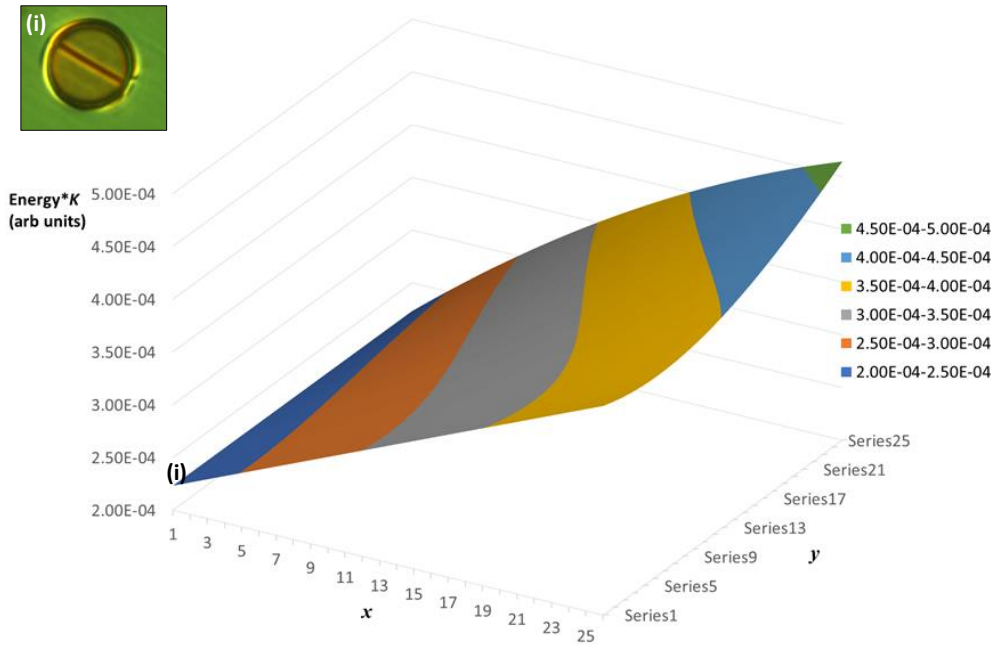


Figure 7.18. An energy surface plot representing a low applied voltage across the polymer cavity, produced using the control parameters $\Delta U = 10^5 K$, $U_{HH} = 5K$ and $U_{HV} = 6K$. Inset: OPM image corresponding to the minimum energy at (i) $x \rightarrow 0$, where the device is in the H_a state with a H_{a1}-H_{a2} boundary across the centre.

Energy Surface Plots:

Energies were plotted in terms of x (varying between 0 and $2R$) and y as a fraction of its maximum value (varying between zero and $x/2$). A series of plots are produced using arbitrary estimates of the energies as control parameters that are scaled to an elastic constant K, where ΔU from (7.32) is the energy difference per unit area between the H_a state and the V state, U_{HV} estimated from (7.33) is the energy per unit length of the H-V wall and U_{HH} from (7.34) is the energy per unit length of the H_{a1}-H_{a2} wall.

The plot in Figure 7.18 shows the case that might represent a lower applied voltage, when the control parameters are $\Delta U = 10^5 K$, $U_{HH} = 5K$ and $U_{HV} = 6K$. A clear minimum can be seen at $x = y = 0$, such that there is no circular region of V-state within the polymer cavity according to the system set-up in Figure 7.16. Therefore, the lowest energy region resembles the OPM image inset in Figure 7.18 whereby the device is in

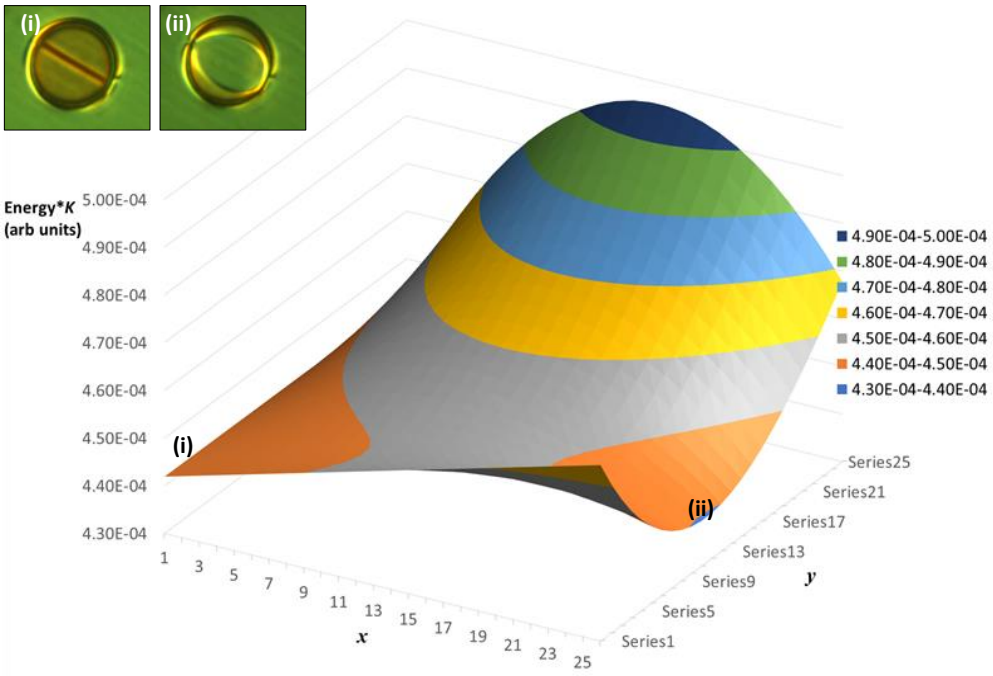


Figure 7.19. An energy surface plot representing a moderate voltage applied across the polymer cavity, produced using the control parameters $\Delta U = 1.7 \times 10^5 K$, $U_{HH} = 11K$ and $U_{HV} = 6K$. Inset: OPM images corresponding to the two energy minima at (i) $x = y = 0$, where the alignment within the cavity is in the H_a state with a H_{a1}-H_{a2} boundary across the centre, and (ii) $x = 2R$, $y \sim x/5$, where the bulk LC is in bend alignment and the H_a state can be seen nucleating from the topologically continuous planar anchoring at the LC-polymer interface. The energy barrier separating (i) and (ii) suggests that the device would remain in its previous state i.e. at the closest minimum energy state.

the H_a state, with a H_{a1}-H_{a2} boundary wall across the centre, as observed experimentally at lower applied electric fields.

The energy surface plot in Figure 7.19 represents a higher applied voltage with estimated control parameters of $\Delta U = 1.7 \times 10^5 K$, $U_{HH} = 11K$ and $U_{HV} = 6K$. Here, the energy difference between the H and V-states and the H_{a1}-H_{a2} wall energy are both increased, while the HV-wall energy is kept constant as it is not expected to be a strong function of the applied electric field. The plot reveals two minima; one at $x = 0$ as before for the lower applied voltage case, and the second with x at its maximum value and $y \sim x/5$. The inset OPM images show the two LC alignments that correlate to these x and y parameters. The key result here is that the two minimum energy states are

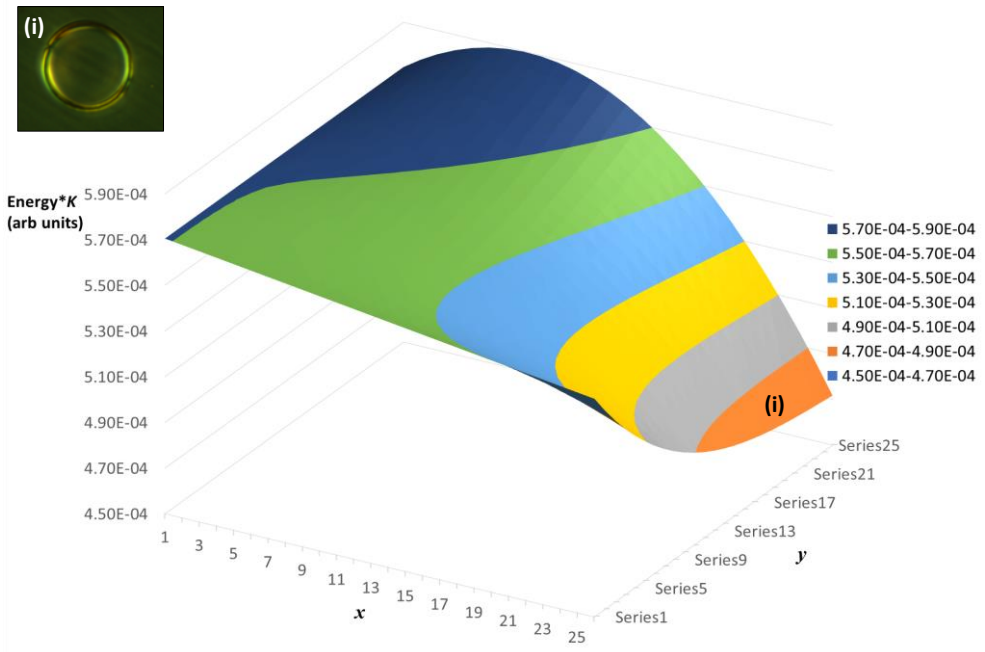


Figure 7.20. An energy surface plot representing a high voltage applied across the polymer cavity, produced using the control parameters $\Delta U = 2.5 \times 10^5 K$, $U_{HH} = 13K$ and $U_{HV} = 6K$. Inset: OPM image corresponding to the minimum energy at (i) $x = 2R$, $y = x/2$, where the bulk LC within and surrounding the planar aligned polymer cavity is in the bend state.

separated by an energy barrier, such that the device may remain in the previous state i.e. the lower applied voltage case with the H_{a1}-H_{a2} wall across the centre of the cavity. This is in agreement with the experimental observations whereby it is necessary to drive the device into the bend state with a sudden voltage input in order to overcome this energy barrier. Gradually decreasing the applied electric field then generates the second minimum energy state where $x = 2R$ and $y \sim x/5$. Equally, if the applied voltage is decreased further until the H_{a1}-H_{a2} boundary wall forms (as shown in the penultimate image of Figure 7.12), then it is no longer possible to electrically tune the defect as the bulk LC within the polymer cavity collapses into the other minimum energy state (i) consisting of the two H_a states separated by the H_{a1}-H_{a2} boundary wall.

Figure 7.20 shows the surface at even higher applied voltages with example

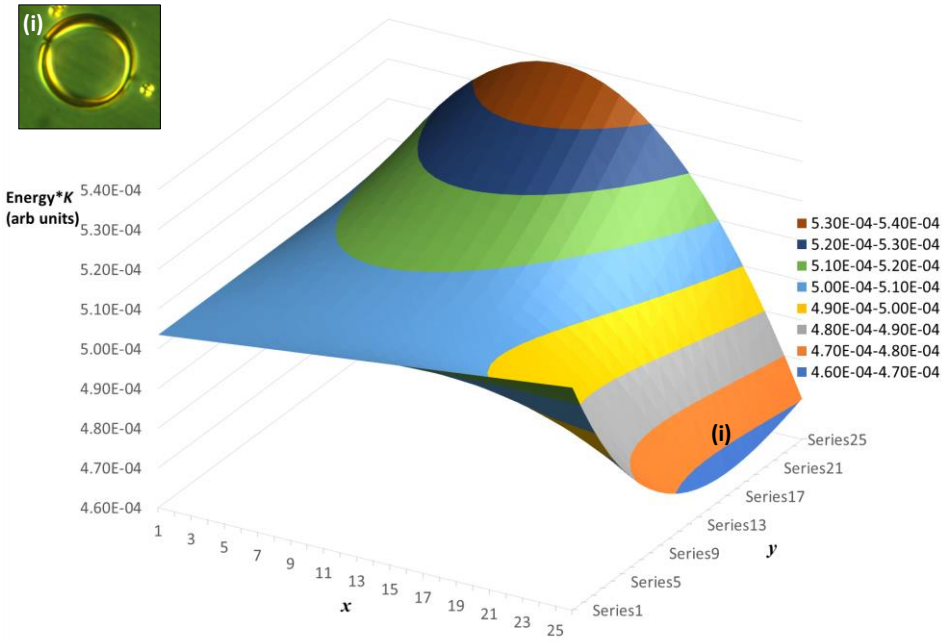


Figure 7.21. An energy surface plot of the polymer cavity representing a slightly reduced applied voltage from the data in Figure 7.20, produced using the control parameters $\Delta U = 2.2 \times 10^5 K$, $U_{HH} = 11.5K$ and $U_{HV} = 6K$. Inset: OPM image corresponding to the minimum energy at (i) $x = 2R$, $y < x/2$, where the bulk LC is in bend alignment and the H_a state can be seen nucleating from the topologically continuous planar anchoring at the polymer cylinder.

parameters of $\Delta U = 2.5 \times 10^5 K$, $U_{HH} = 13K$ and $U_{HV} = 6K$. Again, the HV-wall energy is kept constant while the other two energy parameters are increased. The minimum energy is now with x and y at their maximum values ($x = 2R$, $y = x/2$), such that the V-state extends over the entire area of the cylinder as demonstrated by the inset OPM image.

Lastly, the plot in Figure 7.21 is with a slightly reduced applied voltage obtained using control parameters of $\Delta U = 2.2 \times 10^5 K$, $U_{HH} = 11.5K$ and $U_{HV} = 6K$. Here, the parameters have been decreased slightly from the state in Figure 7.19. As a result, the minimum is with x at its maximum value ($2R$), but y at a smaller value. There is also another minimum with x at its lowest value of zero, although this is a higher energy minimum. Therefore, x would extend across the cylinder with $y < x/2$, which can be

seen in the inset OPM image. It is worth noting that when the voltage is further reduced, the device returns to the H_{a1}-H_{a2} state as the lowest energy. In practice, this state occurs through the growth of the H_{a1}-H_{a2} boundary wall, although that mechanism is not reproduced by this simple analysis.

7.3.3. Arrays & Concentricity

In order to gauge whether the behaviour of the defects depends on the size of the polymer structures, arrays of polymer cylinders were fabricated with different diameters. Figure 7.22 shows a set of three 40, 30 and 20 µm-diameter polymeric cylinders. The series of OPM images were taken after applying a sudden voltage input, which decreases the transition time to the bend state, and subsequently decreasing the applied electric field strength.

The two H_a states that are topologically continuous with the planar-aligned polymeric structures emerge from the walls of the cylinders, as seen previously. In this example, the fabricated cylindrical structures are partially discontinuous (c.f. Figure 7.12) therefore the H_{a1}-H_{a2} boundary wall nucleates from one side of the cylinder, parallel to the rubbing direction, and the discontinuity in the structure pins the ±1/2 defect at the opposing end.

It is clear from the sequence of images that the smaller diameter cylinders lead to the generation of the ±1/2 strength defect and subsequent coalescence of the two H_a states earlier on (i.e. at larger applied electric field strengths). One of the 30 µm diameter cylinders spontaneously collapses into the H_a states at a fairly high voltage (V = 2.75 Vrms or E = 0.55 V/ µm) relative to the other structures. Moreover, all of the 20 µm cavities collapse into the H_{a1}-H_{a2} states separated by the boundary wall by the fourth

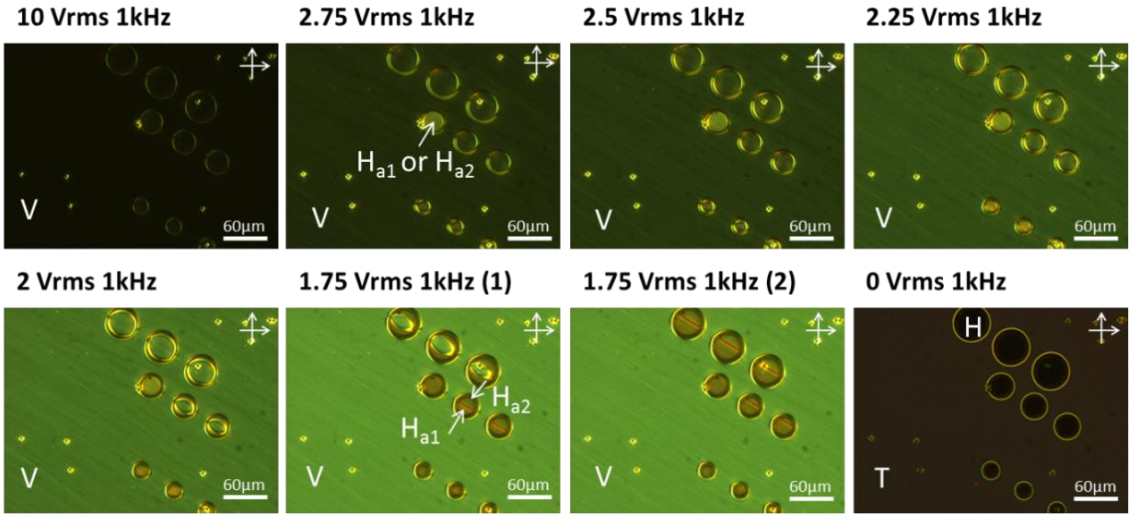


Figure 7.22. A series of OPM images taken between crossed polarizers showing a set of three 40, 30 and 20 µm diameter polymeric cylinders that were written in the H-state and imaged as the applied electric field is reduced from 2 V/µm (10 Vrms) to zero.

image in the series. Therefore, there is limited tuning of the defects within smaller cavities. This is due to the increased cost in energy required to 'hold' the topologically discontinuous bend and splay states within a smaller cavity, resulting in limited tuning of the defects relative to the larger cavities. However, the overall behaviour of the director is consistent between the different sized structures indicating that the diameter at these scales (i.e several times larger than the device thickness) is not significant. The final image in the sequence of Figure 7.22 was taken as soon as the electric field was removed (before the device had time to relax to the ground state), revealing the collapse of the alignment within the bulk and the polymer cavities to their topologically continuous counterparts i.e. the transient twist state and splay states, respectively.

So far, the work in this chapter has covered polymer structures that were separately, in either the bend or splay states. Figure 7.23 shows two microscope images of concentric structures that 'lock-in' a state within a state. The image on the left of Figure 7.23 contains H-V concentric squares, whereby the outer square was written in the

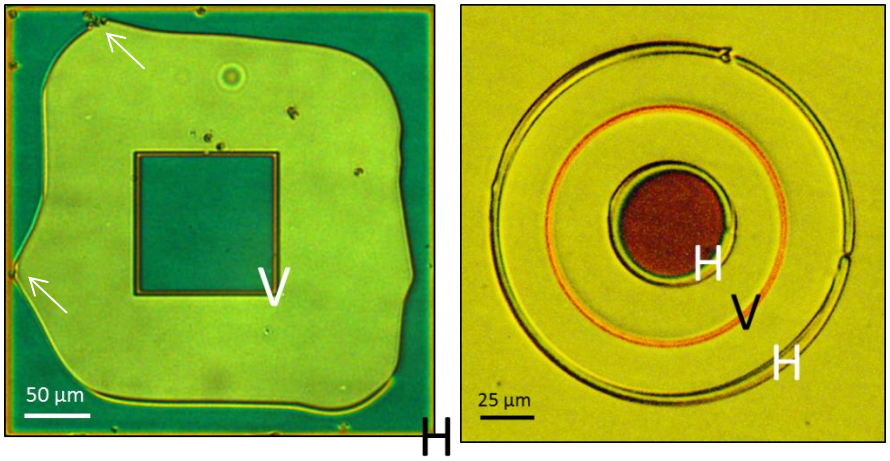


Figure 7.23. OPM images showing concentric polymer structures written in the H and V states (as labelled). Left: The image was taken under the application of 1.7 Vrms square wave. The H-V defect wall can be seen as it nucleates from the H-polymer square. The white arrows indicate pinning of the defect by the spacer beads. Right: The image was taken upon removal of an applied electric field, whereby the bulk LC alignment has collapsed into the twist state, while the LC confined within the inner polymer cavity that has planar anchoring is in the splay state.

ground splay state, and the inner square written in the bend state at a separation of 100 µm. The image was taken once the disclination line appeared 'frozen-in' at an applied voltage of ~1.7 V.

The image on the right of Figure 7.23 shows H-V-H concentric rings, whereby the rings were written in the splay, bend and splay states from the outer to inner rings, respectively. The image was taken upon removal of an applied field, after the device was driven into the bend state, where the bulk LC has collapsed into the transient twist state. Despite the bulk alignment, the planar anchoring of the inner polymer cylinder has promoted the collapse of the LC confined within the cavity into the splay state. This is also in agreement with observations of the H-polymer cavities in Figure 7.22 that instantaneously collapsed into the splay state upon removal of an external electric field. It is worth noting that the spacer beads (used to ensure a consistent device thickness in the manufacturing process) were found to interfere with the tuning of the defects such that the disclinations lines would become pinned at the spacer beads (indicated by the

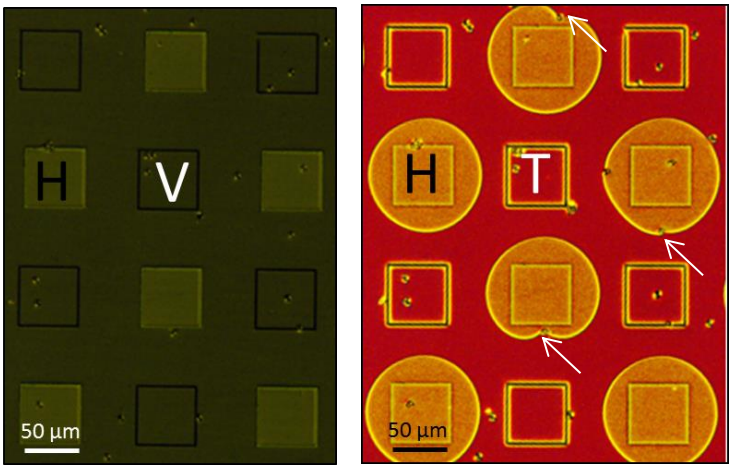


Figure 7.24. A checkerboard of square-shaped polymer structures that were written in the H and V states. Left: As the applied electric field is decreased, regions of LC within the square-shaped polymer cavities collapse into the lower energy H-state, while the remainder of the bulk is aligned in the V-state. Right: Defects are seen to nucleate out of the structures written in the H-state upon removal of the applied electric field, while the bulk alignment collapses to the transient T-state. The white arrows indicate pinning of the defect by the spacer beads.

white arrows). Fabricating devices that have the spacer beads within the glue at the edges of the substrates rather than dispersing them in the bulk would minimize the presence of additional defect sites that disrupt the movement of the disclination lines.

Lastly, Figure 7.24 shows OPM images of a checkerboard of H-V square-shaped polymer cavities taken in the bend state (left) and upon removal of an applied electric field (right). Under the application of an electric field, the bulk LC within the H-squares collapse into the H_a state while the rest of the device remains in the bend state. Upon removal of the applied field, the defects seed out of the H-squares while the regions that were previously in the bend state collapse into the topologically continuous twist state. Although the disclination lines appear pinned to the spacer beads (indicated by the white arrows), regions without spacer beads reveal homogeneous tuning of the defect such that its size and position can be controlled to high precision. Moreover, the fabrication of arrays and more complex, concentric structures demonstrates that it is

possible to confine topologically discontinuous LC states to different regions within a device, whilst having the additional control of localizing the high energy defect separating the two regions. The level of control resultant from the fabrication of topologically distinct polymer structures shows great potential to control other materials dispersed within a liquid crystalline host medium. The next section addresses the potential that this technique has in localizing colloidal particles within tunable defects.

7.3.4. Colloidal Dispersions

Colloidal particles of a similar density to their LC host tend to drift toward the strong distortion field associated with disclination lines [19-21]. Thus, particles dispersed into a nematic pi-cell device are expected to localize at the defect cores. The ability to electrically tune the position of these defects through the fabrication of polymer structures, as illustrated for instance between the H-V polymer walls in §7.3.1, should in turn present the possibility of controlling the position of colloidal particles situated within the defects.

Figure 7.25 shows the bright and dark states of a pi-cell device filled with the fluorescent nanoparticles that were dispersed within the nematic host E7. The nanoparticles are only visible on the microscope when they form aggregates, as seen in both (a) and (b) of the OPM images of Figure 7.25. It was found that increasing and decreasing the applied electric field strength results in the nanoparticles moving back and forth, the direction of which is indicated by the blue arrows. However the pinning of the disclination lines at the spacer beads disrupts the movement of the particles.

The device presented in Figure 7.25 did not include any fabricated polymer structures but was investigated as a proof-of-principle to observe whether the colloidal

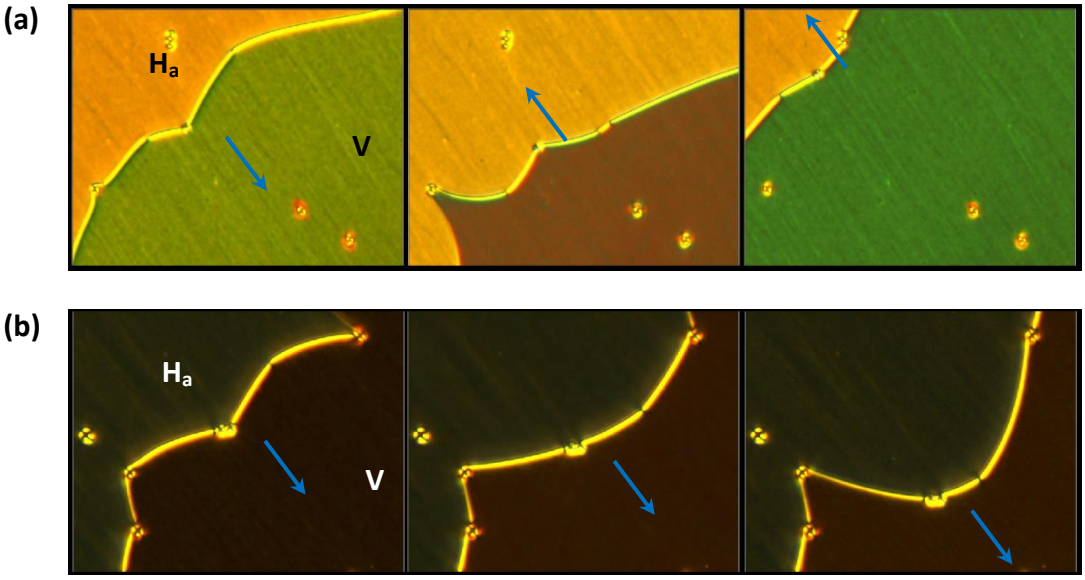


Figure 7.25. A sequence of OPM images taken when the device was oriented (a) 45° and (b) 0° to the polarizer. The images show aggregates of fluorescent nanoparticles trapped at a defect site; their location can be controlled by electrically tuning the position of the defect through perturbations in the applied electric field (indicated by the blue arrows). The stationary particles seen in the surrounding bulk of the images, and to which the disclination lines are pinned, are spacer beads that dictate the device thickness.

particles would migrate to the distortion field of the ±1/2 topological defect. The second colloidal mixture (c.f. §7.2.1 for further details) was also capillary-filled into a pi-cell device that did not contain polymer structures (not shown here), to ensure that they behaved in the same way. Despite silica having approximately double the density of E7 [21], the position of the particles could still be tuned with the defect.

Based on the findings above, namely that the fluorescent nanoparticles could not be imaged unless they were in clusters, the silica-based colloidal mixture was selected to investigate how the particles would be tuned between the fabricated polymer structures. After laser writing and characterization under the microscope, the device containing the polymer structures was immersed in a bath of acetone overnight in order to remove the LC-monomer mixture. Once the washing out stage was complete, the resultant template was capillary-filled with the SiO_2-E7 mixture in the isotropic phase.



Figure 7.26. The sequence of OPM images taken upon removal of an applied electric field reveal a 1 μm-diameter silica bead trapped within a defect between the H-V polymer walls. The position of the silica bead is dictated by the movement of the defect, from left to right as the device relaxes into the lower energy ground splay state.

Figure 7.26 shows microscopes images taken after refilling the template containing the fabricated polymeric structures with the SiO_2-E7 mixture. The sequence of OPM images show the silica bead being swept from left to right between the HV-polymer walls, as the device relaxes into the splay state upon removal of an applied field. The geometry and polarity of the particle trajectory is clearly dictated by the design of the fabricated structure, whereby the silica bead appears trapped between the two polymer walls and its position can be tuned in both directions depending on the size of the applied field. Once the silica bead was deposited at the V-polymer wall however, it was no longer possible to further control its position with the applied electric field. Additionally, it was not possible to observe the tuning effect of the colloids within the 'closed' structures i.e. the polymer cavities and concentric rings, as the colloids were too large to drift through the porous polymer network.

Re-capturing colloidal particles after they had drifted away from the vicinity of a defect core due to their deposition at an interface (substrate/spacer bead/polymer structure) was non-trivial. The colloids also tended to sink to the substrate over time. The director profiles in §7.3.1.1 illustrated the changing position of the defect as it drifts vertically from the bulk to the cell surfaces when the device is switched from the H to H_a states. Therefore, any colloids trapped within a defect would eventually be dragged

to one of the cell surfaces during electrical tuning of the defect position. One potential solution might involve working in the low voltage regime to prevent H_a state drifting to particle to substrate

7.4. CONCLUSIONS

The generation of electrically tunable topological defects has been demonstrated experimentally and theoretically through the fabrication of polymeric structures of varying shapes and sizes by direct laser writing in-situ in a nematic pi-cell device. The defects form as a consequence of the difference in elastic energy occurring at the voltage transition between two topologically distinct states. Numerical and analytical models have been developed to describe the behaviour of the defects under different voltage conditions, which show good agreement with the experimental observations.

An extension of the work on electrically tunable defects has shown that it is possible to control the position of particles by localizing them at the defect sites, thereby enhancing the functionality of the LC device. The potential applications of the colloidal systems ranges from the generation of switchable nanowires by dispersion of conductive particles in the LC matrix to form a micro-necklace at the defect site [21] to studies of aggregation-induced emission (AIE) using photoluminescence (PL) measurements [22, 23]. For example, quantum dots (QDs) possess remarkable electro-optic characteristics as highly efficient semi-conductors whereby their emission can be tuned in accordance with their size. Yet, the functionalization of QDs is vital to prevent quenching of their fluorescence through the formation of aggregates. It would therefore be informative to carry out studies on the change in their emissivity as the QDs approach one another. More recently, QDs demonstrating AIE have also been

synthesized, yet their behaviour is not fully understood and there are conflicting reports of whether aggregation does in fact cause quenching or fluorescence. Therefore, utilizing a system such as that presented in this chapter, whereby in-situ tuning of the particle position would be possible at low applied voltages, may prove informative for academic studies of different emissive materials.

7.5. REFERENCES

[1] P. G. de Gennes and J. Prost, *The Physics of Liquid Crystals*, 2nd Edition, Clarendon Press, Oxford (1993).

[2] C. Peng, T. Turiv, Y. Guo, Q.-H. Wei, O. D. Lavrentovich, *SCIENCE*, **354**, 882 (2016).

[3] H. Kikuchi, M. Yokota, Y. Hisakado, H. Yang and T. Kajiyama, Nat. Mater. 1, 64 (2002).

[4] F. Castles, F. V. Day, S. M. Morris and D-H. Ko, D. J. Gardiner, M. M. Qasim, S. Nosheen, P. J. W. Hands, S. S. Choi, R. H. Friend and H. J. Coles, *Nat. Mater.* **11** (2012).

[5] J. Xiang and O. D. Lavrentovich, *Appl. Phys. Lett.* **103**, 51112 (2013).

[6] X. Wang, Y.-K. Kim, E. Bukusoglu, B. Zhang, D. S. Miller and N. L. Abbott, *Phys. Rev. Lett.* **116**, 147801 (2016).

[7] Y. Li, E. Prince, S. Cho, A. Salari, Y. M. Golestani, O. D. Lavrentovich, *PNAS* **2017**, 114, 2137.

[8] J.-H. Kim, M. Yoneya, J. Yamamoto, H. Yokoyama, *Nanotechnology* **13**, 2155 (2002).

[9] J.-W. Park, J. Choa, E. L. Thomaas, *Soft Matter* **4**, 739 (2008).

[10] E. A. Shteyner, A. K. Srivastava, V. G. Chigrinov, H.-S. Kwok, A. D. Afanasyev, *Soft Matter* **2013**, 9, 5160.

[11] Y. Guo, M. Jiang, C. Peng, K. Sun, O. Yaroshchuk, O.Lavrentovich, Q.-H. Wei, *Adv. Mater*. **28**, 2353 (2016).

[12] R. B. Meyer, *Mol. Cryst. Liq. Cryst.* **16**, 355 (1972).

[13] E. M. Terentjev, *Phys. Rev. E* 51, 1330 (1995).

[14] S. Ramaswamy, R. Nityananda, V. A. Raghunathan and J. Prost, *Mol. Cryst. Liq. Cryst. Sci. Technol., Sect. A* **288**, 175 (1996).

[15] Y. Gu and N. L. Abbott, *Phys. Rev. Lett.* **85**, 4719 (2000).

[16] M. Skarabot, M. Ravnik, S. Zumer, U. Tkalec, I. Poberaj, D. Babic and I. Musevic, *Phys. Rev. E* **77**, 061706 (2008).

[17] C. Peng, T. Turiv, R. Zhang, Y. Guo, S. V. Shiyanovskii, Q.-H. Wei, J. de Pablo and O. D. Lavrentovich, *J. Phys.: Condens. Matter*. **29**, 014005 (2017)

[18] N. Mottram and C. Newton, *Soft Condens. Matter*. arXiv:1409.3542 (2014).

[19] D. Pires et al., *Phys. Rev. Lett*., **2007,** 98, 247801.

[20] Y.-K. Kim et al., *Nat. Comms.*, **2012**, 3, 1133.

[21] O. P. Pishnyak, S. Tang, J. R. Kelly, S. V. Shiyanovskii, O. D. Lavrentovich, *Phys. Rev. Lett*. **2007**, 99, 127802.

[22] H. Wang, E. Zhao, J. W. Y. Lam and B. Z. Tang, *Mater. Today*, **18**, 365 (2015).

[23] M. Mou, Y. Wu, Q. Niu, Y. Wang, Z. Yan and S. Liao, *Chem. Commun*. **53**, 3357 (2017).

8

RECONFIGURABLE OPTICAL ELEMENTS

8.1. INTRODUCTION

A range of multi-dimensional polymeric structures were presented in Chapter 5 to illustrate the versatility of the powerful in-situ direct laser writing (DLW) fabrication technique. Amongst these were cylindrical pillar-shaped polymer network structures written into a nematic pi-cell device. In this chapter, an extension of this work is presented through the fabrication of arrays of polymer pillars in a planar (anti-parallel rubbed) Fréedericksz cell under different applied voltages and with different lattice spacings. These variations result in the formation of polymer network structures that can be made 'invisible' at specific electric field amplitudes when addressing the liquid crystal (LC) device post-fabrication. An in-depth image analysis is carried out in L*a*b* colorspace in order to quantify the reconfigurable aspect of these birefringent structures under different voltage applications. A numerical model based upon the full Q-tensor theory that was developed in collaboration with the Physics of Soft and Partially Ordered Matter theoretical group [1] at the University of Ljubljana (Slovenia), was used to simulate the fabricated structures and their corresponding director profiles.

In recent years, there has been a growing interest in controlling the alignment and orientation of LC molecules using more elaborate fabrication techniques, resulting in the structuring of the nematic, chiral nematic and blue phase mesophases on the micron and potentially even the nanometre scale [2-7]. This has important implications in the design of photonic metamaterials, and structures for advanced display applications including 3D, augmented and virtual reality. While the process of rubbing a thin polymer layer has proved an effective method for aligning LCs, it does not allow for more complex arrangements and structuring of the LC phases to be realised. With the advent of new advanced manufacturing techniques, researchers have recently demonstrated an array of exciting new configurations including the creation of tunable 3D photonic crystals, gratings, lenses as well as complex topological structures that have been formed using plasmonic metamasks [2, 8-11].

Techniques that have been explored so far include the application of photo-alignment layers to create complex 2D spatial arrangements of the LC molecules in the form of circular and radial patterns, the distortion field of which can be used in the command of active matter (c.f. Chapter 7). These alignment methodologies have also enabled tunable LC axicons to be developed for controlling the beam characteristics of laser devices [12]. On the finest length scales, researchers have begun to use ever more sophisticated tools, such as atomic force microscopy (AFM) and e-beam lithography, to structure LCs on the nanometre scale [13-15]. This has paved the way for LCs as agile transformational optical elements that can mould the flow of light in photonic crystals, photonic crystal fibres, and optical micro- and nanocavities, but also key components that can alter the magnetic and dielectric properties in tunable metamaterials [16-18].

In this chapter, a single-step process is used to fabricate reconfigurable director profiles in polymerizable LC devices resulting in optical patterns that can be made to alter their appearance or disappear entirely with the application of a low voltage. These micron-sized polymer features have been encoded directly into LC devices using the DLW facility presented in Chapter 5, which is equipped with aberration correction to allow for sculpturing of the director profile in a fully-assembled device. By interrogating the devices with the same voltage amplitude that was used during fabrication, arrays of micron-sized pillars can be made to disappear as the director profile becomes continuous with the surrounding regions. Tailoring the voltage during fabrication can also remove or introduce different features at specific locations within the array. This work is also extended to demonstrate a micron-sized emoticon, which is formed in a polymerizable LC device that can be reconfigured by dialling in different voltages. The findings in this Chapter are potentially important in the development of new soft photonic materials for covert and security applications, advanced diffractive and transformational optical elements and novel metamaterials.

8.2. EXPERIMENTAL PROCEDURE

Unlike the photo-alignment and AFM/e-beam techniques, which are generally limited to sculpturing of the director profile either at or close to the surfaces, the aberration corrected DLW technique allows the director field to be altered directly within the bulk of the device, as already demonstrated in the previous three chapters. The fabrication process of writing polymer pillars is again illustrated in Figure 8.1 (a) (c.f. Figure 5.5 for a detailed schematic of the DLW optical set-up). Polymer pillars were formed in a photosensitive sample composed of 30 wt% reactive mesogen RM257 (Merck

Chemicals Ltd) and 1 wt% of the photoinitiator mixture IRG819 (Merck Chemicals Ltd dissolved in the nematic liquid crystalline host material, E7 (Merck Chemicals Ltd.). The LC host was selected on account of its positive dielectric anisotropy ($\Delta\varepsilon = 13.7$ at 1 kHz at a temperature of $T = 20°C$) that permits tuning of the macroscopic molecular configuration under externally applied electric fields (see Table A.3. of the Appendix). A 20 μm-thick planar (anti-parallel rubbed) Fréedericksz was capillary-filled with the mixture when in the isotropic phase on a hot-plate at $T = 70°C$. After cooling to room temperature, the LC device was mounted on the *xyz*-translation stage shown in Figure 8.1 (a) and connected to a waveform generator. Reactive mesogens in the device were polymerized upon exposure to the ultrafast pulses of laser light ($\lambda = 790$ nm), which were tightly focused into the sample by a 20× Zeiss objective lens with a 0.3 numerical aperture (NA) and a working distance of 2 mm. The laser was operated at a power of 26 mW and a repetition rate of 80 MHz. The pillars were formed sequentially using a 50 ms gate open time on the shutter.

As discussed in Chapter 5, the custom-built DLW set-up incorporates an adaptive optics element in the form of a phase-only LC spatial light modulator (SLM). This SLM plays a key role as it corrects for aberrations introduced by the mismatch in the refractive indices between the thick glass (0.7 mm-thick) walls and the comparatively thin, LC film that is sandwiched between them. Correcting for optical aberrations in the fully assembled LC device permits in-situ fabrication of the polymer network, whereby the resultant pillar-shaped polymer structures effectively ‘memorise’ the director alignment at the moment of exposure to the laser light. Voltage-dependent LC states can therefore be ‘frozen’-in to the network by electrically switching the device during the laser writing procedure. Due to the nonlinear nature of the two-photon polymerization

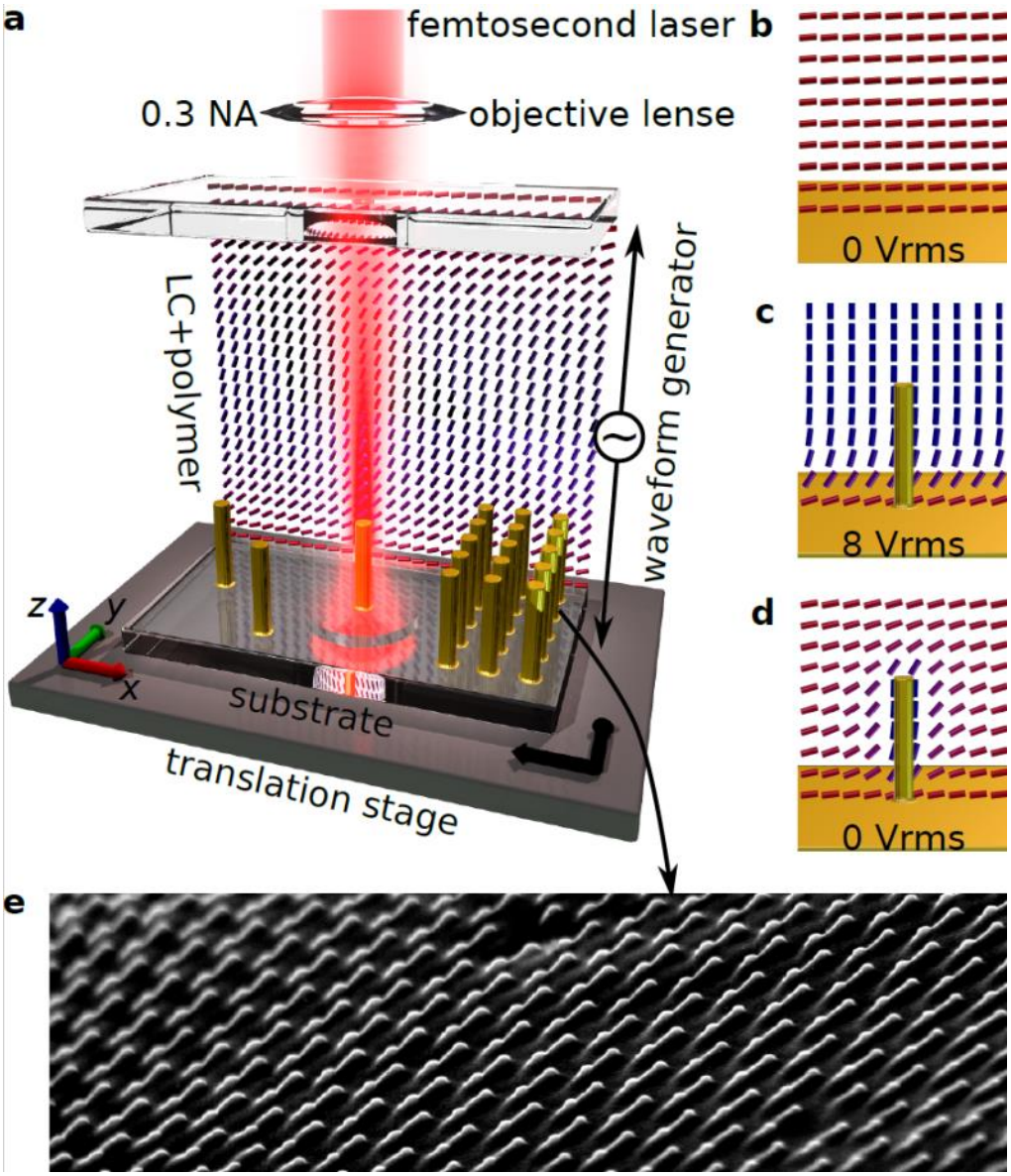


Figure 8.1. In-situ direct laser writing of birefringent structures in a polymerizable liquid crystal device. (a) Configuration of the direct laser writing technique: using a 0.3 NA objective lens the 100 fs laser pulses are tightly focused into the photopolymerizable liquid crystal device, which is connected to a waveform generator and mounted on an *xyz*-translation stage. (b) Simulated director profile for a Fréedericksz (anti-parallel rubbed alignment) cell without polymer structures and in the absence of an applied electric field. (c) Simulated director profile when a polymer pillar is written in the Fréedericksz cell under an applied voltage of 8 Vrms and (d) simulated director profile following the removal of the applied electric field. The anchoring on the surface of the polymer pillar imposes an alignment upon the surrounding region of LC that is distinct from the bulk. (e) SEM image of the pillar array, obtained using a secondary electron detector at an electron beam voltage of 20 kV and a working distance of 11.5 mm. Pillar dimensions are found to measure ~1 μm in diameter and ~5 μm in height. The simulated director profiles were obtained in collaboration with Jure Aplinc and Miha Ravnik at the University of Ljubljana, Slovenia.

process, the ‘recorded’ director field is localised solely to regions of the developed polymer, such that the uncured bulk material remains free to switch in the presence of an applied electric field post-fabrication.

Numerical simulations of the reconfigurable birefringent structures were carried out to better illustrate the laser-induced recording of the director profile and to compare with the experimental findings (c.f. §8.3 for details of the model). The simulations were performed by Jure Aplinc and Miha Ravnik at the University of Ljubljana in two consecutive stages in order to mimic the novel laser writing process of ‘locking-in’ spatially dependent director fields and creating arbitrarily complex anchoring within the bulk of the device. Firstly, the director profile was calculated in a Fréedericksz cell without the presence of the polymeric structure and an applied voltage, as shown in Figure 8.1 (b), highlighting the typical planar alignment of the director that is observed in such a configuration. The director profile was then simulated for different voltages and these profiles were used to define the anchoring on the polymer pillars that were fabricated using laser writing, which is assumed to be strong and spatially dependent. Figure 8.1 (c) shows the director field when a polymer pillar is written at an applied voltage of 8 Vrms, which in turn defines the surface profile of the pillar. Figure 8.1 (d) shows the resultant change in the director field from (c) when the device subsequently relaxes back to its equilibrium ground state upon removal of the applied field. The simulations clearly show a distortion in the director profile in the region surrounding the pillar since the alignment that was present at 8 Vrms during the writing process has now been locked-in by the polymer irrespective of the applied field.

Scanning electron microscopy (SEM) was employed to confirm the dimensions of the pillar structures that consisted of the laser-written polymer network. After

characterization was complete under the microscope, the devices were immersed in a bath of acetone for 24 hours in order to remove the unreacted liquid crystalline material. The substrate and superstrate were then disassembled, and coated in a 27.5 nm-thick gold layer for SEM imaging using a secondary electron detector. A 20 kV electron beam voltage was used at a working distance of 11.5 mm. Figure 8.1 (e) shows a scanning electron micrograph taken of an array of pillars from an isometric viewpoint. Individual pillar dimensions were found to measure ~1 μm in diameter and ~5 μm in height and were in accordance with the voxel size created by the combination of the focusing of the ultrafast laser beam and the scanning of the translation stage.

8.3. NUMERICAL MODEL

The simulation of the nematic LC ordering in the Fréedericksz cell containing polymer pillars relies upon a continuum model that uses the Landau-de Gennes free-energy minimisation approach. This approach incorporates the orientation of the director, $\hat{\mathbf{n}}$, the possible biaxial ordering relative to the director, a scalar degree of the order parameter S and the biaxiality P [19]. The main focus of this study was to explore the effects of the externally applied electric field interacting with the LC elastic anisotropy; therefore, the three-constant elastic approximation was used. Additionally, the anchoring on the pillars was assumed to be strong and spatially dependant in order to replicate the powerful laser writing technique. A tensor order parameter Q_{ij} describes the orientational order of the LC molecules, while the tensorial invariants of Q_{ij} constitute the total free energy F, including both the bulk and surface free energies to account for the anchoring on both the cell surfaces and the polymer pillar/bulk LC interface [20]. The total free energy reads:

$$F = \int_{LC} \left\{ \frac{A}{2} Q_{ij} Q_{ji} + \frac{B}{3} Q_{ij} Q_{ji} Q_{ki} + \frac{C}{4} \left(Q_{ij} Q_{ji} \right)^2 \right\} \mathrm{dV}$$

$$+ \int_{LC} \left\{ \frac{L_1}{2} \frac{\partial Q_{ij}}{\partial x_k} \frac{\partial Q_{ij}}{\partial x_k} + \frac{L_2}{2} \frac{\partial Q_{ij}}{\partial x_j} \frac{\partial Q_{ik}}{\partial x_k} + \frac{L_3}{2} \frac{\partial Q_{kl}}{\partial x_i} \frac{\partial Q_{kl}}{\partial x_j} \right\} \mathrm{dV}$$

$$- \int_{LC} \left\{ \frac{1}{2} \epsilon_0 \left(\bar{\epsilon} E_i^2 + \frac{2}{3} \epsilon_a^{mol} Q_{ij} E_i E_j \right) \right\} \mathrm{dV}$$

$$+ \int_{Surf} \left\{ \frac{W}{2} \left(Q_{ij} - Q_{ij}^{(0)} \right) \left(Q_{ij} - Q_{ij}^{(0)} \right) \right\} \mathrm{dS}, \qquad (8.1)$$

where *LC* and *Surf* denote integration over the bulk LC and surface of the gyroid matrix, respectively. The first term in (8.1) accounts for the variation of the nematic degree of order, where *A*, *B* and *C* are material parameters. The second term penalises elastic distortions, where L_i are the elastic constants. The third term represents the dielectric coupling, in which ε_0 is the dielectric vacuum permittivity constant, $\bar{\varepsilon}$ is the average LC permittivity, ε_a^{mol} is the molecular dielectric anisotropy, and E_i is the externally applied electric field. The final term in *F* accounts for the LC interaction with the surfaces [21], where *W* is the anchoring strength, and homeotropic (perpendicular) anchoring is assumed over the substrate surface, although the anchoring on the polymer pillar is spatially dependent.

Simulations of the Fréedericksz nematic cell were performed on a square grid consisting of 260 × 260 × 400 simulation points (for a single pillar) or less (for the pillar arrays). The cylindrically shaped polymer pillars consist of 20 points in diameter and 100 points in height. Numerical calculations were performed with the following material parameters for the E7 LC: K_{11} = 10.7 pN, K_{22} = 6.5 pN, K_{33} = 16.2 pN, A = -0.172 × 10^6 Jm^{-3}, B = -2.12 ×10^6 Jm^{-3}, C = 1.73 × 10^6 Jm^{-3}, strength of the surface anchoring W = 10^{-2} Jm^{-2}, birefringence Δn = 0.219 and the dielectric anisotropy $\Delta\varepsilon$ = 13.7.

Theoretically, polarised microscopy is modelled using the Jones 2 × 2 matrix formalism introduced in §1.4.2. Matrices are used to represent the mixing and phase delay of orthogonal polarisation states imposed by the thin slab of birefringent LC material. The intensity of the transmitted light is obtained by evaluating the product of these matrices across the same thickness, applying it to the incoming polarisation, and projecting it onto the analyser direction. Transmission polarisation micrographs are thus calculated from the simulated director fields using the 2 × 2 matrix.

8.4. RESULTS & DISCUSSION

After the fabrication process was complete, the device was mounted on an optical polarizing microscope (OPM) between crossed polarizers for characterization. A UV-filter was inserted above the microscope's halogen bulb to prevent polymerization of the residual uncured material (see Figure 4.2 for the transmittance spectrum). As before, device characterization was carried out in a dark room. Figure 8.2 shows the experimental and simulated (inset) OPM images and the simulated director fields of a pillar written at a fixed fabrication voltage, V_f = 4 Vrms, under the application of six different characterization voltages: (a - b) V_c = 0, 1, 2 Vrms and (c - d) V_c = 3, 4, 5 Vrms. At this fabrication voltage, the bulk LC director profile is tilted in the direction of the applied electric field and planar near the substrates (due to the boundary conditions imposed by the alignment layers of the glass cell). This can be visualized from the simulated director profile for V_c = 4 Vrms in Figure 8.2 (d). Since the birefringence of the polymer network is similar to that of the surrounding LC at the time of fabrication, the pillars can be distinguished as a result of changes in the phase of the linearly polarised light transmitted through the device. This phase change can therefore only be

achieved by a deformation in the surrounding LC. As a result, the elastic distortion around the pillars is pronounced at lower V_c values, where the predominantly planar LC alignment in the bulk is more distinct relative to the hybrid alignment locked-in at the surface of the pillars. The OPM images in Figure 8.2 (a) reveal a clear mismatch between the birefringence in the polymer and the surrounding bulk, as light of different colours is transmitted through the distorted region around the pillar. As the value of V_c increases however, the distortion around the structures decreases significantly until $V_c \equiv V_f$ = 4 Vrms (Figure 8.2 (c)) wherein the polymer structure can no longer be differentiated from the surrounding LC. Therefore, if the applied voltage does not equal the fabrication voltage ($V_c \neq V_f$), the mismatch between the anchoring on the pillar and the bulk ordering induces a continuous deformation of the director field, yet if $V_c \equiv V_f$, the pillars seem 'invisible'. This voltage-induced 'invisibility' is also confirmed by the simulated OPM image inset in Figure 8.2 (c) for V_c = 4 Vrms.

As a further demonstration of the invisibility, and to show that this can be tailored for different voltage conditions, Figure 8.3 shows experimental and simulated OPM images of a 6 × 6 pillar array with a lattice spacing of 40 μm, along with the corresponding director fields when $V_c \equiv V_f$,. The device was imaged under six different voltage conditions: (a - c) V_c = 0, 1, 2 Vrms and (d - f) V_c = 3, 4, 5 Vrms. Each column of pillars, excluding the first in the array (that was written in the ground state - 0 Vrms), was fabricated under the application of a 1 kHz square wave with increasing amplitudes from 1 to 5 Vrms (left to right of array). Columns of pillars with equivalent fabrication and characterization voltages are indicated by the arrows. Under these conditions ($V_c \equiv V_f$), the birefringence in the bulk matches the surface conditions of the pillars resulting in structures that appear 'invisible', as observed for the single pillar case in Figure 8.2.

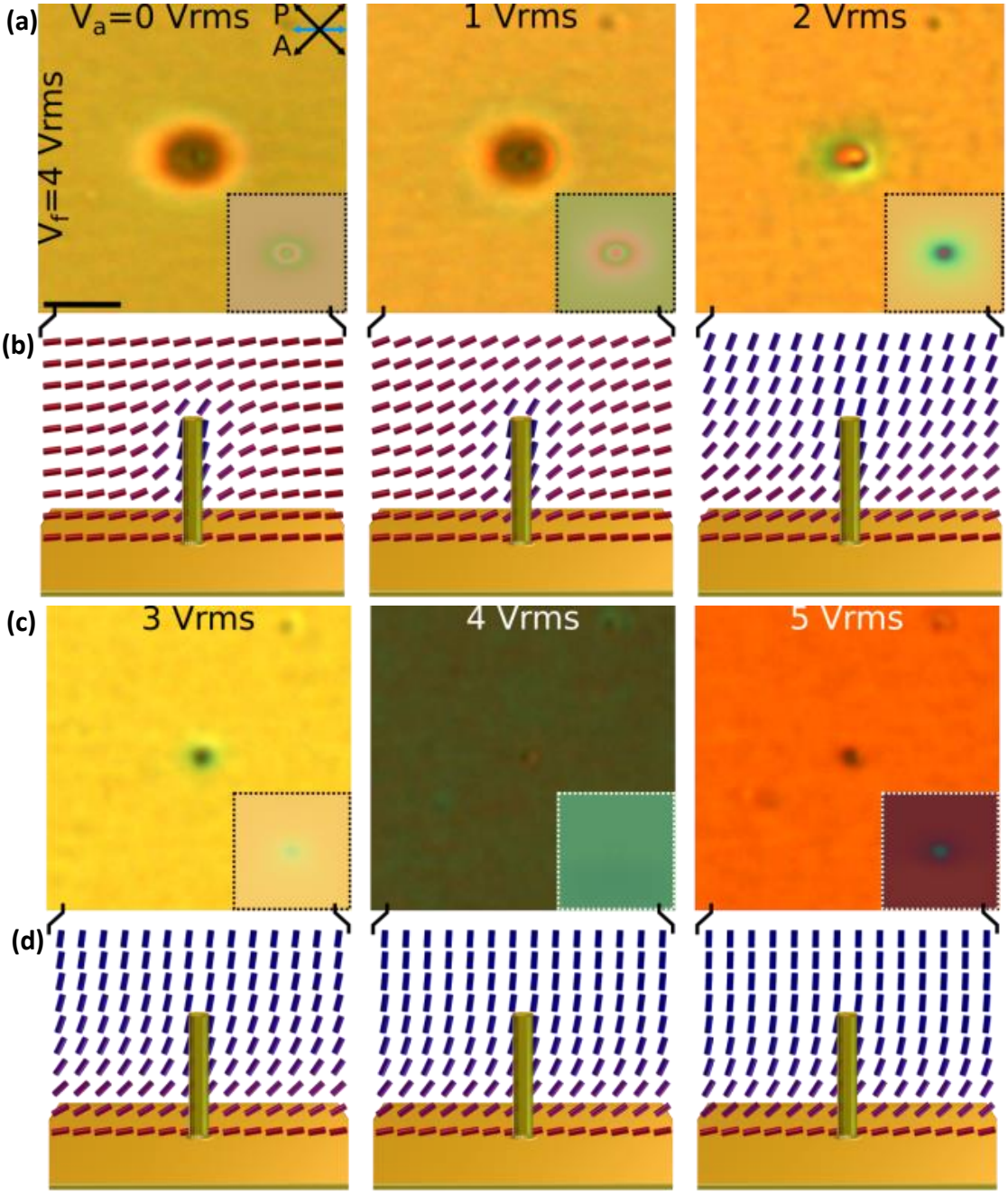


Figure 8.2. LC-polymer elastic deformations. OPM images of a single pillar fabricated at V_f = 4 Vrms taken under six different characterization voltages: (a) V_c = 0, 1, 2 Vrms and (c) V_c = 3, 4, 5 Vrms. The direction of the crossed polarizers and LC optic axis are indicated by the black and blue arrows, respectively. The elastic distortion around each pillar is reduced as V_c tends towards the V_f value. Inset in (a) and (c): Simulated OPM images that reveal the same phenomena as the experimental data. At $V_c \equiv V_f$ = 4 Vrms, the surrounding director field matches the director profile of the anchoring on the pillar such that no deformation is visible. The simulated director profiles reveal the deformation of the LC alignment surrounding each polymer pillar when (b) $V_c \neq V_f$, whilst a continuity in the alignment is observed as (d) V_c approaches V_f. Scale bar is 10 µm.

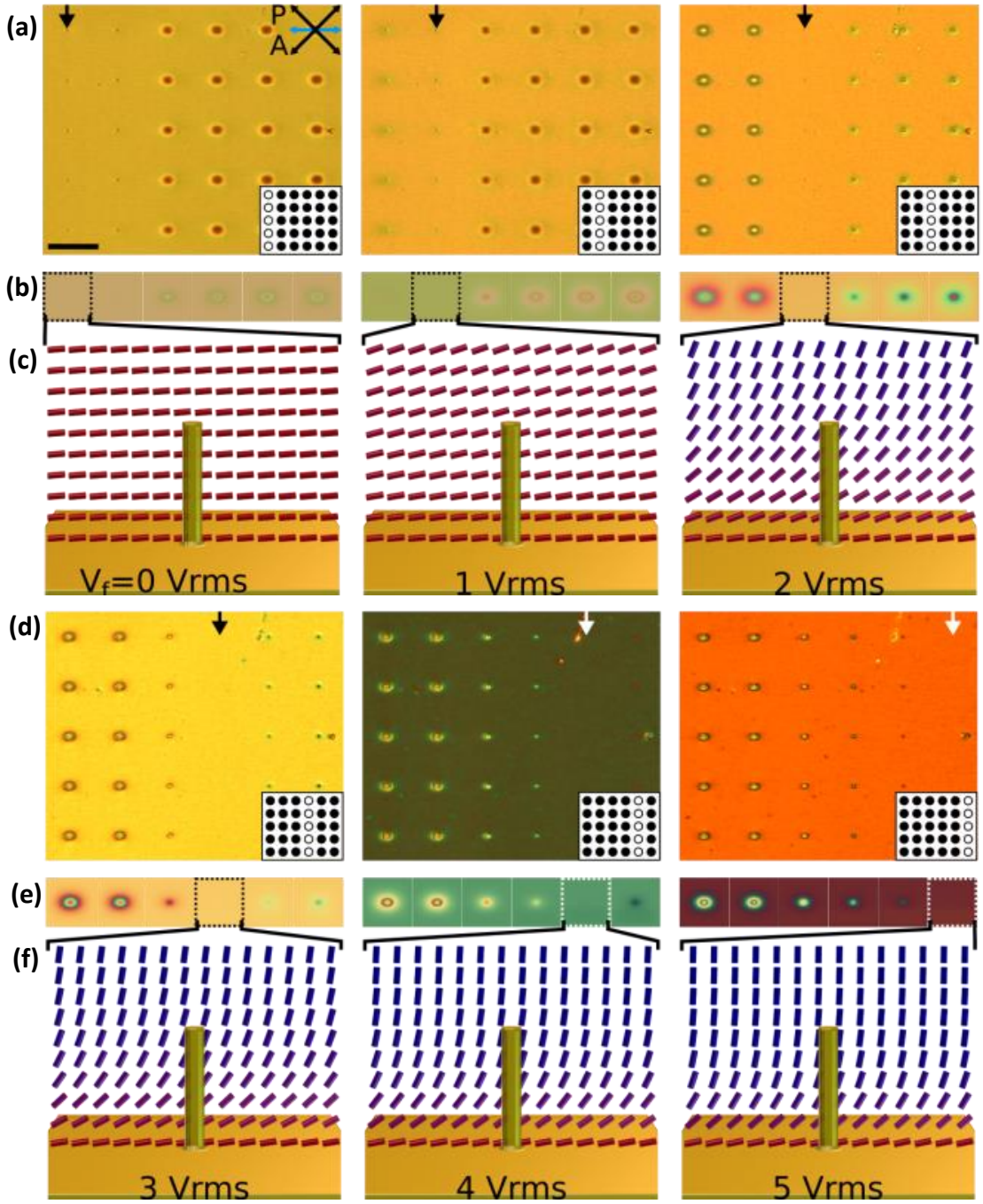


Figure 8.3. Voltage-induced invisibility. Columns of pillars in a 40 µm spaced array are written under the application of incremental voltages (V_f = 0, 1, 2, 3, 4, 5 Vrms from the left to the right of the array). OPM images were taken during characterization of the polymeric structures under the same applied voltage values: (a) V_c = 0, 1, 2 Vrms and (d) V_c = 3, 4, 5 Vrms. The arrows and inset schematics indicate the invisible regime whereby $V_c \equiv V_f$. Simulated OPM images confirm the invisibility when $V_c \equiv V_f$: (b) V_c = 0, 1, 2 Vrms and (e) V_c = 3, 4, 5 Vrms. The simulated director profiles illustrate the continuity of the LC alignment surrounding the polymer pillars when $V_c \equiv V_f$: (c) V_c = 0, 1, 2 Vrms and (f) V_c = 3, 4, 5 Vrms. Scale bar is 40 µm.

The inset schematics of the array illustrate the column that has effectively been 'switched off' during characterization. Moreover, the surrounding director field matches the director profile of the anchoring on the pillar, evidenced from the simulated results in (c) and (f). It is worth noting, however, that the pillars are slightly more distinguishable for the $V_c \equiv V_f = 1$ Vrms case as this voltage value corresponds to the Fréedericksz threshold (V_{th}) of the device, which is estimated to be ~0.9 V based on the host LC material parameters (see Table A.3 of the Appendix). The visibility of the pillars is restored when $V_c \neq V_f$. The elastic distortion surrounding the pillars is more pronounced for higher fabrication voltages ($V_f \geq 3$ Vrms) when $V_c < V_f$, due to the transition in the bulk director profile from planar to homeotropic at larger applied electric field strengths. The data shown in Figures 8.2 and 8.3 demonstrate the creation of a reconfigurable optical element by virtue of the in-situ fabrication technique that allows structuring of the polymer network under different voltage applications.

8.4.1. Image Analysis

In order to correctly quantify the visibility of the pillars under different voltage regimes, it is important to first consider the colorspace in which the analysis is carried out. This is due to the fact that various challenges occur in the accurate colour representation of digital image data. One of the complexities arises from different background colours; for example, a shade of grey appears lighter on a dark background but darker on a light background. Another complexity in accurate colour representation is the intensity of a colour rendered by the display device whereby certain colours appear visually brighter than others leading to the illusion that their intensity is greater. This problem may be overcome through estimations of the luminosity or perceived brightness of a colour.

L*a*b* colorspace was developed in 1976 with the intention of replicating human vision through perceptual uniformity, such that colour differences are proportional to changes in their visual importance [22-24]. The colorspace incorporates estimates of luminance (L*) and chromaticity, with the latter separated into hues of red-green (a*) and blue-yellow (b*). L*a*b* colorspace exceeds the colour gamut of the RGB and CMYK colour models. Another crucial feature is its device independence, providing absolute colour values that are independent of the way in which they were created.

The primary advantge of working in L*a*b* colorspace is the separation of luminosity and chromaticity components to ensure that the image analysis has a direct correlation to what is perceived by eye. Therefore, the image data presented in Figures 8.2 and 8.3 were processed in L*a*b* colorspace in Matlab. Figure 8.4 shows maps of the local standard deviation (measured from the 3-by-3 neighbourhood around a corresponding pixel) in the luminance (L*) of the pillars from the experimental data presented in Figure 8.2. The maps for V_c = 0 Vrms (i) and 1 Vrms (ii) produce almost identical results, whereby the elastic distortion around the pillar diminishes as V_c increases. The largest local standard deviation is recorded at V_c = 2 Vrms (iii), revealing a bright central region of the pillar that can also be seen from the experimental and simulated OPM images in Figure 8.2 (a). At higher V_c values, the local standard deviation falls until it reaches a minimum in the ‘invisible’ regime (v). Thus, measurements of the luminosity are in good agreement with observations of the experimental data. Note that the greatest standard deviation around the pillars is only marginally greater than the Just Noticeable Difference (JND) (~ 1 in CIELab [25]), indicating that changes in luminosity are difficult to detect between visible and invisible regimes.

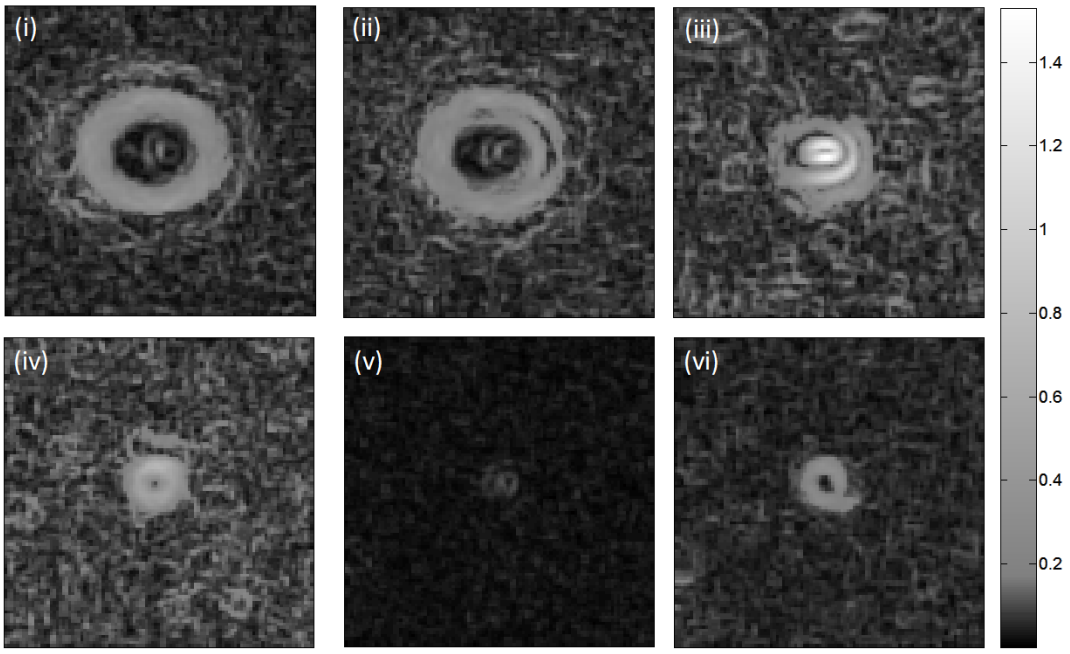


Figure 8.4. Local standard deviation in L*a*b* colorspace. Local standard deviation (measured across the 3-by-3 neighbourhood around a corresponding pixel) in the luminosity L* from a pillar written at V_f = 4 Vrms for V_c = (i) 0 Vrms (ii) 1 Vrms (iii) 2 Vrms (iv) 3 Vrms (v) 4 Vrms and (vi) 5 Vrms. Again, a minimum in the local standard deviation can be seen in the 'invisible' regime (v) $V_f \equiv V_c$ = 4 Vrms. The regions of greatest standard deviation that appear around the pillars are only just above the JND (~1 in CIELab), indicating that changes in the luminosity are difficult to detect between the visible and invisible states.

Figure 8.5 shows line profile plots of the variance in chromaticity (a*, b*) measured from the experimental data in Figure 8.2. The variance is calculated for each column of values in the processed image data and plotted against the number of columns i.e. the length of the image, *x*. For V_c = 0 Vrms (i) and 1 Vrms (ii), a larger variance can be seen in the a* component surrounding the pillar and a smaller variance measured in the b* component within the central region of the polymer network. For V_c = 2 Vrms (iii), the variance in the a* component was found to increase by a factor of four at the centre with a relatively small variance in the b* component detected across the structure.

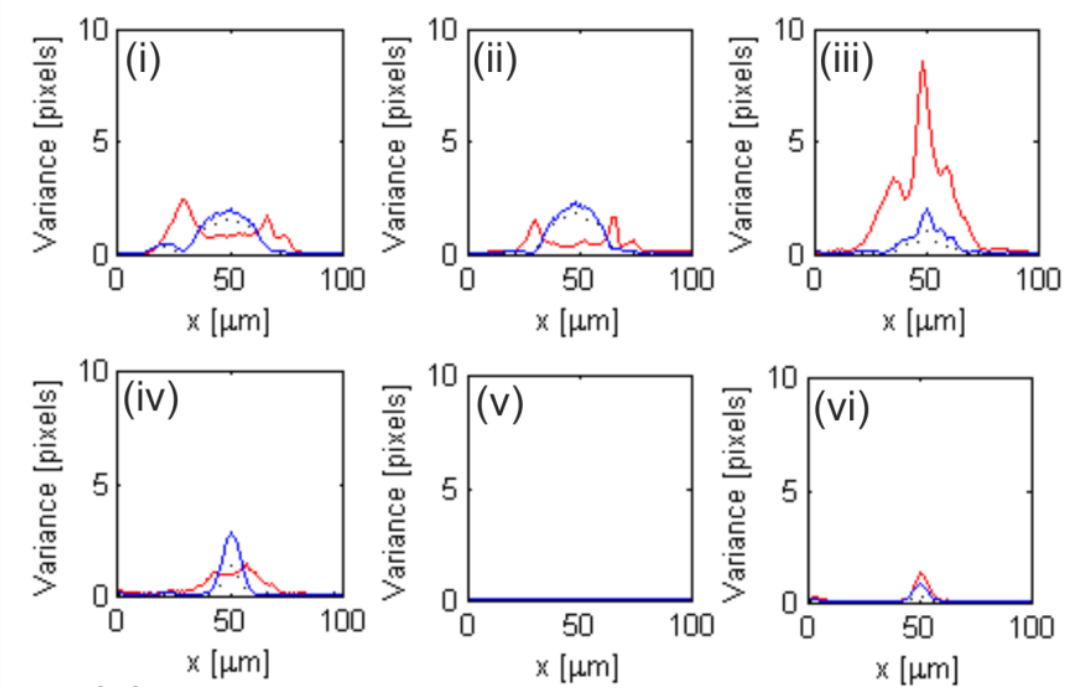


Figure 8.5. Variance in L*a*b* colorspace. Variance in chromaticity measured across a single pillar written at V_f = 4 Vrms and the surrounding bulk for V_c = (i) 0 Vrms (ii) 1 Vrms (iii) 2 Vrms (iv) 3 Vrms (v) 4 Vrms and (vi) 5 Vrms. A minimum in the variance is recorded in the 'invisible' regime (v) $V_f \equiv V_c$ = 4 Vrms. Note – a* - red line, b* - blue line.

As discussed previously for this value of V_f, the elastic distortions decrease significantly at higher V_c values due to a predominantly homeotropic alignment in the bulk director field. This uniformity in the alignment can be seen by the decrease in the variance for both chromaticity components at V_c = 3 Vrms, shown in Figure 8.6 (iv). The plot in (v) meets the condition for 'invisibility', $V_c \equiv V_f$ = 4 Vrms, wherein a negligible variance is detected from the image compared with the other voltage applications. Thus, there is negligible contrast between the polymer pillar and surrounding LC on account of the uniform alignment and resultant match in birefringence across the bulk. Lastly, at V_c = 5 Vrms (vi), minimal variance is detected in both colour components on account of the reduction in the distortion when $V_c > V_f$ at this fabrication voltage.

8.4.2. Colour Filters

The image analysis measures the amount of each colour component (a* or b*) in and around the polymer network structures relative to the transmission from the surrounding bulk material, for each voltage value. Using this information additional colour filters provided by LEE filters were carefully selected to remove the predominant colour component detected in the 'invisible' regime ($V_c \equiv V_f$) and decrease the contrast of the pillars further relative to the surrounding bulk material to render them undetectable. Details of the selected colour filters based on a combination of experimental observations and the image analysis results are summarized in Table 8.1.

V_f (Vrms)	EXPERIMENTAL OBSERVATIONS $V_c \equiv V_f$	MAXIMUM VARIANCE (a*b*)	SELECTED COLOUR FILTER	NO FILTER $V_c \equiv V_f$	COLOUR FILTER $V_c \equiv V_f$
0	Pillar – Red/Orange Centre, Green Outline Bulk – Dark Yellow	a*	Orange 105		
1	Pillar – Red/Blue Centre, Green Side Bulk – Yellow/Orange	a*	Fire HT 019		
2	Pillar –Red/ Green Bulk – Orange	a*	Orange 105		
3	Pillar – Red Centre, Light Green Outline Bulk – Yellow	a*	Bright Pink 128		
4	Pillar – Dark Red/Green Bulk – Dark Red/Green	a*	Deep Straw HT 015		
5	Pillar – Dark Red Bulk – Fiery Red	a*	Fire HT 019		

Table 8.1. Selection of colour filters to improve the 'invisible' regime. Variance measurements for $V_c \equiv V_f$ reveal the dominant colour component (a*b*) detected from the polymer pillars. Using this information combined with experimental observations on the optical polarizing microscope, individual colour filters were selected for each fabrication voltage value, V_f.

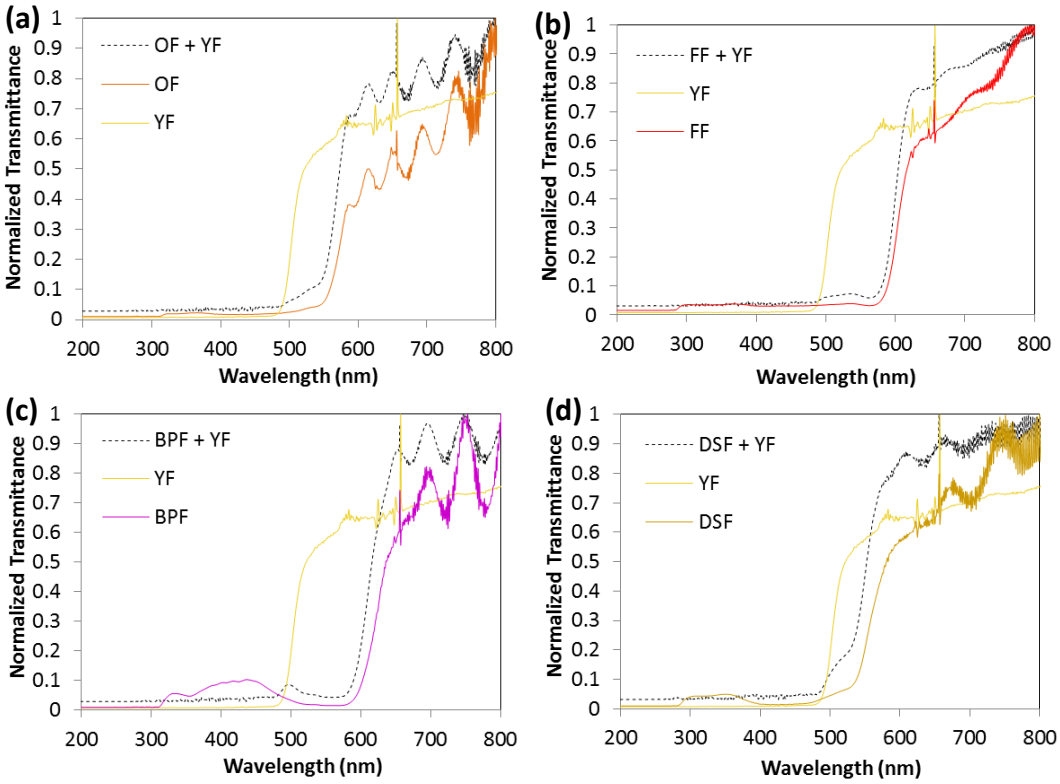


Figure 8.7. Spectra of colour filters. (a) Spectrum of orange filter (OF) used for V_f = 0 Vrms and V_f = 2 Vrms. (b) Spectrum of fire filter (FF) used for V_f = 1 Vrms and V_f = 5 Vrms. (c) Spectrum of bright pink filter (BPF) used for V_f = 3 Vrms. (d) Spectrum of deep straw filter (DSF) used for V_f = 4 Vrms. The spectrum of the UV-filter (YF) used throughout the investigation to prevent bulk polymerization is also shown when combined with each colour filter selected for each value of V_f.

Figure 8.7 shows the spectra of the selected colour filters listed in Table 8.1 measured using the UV-Visible spectrometer. Each spectrum includes that measured from the UV-filter alone, (used throughout the analysis to prevent bulk polymerization during characterization), the selected colour filter and the combined spectra from the UV and colour filters. Individual colour filters were mounted on the optical microscope to capture OPM images for each pillar in the $V_c \equiv V_f$ regime and a further image analysis was carried out.

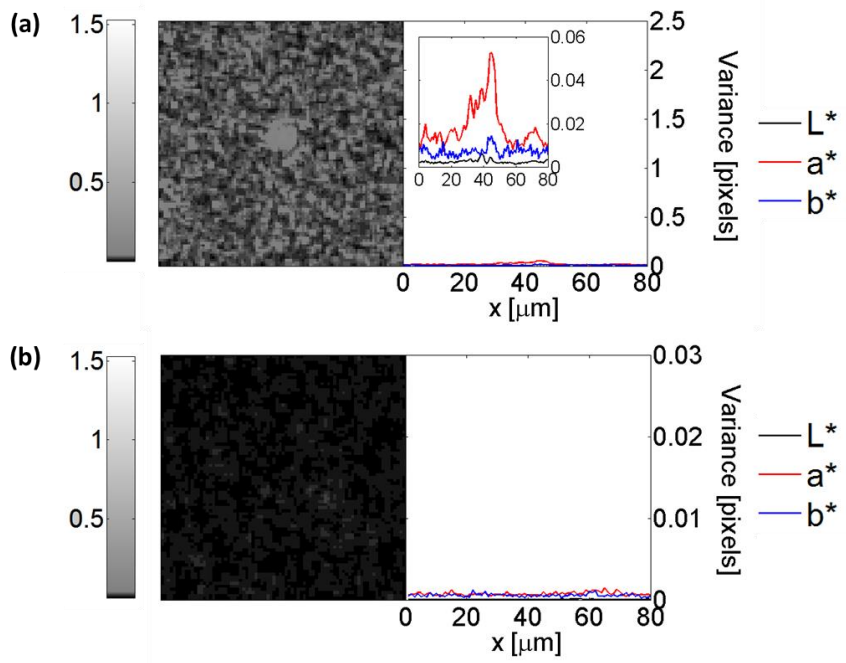


Figure 8.8. Image analysis in the 'invisible' regime with a colour filter. Local standard deviation map of the luminosity (left) and variance line profile plots of L*a*b* colorspace components (right) for a single pillar at $V_f \equiv V_c = 4$ Vrms characterized before (a) and after (b) the addition of a deep-straw colour filter. The pillar is almost indistinguishable in the local standard deviation map while the variance detected across the pillar has decreased one hundred-fold after the addition of the colour filter.

Figure 8.8 shows the local standard deviation map in the luminosity and plots of the variance in L* (black line), a* (red line) and b* (blue line), before (a) and after the addition of a deep-straw colour filter (b) for a pillar written at $V_f = 4$ Vrms in the 'invisible' regime ($V_c \equiv V_f$). The range in the L*a*b* variance plots has decreased one hundred-fold with the addition of the colour filter. Although the colour filter was selected based on an analysis of the predominant colour component detected from each pillar, the local standard deviation maps show that the brightness of the pillar also decreases significantly. This behaviour is expected as visible light above ~550 nm is blocked by the UV and colour filters combined, which is shown in the spectrum of Figure 8.7 (d). As a result, the pillar is almost indistinguishable in the local standard deviation map shown in Figure 8.8 (b).

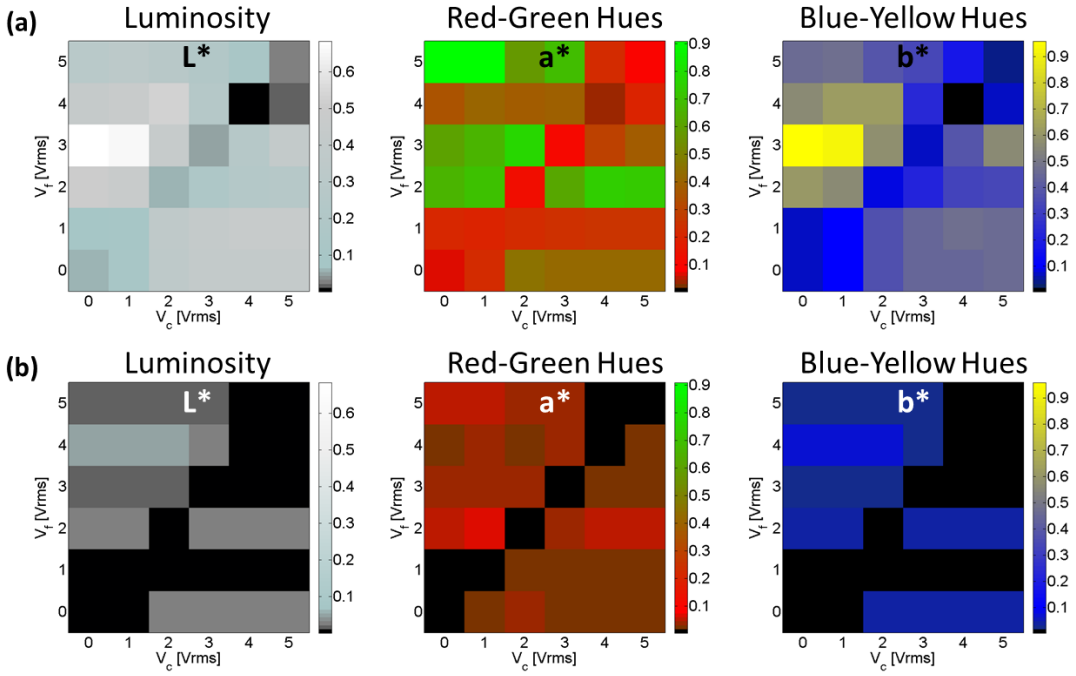


Figure 8.9. Standard deviation in L*a*b* colorspace for all voltages. Contour maps showing the standard deviation in luminosity and colour contrast (red-green, blue-yellow hues) across a single pillar that was written at six different fabrication voltages, V_f = 0, 1, 2, 3, 4, 5 Vrms, and characterized under the equivalent voltage values, V_c, (a) before and (b) after the addition of individual colour filters. A minimum can be seen along the diagonals in the invisible regime, $V_c = V_f$, of each contour map. A ten-fold decrease in the standard deviation is measured with the addition of each colour filter.

Figure 8.9 shows a summary of the image analysis obtained before (a) and after (b) the addition of the colour filters. Contour maps are shown of the standard deviation in the luminosity/brightness and colour components measured across the individual pillars under the six different voltage conditions (0, 1, 2, 3, 4, 5 Vrms). In both (a) and (b), the correlation between the fabrication and characterization voltages is well defined by the minima arising in the invisible regime, $V_c \equiv V_f$ of each contour map. The standard deviation away from the minima reveals an increase in both the brightness and colour contrast relative to the background, as the difference in the two voltage values, V_f and V_c, increases. The smallest standard deviation is observed for the $V_c \equiv V_f$ = 4 Vrms case where the structures disappear against the dark green background colour. Figure 8.9 (b)

shows a substantial decrease in the standard deviation (tenfold) with the addition of the colour filters selected to improve the 'invisible' regime ($V_c \equiv V_f$). There is also some reduction in the standard deviation when $V_c \neq V_f$, however, this is expected as light of certain wavelengths are filtered out (as shown in the spectra of Figure 8.7) with the addition of the different colour filters. This result suggests that the embedded polymer structures can be made to be more 'invisible' with the use of a carefully selected monochromatic light source. In addition, the combined spectra reveal the extent to which the UV-filter modifies the spectrum of light transmitted through the colour filters. Washing out the remaining non-crosslinked mesogens in a solvent bath after laser fabrication is complete would remove the need for a UV-filter altogether, so that the template of pillars could be refilled with non-polymerizable LC.

8.4.3. Spatial Tuning of Arrays

Thus far, the ability to make polymer structures simply disappear in the surrounding LC host has been demonstrated using different fabrication and characterization voltages for a fixed lattice spacing. Figure 8.10 shows OPM images of arrays of pillars for three different lattice spacings (40, 20 and 10 μm) written at a fixed voltage, V_f = 4 Vrms. During characterization, the amplitude of the applied waveform (V_c) was increased in 2 Vrms voltage increments, from 0 to 8 Vrms. Under different V_c values, a trend emerges in the LC alignment around the polymer network for all three lattice spacings. As before, the structures appear invisible when $V_c \equiv V_f$ = 4Vrms. For $V_c < V_f$, the planar and tilted planar alignments in the bulk at 0 Vrms and 2 Vrms, respectively, generates a larger elastic distortion around the individual pillars in the arrays. In addition, localised effects in the LC alignment arise when the structures are confined to lattice spacings of

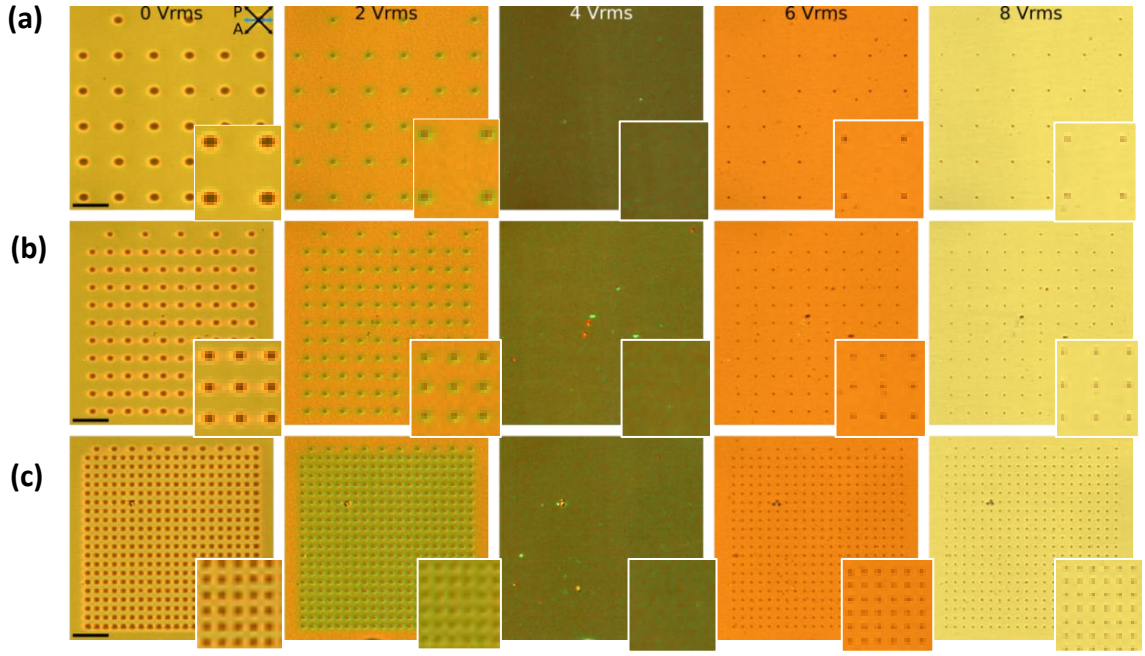


Figure 8.10. Spatially tuning birefringent structures. Pillar arrays written at a fixed voltage of 4 Vrms, and variable lattice spacings of (a) 40 µm (b) 20 µm and (c) 10 µm under the application of different characterization voltages, V_c (as labelled at the top of the images). Scale bar is 40 µm. Inset: Scaled image sizes to show how the LC alignment changes between the pillars at different lattice spacings.

10 µm or less. For $V_c > V_f$, the director field is primarily homeotropic (or highly tilted) in the bulk, reducing the elastic distortion around the pillars.

Each pillar induces a deformation in the surrounding LC if the applied voltage does not correspond to the fabrication voltage ($V_c \neq V_f$). Figure 8.10 (a) shows the pillar array with 40 µm lattice spacing. The pillars are spaced so far apart from each other that they effectively behave as single pillars. If the lattice spacing is diminished by a factor of four as shown in Figure 8.10 (c), the director deformation induced by the polymer pillars becomes more amplified in the intermediate space in the array. This effect is best observed at an applied voltage V_c = 2 Vrms, on account of the mismatched birefringence between the pillars and the bulk generating a distinct colour around the pillars. Note that this distortion in the local LC alignment was also seen in Chapter 5 for the pillar arrays fabricated in the nematic pi-cell device, at a lattice spacing of 5 µm. These interesting

effects demonstrate the potential to tune the birefringence from the fabricated structures, either spatially through the creation of different sized arrays or dielectrically, through variations in the voltages applied during laser writing. Varying both parameters may therefore lead to the creation of complex structures encoded with different patterns, as will be explored in the following section.

8.4.4. Complex Structures

Exploiting the ability for the polymer network structures to appear and disappear, it is possible to reconfigure the structures so that different features or patterns emerge under different voltage conditions. Figure 8.11 shows two examples of structures that illustrate the power of this approach. The first is a configuration of pillars that has been written at different voltages and lattice spacings so as to form an emoticon. The outline of the face was written at a small spacing of 3 μm in the absence of an applied electric field, to enhance its appearance in the visible regime due to localized alignment effects ($V_c \neq 0$ Vrms). The remaining structures were fabricated at a larger spacing of 10 μm. The outline of the eyes and the smile were written at a fabrication voltage of $V_f = 4$ Vrms, while the structures within the eyes and the top of the mouth were fabricated at $V_f = 2$ Vrms. By encoding different features at different voltages and then carefully tuning the voltage to a desired setting, it is possible to dial-in emoticons displaying a variety of expressions. The encoded features are best illustrated for the applied characterization voltages of $V_c = 2$ Vrms and $V_c = 4$ Vrms. Driving the device to a different voltage level alters the emoticon in accordance with the condition for invisibility, $V_c \equiv V_f$. In the second example, an arrangement of the polymer pillars results in an image of the New College Crest, Oxford, which was again written at different lattice spacings under a

fixed voltage of V_f = 4 Vrms; the crest appears invisible when switched with this voltage amplitude. In this example, the crest disappears entirely when $V_c \equiv V_f$ = 4 Vrms.

The sequence of images in Figure 8.11 (a) reveal the ability to encode the LC device and switch between complex patterns formed in the polymer network structures. A reconfigurable optical element created in this way could for example, be used to tune the wavelength of light diffracted from the periodic structures under different voltage applications. Figure 8.11 (b) also demonstrates the possibility to embed covert features within the polymer-LC composite. This could impact photonic technologies that require additional security tags in the form of a barcode or serial number that can be probed under the relevant voltage applications. The creation of spatially and electrically tunable birefringent structures therefore highlights the versatility that is inherent in the in-situ DLW technique and its potential impact on the next generation of photonics technologies.

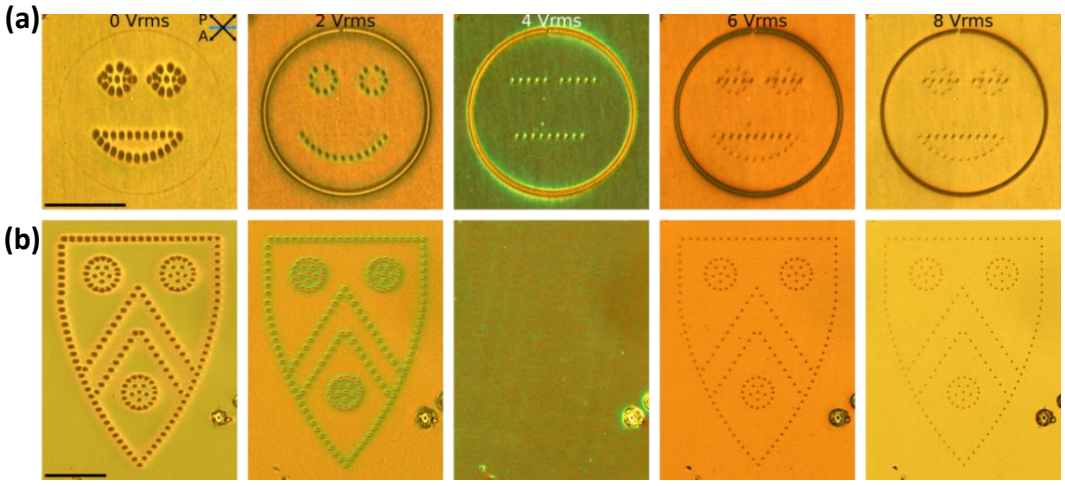


Figure 8.11. Reconfigurable polymer structures. (a) Pillars in the face outline are spaced at 3 µm and written at 0 Vrms. The outline of the eyes and smile were written at a spacing of 10 µm and at a fabrication of voltage of 4 Vrms, while the structures within the eyes and the top of the mouth were written at 2 Vrms with the same pillar spacing. Changes in the facial expression can be seen at different values of V_c (as labelled at the top of the images). (b) The Oxford New College Crest was written at 4 Vrms. The pillars in the flowers are spaced at 8 µm and the outline of the shield was written at a spacing of 10 µm. Scale bar is 100 µm.

8.5. CONCLUSIONS

In conclusion, the use of an in-situ direct laser writing facility to structure polymer networks in LC devices has permitted the demonstration of a reconfigurable optical element whereby the polymer structures can be made to disappear with the application of a voltage that matches the voltage employed during the fabrication procedure. The ability to apply different voltages during fabrication in the photocrosslinkable LC device has shown that the polymer network is able to 'memorize' the local orientation of the director at the precise moment of laser writing, such that different patterns can be successfully encoded within the device. Subsequent switching of the device with the same applied voltage as that used during fabrication ensures a uniform director profile between the bulk alignment and the alignment of the director that is imposed by the surface anchoring conditions of the polymer structures. This continuity in the alignment reduces the elastic distortion around the polymer network to match the birefringence between the polymer and the bulk LC, such that the pillars are no longer visible. Through this investigation, it has been shown that the ability to electrically and spatially tune these birefringent structures to encode different features at different voltages can be recovered by applying the appropriate voltage amplitude. This work could have a significant impact in the development of reconfigurable optical elements, tunable metamaterials, and novel transformational optical components.

8.6. REFERENCES

[1] 'The Physics of Soft and Partially Ordered Matter', Theory and Simulation research group, University of Ljubljana, http://softmatter.fmf.uni-lj.si/main.php.

[2] Y. Guo, M. Jiang, C. Peng, K. Sun, O. Yaroshchuk, O. Lavrentovich, Q.-H. Wei, *Adv. Mater.* **28**, 2353 (2016).

[3] E. A. Shteyner, A. K. Srivastava, V. G. Chigrinov, H.-S. Kwok, A. D. Afanasyev, *Soft Matter* **9**, 5160 (2013).

[4] J.-H. Kim, M. Yoneya, J. Yamamoto, H. Yokoyama, *Nanotechnology* **13**, 2155 (2002).

[5] J.-W. Park, J. Choa, E. L. Thomaas, *Soft Matter* **4**, 739 (2008).

[6] C. C. Tartan, P. S. Salter, M. J. Booth, S. M. Morris, S. J. Elston, *J. Appl. Phys.* **119**, 183106 (2016).

[7] F. Castles, F. V. Day, S. M. Morris, D.-H. Ko, D. J. Gardiner, M. M. Qasim, S. Nosheen, P. J. W. Hands, S. S. Choi, R. H. Friend, H. J. Coles, *Nat. Mater.* **11**, 599 (2012).

[8] S. M. Weiss, H. Ouyang, J. Zhang, P. M. Fauchet, *Opt. Express* **13**, 1090 (2015).

[9] D. Engstrom, R. P. Trivedi, M. Persson, M. Goksor, K. A. Bertnessd, I. I. Smalyukh, *Soft Matter* **7**, 6304 (2011),

[10] L. Marrucci, C. Manzo, D. Paparo, *Phys. Rev. Lett.* **96**, 163905 (2006).

[11] P. F. McManamon, P. J. Bos, M. J. Escuti, J. Heikenfeld, S. Serati, X. Huikai, E. A. Watson, *Proc. IEEE* **97**, 1078 (2009).

[12] W. T. Chen, M. Khorasaninejad1, A. Y. Zhu, J. Oh, R. C. Devlin, A. Zaidi and F. Capasso, *Light: Science & Applications* **6**, e16259 (2017)

[13] P, Avouris, T. Hertel and R. Martel, *Appl. Phys. Lett.* **71**, 285 (1997).

[14] C. Vieu, F. Carcenac, A. Pepin, Y. Chen, M. Mejias, A. Lebib, L. Manin-Ferlazzo, L. Couraud, H. Launois, *Appl. Surf. Sci.*, **164**, 111 (2000).

[15] L. J. Guo, *Adv. Mater.* **19**, 495 (2007).

[16] N. I. Zheludev and Y. S. Kivshar, *Nature Mater.* **11**, 917 (2012).

[17] I. C. Khoo, *IEEE J. Selec. Topics Quant. Elec.* **16**, 2 (2010).

[18] J. Zhong, Y. Huang, G. Wen, H. Sun and W. Zhu, *Procedia Eng.* **29**, 802 (2012).

[19] P. G. de Gennes and J. Prost, *The Physics of Liquid Crystals*, 2nd Edition, Clarendon Press, Oxford (1993).

[20] M. Ravnik and S. Zumer, *Liq. Cryst*. **36**, 1201 (2009).

[21] M. Nobili and G. Durand, *Phys. Rev. A* **46**, R6174 (1992).

[22] R. S. Hunter, *JOSA* **38**, 7, 661 (1948).

[23] R. S. Hunter, *JOSA* **38**, 12, 1094 (1948).

[24] M. D. Fairchild, *Color and Image Appearance Models,* John Wiley and Sons (2005).

[25] J. Schwiegerling, *Field Guide to Visual and Opthalmic Optics*, SPIE Press Book (2004).

9

CONCLUSIONS

This thesis begins with the characterization of flexoelectric phenomena in liquid crystalline systems, followed by the manipulation of dielectric effects for the creation of soft matter photonics based technologies. The fast-switching flexoelectric effect has been considered in hybrid aligned nematic (HAN) systems. A strong splay-bend distortion field that arises in the bulk due to the asymmetric cell surfaces makes hybrid aligned systems favourable for measurements of the splay and bend flexoelectric coefficients. However, the asymmetric treatment of the cell surfaces induces an internal bias in the device that behaves in a similar manner to the polar flexoelectric response. In addition, the induced flexoelectric polarization gives rise to an effective flexoelectric internal bias. Thus, distinguishing between polar responses becomes non-trivial. Liquid crystalline materials with a high ionic content however, revealed a transient response to a voltage offset applied to an oscillating waveform, whereby the ions act to screen out a voltage offset. Thus, the assumption followed that the ions also screen out the internal bias due to the different surface alignment polarities in a hybrid director configuration. Applying voltage waveforms with frequencies smaller than the ionic transport time ensured that this was indeed the case.

A one-dimensional numerical model was developed based upon the continuum theory of liquid crystals to model the electro-optic response of a HAN cell. Under the assumption that any internal bias is screened out by ions, data-theory fits of the transmission as a function of time were carried out and the measurement of the flexoelectric sum for the standard commercial eutectic E70 liquid crystalline mixture, found to be $|e_1 + e_3| = 10$ pCm^{-1}, was in agreement with values reported in the literature.

The assumption that ions screen out the internal bias in a hybrid aligned device is only valid for liquid crystals that have a high ionic concentration. This was confirmed by transmission measurements for a HAN cell that was filled with a pure (low ionic) LC material, which, under the application of a voltage offset, did not return to its equilibrium value. The strong splay-bend distortion field induced in a HAN cell is thought to be due to the asymmetry in the director profile. Thus, the data-theory method developed for the measurement of the flexoelectric coefficients was extended to nematic pi-cell devices that form asymmetric director profiles under different voltage amplitudes. Crucially, the symmetric treatment of the cell surfaces was expected to remove the reliance on ionic liquid crystals due to the absence of an internal bias in the system. However, through simulations of the flexoelectric effect in the so-called asymmetric H state, it was found that the presence of ions significantly enhanced the asymmetry in the modulation of the electro-optic response. This result highlights the complex interplay between the different processes in the device when driven dynamically under an oscillating field. Data-theory fits were carried out in the asymmetric H state of a nematic pi-cell device and flexoelectric measurements of the nematic liquid crystal, E7, were found to be in agreement with previously reported values, $|e_1 + e_3| = 10$ pCm^{-1}. The estimated ionic content, however, was found to be an

order of magnitude less than that reported in the literature for E7. The inherent covariance between the ionic concentration and the flexoelectric coefficients in the method was therefore highlighted through this investigation.

Observations of flexoelectricity in more complex, chiral nematic systems are also non-trivial, as the splay-bend distortion associated with the electro-optic effect is observed in an inherently unstable LC state. The fast-switching flexoelectro-optic (FEO) effect is induced when an electric field is applied perpendicular to the helical axis of a chiral nematic liquid crystal. For conventional liquid crystal cells, where the electrodes are located on the top and bottom glass substrates, aligning the helical axis in the plane of the cell generates inherent instabilities. The so-called uniform lying helix (ULH) state was investigated using conventional annealing techniques and bulk polymerization was employed in order to stabilise the alignment so that measurements of the flexoelectric coefficients, e_1 - e_3, could be carried out. However, the formation of a polymer network was found to degrade the quality of the ULH alignment, which is manifested by a significant reduction in the FEO response. Based on previous analytical derivations of a pitch constraint study, which suggests that imposing a pitch of fixed length on a chiral nematic of a longer (constrained) pitch enhances the flexoelectric tilt angle, a polymer templating method was employed to improve the electro-optic performance of the chiral nematic device. Polymer scaffolds, formed from a short-pitch chiral nematic material were refilled with a chiral nematic LC of a longer pitch. Refilling the template with a pitch twice the length of the imposed pitch generated inconsistencies in the results, whereby the flexoelectro-optic response was enhanced in some cases and reduced in others. The inconsistencies may have been a result of the large error margins present during the measurement process involving very small tilt

angles. In contrast, refilling a polymer template with a material of infinite pitch induced a larger tilt angle (compared with the bulk polymerization response) in all cases. The latter result also demonstrates that the chiral templates successfully imparted their structural properties onto achiral nematic LCs, using a simple and repeatable fabrication procedure. Yet despite the promising results from the templating study, overall, the electro-optic performance was still significantly reduced compared with that measured from the device before any polymerization process had been initiated as the liquid crystal molecules are hindered by the polymer network formed in the bulk.

An alternative method to stabilizing the ULH state has been demonstrated through the introduction of periodic anchoring conditions at the cell surfaces, eliminating the need to form a polymer network in the bulk of a device. To address the issue of the degradation in the FEO response due to poor ULH alignment, a direct laser writing technique was employed that could localise the polymer network to specific regions within the device through the generation of periodic surface relief structures. A custom-built fabrication technique was employed that was modified to include an adaptive optics element in the form of a spatial light modulator (SLM). The SLM corrected for aberrations induced by the thick glass substrates of the liquid crystal device, making it possible to electrically address the device during fabrication. In this way, energetically favourable director configurations can be exploited in-situ in order to promote the formation of the ULH state.

Periodic polymer walls were formed both in the nematic and chiral nematic phases. The former was realized by electrically addressing the chiral nematic device with electric field strengths above the value of the critical unwinding field for a liquid crystal of positive dielectric anisotropy. For writing in the chiral nematic phase directly, the

ULH state was initially formed using the conventional annealing technique and polymer walls were subsequently written in the device to pin the state within localised regions.

Writing in the nematic phase with a homeotropic alignment was found to spontaneously induce a ULH state upon reduction of the applied electric field for a wall periodicity of the order of the device thickness. Moreover, the FEO response was enhanced relative to that measured after the bulk polymerization process. However, diffusion of the polymer network into the microchannels between the polymer walls limited the switching compared with a device that was free of a polymer network. The polymer walls formed in the chiral nematic phase also improved the electro-optic performance of the device relative to a bulk polymerization technique, although the response was inferior to that resulting from fabrication in the nematic phase.

The structuring of polymer networks using the direct laser writing system was explored further to exploit the in-situ capability of the technique. A number of structures were fabricated in a nematic pi-cell device that undergoes various transitions under different voltage applications, as observed during the flexoelectric investigation for the measurement of the coefficients. Writing polymer walls in topologically discontinuous states revealed the ability to electrically tune defects arising within the discontinuous regions of the director field. Through perturbations in the applied voltage, the shape and position of a defect could be finely tuned between the different polymer structures that ‘lock-in’ the state in which they were written. Simulations of the order parameter and director profile from a two-dimensional numerical model based on the Q-tensor method were found to be in good agreement with the experimental observations.

Defects arising between topologically discontinuous liquid crystalline states are conventionally undesirable in commercial displays applications. Yet, a potential

application of the tunable defects was explored in terms of colloidal dispersions, whereby particles were found to migrate towards the defect site such that their position could also be electrically tuned. The ability to control the position of particles could also be used for studies of aggregation-induced emission.

Finally, three-dimensional micron-scale pillars were written at different periodicities, with individual pillars extending into the bulk of the device. Writing the structures at different voltages revealed the ability to electrically tune the birefringence of the polymer network, whereby the structures appeared 'invisible' when the same voltage value was applied across the device post-fabrication. The uniformity between the liquid crystals alignment in the bulk and that in the polymer pillar generated a match in the birefringence so that the structures were no longer distinguishable. This phenomena was further investigated through an image analysis in L*a*b* colorspace, which also revealed that interrogating the device using colour filters or a monochromatic light source reduces the contrast between the pillars and the bulk thereby enhancing their 'invisibility'. The birefringence of the polymer structures could also be spatially tuned as localised effects in the liquid crystal alignment become apparent at lattice spacings smaller than the order of the device thickness. Consequently, structures written within the vicinity of one another appear more pronounced than those written at larger separations. This work has led to the creation of complex polymer structures with covert features embedded in the liquid crystal-polymer device, which could be interrogated to reveal different patterns upon different voltage applications. Crucially, this is the first demonstration of a reconfigurable optical element formed in-situ using a one-step fabrication procedure.

10

FUTURE WORK

The first half of the thesis focused on the use of ionic nematic liquid crystals (LCs) to differentiate between different polar responses and consequently identify the electro-optic response due to flexoelectricity. Although the numerical model developed in Chapter 2 to incorporate the ions reproduced the experimental data well, the data-theory fitting procedure for both the hybrid aligned nematic and pi-cell devices revealed the potential covariance between the model parameters, primarily the flexoelectric coefficients and the ionic concentration. Covariance may generate inaccuracies in the values estimated from the data-theory fits. It would, therefore, be useful to explore the validity of the method through flexoelectric measurements of other LC materials that have varying ionic concentrations, and compare these values to independent measurements of the ionic content, either through conductivity experiments or those reported in literature. Estimations of the ionic concentration combined with the flexoelectric coefficients for a number of materials would clarify the extent of the covariance and any resultant errors in the data-theory measurements, as well as helping to identify whether the assumptions on which the model is based are valid e.g. the ionic screening of the internal bias due to different surface alignment polarities. Future work

could also be carried out to improve the model or reduce the number of assumptions on which it is based i.e. negligible surface interactions.

The experimental work in Chapter 4, successfully demonstrated the creation of chiral polymer templates that can be used to impart distinct properties from one material to another. Yet, discrepancies arose in the obtained electro-optic data, which did not align with the background theory for the constrained pitch study. Further work could therefore be carried out using chiral nematics of different pitches, to obtain a more detailed study of the effect that the imposed pitch has on the constrained pitch and vice versa. In addition, it would be more beneficial to create templates from materials that are synthesized to have large flexoelastic ratios i.e. bimesogens, so as to observe whether the large flexoelectric modulation would be imparted onto non-bimesogenic LCs. If the templating procedure can be reproduced using bimesogens, there would be significant potential for this technique to become commercially viable, since the main challenge in ULH stabilisation is preserving the flexoelectro-optic performance.

To overcome this issue, the high resolution, in-situ direct laser writing (DLW) facility introduced in Chapter 5 permitted the localization of polymer network and significantly improved the device performance. The polymer walls formed in the chiral nematic phase were written at a fixed periodicity, of the order of the device thickness. It may be worth fabricating walls of different periodicities in the future to investigate how the pitch of the material relates to the spacing between the polymer walls. As discussed in Chapter 6, the issue of polymer diffusion might also be addressed through the addition of a monomer to control the phase separation, and the use of dual frequency LCs for fabrication in the nematic phase would remove the dependence on the dielectric

anisotropy of the material, so that the flexoelastic ratio could be enhanced at certain frequencies.

The extension of the DLW work to achiral nematic systems generated interesting phenomena, such as the ability to electrically tune the position of defects in pi-cells. The 2D numerical model developed in Chapter 7 for simulations of the splay-bend walls reproduced the results well. However, the defect was made artificially large to prevent its entrapment at a grid point. A potential improvement might therefore involve employing adaptive grid methods such as local adaptive mesh refinement or finite element methods with mesh adaptivity.

The extension of the tunable defects work to colloidal dispersions led to issues with the consistency in the localization of the particles at the defect sites, whereby some tended to aggregate while others were pinned to the substrate when the device was in the asymmetric H state. The colloids were also too large to diffuse through the nano-porous polymer network. Future work should be carried out to improve the localization of the particles at the defects, initially through the fabrication of 'open' structures between which the position of the colloids can be electrically tuned. It would also be interesting to fabricate structures that induce strong bend-splay distortion fields, for example, a spiralling vortex director pattern. Alternatively, the colloids could be dispersed into the photosensitive mixture before the laser writing commences.

Another challenge that needs to be addressed is improving the dispersion of the colloids so that they remain within the defects, and do not migrate towards the cell substrates. This could be achieved by treating the surface of the particles with a certain surfactant to ensure that they remain within the defect core, or alternatively by working

in a lower voltage regime so that the asymmetric H state does not cause the particle to drift to the cell surface.

Finally, the work presented in Chapter 8 shows great potential for applications in technologies that require covert features, such as barcodes or security tags. The image analysis carried out in L*a*b* did demonstrate the contrast in luminosity and colour between the visible and invisible states. However, there is room for improvement as the luminosity, for example, was only marginally above the Just Noticeable Difference for the largest recorded standard deviation. This could be a point of further investigation when considering applications, such as machine readable systems, in which variations in luminosity are of greater importance to ensure that the encoded pattern is properly detected.

Overall, the fabrication of multi-dimensional polymer structures presented in the latter half of the thesis for the generation of fast-switching photonics states, electrically tunable topological phenomena and reconfigurable optical elements collectively highlight the vast potential of the bespoke DLW technique. One avenue that would be interesting to explore using this technique is in the creation of new liquid crystalline states or phases. Blue phases, which are based on three-dimensional defect lattices, are notoriously difficult to grow and additionally, they exist over a short temperature range. The potential to use the high resolution fabrication system in conjunction with externally applied electric fields to write complex structures that may resemble the morphology of a blue phase could give rise to the formation of artificial phases. Additionally, the experiments presented in this thesis utilized commercial cells to demonstrate the correction of aberrations induced from the thick-glass substrates. It

would be interesting to combine the writing technique with tailor-made cells to explore the creation of nano-scale structures at optical wavelengths.

As a preliminary demonstration of these concepts, examples of 3-dimensional polymer structures are shown that have been written into LC devices with and without the presence of an electric field. Initially, 3-dimensional helical polymer ribbons were fabricated into a 20 µm-thick, nematic Fréedericksz LC device that was filled with the LC - monomer mixture reported in Chapter 5. The helical structures, 10 µm in diameter, shown in the microscope images of Figure 10.1 (a) and (b) were written whilst dynamically switching the electric field through the bulk and under continuous application of the field, respectively. In this example, the device was fabricated with a thin glass coverslip acting as the superstrate, permitting the use of higher numerical aperture objectives (1.4 NA oil immersion lens) that gives a greater resolution (<1 µm) in the axial direction for scanning through the bulk. the polymer helices extend through the bulk of the device from one glass substrate to the other.

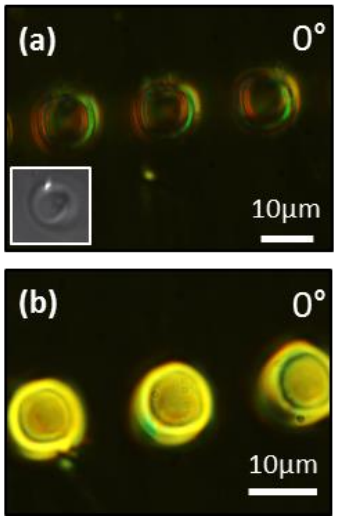


Figure 10.1. Helical ribbons as exotic topological structures. (a) OPM image of a 10 µm diameter helical polymer ribbon fabricated in the absence of an electric field. Inset (bottom left): a snapshot of the structure recorded on the built-in CCD camera of the fabrication system at the point when the laser beam reaches the top substrate. (b) Microscope image of a 10 µm diameter helical polymer ribbon fabricated under the application of an electric field of E = 0.4 V/µm.

Previously, investigations have been carried out on the fabrication of complex topological structures, such as knots in colloidal systems, to investigate self-assembled superstructures of knotted particles and defect networks with nanoparticles [1, 2]. In those cases however there was no control of the alignment of the LC using an in-situ electric field. Inspired by this work and in addition to the helical ribbons, Figure 10.2 shows 3D polymer knots that were fabricated in the presence of an E = 0.4 V/μm electric field. Similar to the ribbons, these knots were also written whilst scanning through the bulk of the device. The higher magnification images in Figure 10.2 (a) reveal how the transmission through the knot varies when the device is rotated between crossed polarizers, marking a clear distinction between the bright and dark optical states.

The electro-optic characteristics of the LC devices containing the polymer knots can be seen in Figure 10.2 (b) for two different applied electric field strengths, oriented in the bright and dark states of the device. The knots that have been circled in each image were written at the same electric field strength (i.e. E = 0.2 V/μm and E = 0.4 V/μm) as the characterization field applied during the image capture. When imaged using the corresponding field strength, it is clearly shown that the alignment of the LC appears continuous between the encircled polymer structures and the surrounding regions. For the remaining polymer structures, which were written at different electric field strengths, there is a clear distinction in the alignment between the region defined by the knots and the surrounding nematic LC. The structures possess unique optical properties on account of the voltage-dependent LC states that are induced during the fabrication procedure. These results therefore show promise for the generation of ‘exotic’ topological structures with intricate features scanning in three dimensions.

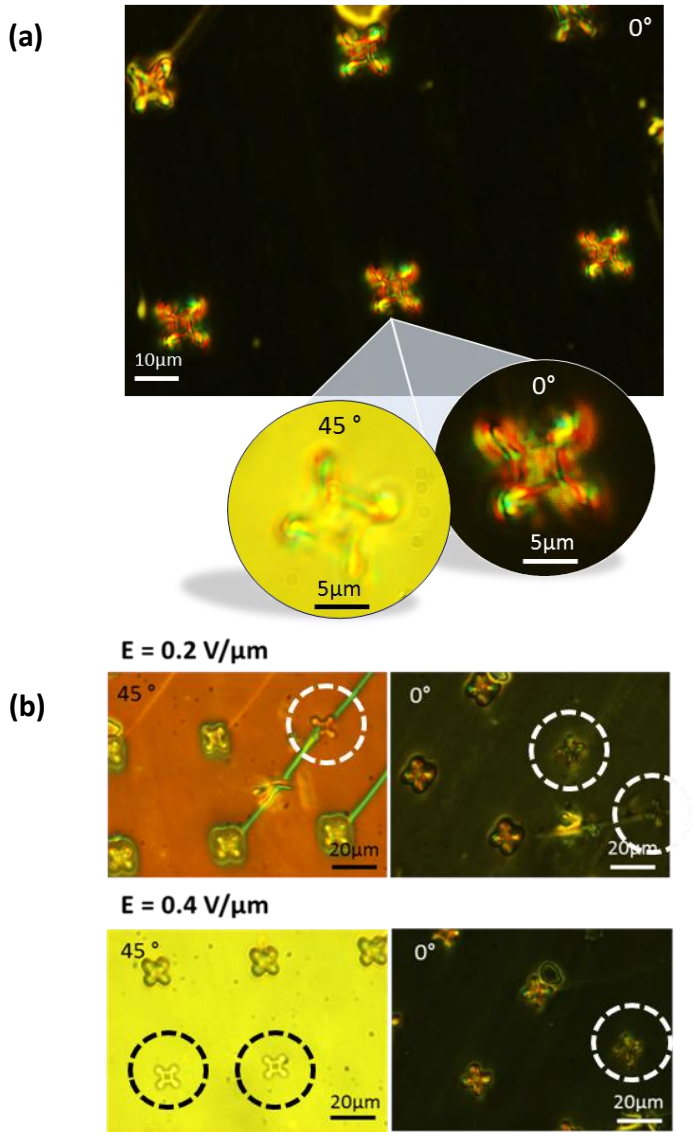


Figure 10.2. 3D polymer knots as exotic topological structures. (a) Microscope image of a 10 µm diameter polymer knot array showing the bright and dark states of an individual knot when rotated between crossed polarizers. (b) Images showing the bright and dark states of the array of knots when rotated between crossed polarizers for different electric field strengths.

10.1. REFERENCES

[1] B. Senyuk, Q. Liu, S. He, R. Kamien, T. Lubensky and I. Smalyukh, *Nature*, **493**, 200 (2013).

[2] Martinez, M. Ravnik, B. Lucero, R. Visvanathan, S. Zumer And I. Smalyukh, *Nat. Mater*. **13**, 258 (2014).

A

APPENDIX

A.1. MATERIAL PARAMETERS

E70

Elastic	K_{11}	10 pN
	K_{22}	5.8 pN
	K_{33}	10.4 pN
Dielectric	$\varepsilon_{//}$	15.77
	$\varepsilon_{\perp}$	5.40
	$\Delta\varepsilon\varepsilon_0$	91.8 pFm^{-1}
Birefringence	$n_{//}$	1.682
	$n_{\perp}$	1.517
	Δn	0.165

Table A.1. E70 parameters at T = 20°C and λ = 632.8 nm (Merck Chemicals Ltd.).

MAT-13-1803

Elastic	K_{11}	24.6 pN
	K_{33}	80.3 pN
Dielectric	$\varepsilon_{//}$	10.9
	$\varepsilon_{\perp}$	3.7
	$\Delta\varepsilon\varepsilon_0$	62.8 pFm^{-1}
Birefringence	$n_{//}$	1.751
	$n_{\perp}$	1.519
	Δn	0.232

Table A.2. MAT-13-1803 parameters at T = 20°C and λ = 589.3 nm (Merck Chemicals Ltd).

E7

Elastic	K_{11}	10.7 pN
	K_{22}	6.5 pN
	K_{33}	16.2 pN
Dielectric	$\varepsilon_{//}$	18.9
	$\varepsilon_{\perp}$	5.2
	$\Delta\varepsilon\varepsilon_0$	121 pFm^{-1}
Birefringence	$n_{//}$	1.738
	$n_{\perp}$	1.519
	Δn	0.219

Table A.3. E7 parameters at T = 20°C and λ = 632.8 nm (Merck Chemicals Ltd).